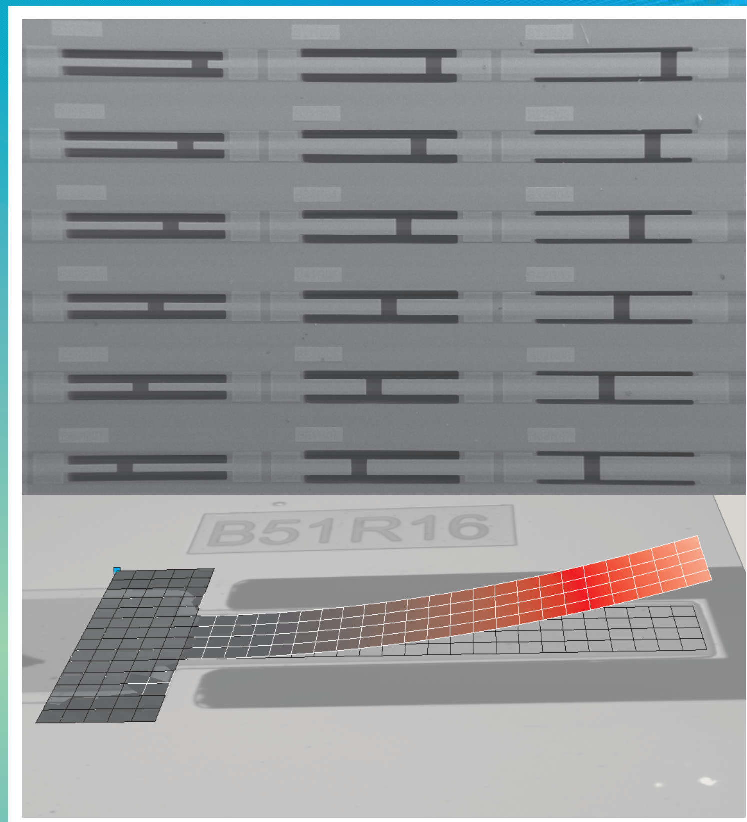

M. D. Nguyen Ferroelectric and Piezoelectric properties of epitaxial PZT films and devices on silicon 2010

Ferroelectric and Piezoelectric properties of epitaxial PZT films and devices on silicon

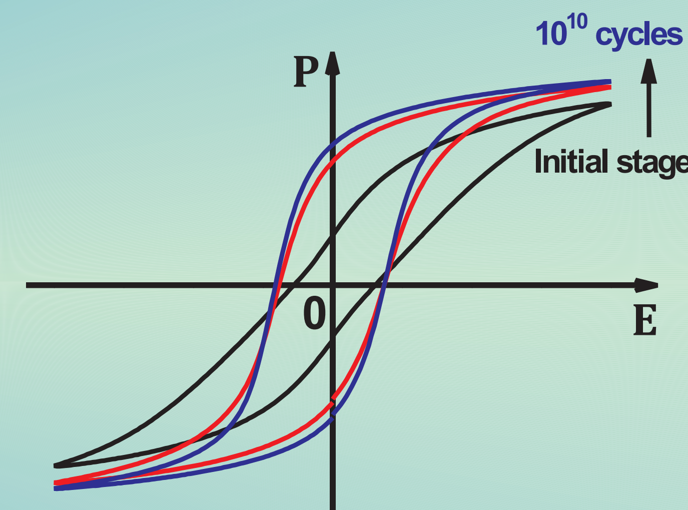

Minh Duc Nguyen

INVITATION

It is my pleasure to invite you to the public defense of my Ph.D. thesis:

Ferroelectric and piezoelectric properties of epitaxial PZT films and devices on silicon

The public defense will take place on Wednesday, June 30th, 2010 at 16:45 in lecture 4 of the Waaier building of the University of Twente.

Prior to the defense, at 16:30, I will give a brief introduction to my thesis. You are welcome to the reception that will follow the promotion and the party in the evening (organized together with my colleague Sajid Khan).

Minh Duc Nguyen
Emmastraat 210-511
7513 BH Enschede
The Netherlands
d.m.nguyen@utwente.nl

Ferroelectric and Piezoelectric properties

of epitaxial PZT films and devices on silicon

Ph.D. Committee:

Chairman and secretary:

Prof. Dr. G. van der Steenhoven	University of Twente

Supervisors:

Prof. Dr. ing. D. H. A. Blank	University of Twente
Prof. Dr. ing. A. J. H. M. Rijnders	University of Twente

Members:

Prof. Dr. K. J. Boller	University of Twente
Prof. Dr. J. Schmitz	University of Twente
Prof. Dr. J. G. E. Gardeniers	University of Twente
Prof. Dr. B. Noheda	University of Groningen
Dr. R. T. F. van Schaijk	IMEC Eindhoven

Cover: The increase of remnant polarization as well as the improvement of the squareness of *P*-*E* loops with increasing cumulative switching cycles for the (110)-oriented PZT thin films grown on $SrRuO_3$ buffered YSZ/Si substrates (*front*); The SEM of PZT cantilever arrays and the displacement of a cantilever beam under the applied voltage (*back*).

The research described in this thesis was carried out at the Inorganic Materials Science department at the Faculty of Science and Technology and the MESA+ Institute for Nanotechnology, University of Twente, The Netherlands. This research was financially supported by the Smart-Mix Program (Smart-Pie) of the Netherlands Ministry of Economic Affairs and the Netherlands Ministry of Education, Culture and Science and by the Vietnamese Overseas Scholarship Program under MOET-VOSP Project 322.

M. D. Nguyen

Ferroelectric and Piezoelectric properties of epitaxial PZT films and devices on silicon

Ph.D. thesis, University of Twente, Enschede, The Netherlands.

ISBN: 978-90-365-3047-7

Printed by Printpartners Ipskamp, Enschede

© M. D. Nguyen, 2010

FERROELECTRIC AND PIEZOELECTRIC PROPERTIES OF EPITAXIAL PZT FILMS AND DEVICES ON SILICON

PROEFSCHRIFT

ter verkrijging van
de graad van doctor aan de Universiteit Twente,
op gezag van de rector magnificus,
prof. dr. H. Brinksma,
volgens besluit van het College voor Promoties
in het openbaar te verdedigen
op woensdag 30 juni 2010 om 16:45 uur

door

Minh Duc Nguyen

geboren op 15 maart 1977
te Ha Tay (Vietnam)

Dit proefschrift is goedgekeurd door:

Prof. Dr. ing. D. H. A. Blank (promotor) en
Prof. Dr. ing. A. J. H. M. Rijnders (co-promotor)

Table of Contents

1 Introduction **9**

1.1 Motivation 10

1.2 Outline of thesis 11

1.3 References 12

2 Fabrication and characterization **15**

2.1 Introduction 16

2.2 Thin film growth by pulsed laser deposition 16

2.2.1 Mechanisms of PLD 16

2.2.2 Experimental setup 17

2.3 Structure of PZT film capacitors 19

2.3.1 Substrates 19

2.3.2 Buffer-layers 20

2.3.3 Conductive-oxide electrodes 20

2.4 Structuring process of SRO/PZT/SRO devices 21

2.5 Characterization techniques 23

2.5.1 Structural analysis 23

2.5.2 Morphological analysis 24

2.5.3 Compositional analysis 25

2.5.4 Electrical characterization 25

2.5.5 Mechanical characterization 30

2.6 Summary and conclusions 31

2.7 References 32

3 Control of crystallographic orientation of epitaxial Pb(Zr,Ti)O_3 thin films **35**

3.1 Introduction 36

3.2 Fabrication and characterization 37

3.2.1 Sample fabrication 37

3.2.2 Characterization 37

3.3 Stability of epitaxial SRO thin films 38

3.4 Control of crystallographic orientation of epitaxial PZT thin films on silicon substrates by a single process step 41

3.5 Effects of substrate types on the crystallinity of PZT thin films 46

	3.5.1	*X-ray diffraction spectra*	47
	3.5.2	*XRD reciprocal space mapping*	50
	3.6	Summary and conclusions	54
	3.7	References	56
4	**Polarization switching and Role of conductive-oxide electrodes**		**59**
	4.1	Introduction	60
	4.2	Experimental procedure	61
	4.3	Switching process of the polarization hysteresis loop	62
	4.4	Polarization fatigue in ferroelectric thin films	64
	4.5	Orientation effects on ferroelectric properties	69
	4.6	Effects of film quality and residual stress on the electrical properties of PZT thin films	73
	4.7	Effect of measuring factors on ferroelectric properties of PZT thin films	77
	4.7.1	*Polarization hysteresis loop*	77
	4.7.2	*Polarization switching*	80
	4.8	Summary and conclusions	83
	4.9	References	84
5	**Dependence of film thickness and composition on ferroelectric properties**		**89**
	5.1	Introduction	90
	5.2	Experimental procedure	90
	5.3	Interfaces between ferroelectric films and electrodes	91
	5.3.1	*Principle of the electrical contact at the interface*	91
	5.3.2	*"Intrinsic" interfacial layer fabrication*	92
	5.3.3	*"Extrinsic" interfacial layer formation*	94
	5.3.4	*Leakage current mechanisms in ferroelectric film capacitors*	95
	5.4	Effect of film thickness on the properties of PZT film capacitors	99
	5.4.1	*PZT films on silicon substrates*	99
	5.4.2	*PZT films on $SrTiO_3$ substrates*	108
	5.5	Effect of Zr/Ti ratio on the properties of PZT thin film capacitors	110
	5.5.1	*PZT thin films on silicon substrates*	110

5.5.2 *PZT thin films on $SrTiO_3$ substrates* 114

5.6 Summary and conclusions 116

5.7 References 117

6 Relationships between ferroelectric and piezoelectric properties in PZT films 121

6.1 Introduction 122

6.2 Experimental procedure 122

6.3 Piezoelectric responses in PZT films 123

6.3.1 *Piezoelectric hysteresis loop* 123

6.3.2 *Piezoelectric displacement response* 127

6.4 Ferroelectric-piezoelectric relationship in PZT films 129

6.4.1 *Film thickness effects* 129

6.4.2 *Zr/Ti composition effects* 131

6.4.3 *Thermal residual stress effects* 132

6.5 Summary and conclusions 134

6.6 References 135

7 Integration of epitaxial PZT films onto silicon cantilever beams 137

7.1 Introduction 138

7.2 Cantilever fabrication and experimental methods 139

7.2.1 *Deposition of multilayer piezoelectric stack* 139

7.2.2 *Cantilever fabrication* 140

7.2.3 *Characterization methods* 141

7.3 Structure and ferroelectric properties of cantilevers 141

7.4 Initial bending of cantilevers 143

7.5 Dynamic behavior of cantilevers 146

7.6 Effect of film thickness and gold-layer coating 153

7.7 Effect of conductive-oxide electrodes 156

7.8 Summary and conclusions 157

7.9 References 158

Summary 161

Samenvatting 165

List of publications 169

Acknowledgements 171

1.
Introduction

1.1 Motivation

To increase the number of applications, both sensing and actuation properties of microelectromechanical systems (MEMS) devices with silicon-based integrated circuits can be significantly increased by incorporating piezoelectric thin films [1-4]. Among piezoelectric thin film materials, $Pb(Zr,Ti)O_3$ (PZT) thin films can offer an attractive option for MEMS technology due to their superior ferroelectric and piezoelectric properties [5].

In order to identify a feasible way to fabricate PZT thin films, some fabrication processes have been proposed to deposit PZT films. Currently, many thin film manufacturing techniques used to obtain high-crystalline quality PZT thin films, including both chemical and physical routes, have been reported. The physical methods include sputter deposition [6-8], pulsed laser deposition (PLD) [9-13], and evaporation [14, 15]. Among the chemical methods, there are metalorganic chemical vapor deposition (MOCVD) [16, 17], plasma enhanced chemical vapor deposition (PECVD) [18, 19], and sol-gel processing [20-24].

Over the past few years, the PLD technique is one of the most popular and versatile for the deposition of thin films [11, 25]. In comparison with other common deposition techniques, the PLD technique offers some advantages. Most important is its ability to transfer material stoichiometrically from a multicomponent target to a growing film. This is very important for complex oxides such as PZT, because their physical properties strongly depend on the precise control of the chemical composition [26]. Second, PLD is a promising technique for thick film fabrication because it offers the advantage of a high deposition rate. Because of high deposition rate in a deposition pulse, the mass transfer from the ablation plume to solid thin films is improved. Therefore, PLD allows deposition at high growth temperature, especially for epitaxial growth of volatile materials. In case of PZT thin film deposition, it results in a less significant loss of the more volatile elements, like lead (Pb).

It is worth noting that the crystalline quality of the ferroelectric film is an important factor. Epitaxial PZT thin films showing high crystalline quality display better ferroelectric and piezoelectric properties than polycrystalline films [27], and the leakage currents are expected to be lower than those of polycrystalline films [28-30]. There is a vast amount of research presenting the fabrication of epitaxial PZT thin films by PLD. However, most of these studies are on single-crystal oxide substrates like $SrTiO_3$ (STO), yttria-stabilized zirconia (YSZ), $LaAlO_3$ (LAO), and MgO [9-12].

For ferroelectric device applications, the epitaxial growth of ferroelectric thin films on silicon substrates is considered to be a key technology for fabricating thinner and smaller electronic devices [28]. In the present study, I present results of all-epitaxial $SrRuO_3$/PZT/$SrRuO_3$ thin film devices which fabricated using the PLD technique. Conductive-oxide electrodes, like $SrRuO_3$ and $LaNiO_3$, are expected to be an important consideration for long-term stability and reliability of the PZT thin film devices [31-34].

1.2 Outline of thesis

The aim of the study described in this thesis is focused on the fabrication and characterization of epitaxial PZT film devices. This thesis consists of seven chapters. In chapter 1, a brief introduction on the PLD technique and epitaxial PZT thin films is presented. Chapter 2 introduces the fabrication of silicon-based PZT thin films by the PLD. As mentioned before, the choice of this technique is based on the required epitaxial growth of all oxide layers.

In order to control the orientation of epitaxial PZT thin films grown on Si substrates, a deposition procedure has been developed for both buffer-layer(s) and bottom-electrode. Chapter 3 describes the control of thin film orientation as well as the optimization process for PZT thin films grown on Si substrates. Furthermore, the effects of residual stress, caused by the substrate/film thermal expansion mismatches, on the crystal and domain orientations of the PZT thin films are also investigated.

In chapter 4, the influence of conductive-oxide electrodes with a perovskite structure such as $SrRuO_3$ (SRO) on the polarization switching (polarization fatigue) process is also discussed. The behavior of polarization switching, due to twin-related domains and in-plane structural coherence in the (110)- and (001)-oriented PZT thin films on Si substrates, respectively, is studied. Thermal residual stress in PZT thin films induced by the difference of thermal expansion between film and substrate is crucial for the domain orientation and therefore, its effect on the ferroelectric and piezoelectric properties are discussed.

In chapter 5 we report the effect of film thickness on the structure and electrical properties of PZT films. The contributions of interfacial layers between PZT films and electrodes, and residual stress between PZT films and substrates on the electrical properties are investigated. Moreover, the PZT thin films with various compositions (Zr/Ti ratios: 60/40, 52/48, 40/60 and 20/80) are also studied. The data, obtained by polarization and dielectric constant measurements, reveals the PZT thin films are strongly dependent on their compounds.

In chapter 6, based on the results found in chapter 5, we describe the effects of the fabrication characteristics of PZT films, such as film thickness, Zr/Ti composition and thermal residual stress, on the piezoelectric coefficients. The main purpose of this study is to discriminate the contribution of domain-wall motion (extrinsic contribution) and lattice variation (intrinsic contribution) on the d_{33} coefficient. Furthermore, elemental factors affecting the d_{33} coefficient, like polarization and dielectric constant, are analyzed based on a semi-empirical equation.

The design and fabrication of epitaxial PZT films integrated onto Si cantilever beams through the PLD technique and MEMS micro-fabrication process is presented in chapter 7. The cantilever performance was characterized by white-light interferometer and for comparison, a finite element analysis (FEA) simulation and a calculation method were carried

out. Finally, the dependences of the cantilever displacement, resonance frequency and quality factor (*Q*-factor) on the cantilever geometry (length, width and film thickness) are investigated.

At the end of this thesis, a summary is given.

1.3 References

1. P. Muralt, *Ferroelectric thin films for micro-sensors and actuators: a review*, J. Micromech. Microeng. **10** (2000) p. 136-146.
2. S. Trolier-McKinstry and P. Muralt, *Thin Film Piezoelectrics for MEMS*, J. Electroceram. **12** (2004) p. 7-17.
3. R. A. Dorey and R. W. Whatmore, *Electroceramic Thick Film Fabrication for MEMS*, J. Electroceram. **12** (2004) p. 19-32.
4. J. Baborowski, *Microfabrication of Piezoelectric MEMS*, J. Electroceram. **12** (2004) p. 33-51.
5. J. F. Scott and C. A. Paz de Araujo, *Ferroelectric Memories*, Science **246** (1989) p. 1400-1405.
6. T. Hata, S. Kawagoe, W. Zhang, K. Sasaki, and Y. Yoshioka, *Proposal of new mixture target for PZT thin films by reactive sputtering*, Vacuum **51** (1998) p. 665-671.
7. C. Wang and M. H. Kryder, *Low Fatigue in Epitaxial $Pb(Zr_{0.2}Ti_{0.8})O_3$ on Si Substrates with $LaNiO_3$ Electrodes by RF Sputtering*, J. Electron. Mater. **38** (2009) p. 1921-1925.
8. R. Bouregba, N. Sama, C. Soyer, and D. Remiens *Analysis of size effects in $Pb(Zr_{0.54}Ti_{0.46})O_3$ thin film capacitors with platinum and $LaNiO_3$ conducting oxide electrodes*, J. Appl. Phys. **106** (2009) p. 044101(1-7).
9. T. Yu, Y. -F. Chen, Z. -G. Liu, S. -B. Xiong, L. Sun, X. -Y. Chen, L. -J. Shi, and N. -B. Ming, *Epitaxial $Pb(Zr_{0.53}Ti_{0.47})O_3/LaNiO_3$ heterostructures on single crystal substrates*, Appl. Phys. Lett. **69** (1996) p. 2092-2094.
10. T. Morita, Y. Wagatsuma, Y. Cho, H. Morioka, H. Funakubo, and N. Setter, *Ferroelectric properties of an epitaxial lead zirconate titanate thin film deposited by a hydrothermal method below the Curie temperature*, Appl. Phys. Lett. **84** (2004) p. 5094-5096.
11. L. Feigl, S. J. Zheng, B. I. Birajdar, B. J. Rodriguez, Y. L. Zhu, M. Alexe, and D. Hesse, *Impact of high interface density on ferroelectric and structural properties of $PbZr_{0.2}Ti_{0.8}O_3/PbZr_{0.4}Ti_{0.6}O_3$ epitaxial multilayers*, J. Phys. D: Appl. Phys. **42** (2009) p. 085305(1-6).
12. D. Walker, P. A. Thomas, and S. P. Collins, *A comprehensive investigation of the structural properties of ferroelectric $PbZr_{0.2}Ti_{0.8}O_3$ thin films grown by PLD*, physica status solidi (a) **206** (2009) p. 1799-1803.

13. M. D. Nguyen, R. J. A. Steenwelle, P. M. te Riele, J. M. Dekkers, D. H. A. Blank, and G. Rijnders, *Growth and properties of functional oxide thin films for PiezoMEMS*, in *EUROSENSORS XXII*, Dresden-Germany (2008) p. 810-813.

14. E. Tokumitsu, S. Ueno, R. -I. Nakamura, and H. Ishiwara, *Characterization of $Pb(Zr_xTi_{1-x})O_3$ films prepared by vacuum evaporation method*, Integrated Ferroelectrics **7** (1995) p. 215-223.

15. B. -E. Park, S. Shouriki, E. Tokumitsu, and H. Ishiwara, *Fabrication of $PbZr_xTi_{1-x}O_3$ Films on Si Structures Using Y_2O_3 Buffer Layers*, Jpn. J. Appl. Phys. **37** (1998) p. 5145-5149.

16. C. -Y. Pan, Y. -L. Chen, and D. -S. Tsai, *Synthesis and properties of lead zirconate titanate thin films via metalorganic chemical vapor deposition*, J. Mater. Res. **17** (2002) p. 1536-1542.

17. Y. Otani, S. Okamura, and Tadashi Shiosaki, *Recent Developments on MOCVD of Ferroelectric Thin Films*, J. Electroceram. **13** (2004) p. 15-22.

18. H. -C. Lee and W. -J. Lee, *Characterization of $Pb(Zr,Ti)O_3$ thin films fabricated by plasma enhanced chemical vapor deposition on Ir-based electrodes*, J. Vac. Sci. Technol. A **20** (2002) p. 1939-1947.

19. H. -C. Lee and W. -J. Lee, *Preparation and Characterization of $Pb(Zr,Ti)O_3$ Films Deposited on Pt/RuO_2 Hybrid Electrode for Ferroelectric Random Access Memory Devices*, Jpn. J. Appl. Phys. **40** (2001) p. 6566-6573.

20. Y. -C. Hsu, C. -C. Wu, C. -C. Lee, G. Z. Cao, and I. Y. Shen, *Demonstration and characterization of PZT thin-film sensors and actuators for meso- and micro-structures*, Sensors and Actuators A **116** (2004) p. 369-377.

21. H. Han, J. Zhong, S. Kotru, P. Padmini, X. Y. Song, and R. K. Pandey, *Improved ferroelectric property of $LaNiO_3/Pb(Zr_{0.2}Ti_{0.8})O_3/LaNiO_3$ capacitors prepared by chemical solution deposition on platinized silicon*, Appl. Phys. Lett. **88** (2006) p. 092902(1-3).

22. A. Bhaskar, T. -H. Chang, H. -Y. Chang, and S. -Y. Cheng, *$Pb(Zr_{0.53}Ti_{0.47})O_3$ thin films with different thicknesses obtained at low temperature by microwave irradiation*, Appl. Surf. Sci. **255** (2009) p. 3795-3800.

23. H. N. Vu, M. V. Le, H. T. Bui, and M. D. Nguyen, *Improvement of electrical property for $Pb(Zr_{0.53}Ti_{0.47})O_3$ ferroelectric thin film deposited by sol-gel method on SRO electrode*, J. Phys.: Conf. Ser. **187** (2009) p. 012063(1-6).

24. T. Schneller and R. Waser, *Chemical modifications of $Pb(Zr_{0.3},Ti_{0.7})O_3$ precursor solutions and their influence on the morphological and electrical properties of the resulting thin films*, J. Sol-Gel Sci. Technol. **42** (2007) p. 337-352.

25. E. J. Tarsa, J. H. English, and J. S. Speck, *Pulsed laser deposition of oriented In_2O_3 on (001) InAs, MgO, and yttria-stabilized zirconia*, Appl. Phys. Lett. **62** (1993) p. 2332-2334.

26. S. Yokoyama, Y. Honda, H. Morioka, S. Okamoto, H. Funakubo, T. Iijima, H. Matsuda, K. Saito, T. Yamamoto, H. Okino, O. Sakata, and S. Kimura, *Dependence of electrical properties of epitaxial $Pb(Zr,Ti)O_3$ thick films on crystal orientation and Zr/(Zr + Ti) ratio*, J. Appl. Phys. **98** (2005) p. 094106(1-8).

27. D. Akai, M. Yokawa, K. Hirabayashi, K. Matsushita, K. Sawada, and M. Ishida, *Ferroelectric properties of sol-gel delivered epitaxial $Pb(Zr_x,Ti_{1-x})O_3$ thin films on Si using epitaxial γ-Al_2O_3 Layers*, Appl. Phys. Lett. **86** (2005) p. 202906(1-3).

28. M. Kondo, K. Maruyama, and K. Kurihara, *Epitaxial ferroelectric thin films on silicon substrates for future electronic devices*, FUJITSU Sci. Tech. J. **38** (2002) p. 46-53.

29. S. Yamauchi and M. Yoshimaru, *Growth of [111]-oriented lead zirconate titanate thin film with smooth surface to improve electrical properties*, Jpn. J. Appl. Phys. **35** (1996) p. 1553-1556.

30. C. J. Kim, D. S. Yoon, J. S. Lee, C. G. Choi, W. J. Lee, and K. No, *Electrical characteristics of (100), (111), and randomly aligned lead zirconate titanate thin films*, J. Appl. Phys. **76** (1994) p. 7478-7482.

31. M. -S. Chen, T. -B. Wu, and J. -M. Wu, *Effect of textured $LaNiO_3$ electrode on the fatigue improvement of $Pb(Zr_{0.53}Ti_{0.47})O_3$ thin films*, Appl. Phys. Lett. **68** (1996) p. 1430-1432.

32. V. Bornand, S. Trolier-McKinstry, K. Takemura, and C. A. Randall, *Orientation dependence of fatigue behavior in relaxor ferroelectric-$PbTiO_3$ thin films*, J. Appl. Phys. **87** (2000) p. 3965-3972.

33. M. Dekkers, M. D. Nguyen, R. Steenwelle, P. M. te Riele, D. H. A. Blank, and G. Rijnders, *Ferroelectric properties of epitaxial $Pb(Zr,Ti)O_3$ thin films on silicon by control of crystal orientation*, Appl. Phys. Lett. **95** (2009) p. 012902(1-3).

34. M. D. Nguyen, H. Nazeer, K. Karakaya, S. V. Pham, R. Steenwelle, M. Dekkers, L. Abelmann, D. H. A. Blank, and G. Rijnders, *Characterization of epitaxial $Pb(Zr,Ti)O_3$ thin films deposited by pulsed laser deposition on silicon cantilevers.* J. Micromech. Microeng. (2010) *submitted for publication.*

2.
Fabrication and characterization

Abstract. This chapter describes the experimental procedures used to fabricate and characterize ferroelectric $Pb(Zr_xTi_{1-x})O_3$ film capacitors. All epitaxial oxide layers are fabricated by the pulsed laser deposition technique and this technique is also discussed in this chapter. The morphological and structural analyses, as well as the electrical and electromechanical characterizations, of ferroelectric capacitors are given in the following sections.

2.1 Introduction

Since laser was first demonstrated in 1960, it has been developed in a powerful tool in many application [1]. Laser possesses many unique properties such as narrow frequency bandwidth, coherence and high power density. Often the light beam is intense enough to vaporize the hardest and most heat resistant materials. Furthermore, due to its high precision, reliability and spatial resolution, it is widely used in material processing industry for machining of thin films, modification of materials, material surface heat treatment, welding and micro-patterning. Apart from these, multi-component materials can be ablated and deposited onto substrates to form stoichiometric thin films. This last mentioned application of laser is the so-called pulsed laser deposition (PLD) [1]. Since the development of high-temperature superconductivity [2, 3], the PLD technique becomes wide spread. Nowadays, the advantages of PLD in the deposition of oxide thin films such as film-to-film reproducibility, accurate stoichiometry, single-phase purity or crystalline orientation have been successfully utilized for many complex ceramics in order to exploit their unique properties. Moreover, the deposition of oxides takes place in a well-controlled oxygen atmosphere, allowing oxygen incorporation in the growing film.

In this chapter, the PLD technique used for growing epitaxial oxide thin films will be addressed in section 2.2. The precisely and well-controlled micro-patterning technology for complete structure to obtain the clear PZT micro-capacitor structure are discussed in sections 2.3 and 2.4. An overview of the analytical tools used to characterize the PZT film capacitors is presented briefly in section 2.5.

2.2 Thin film growth by pulsed laser deposition

2.2.1 Mechanisms of PLD

Epitaxial ferroelectric PZT film capacitors were deposited by pulsed laser deposition (PLD). In principle, PLD is an extremely simple technique which uses pulses of laser energy to remove material from the surface of a target, as shown schematically in Fig. 2.1. In general, the PLD technique involves several complex physical aspects. First, the laser beam is delivered on the solid-target surface. Due to its high-power pulsed radiation and in the short period of the laser pulse, the very high temperature is formed in a small volume of the target leading to immediate decomposition, ionization, and evaporation of the materials (second step). The collection of particles constituting plasma is called the plume. The third step is the transfer of the ablated material through the plume onto the heated substrate surface to form a film. Thus, the thin film formation process in PLD generally can be divided into the following four stages.

i. Laser radiation interaction with the target
ii. Transfer of the ablation material
iii. Deposition of the ablation material on the substrate
iv. Nucleation and growth of a thin film on the substrate surface

Each stage in PLD is crucial for the fabrication of epitaxial thin films of high crystalline quality with uniform orientation, stoichiometry, and surface roughness.

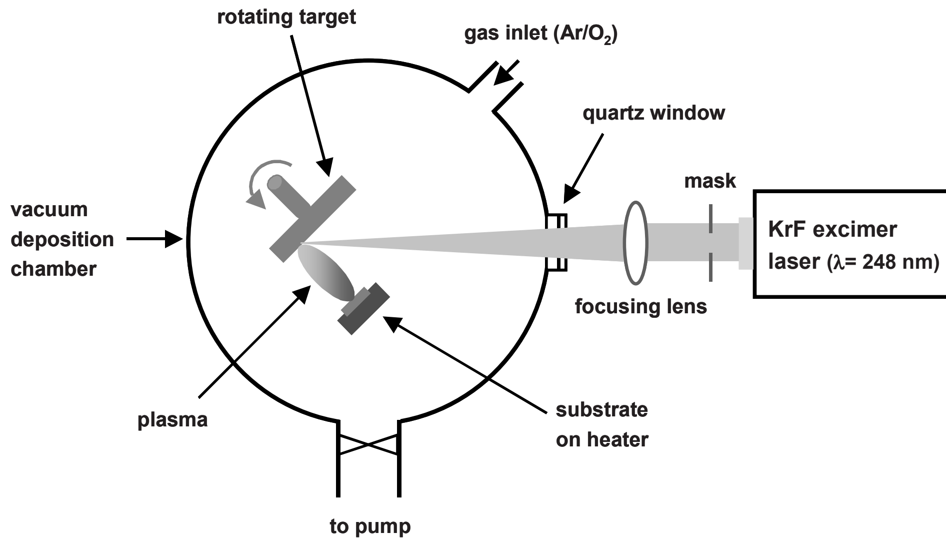

Figure 2.1: Schematic view of a pulsed laser deposition (PLD) setup.

2.2.2 Experimental setup

The experimental set-up, which used in this study, consists of a KrF excimer laser with a wavelength of λ= 248 nm, a pulse duration of 25 ns (FWHM of pulse), and a vacuum system with a base pressure of 10^{-6} - 10^{-7} mbar. A laser pulse energy density of 1-5 J/cm^2 and repetition rate between 1 and 50 Hz is delivered on the target surface depending on the material being deposited. Selection of the beam profile is made by a mask for better homogeneous energy density and control over the plasma expansion dynamics [2]. The laser beam is focused by a lens, passed through the chamber window and is projected at an angle of 45° to the target normal. The laser spot size, in the order of a few square millimeters, can be changed by adjusting the lens and mask positions. To minimize the measurement errors originating from the loss caused by mirrors in the beam path, the deposition energy is measured behind the lens.

During deposition, the pressure inside the chamber can be controlled in the range of 10^{-3} and 10^{0} mbar by changing the flow rate of deposition gas (argon or oxygen) using mass-flow controllers (0-40 ml/minute). To obtain good thermal contact between substrate and heater, the substrate is glued to the heater surface by silver paint [i]. A proportional–integral–derivative (PID) temperature controller is used to adjust the substrate temperature from room temperature (RT) up to 950 ^{o}C.

---

[i] Silver filled epoxy EE129-4, Epoxy Technology, Inc. Billeria, USA

Table 2.1: PLD parameters for YSZ, CeO_2, SRO, and PZT thin films growth.

Parameter	YSZ [i]	CeO_2	$SrRuO_3$ (SRO)	$Pb(Zr_xTi_{1-x})O_3$ (PZT)
Ambient pressure (mbar)	0.02 (Ar/O_2)	0.02 (O_2)	0.13 (O_2)	0.10 (O_2)
Energy density (J/cm^2)	2.1	2.5	2.5	3.5
Deposition temperature (^oC)	800	800	600	600
Laser pulse frequency (Hz)	7	4	4	10
Target-to-substrate distance (mm)	59	58	49	60
Deposition rate (nm/pulse)	0.024	0.041	0.022	0.042

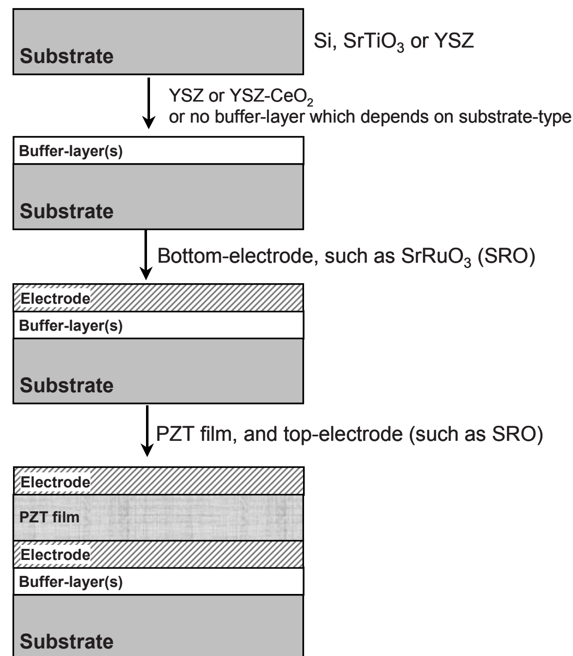

Figure 2.2: Fabrication process of epitaxial PZT film capacitors using PLD technique.

Target-substrate distance, oxygen ambient pressure, deposition temperature, laser pulse energy density and pulse repetition are the main five parameters that need to be optimized to get the desired films. Results of optimum parameters to obtain thin films with good crystalline quality are shown in Tab. 2.1. The fabrication process of PZT film capacitors is illustrated in Fig. 2.2.

[i] 8 mol% yttria-stabilized zirconia (mixture of 8 mol% Y_2O_3 and 92 mol% ZrO_2)

2.3 Structure of PZT film capacitors

2.3.1 Substrates

Silicon (Si) is the most popular substrate for microelectronics and is also widely adopted in MEMS applications. The advantages of silicon are (i) that it is available at low price with a very high surface quality necessary for the subsequent thin film processing, (ii) that it has a good thermal conductivity and (iii) that a large number of processing options and processing tools are available from standard silicon technology. In this thesis, we present results on integration of ferroelectric films with the silicon substrate for both research and applications. In the applications of ferroelectric devices, such as membranes and cantilevers for instance, SOI (silicon on insulator) substrates are frequently used. SOI refers to the use of a layered silicon-insulator-silicon substrate in instead of conventional silicon substrates in semiconductor manufacturing. For research purposes, moreover, the single-crystal substrates (such as $SrTiO_3$, YSZ) are also used.

Table 2.2: Lattice parameters of the materials used for the creation of all oxide PZT piezoelectric and ferroelectric devices. These values are obtained from their ICDD.

Material	***Structure***	***a*** (Å)	***b*** (Å)	***c*** (Å)	***ICDD*** [i]
Si	Cubic	5.43	5.43	5.43	00-001-0787
$SrTiO_3$	Cubic	3.905	3.905	3.905	00-005-0634
YSZ	Cubic	5.14	5.14	5.14	00-030-1468
$Pb(Zr_{0.52}Ti_{0.48})O_3$	Tetragonal	4.05	4.05	4.11	01-070-4060

Substrate cleaning

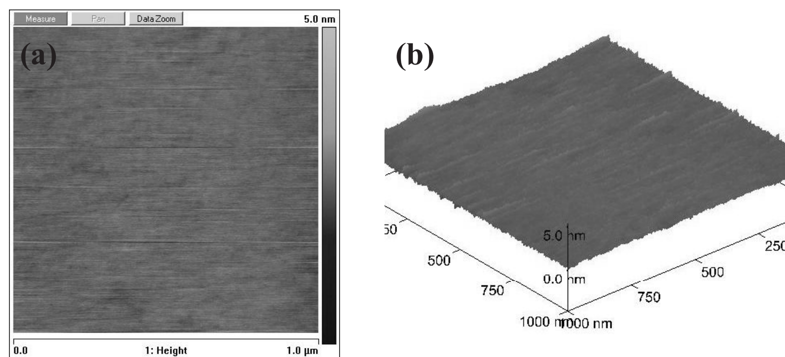

Figure 2.3: The atomic force microscopy (AFM) of silicon (Si) substrate after cleaning: (a) 2-dimensional and (b) 3-dimensional AFM images. Image size is 1×1 μm^2 with a depth scale of 5 μm.

[i] ICDD: International Centre for Diffraction Data (Database code)

First, all substrates were cut down to 10×10 mm^2 or 5×5 mm^2, and then cleaned by ultrasonic cleaning for 10 minutes in acetone and ethanol. The cleaning procedure was repeated until substrates are free of particulates. Figure 2.3 shows the AFM images of the Si substrate after cleaning, and its surface is extremely smooth with a root mean square (RMS) roughness value of 0.16 nm.

2.3.2 Buffer-layer(s)

At the growth temperature (500-650 ^{o}C) of $Pb(Zr,Ti)O_3$ (PZT) films, lead can diffuse into silicon substrate to form lead silicates, which can form a liquid phase. The lead diffusion also may cause degradation of the ferroelectric and piezoelectric properties [3, 4]. In order to prevent this reaction, a buffer-layer such as YSZ, CeO_2 or $SrTiO_3$ was inserted between the PZT film and the silicon substrate. Among these buffer-layers, YSZ is widely used because it has high chemical stability, high resistivity and a large relative dielectric constant of about 30 at room temperature (ε_{YSZ}~30, ε_{SiO2}~3.9) [5]. Moreover, YSZ layer can grow heteroepitaxially on silicon substrate.

2.3.3 Conductive-oxide electrodes

Epitaxial $SrRuO_3$ (SRO) thin films, one of the conductive materials (perovskite), are not only a promising candidate for electrode materials in electroceramic-based devices [8-10], it also plays an important role in buffer technology for improving the quality of the device layer in multi-layers systems [6, 7]. It has a quasi-cubic perovskite structure with a cell parameter of 3.92 Å. Moreover, SRO films are well-known for their remarkable chemical stability, which is very important for the performance of MEMS with PZT films as the active layers. In this process, PZT thin films are patterned by chemical wet-etching in the HF/HCl solution. The etching process for the PZT thin films will be presented in section 2.4.

The close chemical and structural similarity between SRO electrodes and the functional materials (e.g., PZT) minimize interface electrochemical reactions, charge injection in PZT layer and other detrimental processes. Thus, the fatigue resistance of PZT thin films can be improved. Figure 2.4 shows the structure of PZT film capacitors, which depends on the substrate-type, or the purpose of fabrication.

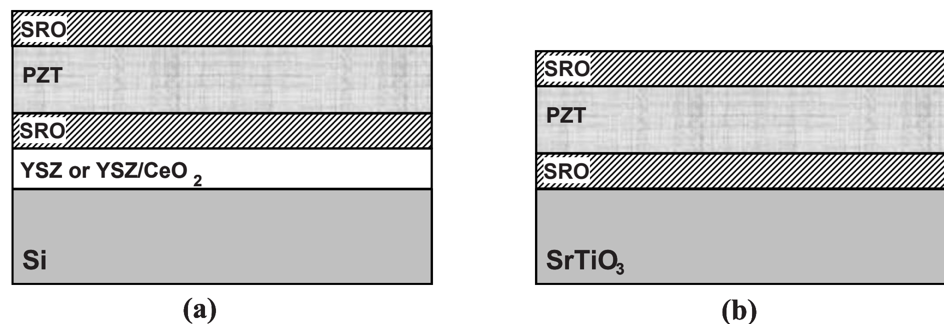

Figure 2.4: A schematic of the structure of PZT film capacitor grown on (a) Si and (b) STO substrates.

2.4 Structuring process of SRO/PZT/SRO devices

MEMS usually consist of a stack of different material layers, which are conformably deposited on each other; photolithography and etching processes are used for the structuring [8]. To incorporate PZT into silicon micro-electronics technology, we developed an etch process for PZT thin film-patterning. Etching the PZT thin film is an essential step in the device fabrication process and has attracted considerable attention in recent years. However, depending on the electrode-type such as metal (Pt) or oxide electrode ($SrRuO_3$, $LaNiO_3$), a suitable wet-etching process is developed.

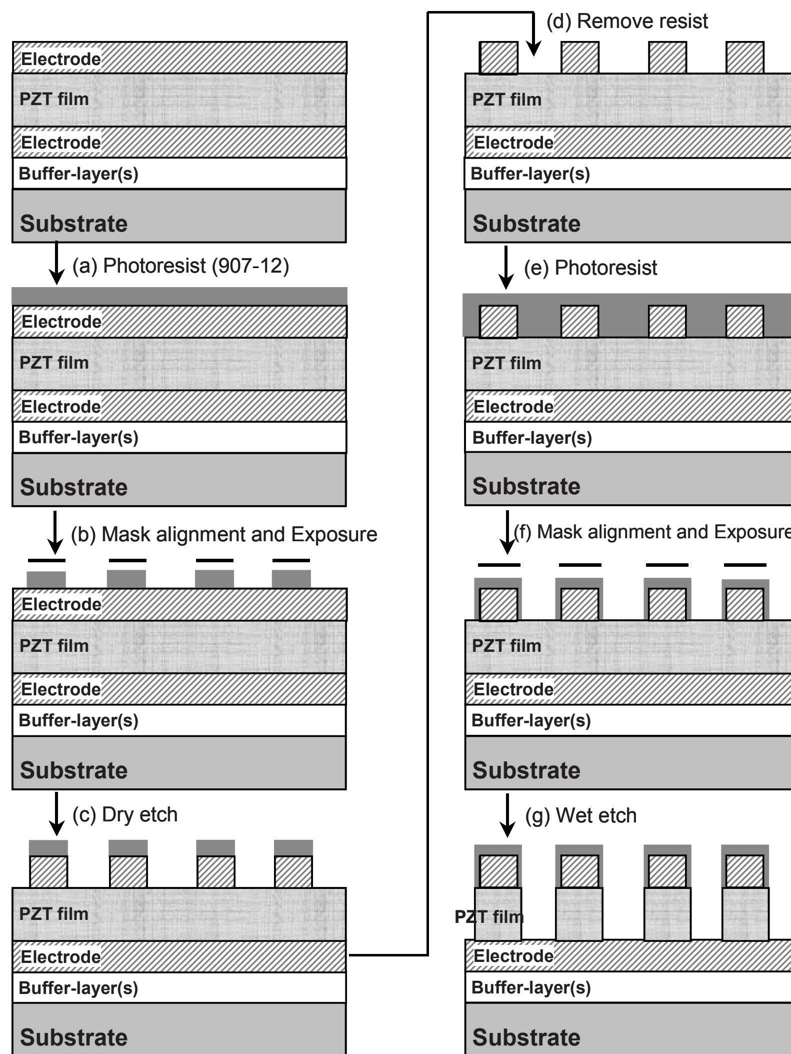

Figure 2.5: Flow diagram for etching process of epitaxial PZT film capacitors.

In general, various dry-etching processes, including reactive ion etching (RIE) [9], ion-beam etching (IBE) [10] or electron cyclotron resonance (ECR) plasma [11] have been developed to pattern PZT films. However, the RIE or IBE process may decrease the electrical properties because of physical damage and chemical residue contamination. Another problem of IBE is the carbonization of the photoresist layer, which results from the bombardment of the high-energy ion beam (Ar gas) during long-time etching. The carbonized photoresist is very hard to remove completely.

Compared with dry-etching, wet-chemical etching a PZT thin film is a conventional and effective technique due to its high etching rate and low cost. In this thesis, we used a process for PZT thin film wet-etching using BHF or a modified wet etching recipe solution as the etchant. Figure 2.5 shows the positive lithography and etching processes of PZT film MEMS devices. The whole process consists of two main steps namely patterning the SRO top electrode and patterning the PZT layer.

Because SRO electrode is well-known for its remarkable chemical stability, and then it is not affected by the wet-etch patterning (in HF acid) of the PZT thin films. In this thesis, the etch process for SRO/PZT/SRO structure is as follows:

- SRO top-electrode is etched by Ar-beam dry-etching: etching rate ~ 10 nm/minute (Fig. 2.5(c)).
- PZT is etched by BHF (HF 12.5%), as shown in Fig. 2.5(g).

Table 2.3: Wet-etching process for SRO/PZT/SRO structure patterning.

Step	Process	Remark
1	BHF (HF 12.5%) $Pb(Zr_xTi_{1-x})O_3 + 6H^+ \rightarrow Pb^{2+} + xZr^{4+} + (1-x)Ti^{4+} + 3H_2O$ Note: Formation of metal-fluoride residues on bottom-electrode surface and dissolving them with HCl solution.	Etching rate: 10 nm/s
	Deionized (DI) water rinsing and nitrogen gun drying	Check resistance
2	HCl (16%) solution at 45 ^oC	Time: 20-30 s
	DI rinsing and nitrogen gun drying	Check surface cleaning
3	Results after wet-etching process: • Resistance (use of two-point probe) of bottom-electrode: 30-60 Ω (or 2-4 mΩ.cm) • Clean etched surface	

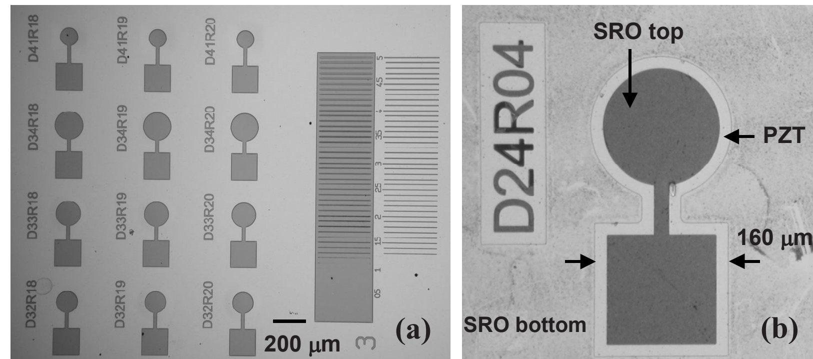

Figure 2.6: Optical photomicrograph of PZT film devices.

Figure 2.6 shows the top-views of PZT/SRO film devices after completion. It can be seen that the etched bottom surface is very clean and residue-free. SEM image of an obtained PZT-electrode stack pattern is shown in Fig. 2.7(b). The edge profile (undercutting) of the obtained PZT pattern after etching is about 2-5 μm and clear PZT patterns with low undercutting and high selectivity can be achieved.

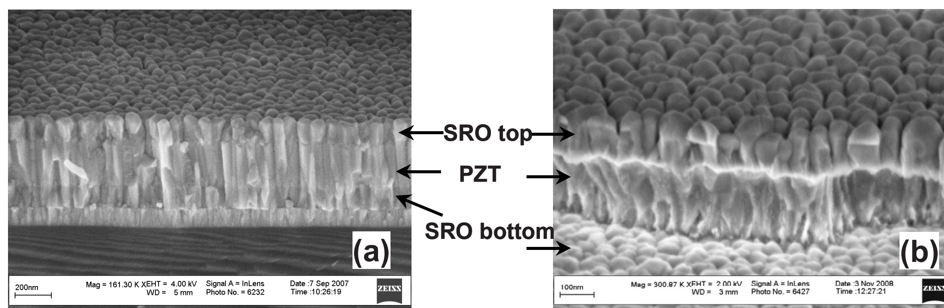

Figure 2.7: (a) Cross-sectional SEM image PZT/SRO film capacitor and (b) Side-view SEM image of an obtained PZT-electrode stack. The thickness of the PZT film was 250 nm.

2.5 Characterization techniques

2.5.1 Structural analysis

X-ray diffraction (XRD) [12] is used to obtain crystal structure information of the sample. Our routine XRD experiments were performed by high-resolution x-ray diffraction (Bruker D8 Discover) with a Cu-Kα cathode in Bragg-Brentano geometry [i]. This system operates at 40 kV and 40 mA with the minimum resolution of 0.001°. The crystalline structure is analyzed by performing several scans, such as θ-2θ scans, rocking curve (ω-scans) and phi-

[i] This measurement is performed at Inorganic Materials Science group (MESA+, University of Twente, The Netherlands)

scans (ϕ-scans) to determine orientation, epitaxy, and quality of samples. Moreover, x-ray reciprocal space mapping is recorded to measure in-plane lattice parameters.

2.5.2 Morphological analysis

A Scanning Electron Microscope (SEM) [13] is a type of electron microscope that images the sample surface by scanning it with a high-energy beam of electrons in a raster scan pattern which could be seen in the image on the display screen. The resulting image is similar to what would be seen through an optical microscope: the illumination and shadowing show a natural-seeming topography. However, the SEM can produce images of high resolution, which means that closely spaced features can be examined at a high magnification. SEM surface analysis was carried out on Zeiss-1550 HRSEM (Zeiss, Germany) operating between 0.2 and 30 kV [i]. The lateral resolution is 1.5 nm at 20 kV or 3 nm at 1 kV and the magnification is 40-1.500.000 times. Film-growth structure and film-thickness were also performed using cross-sectional SEM.

Atomic Force Microscopy (AFM) is a sensitive force measurement instrument. The force sensitivity of the AFM probe is related to the spring constant (*k*) of cantilever tip and the distance between the tip and the sample surface (*z*) [14].

$$F = -k.z \tag{2.1}$$

The AFM is operated in either of two modes: contact mode and tapping mode. In contact mode, the vertical deflection signal is used to provide the dynamic feedback signal for surface height tracking. In tapping mode, on the other hand, forces may be observed by measuring changes in the tip deflection, phase or root-mean-square (RMS) amplitude. The specifications of the AFM tips for contact mode and tapping mode is shown in Tab. 2.4.

Table 2.4: Parameters for AFM tips [ii]

	Contact mode	**Tapping mode**
Cantilever-type	n^+-silicon, ρ=0.01-0.02 Ω.cm, Al coating	
Thickness/length/width	2±1 μm/450±10 μm/50±7.5 μm	4±1μm/125±10μm/30±7.5μm
Resonance frequency	6 - 21 kHz	204 - 497 kHz
Spring constant (*k*)	0.02 - 0.77 N/m	10 - 130 N/m
Tip height	10 - 15 μm	

The contact-mode AFM was performed on a Multimode Scanning Probe Microscope (Veeco, Digital Instruments, Santa Barbara, USA), with a Digital Instruments Nanoscope III

[i] This measurement is performed at the Central Materials Analysis Laboratory (MESA+, University of Twente, The Netherlands)

[ii] AFM tips are supported by NANOSENSORS™

controller [i]. This measurement is done by sensing the repulsive force between the probe tip and the surface. The tip is then scanned over the area of interest on the sample and the topography of sample with atomic resolution would be observed. The maximum scan range is 50×50 μm^2.

2.5.3 Compositional analysis

X-ray photoelectron spectroscopy (XPS) data is collected by a PHI Quantera Scanning ESCA Microprobe [ii]. This analysis tool is based on the photo electrical effect and is a quantitative spectroscopic technique that measures the elemental composition, chemical state and electronic state of the elements that exist within a material [15].

The XPS technique is highly surface specific due to the short escape depth of the photoelectrons that are excited from the solid. The energy of the photoelectrons leaving the sample is determined using a HDA (Hemispherical Deflection Analyser) and this gives a spectrum with a series of photoelectron peaks. The binding energy of the peaks is characteristic of each element. The peak areas can be used (with appropriate sensitivity factors) to determine the composition of the materials surface. The shape of each peak and the binding energy can be slightly altered by the chemical state of the emitting atom. In this thesis, XPS is used to quantify the surface composition and depth-profile of a film or a complete structure of a capacitor.

2.5.4 Electrical characterization

Polarization hysteresis loop

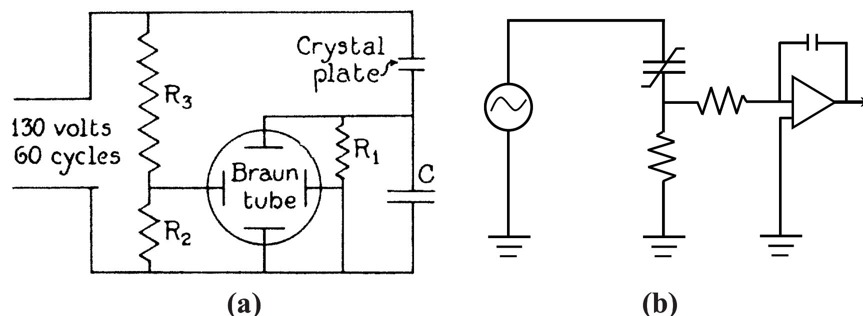

Figure 2.8: (a) The original Sawyer-Tower circuit and (b) The modified Sawyer-Tower circuit for polarization hysteresis loop measurement.

---

[i] This measurement is performed at Inorganic Materials Science group (MESA+, University of Twente, The Netherlands)

[ii] This measurement is performed at the Central Materials Analysis Laboratory (MESA+, University of Twente, The Netherlands)

One of the key measurements for ferroelectric materials is, naturally, the measurement of the polarization hysteresis loop. The Sawyer-Tower circuit [16], as shown in Fig. 2.8(a), is well-known as the (first) traditional hysteresis loop measurement setup, and this circuit has been modified to avoid noise by applying a virtual ground [17] (Fig. 2.8(b)). Nowadays, most testing of the ferroelectric capacitors is carried out using commercial apparatus available from one of two companies, Radiant Technologies and aixACCT. Both machines can carry out the polarization hysteresis loop and they also offer automated measurement of characteristics such as fatigue, imprint and retention. In this thesis, ferroelectric properties of PZT film capacitors have been measured using the ferroelectric mode of an aixACCT Analyzer TF2000 [i].

Ferroelectrics possess spontaneous polarization whose direction may be reversed by applying an opposite external electrical field. The polarization switching process can be depicted by a polarization-electric field (*P*-*E*) hysteresis loop diagram and is characterized by the following parameters: applied electric field (*E*), remnant polarization (P_r), switchable polarization (P_{sw}), nonswitchable polarization (P_{ns}). The hysteresis measurement parameters shown in Fig. 2.9 are defined as follows: $E_{c(+)}$-the point at which the hysteresis loop intersects the positive *x*-axis and $E_{c(-)}$-the point at which the hysteresis loop intersects the negative *x*-axis.

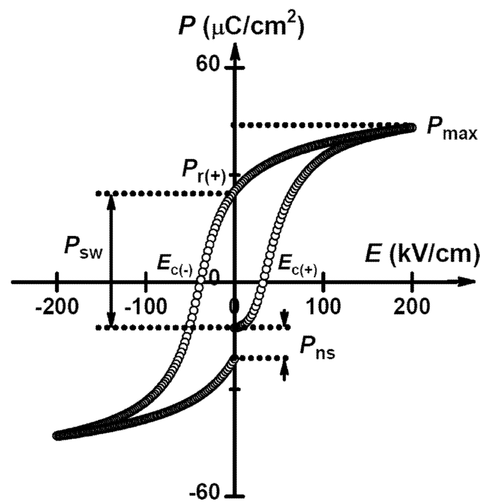

Figure 2.9: Notation for switching characteristics extracted from the polarization hysteresis loop.

A pulse response is measured after each hysteresis measurement. The pulse response is measured using triangular pulses with a 1 second delay between each pulse. The pulse widths are in range of 50-0.25 milliseconds (10-2000 Hz frequency).

[i] This measurement is performed at Inorganic Materials Science group (MESA+, University of Twente, The Netherlands)

Polarization switching (fatigue) behavior

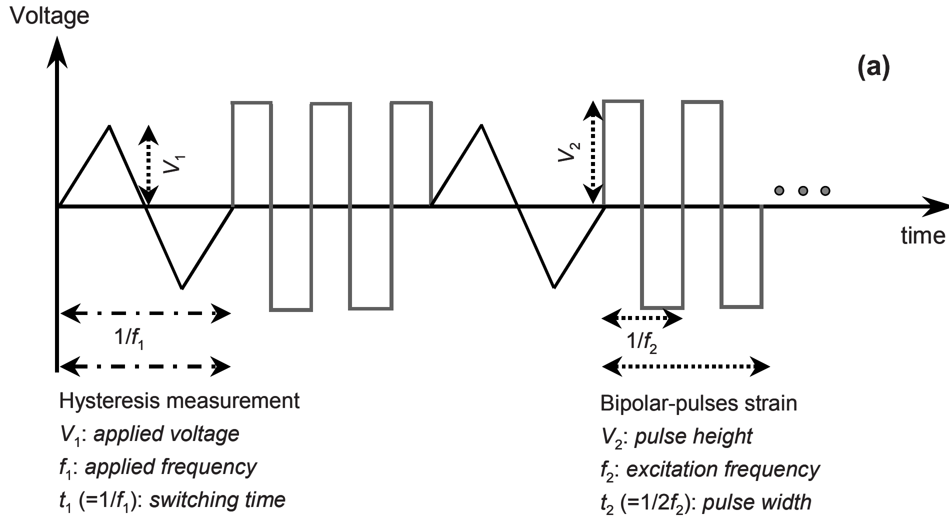

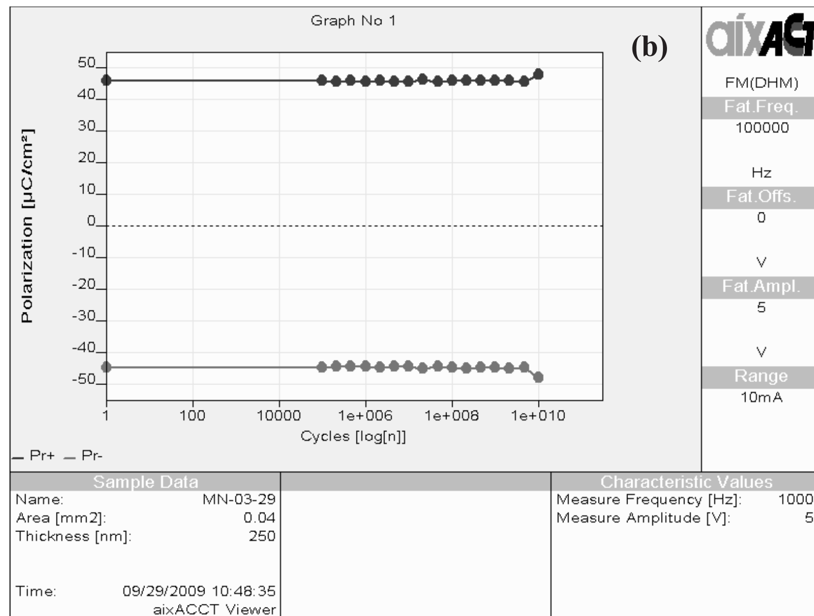

Figure 2.10: (a) Sketch of the typical fatigue excitation signal, and (b) Remnant polarization (P_r) of the (001)-oriented SRO/PZT/SRO/STO capacitors, for instance, as a function of cumulative switching cycles using bipolar pulses of 200 kV/cm (pulse height) in combination with the pulse width corresponding to the 100 kHz (pulse width ~ 5 microseconds) and the *P-E* loops were measured at ±200 kV/cm (5 V) amplitude and 1 kHz frequency.

The influence of amplitude and frequency of the rectangular excitation signal can be investigated as the number of switching cycles. After measuring an initial hysteresis, the fatigue signal sequence (see e.g. Fig. 2.10(a)) is applied to the sample. The fatigue treatment is interrupted regularly for hysteresis measurements. These intermediate hysteresis measurements are performed with time intervals in such a way that in a logarithmic plot data points are depicted with an equal spacing. This procedure is similar for all fatigue (polarization switching) measurements.

A typical result of a fatigue measurement combined with hysteresis is shown in Fig. 2.10(b), for the (110)-oriented PZT thin films grown on SRO/YSZ/Si substrates. It displays the remanent polarization of the in between recorded hysteresis loops versus the logarithm of the total number of cycles. These remnant polarization values can be extracted from their polarization hysteresis (*P-E*) loops.

The occurrence of polarization switching is usually described by plotting P_r, P_{sw}, or P_{ns} as a function of the number of switching cycles in log scale. The terminology used in Fig. 2.8 is associated with the determination of the switching parameters of ferroelectric capacitors by voltage (or electric field) pulses where P_{sw} and P_{ns} are obtained by integration of the current response for both polarities. An alternative terminology exists when the ferroelectric capacitors are tested with voltage steps. In this case, $P^* = P_{sw} + (P_{max} - P_r)$ represents the switched polarization, whereas $P\hat{} = P_{ns} + (P_{max} - P_r)$ represents the nonswitched polarization.

Capacitance and leakage current measurements

Capacitance is a measurement of the electric charge stored in the dielectric materials. A common form of charge storage device is a parallel-plate capacitor which shown in Fig. 2.11. In a parallel-plate capacitor, capacitance is directly proportional to the surface area of the conductor plates and inversely proportional to the separation distance between the plates. The capacitance was measured as the function of applied electric field (*C-E)* and frequency (*C-f*) in the range of 10 kHz - 1 MHz frequency and a small *ac* signal of 4 kV/cm.

The dielectric constant (ε) and dielectric loss ($\tan\delta$) can be calculated if the geometry and the capacitance value of the ferroelectric layer between the electrode-conductors are known. The capacitance and dielectric constant (or dielectric loss) are related according to:

Dielectric constant (ε)

$$\varepsilon = \frac{Cd}{\varepsilon_0 A} \tag{2.2}$$

and *dielectric loss (*$\tan\delta$*)*

$$\tan\delta = \frac{G}{2\pi fC} \tag{2.3}$$

where,

- C is the capacitance in farads, [F].
- A is the area of overlap of the two plates measured in square meters, [m^2]. Capacitance is directly proportional to the surface area of the conductor plates or sheets.
- ε is the dielectric constant (permittivity) of the material between the plates.
- ε_0 (= 8.854×10^{-12} F/m) is the dielectric constant of free space.
- d is the separation between the plates (or PZT film thickness), measured in meters [m].
- G is the conductance, (Siemens, [S]).
- f is the frequency in hertz, [Hz] .

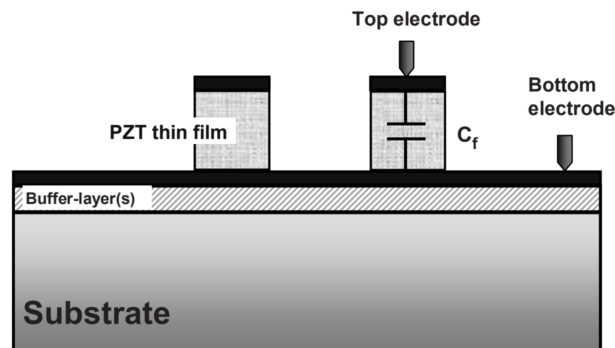

Figure 2.11: Schematic drawing of the parallel-plate ferroelectric capacitors.

The leakage current is an important characteristic of thin film ferroelectric capacitors. It directly limits the charge retention and it influences the polarization hysteresis loop. The leakage current is strongly dependent on the material aspects of the ferroelectric film and of the film-electrode interfaces. In this thesis, the leakage current density-electric field (*J*-*E*) measurements are carried out by applying *dc* electric field.

Measurements of the capacitance and leakage current were performed using a Süss MicroTech PM300 (SUSS MicroTec Test Systems GmbH / Germany) manual probe station equipped with Keithley 4200 Semiconductor characterization system (Keithley Instruments GmbH / Germany) [i].

[i] These measurements were performed at Measure & Test Centre, University of Twente, The Netherlands.

2.5.5 Mechanical characterization

A laser Doppler vibrometer (LDV) is a scientific instrument that is used to make non-contact vibration measurements of a surface [18, 19]. The laser beam from the LDV is directed at the surface of interest, and the vibration amplitude and frequency are extracted from the Doppler shift of the laser beam frequency due to the motion of the surface. The output of an LDV is generally a continuous analog voltage that is directly proportional to the target velocity component along the direction of the laser beam. A schematic of a typical laser vibrometer is shown in Fig. 2.12. In this thesis, a Polytec MSA-400 Micro-scanning laser Doppler vibrometer was used to determine the piezoresponse of PZT film capacitors and PZT film cantilevers.

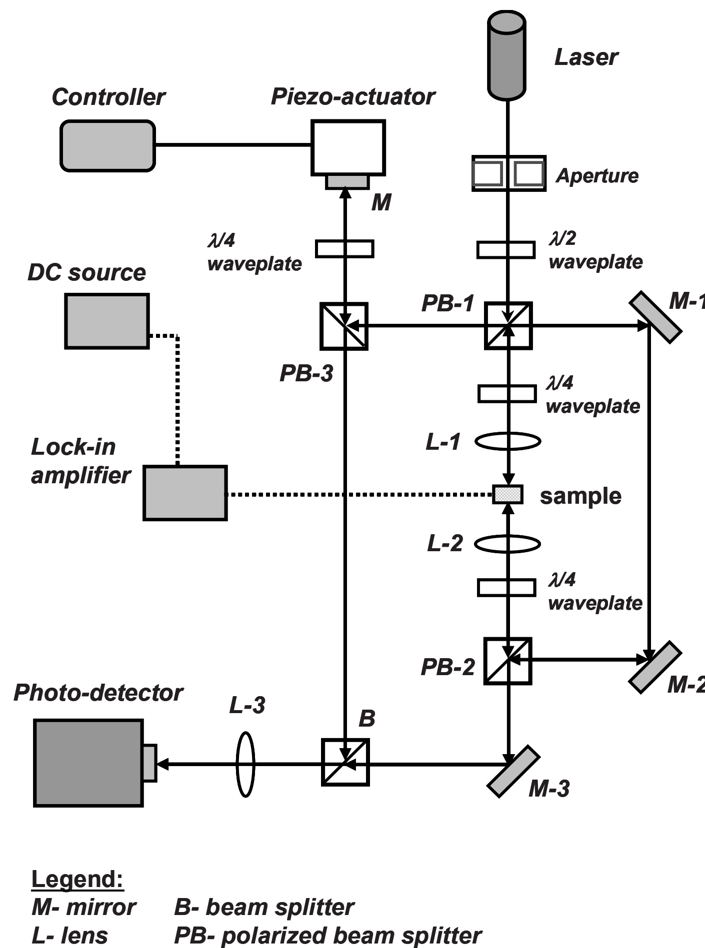

Figure 2.12: Schematic of the double beam laser interferometer used to determine the piezoelectric properties of PZT film capacitors and the displacement of PZT film cantilevers.

As can be seen in Fig. 2.12, the laser beam of a stabilized He-Ne laser (wavelength λ = 632.8 nm) is rotated with a $\lambda/2$ waveplate and then divided by the polarizing beam splitter PB-1 into a measurement beam and a reference beam. The measurement beam leads through a $\lambda/4$ waveplate and the lens L1 to the polished backside of the sample, which is placed perpendicular to the beam. After being reflected by the two 45° placed mirrors M-1 and M-2, the measuring beam is reflected by the PB-2, goes through a $\lambda/4$ waveplate and is then reflected toward M-3. From here the beam is directed to the photodiode passing the beam splitter B. The reference beam is deflected from PB-3 toward a reference mirror passing a $\lambda/4$ waveplate, where the beam is reflected passing PB-3 again and is then deflected by beam splitter B to the photodiode, where the superposition of the measurement and reference beam causes an interference pattern.

Piezoelectric hysteresis loop

A lock-in amplifier (Stanford Research System, SR830) with *ac* signal generator capability is connected to a PC. A Labview® program was developed to control the signal applied to the sample and for the data reading from the lock-in, so that the measurement can be carried out automatically and remotely controlled via network (dotted lines). The piezoelectric coefficient (d_{33}) can be defined from $d_{33}(E)$ hysteresis loop which calculated using Eq. (2.4):

$$d_{33} = \frac{\partial S_{\lambda}}{\partial E_i} = \frac{d_0}{U_m} . \frac{t}{x} \qquad (2.4)$$

where, the symbol S_{λ} denotes the strain tensor component, E_i is the components of electric field intensity, and U_m is the *ac* driving voltage; *x* and *t* are the corresponding length in the direction of capacitor and ferroelectric film thickness, respectively.

Electromechanical large-signal (displacement of capacitor or cantilever) and small-signal (piezoelectric hysteresis loop) measurements are performed with LDV, whereby typical measurement conditions are (1) large-signal measurements: *ac* signal of from 1 to 6 V at 8 kHz frequency and (2) small-signal measurements: *dc* sweep bias from –200 kV/cm to +200 kV/cm, superimposed with a small *ac* signal of 8 kV/cm at 8 kHz frequency.

2.6 Summary and conclusions

A short description of PLD, the deposition technique used for the experiments described in this thesis, and analysis tools such as XRD, AFM, SEM are given. PLD can be distinguished from other thin film deposition techniques by the high energy of material particles arriving at the substrate surface, the high deposition rate, and in-situ growth of all epitaxial oxide thin films. The combination of substrate types, substrate temperature and ambient pressure of buffer layer(s) and electrode can control the orientation and quality of the PZT films.

The performance of PZT film capacitors is tested by several electrical measurements, such as dielectric response, leakage current and polarization characterization. Moreover, the LDV technique was used to measure the piezoelectric coefficient of PZT capacitors and the displacement of PZT cantilevers. Data on the structure, morphology and composition was obtained by XRD, SEM, AFM and XPS.

2.7 References

1. D. B. Chrisey and G.K. Hubler, *Pulsed Laser Deposition of Thin Films*, Wiley-Interscience, New York (1994).
2. P. te Riele, *Direct patterning of oxides by pulsed laser stencil deposition*, PhD thesis, University of Twente, The Netherlands (2008).
3. F. F. C. Duval, R. A. Dorey, R. W. Wright, Z. Huang, and R. W. Whatmore, *Fabrication of PZT composite thick films for high frequency membrane resonators*, J. Electroceram. **13** (2004) p. 267-270.
4. S. Horita, T. Naruse, M. Watanabe, A. Masuda, T. Kawada, and Y. Abe, *Interface control of* $Pb(Zr_xTi_{1-x})O_3$ *thin film on silicon substrate with heteroepitaxial YSZ buffer layer*, Appl. Surf. Sci. **117-118** (1997) p. 429-433.
5. S. J. Wang, C. K. Ong, L. P. You, and S. Y. Xu, *Epitaxial growth of yittria-stabilized zirconia oxide thin film on natively oxidized silicon wafer without an amorphous layer*, Semicond. Sci. Technol. **15** (2000) p. 836-839.
6. J. R. Contreras, H. Kohlstedt, U. Poppe, R. Waser, and Ch. Buchal, *Surface treatment effects on the thickness dependence of the remanent polarization of* $PbZr_{0.52}Ti_{0.48}O_3$ *capacitors*, Appl. Phys. Lett. **83** (2003) p. 126-128.
7. J. H. Kim, A. T. Chien, F. F. Lange, and L. Wills, *Microstructural and ferroelectric properties of a chemical solution deposited epitaxial* $PbZr_{0.5}Ti_{0.5}O_3$ *thin film on a* $SrRuO_3/SrTiO_3$ *substrate*, J. Mater. Res. **14** (1999) p. 1190-1193.
8. J. Baborowski, *Microfabrication of Piezoelectric MEMS*, J. Electroceram. **12** (2004) p. 33-51.
9. K. Saito, J. H. Cho, T. Fukuda, and M. Ohue, *Reactive Ion Etching of Sputtered* $PbZr_{1-x}Ti_xO_3$ *Thin Films*, Jpn. J. Appl. Phys. **31** (1992) p. L1260-L1262.
10. C. Soyer, E. Cattan, and D. Rèmiens, *Ion beam etching of PZT thin films: Influence of grain size on the damages induced*, J. Eur. Ceram. Soc. **25** (2005) p. 2269-2272.
11. S. Yokoyama, Y. Ito, K. Ishihara, K. Hamada, S. Ohnishi, J. Kudo, and K. Sakiyama, *High-Temperature Etching of PZT/Pt/TiN Structure by High-Density ECR Plasma*, Jpn. J. Appl. Phys. **34** (1995) p. 767-770.
12. M. Birkholz, *Thin Film Analysis by X-Ray Scattering*, Wiley (2006).

13. J. Goldstein, D. E. Newbury, D. C. Joy, C. E. Lyman, P. Echlin, E. Lifshin, L. C. Sawyer, and J. R. Michael, *Scanning Electron Microscopy and X-ray Microanalysis*, Springer Science+Business Media Inc., New York (2003).
14. C. R. Blanchard, *Atomic Force Microscopy*, Chem. Educator **1** (1996) p. S1430-4171(96)05059-5.
15. J. F. Moulder, W. F. Stickle, P. E. Sobol, and K. D. Bomben, *Handbook of X-ray Photoelectron Spectroscopy*, Perkin-Elmer Corporation, Eden Prairie, USA (1992).
16. C. B. Sawyer and C. H. Tower, *Rochelle Salt as a Dielectric*, Phys. Rev. **35** (1930) p. 269-273.
17. Y. T. Tsui, P. D. Hinderaker, and F. J. McFadden, *New Ferroelectric Hysteresis Curve Tracer Featuring Compensation and Virtual Sample Grounding*, Rev. Sci. Instrum. **39** (1968) p. 1423-1424.
18. W. Y. Pan and L.E. Cross, *A sensitive double beam laser interferometer for studying high-frequency piezoelectric and electrostrictive strains*, Rev. Sci. Instrum. **60** (1989) p. 2701-2705.
19. A. L. Kholkin, Ch. Wutchrich, D. V. Taylor, and N. Setter, *Interferometric measurements of electric field-induced displacements in piezoelectric thin films*, Rev. Sci. Instrum. **67** (1996) p. 1935-1941.

3.

Control of crystallographic orientation of epitaxial $Pb(Zr,Ti)O_3$ thin films

Abstract. $Pb(Zr,Ti)O_3$ (PZT) thin films between conductive-oxide $SrRuO_3$ (SRO) electrodes were prepared using pulsed laser deposition on CeO_2/yttria-stabilized zirconia buffered (001)-silicon substrates. Different deposition conditions for the initial layers of the bottom SRO electrode result in an orientation switch. Either (110)- or (001)-oriented SRO thin films are obtained and the PZT films deposited on the bottom electrode continued growth in both directions.

The effects of the residual stress (either tensile or compressive stress) induced during cooling from growth temperature to room temperature on the domain structures of epitaxial (001)-oriented PZT thin films were studied on different substrates, such as (001)CeO_2/YSZ/Si, (001)$SrTiO_3$/Si, (001)CeO_2/YSZ, and (001)$SrTiO_3$. It is clarified that compressive stress develops in the PZT films on YSZ or STO substrates, because the coefficient of thermal expansion for the YSZ and STO substrates are larger than that for the PZT films. On the other hand, the coefficient of thermal expansion for the Si substrate is smaller than that for the PZT films; hence, tensile stress developed in the PZT films on CeO_2/YSZ/Si and $SrTiO_3$/Si substrates during the cooling process.

3.1 Introduction

The substrate effect on the properties of ferroelectric thin films has been observed in epitaxial PZT thin films grown on Pt/$SrTiO_3$ [1], and oxide-electrode such as $SrRuO_3$/$SrTiO_3$ [2] and $LaNiO_3$/$SrTiO_3$ [3]. It is shown that controlling the orientation of PZT thin films can be realized easily by using its corresponding orientation of single-crystal $SrTiO_3$ substrates. In applications, however, the integration of ferroelectric films on silicon is used which leads to additional functionalities for the integrated circuit, including on-chip power capacitors, vibration sensors and actuators [4-7].

The advantages of silicon are (i) that it is available at reasonable price with a very high surface quality necessary for the subsequent thin film processing, (ii) that it has a good thermal conductivity, and (iii) that a large number of processing options and processing tools are available from standard silicon technology. It is well known that the heat-treatment process could have an effect on the orientation of ferroelectric films on silicon substrates. Under appropriate heat-treatment control, both (100) and (111)-oriented PZT films prepared by sol-gel technique on the (111)Pt/Ti/SiO_2/Si substrates can be obtained [8, 9]. The (111)-oriented films were obtained by rapidly heating the film to 700 °C for 30 minutes while the (100)-oriented films can be obtained by first pyrolysis at 400 °C for 30 minutes and then by annealing at 700 °C for 30 minutes in air.

For ferroelectric device applications, however, the epitaxial growth of ferroelectric thin films on a silicon substrate is considered to be a key technology for fabricating thinner and smaller electronic devices, because their leakage currents are expected to be lower than those of polycrystalline films [10-12]. Moreover, epitaxial PZT films also exhibited better ferroelectric and pyroelectric properties than polycrystalline PZT films [13]. The orientation of epitaxial PZT thin films is usually studied separately from the type of buffer layers, since different buffer layers or electrode materials are required to switch the crystal orientation of epitaxial PZT films on silicon. Hou *et al*. [14] have studied the growth of perovskite compounds such as Ba(Sr,Ti)O_3 and $SrRuO_3$ (SRO) oxide electrode on the (001)YSZ/Si substrate. The epitaxial relationships between YSZ and these perovskite compounds are (110) of perovskite || (001) of YSZ layer and Si substrate. In the ferroelectric films, the polarization is maximum in the direction perpendicular to the substrate surface. The polarization of ferroelectric film is rotated 45° with respect to the substrate surface if the film is (110) orientation. Then, the polarization of the (110)-oriented film is smaller than that of the (001)-oriented one. In order to change the orientation of PZT thin films from (110) to (001) directions, Kondo *et al*. [10] and Nordseth *et al*. [15] have used CeO_2 as a second buffer-layer.

In section 3.4, we propose the use of an YSZ thin film as a buffer layer and a CeO_2 thin film as a second buffer layer to control the orientation of perovskite materials such as SRO and PZT. Moreover, epitaxial growth of PZT thin films also depends on growth conditions of the bottom SRO electrode like temperature and ambient pressure.

In ferroelectric thin films, especially in epitaxially grown films, the residual stress induced by lattice-matching constraints between the film and the substrate has a strong influence on crystalline properties, domain structure, as well as ferroelectric and piezoelectric properties [16-20]. In general, residual stress builds up in the ferroelectric thin films during the fabrication process, which consists of three main parts: (1) Thermal stress is induced by the thermal expansion mismatch between the film and the substrate; (2) Extrinsic stress is due to the lattice mismatch between the film and the substrate; and (3) Intrinsic stress is relaxed by the phase transformation occurring near the Curie temperature. Residual stress in ferroelectric thin films, however, mainly due to thermal expansion mismatch between the film and the substrate, can be divided into two types: tensile and compressive stresses. The ferroelectric properties of PZT films were also strongly influenced by the residual stress where P_r was found to increase with increasing compressive stress [21].

It is well known that the residual stress is also closely related to the domain orientation in the ferroelectric films. The tensile stress was believed to stabilize domains parallel to the film surface (*a*-domain structure); whereas, compressive stress favored polarization alignment perpendicular to the film plane (*c*-domain structure) [22]. In section 3.5, we investigate the details of the crystalline structure of the PZT thin films on CeO_2/YSZ/Si, STO/Si, CeO_2/YSZ and $SrTiO_3$ substrates to clarify the effect of the substrate on the domain structure and thermal residual stress of PZT thin film.

3.2 Fabrication and characterization

3.2.1 Sample fabrication

Ferroelectric $PbZr_{0.52}Ti_{0.48}O_3$ (PZT) thin films and top/bottom SRO electrodes were deposited by pulsed laser deposition on YSZ/Si(001), CeO_2/YSZ/Si(001), and single crystal CeO_2/YSZ(001) and $SrTiO_3$ (STO, 001) substrates. More details of the pulsed laser deposition (PLD) parameters have been reported in chapter 2. The processing parameters used during the deposition of each layer on different substrates are also summarized in Tab. 3.1. Prior to deposition, Si, YSZ, and STO substrates of $5 \times 5 \times 0.5$ mm^3 dimension were ultrasonically degreased in acetone and ethanol.

3.2.2 Characterization

The orientation of the deposited films was analyzed by high-resolution x-ray diffraction (HRXRD: θ-2θ scan, ω-scan, ϕ-scan) using a Bruker D8 diffractometer. XRD reciprocal space mapping (XRD-RSM) was measured to estimate the out-of-plane and in-plane lattice parameters. The surface roughness (rms) was studied by atomic force microscopy (AFM; Digital Instruments Nanoscope III - Veeco). The thickness and growth-type (granular- or columnar-structures) of the films were observed and measured by high-resolution

scanning electron microscopy (HRSEM; Zeiss 1550). More details of measurements have been reported in chapter 2.

Table 3.1: Table of deposition parameters for PZT film capacitors on different substrates.

***Parameters*/ Substrates**	**YSZ**	**CeO_2**	**SRO-bottom electrode**	**PZT film**	**SRO-top electrode**
Deposition temperature (^oC)	800	800	600	600-650	600
Pressure (mbar / gas)	0.02-Ar/O_2 [i]	0.02-O_2	0.13-O_2	0.10-O_2	0.13-O_2
Fluence (J/cm^2)	2.1	2.5	2.5	3.5	2.5
Thickness (nm)	100	25	100	250	100
Si(001)	x		x	x	x
Si(001)	x	x	x	x	x
STO/Si(001)			x	x	x
YSZ(001)		x	x	x	x
STO(001)			x	x	x

3.3 Stability of epitaxial SRO thin films

Epitaxial perovskite-type SRO thin films have interesting physical and structural properties. Metallic SRO is also a promising candidate for electrode material in electroceramic-based devices [23-25], due to its good conductivity and its high chemical stability [26].

Surface studies of the SRO layer as well as its integration into the device fabrication process are hindered by the chemical stability of oxide surfaces. In order to investigate the chemical behavior of SRO thin films, the thermodynamic behavior in the SrO-RuO_2-SrO system in the SRO layer has been analyzed. Depending of the partial pressure of oxygen and temperature during fabrication, the decomposition of SRO can include oxidation and loss of Ru in an oxygen rich atmosphere [27].

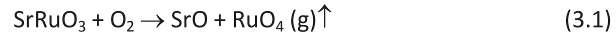

$$SrRuO_3 + O_2 \rightarrow SrO + RuO_4\,(g)\uparrow \quad (3.1)$$

At high temperature ($T_{deposition}$ > 700 ^oC, for instance) and under a strongly reducing oxygen environment, $SrRuO_3$ reduces causing formation of metallic ruthenium (Ru) and SrO with possible formation of intermediate $Sr_{n+1}Ru_nO_{3n+1}$ phases [27, 28]:

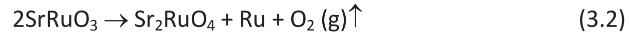

$$2SrRuO_3 \rightarrow Sr_2RuO_4 + Ru + O_2\,(g)\uparrow \quad (3.2)$$

$$SrRuO_3 \rightarrow SrO + Ru + O_2\,(g)\uparrow \quad (3.3)$$

[i] The growth process of YSZ film on Si substrate was divided into 2 stages: The first 5 nm of YSZ was deposited in argon ambient (Ar; 0.02 mbar) and then continuously in oxygen ambient (O_2; 0.02 mbar).

Because of the higher volatility of Ru, the stoichiometric ratio of Sr and Ru can be changed drastically at the high deposition temperature [29], then the reaction (3.2) can be rewritten as:

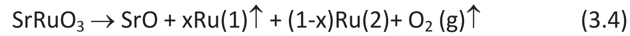

$$SrRuO_3 \rightarrow SrO + xRu(1)\uparrow + (1\text{-}x)Ru(2) + O_2\,(g)\uparrow \qquad (3.4)$$

where Ru(1) is the amount of ruthenium evaporation and Ru(2) is the metallic ruthenium ($0< x <1$). The SrO layer formed during the deposition of the $SrRuO_3$ layer at high deposition temperature is a semiconductor [30].

The thermal evolution of X-ray photoelectron spectroscopy (XPS) spectra of in the 0-1000 eV range for different deposition temperatures (T_s) of the SRO layers, grown on CeO_2/YSZ/Si substrates, is illustrated in Fig. 3.1. According to XPS data, the ratio of elements Sr/Ru is 1.10/1.00 and 1.96/1.00 for SRO layers deposited at 600 and 800 ^oC, respectively.

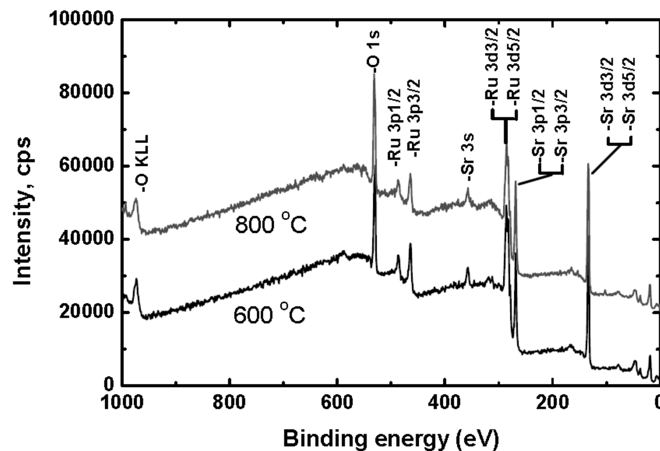

Figure 3.1: XPS spectra from SRO layers deposited at 600 and 800 ^oC.

The evolution of O 1s, Sr 3p, Sr 3d, Ru 3p and Ru 3d peaks is shown in Fig. 3.2. The XPS analysis suggests that the intensity of Ru- and O-peaks decreases while the intensity of Sr-peaks increases with increasing deposition temperature from 600 to 800 ^oC. The quantitative analysis of Sr, Ru, and O peaks ratio suggest that the final stoichiometry of the surface of SRO layers are:

(i) $SrRuO_3$ with the ratio of Sr/Ru is 1.10/1.00 at T_s = 600 ^oC.

(ii) Sr_2RuO_4 and/or mixture of SrO and metallic Ru with the ratio of Sr/Ru is 1.96/1.00 at T_s = 800 ^oC.

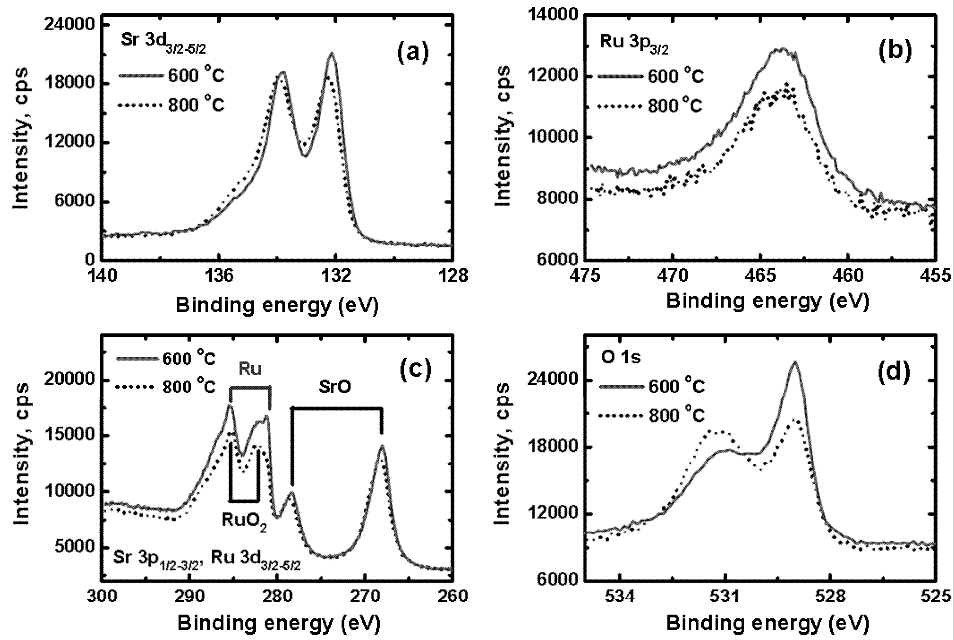

Figure 3.2: XPS spectra in the range of (a) 260-300 eV (Sr $3d_{3/2\text{-}5/2}$), (b) 455-475 eV (Ru $3p_{3/2}$), (c) 260-300 eV (Sr $3p_{1/2\text{-}3/2}$ and Ru $3d_{3/2\text{-}5/2}$) and (d) 525-535 eV (O 1s) for different deposition temperature of the SRO layers grown on CeO_2/YSZ/Si at 600 and 800 ^{o}C.

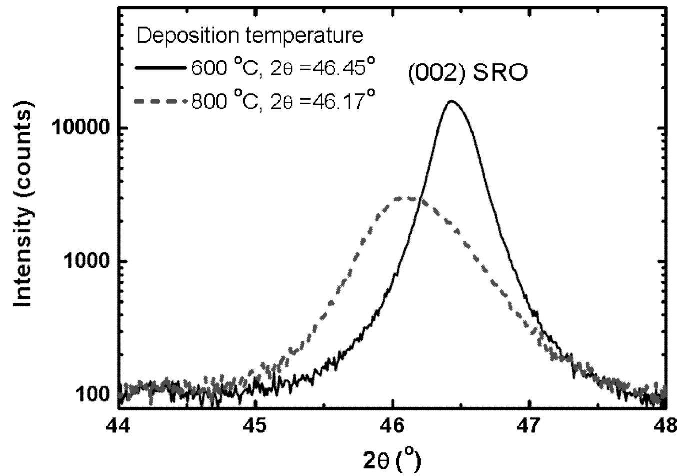

Figure 3.3: Comparison of θ-2θ XRD scans of two 100-nm-thick SRO thin films grown on SRO(1ML) buffered CeO_2/YSZ/Si by PLD. 1 monolayer (ML, ~4 Å thick) of SRO is first deposited at 800 ^{o}C and low oxygen pressure (< 10^{-5} mbar).

In order to get a quantitative indication of the ruthenium loss at high deposition temperature, the change in lattice parameters of two 100-nm-thick (001)-oriented SRO thin films grown on CeO_2/YSZ/Si substrates at 600 and 800 ^oC is measured. As can be seen in Fig. 3.3, the out-of-plane lattice constant of the SRO thin film grown at 800 ^oC (a=3.927 Å) is larger than that of film grown at 600 ^oC with a=3.906 Å. The larger lattice constant of SRO thin film grown at higher temperature can be explained by the Ru-deficiency due to the volatility [31, 32].

3.4 Control of crystallographic orientation of epitaxial PZT thin films on silicon substrates by a single process step

YSZ grows epitaxially on silicon, and can scavenge the native oxide on the surface of the substrate [33]. This allows reproducible coherent growth on non HF-dipped Si substrates. Details concerning the deposition process of YSZ buffer-layer on Si substrates can be found in chapter 2. The crystal structure of the SRO (c=3.94 Å) electrode and the YSZ (c=5.14 Å) buffer-layer are perovskite and fluorite (CaF_2), respectively, and $(110)_{pc}$ SRO || (001) YSZ. If the c-axis is normal to the plane of the (001) YSZ, the unit cells of the $(001)_{pc}$ SRO and the (001) YSZ ($c/\sqrt{2}$ =3.635 Å) layers are rotated by 45° to each other, $(001)_{pc}$ SRO || (001) YSZ, and then the lattice mismatch is 7.74%. Cerium oxide (CeO_2, c=5.41 Å) also grows epitaxially with a cube-on-cube alignment on a YSZ thin film [34, 35]. The in-plane mismatch between the fluorite CeO_2 and pseudocubic SRO is only 2.89% if the perovskite cube is rotated 45° and then CeO_2 ($c/\sqrt{2}$ =3.826 Å) is often used as a second buffer layer to overcome the large mismatch between YSZ and perovskites such as SRO ($(001)_{pc}$ SRO || (001) CeO_2 || (001) YSZ). Since the perovskite PZT almost matches SRO, its crystallographic growth orientation consequently continues that of the underlying electrode.

In order to investigate the effect of the buffer-layer(s) on the orientation of PZT thin films, PZT/SRO layers are deposited on YSZ/Si substrates with and without a second buffer-layer of CeO_2. Figures 3.4(a) and 3.4(b) indicate that the PZT thin films deposited on the buffer-layers all show a (110)-preferred orientation, such as (110) PZT || (110) SRO || (001) YSZ || Si and (110) PZT || (110) SRO || (001) CeO_2 || (001) YSZ || Si, respectively. However, a slight change in the XRD peak intensity and FWHM values of each PZT film was observed in Fig. 3.4(d), in which the higher intensity and slight lower FWHM of (110) PZT peak for film deposited on YSZ/Si than that of film on CeO_2/YSZ/Si.

The in-plane epitaxial relationship between the buffer-layers and the Si substrate was established by the ϕ-scans of the CeO_2(202), YSZ(202) and Si(202) reflections, as shown in Fig. 3.4(c). The rotation angle ϕ of the (202) peak of CeO_2 and YSZ coincides with that of silicon. This indicates that the cube-on-cube epitaxial orientation relationship with the substrate is obtained for both CeO_2 and YSZ layers, described by (001) CeO_2 || (001) YSZ || (001) Si.

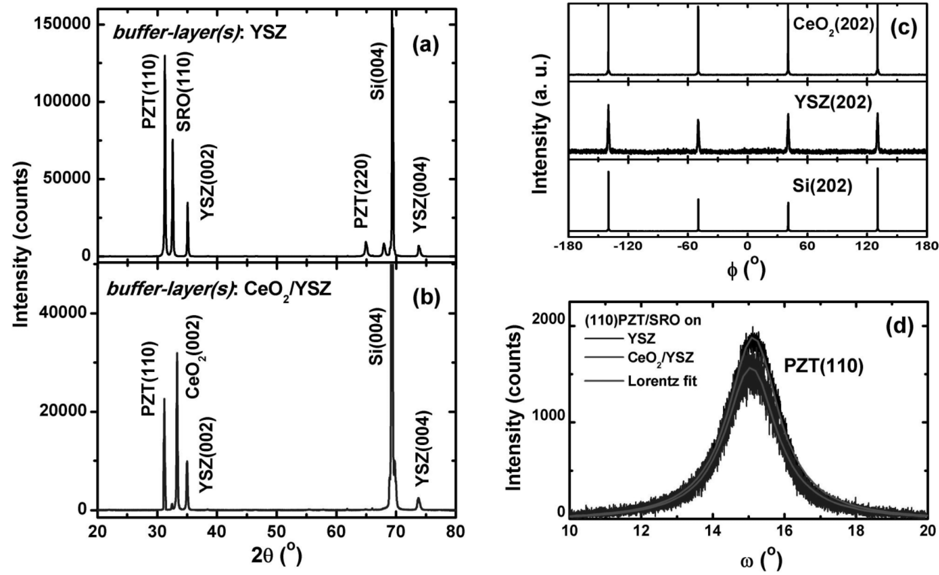

Figure 3.4: θ-2θ X-ray diffractograms of PZT thin films grown on (a) SRO/YSZ/Si(001) and (b) SRO/CeO_2/YSZ/Si(001) substrates. The PZT films show preferred (110) orientation in both cases; (c) and (d) are ϕ-scan profiles of CeO_2(202), YSZ(202) and Si(202) reflections, and rocking curves recorded for the PZT(110) peaks, respectively. The full-width at half maximum intensity (FWHM) of PZT(110) peaks were 1.54 and 1.60^{o} if the films deposited on SRO/YSZ/Si and SRO/CeO_2/YSZ/Si substrates, respectively.

In-plane analysis of the (110)-oriented PZT/SRO thin films by means of ϕ-scans is shown in Fig. 3.5(b). Four identical sets of peaks of SRO(002) deflections are positioned around the reflections corresponding to Si(202). However, instead of a single peak positioned at the Si(202) position, the intensity is divided over two peaks situated at +10° and –10° with respect to Si. This in-plane rotation corresponds to an alignment of the SRO(111) unit-cell body diagonal with the (110) face diagonal of CeO_2 as illustrated in Figs. 3.6(a) and 3.6(b). Since two SRO(002) peaks are expected in a perfect crystal, this means that twin domains exist in the thin film.

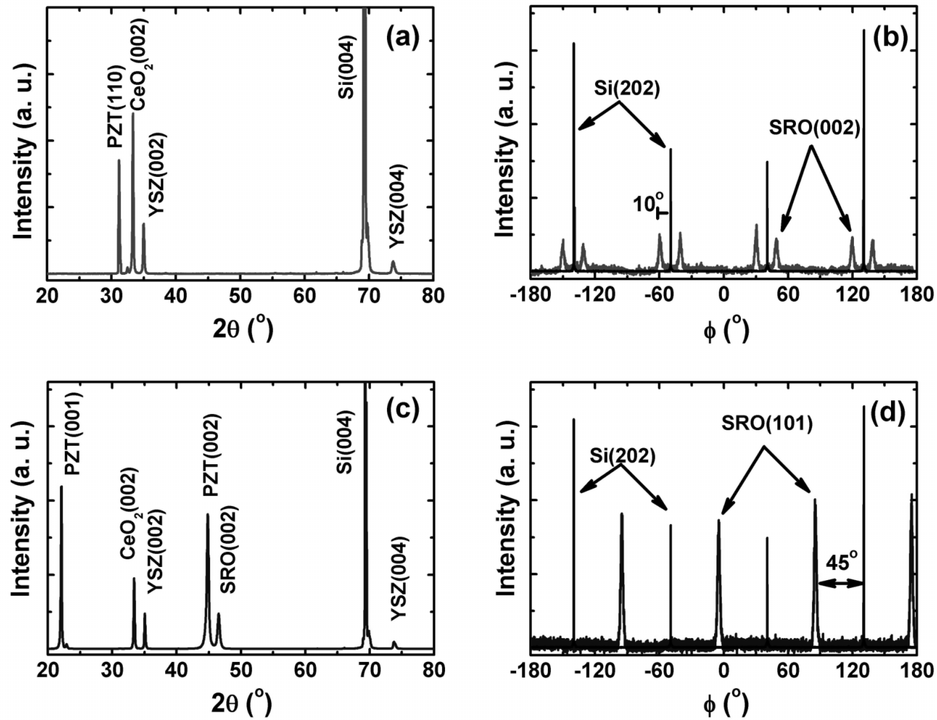

Figure 3.5: XRD patterns of PZT/SRO thin films on (001) CeO_2 || (001) YSZ || (001) Si: (a) (110)-oriented and (c) (001)-oriented of PZT thin films, respectively. ϕ-scan profiles of SRO(002) and Si(202) reflections of the (b) (110)-oriented PZT/SRO and (d) (001)-oriented PZT/SRO layers grown on CeO_2/YSZ/Si substrates.

This in-plane epitaxy has been earlier observed by Hou *et al*. [14] on the single buffer layer of YSZ. These authors assumed that the (111) SRO || (110) YSZ/Si arrangement was preferred over the 45° rotated cube-on-cube (110) SRO || (001) YSZ/Si relation because of the smaller mismatch of the former compared to the latter. Since CeO_2 is used as a second buffer layer, however, the lattice mismatch is larger in our case. Nevertheless, the (111) SRO || (110) YSZ/Si in-plane epitaxy is still preferred. We assume that the specific stoichiometric ratio of the elements during the growth of the first SRO monolayer is responsible for this preferred orientation. Sr and Ru are both present on the CeO_2 surface after the first pulses as both materials are ablated in equal amounts from the stoichiometric target. The SRO unit cell consists of a layered SrO–RuO_2–SrO structure. Given that both Sr and Ru exist in equal amounts, the (110)-type planes are exhibited in the perovskite layers as SRO and PZT [36].

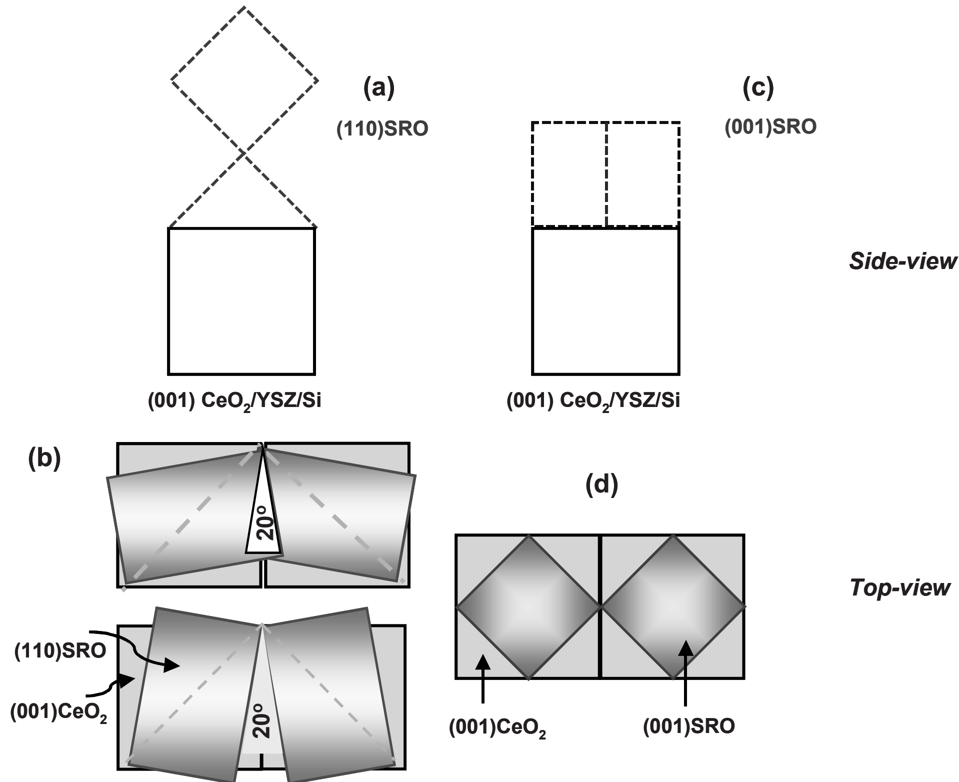

Figure 3.6: Schematic side-view and top-view of (a,b) the (110)-oriented SRO layer and (c,d) the (001)-oriented SRO layer configurations on (001)CeO_2/YSZ/Si substrates.

Because of the higher volatility of Ru, the stoichiometric ratio of Sr and Ru can be changed drastically if the deposition temperature is increased. Consequently, in this study, the first 20 pulses SRO (~4 Å) are deposited on CeO_2/YSZ/Si at high temperature (800 °C) and in a reducing O_2 environment (<10^{-5} mbar) allowing Ru evaporation. Evidenced by XPS data in Fig. 3.1, the starting layer is now Sr-rich. As a result, the formed $Sr_{n+1}Ru_nO_{3n+1}$ layer (Sr_2RuO_4 or mixture of SrO and Ru) acts as a base plane for the perovskite block. Continued growth of SRO layer at a normal deposition temperature (600 °C) results in (001)-oriented growth of the electrode and the PZT layer as is clear from Fig. 3.5(c). This indicates that the PZT, SRO, CeO_2, and YSZ thin films were oriented toward the (001) direction, which is perpendicular to the surface of the silicon substrate ((001) PZT || (001) SRO || (001) CeO2 || (001) YSZ || (001) Si)). The ϕ-scans in Fig. 3.5(d) show a 45° shift of the SRO(101) reflections compared to the Si(202) reflections with a fourfold rotational symmetry. This proves that the unit cells of SRO/PZT/SRO are rotated 45° with respect to that of the CeO_2/YSZ/Si stack as schematically drawn in Figs. 3.6(c) and 3.6(d) [36].

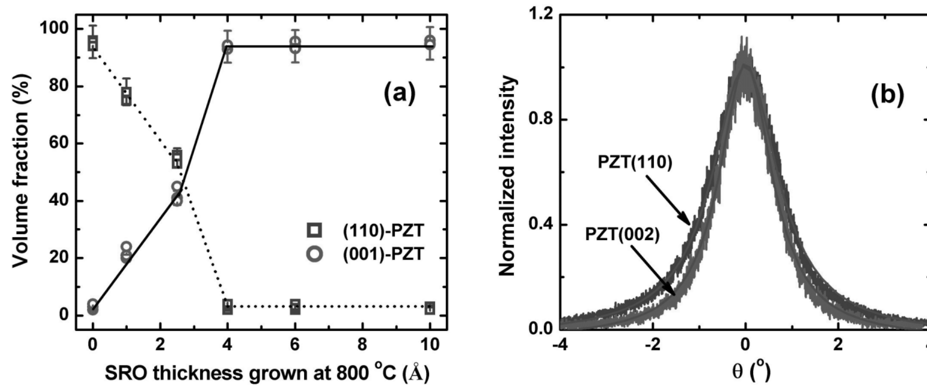

Figure 3.7: (a) The volume fraction of the (110)- and (001)-oriented PZT thin films as a function of the SRO-layer thickness deposited at 800 ^oC and reducing oxygen environment ($<10^{-5}$ mbar); (b) Rocking curves recorded for the leading diffraction peaks of the different orientations. The rocking curve FWHM of the PZT(110) and the PZT(002) diffraction peaks were measured at 1.6 and 1.2^o, respectively.

To deduce the effect of the SRO seed-layer on the crystalline orientation of PZT thin films, the volume fraction of (110)- and (001)-oriented epitaxial PZT thin films are plotted against the thickness of an ultrathin SRO seed-layer deposited at 800 ^oC on the surface of the CeO_2/YSZ/Si substrate in Fig. 3.7. The results shown in Fig. 3.7(a) clearly illustrate that the PZT films are (110) preferential orientation without a SRO seed-layer. The volume fraction of (001)-orientation was increased by using a SRO seed-layer, and the perfectly (001)-oriented PZT thin films were obtained when the thickness of seed-layer exceeds 4 Å. It is shown that, by introduction the addition step in the deposition process, an orientation switch from (110)- to (001)-oriented growth of the electrodes and the thin films on similar buffer-layers can be realized. The rocking curves for PZT(110) and PZT(002) peaks demonstrate that both films have a good crystalline quality (Fig. 3.7(b)), with the full width at half maximum (FWHM) of 1.6 and 1.2^o, respectively.

Furthermore, in order to investigate the effect of the ultrathin SRO seed-layer on the orientation of PZT thin films, the (001)CeO_2/YSZ/Si and (001)YSZ/Si substrates were used. Firstly, 4 Å SRO seed-layers were deposited at 800 ^oC on these substrates, and the SRO bottom-electrode and PZT thin film were then deposited continuously at a deposition temperature of 600 ^oC. The XRD data indicates that the PZT/SRO thin films have (110)- and (001)-orientations when deposited on YSZ/Si (not shown here) and CeO_2/YSZ/Si substrates, respectively.

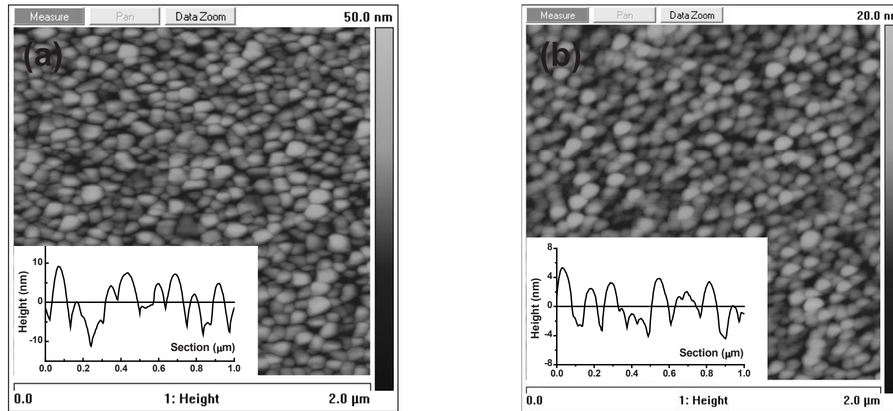

Figure 3.8: AFM images of (a) the (110)-oriented PZT/SRO films and (b) the (001)-oriented PZT/SRO films grown on CeO_2/YSZ/Si substrates, with a corresponding rms surface roughness of 6.5 nm and 3.4 nm, respectively.

From the above experimental evidence, we can summarize that the presence of both the second CeO_2 buffer-layer and an extra SRO seed-layer (~4 Å) deposited at 800 ^{o}C is necessary to provide a method for reliable control of the crystal orientation of PZT thin-films: from (110)- to (001)-orientations.

In order to consider the effect of the orientation of thin films on the surface morphology, the AFM images with a 2-µm × 2-µm scan area of the PZT thin films are shown in Fig. 3.8. The rms surface roughness were 6.2 and 3.4 nm for (110)- and (001)-oriented PZT thin films, respectively.

3.5 Effects of substrate types on the crystallinity of PZT thin films

It is worth noting that the properties of ferroelectric PZT thin films are not only affected by the orientation but also on the crystalline quality. Bornand *et al*. [37] and Tsukada *et al*. [38] have reported the dependence of polarization hysteresis loop as a function of volume fraction of (001)-orientation in the (001)/(100)-oriented films (denoted as {001}), in which the higher the volume fraction of (001)-orientation, the higher the P_r value obtained. It can be explained that an increase in the volume fraction of (001)-orientation or an increase the *c*-axis lattice parameter implies a larger displacement of the central Ti^{4+} ion, and hence, larger switched polarization.

3.5.1 X-ray diffraction spectra

In order to investigate the effect of thin film quality and residual stress on the microstructure and electrical properties of PZT thin films, epitaxial PZT thin films were grown on different substrates (Si, YSZ, STO) and deposited on bare silicon with different buffer-layers (CeO_2/YSZ, STO). Shown in Figs. 3.9(a)-3.9(d) are results for epitaxial $PbZr_{0.52}Ti_{0.48}O_3$ (PZT) thin films grown on SRO-buffered substrates: (001) CeO_2/YSZ/Si, (001) STO/Si, (001) CeO_2/YSZ, and (001) STO. The data indicates that the films have epitaxial growth with {001}-orientation.

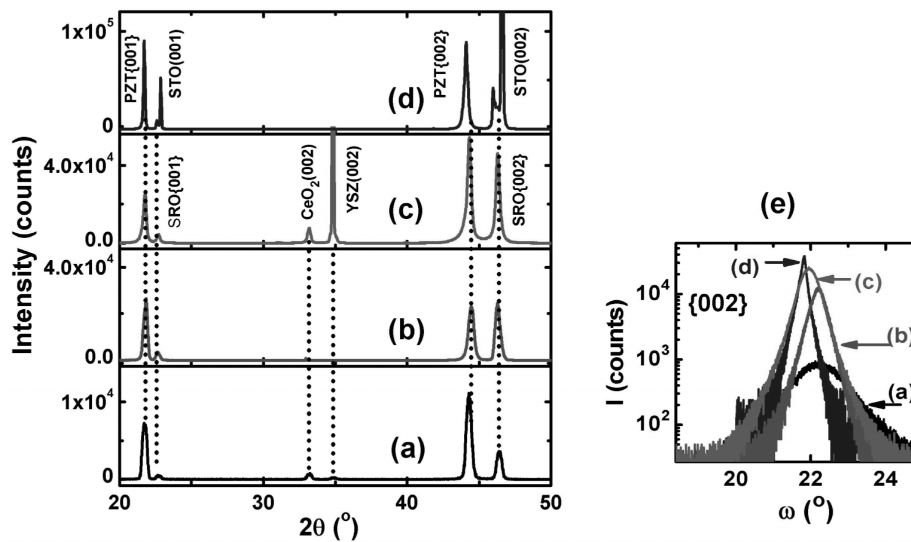

Figure 3.9: XRD patterns of PZT/SRO thin films grown on (a) (001)CeO_2/YSZ/Si, (b) (001)STO/Si, (c) (001)CeO_2/YSZ, and (d) (001)STO substrates; (e) Rocking curves of these above PZT thin films at (002)-diffraction peaks.

As shown in Fig. 3.9(e), the peak position of PZT(002) shifted to a smaller 2θ angle, indicating the increase of the out-of-plane lattice parameter when the silicon substrates were substituted by single-crystal substrates such as YSZ and STO. The full-width at half-maximum intensity (FWHM) values of the rocking curves for PZT(002) peaks were 0.18^o-1.20^o for all these thin films and shown in Tab. 3.2. It is indicated that the thin film with the best quality was grown on the STO substrate, whereas the thin film of least quality was on CeO_2/YSZ/Si.

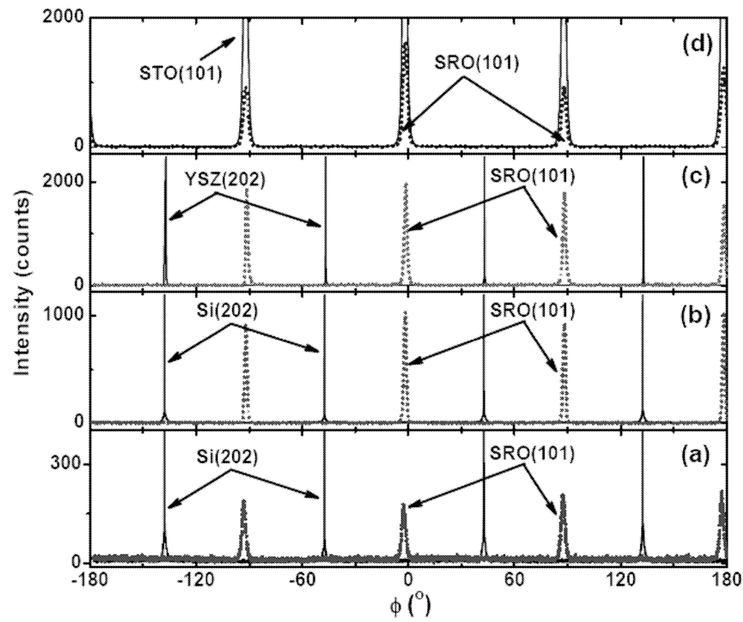

Figure 3.10: ϕ-scan profiles of SRO(101)-reflections on (a) CeO_2/YSZ/Si, (b) STO/Si, (c) CeO_2/YSZ, and (d) on STO substrates.

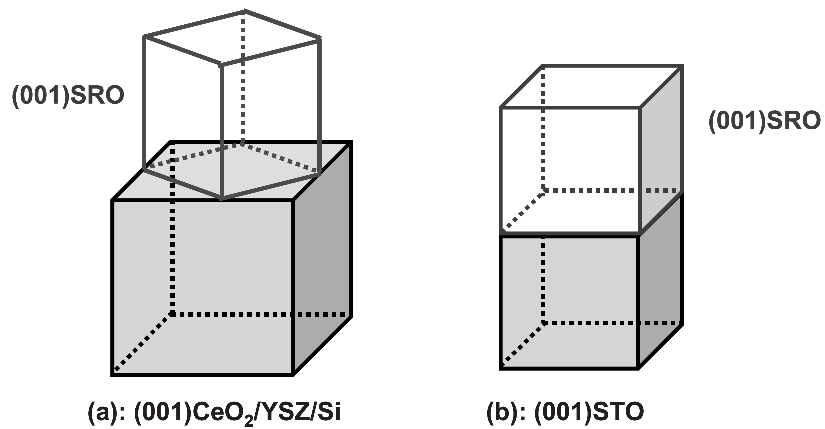

Figure 3.11: Schematic of the (001)-oriented PZT/SRO thin films on CeO_2/YSZ/Si and STO substrates.

The in-plane epitaxial relationships between the films and substrates were estimated by the x-ray ϕ-scans (azimuthal scans) measurement, where ϕ=0 correspond to $(001)_c$-oriented SRO layer, as illustrated in Fig. 3.10. Fourfold symmetry located at the tilting

angle, ψ=45° (ϕ= -90°, 0°, +90°, and +180°) was observed for all SRO bottom-electrodes, suggesting the cube-on-cube epitaxial relationship between SRO and CeO_2/YSZ/Si, STO/Si, CeO_2/YSZ and STO substrates. Since the perovskite PZT thin film almost matches SRO bottom-electrode, its crystallographic growth orientation consequently continues that of the underlying electrode. The ϕ-scans in Figs. 3.10(a)-3.10(c) show a 45° shift of the SRO(101) compared to the CeO_2(202), YSZ(202) and Si(202) fourfold symmetry related peaks. This indicates that the SRO layers rotate 45° with respect to the structure of the CeO_2, YSZ and Si crystal, as schematically drawn in Fig. 3.11(a). Fig. 3.10(d) shows a ϕ-scan of the SRO(101) reflections for the SRO/STO heterostructure. The significant intensities at only ϕ= -90°, 0°, +90°, and +180°, clearly indicate the cube-on-cube epitaxial relationship of (001) PZT || (001) SRO || (001) STO for the *c*-oriented domains whose *c*-axis is parallel to the substrate normal (Fig. 3.11(b)).

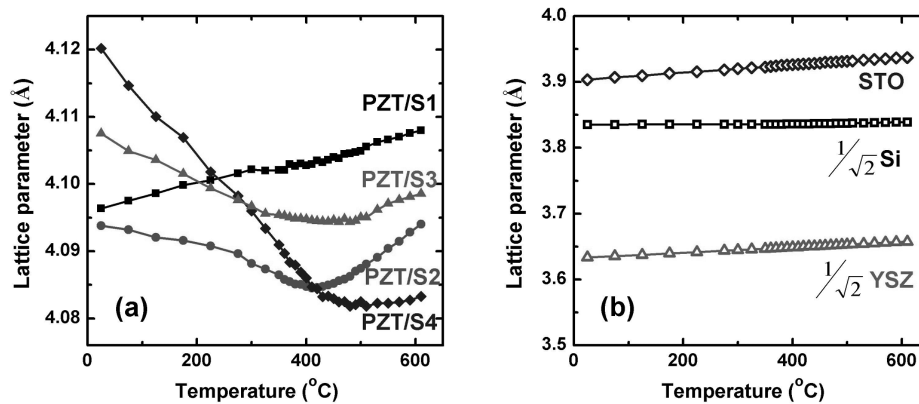

Figure 3.12: (a) Lattice constants of epitaxial PZT thin films grown on (001) CeO_2/YSZ/Si, (001) STO/Si, (001) CeO_2/YSZ, and (001) STO substrates derived from the 2θ values of the (002)-reflections in their XRD data as a function of measured temperature; (b) Variations of lattice constant with temperature for Si, YSZ, and STO substrates.

The lattice constants of epitaxial PZT thin films grown on different substrates, as a function of the measured temperature, are shown in Fig. 3.12. The lattice constants were determined from the 2θ values of the (002) peaks in their XRD patterns. For PZT thin films on YSZ and STO single-crystal substrates, the lattice constants are larger than that of films on Si substrates at room temperature.

Table 3.2: Parameters of (001)-oriented PZT thin films grown on different substrates.

	Sample			
	(001) PZT	**(001) PZT**	**(001) PZT**	**(001) PZT**
Substrate	Si(001)	Si(001)	YSZ(001)	STO(001)
Buffer-layer	CeO_2/YSZ [i]	STO [ii]	CeO_2	none
Top/bottom electrodes	SRO	SRO	SRO	SRO
FWHM (002)-peak of PZT	1.2°	0.51°	0.56°	0.18°
rms roughness (nm)	3.4	2.4	2.2	1.5
a=*b* (Å) [iii]	4.108	4.088	4.062	4.061
c (Å) [iv]	4.087	4.080	4.092	4.113
c/*a*	0.995	0.998	1.007	1.013
V ($Å^3$)	68.97	68.18	67.52	67.83

3.5.2 XRD reciprocal space mapping

Figures 3.13 and 3.14 show the XRD reciprocal space mappings around the PZT(103) diffraction peak for the (001)-oriented PZT thin films grown on (001)CeO_2/YSZ/Si, (001)STO/Si, (001)CeO_2/YSZ, and (001)STO substrates. The horizontal and vertical axes correspond to the reciprocal of the in-plane and out-of-plane lattice spacing, respectively.

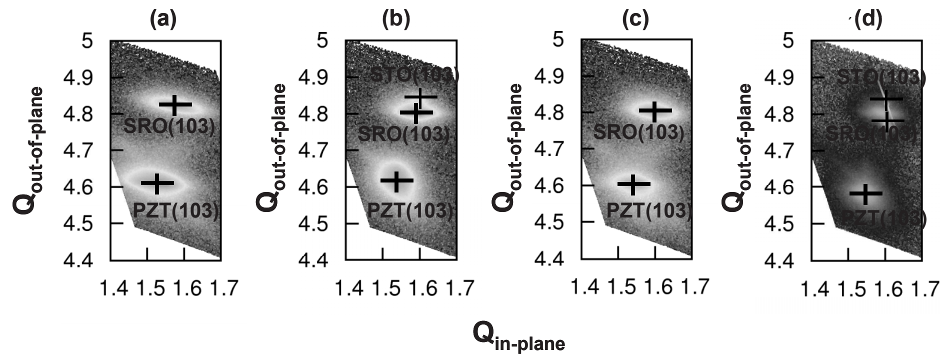

Figure 3.13: XRD reciprocal space mappings of the SRO(103) and PZT(103) diffractions for PZT/SRO thin films grown on (a) (001) CeO_2/YSZ/Si, (b) (001) STO/Si, (c) (001) CeO_2/YSZ, and (d) (001) STO substrates.

[i] Deposited by PLD
[ii] Deposited by MBE
[iii] Calculated from x-ray reciprocal space mapping
[iv] Calculated from x-ray reciprocal space mapping

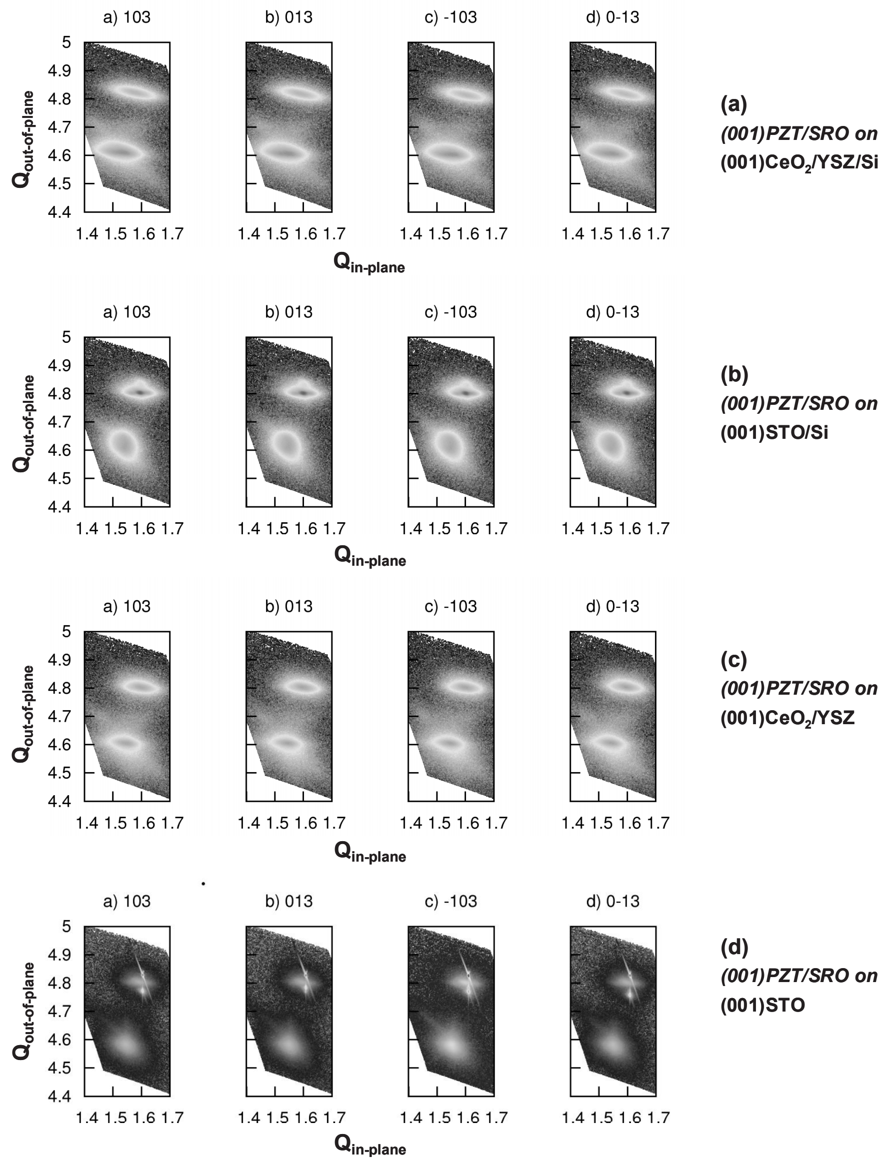

Figure 3.14: XRD reciprocal space mappings around $(103),(013),(\bar{1}03),(0\bar{1}3)$ diffractions for PZT and SRO thin films grown on (a) (001) CeO_2/YSZ/Si, (b) (001 STO/Si, (c) (001) CeO_2/YSZ, and (d) (001) STO substrates. The (103) planes of the CeO_2, YSZ buffer-layers and silicon substrate could not be detected, because they are rotated 45° in-plane with respect to the SRO and PZT thin films.

As shown in Fig. 3.13, the position of the PZT(103) diffraction spot was increased along the horizontal direction and the direction towards the higher $Q_{in\text{-}plane}$ value, indicating that the in-plane lattice parameter was decreased when single-crystal substrates such as YSZ and STO were substituted for silicon substrate. Along the vertical direction, however, the position of the PZT(103) diffraction was decreased, indicating that the out-of-plane lattice parameter was increased. The in-plane (*a*, *b*) and out-of-plane (*c*) lattice parameters of the PZT thin films, grown on (a) (001) CeO_2/YSZ/Si, (b) (001) STO/Si, (c) (001) CeO_2/YSZ, and (d) (001) STO substrates, were calculated by the $Q_{in\text{-}plane}$ and $Q_{out\text{-}of\text{-}plane}$ of the (103) spots for PZT thin films and summarized in Table 3.2.

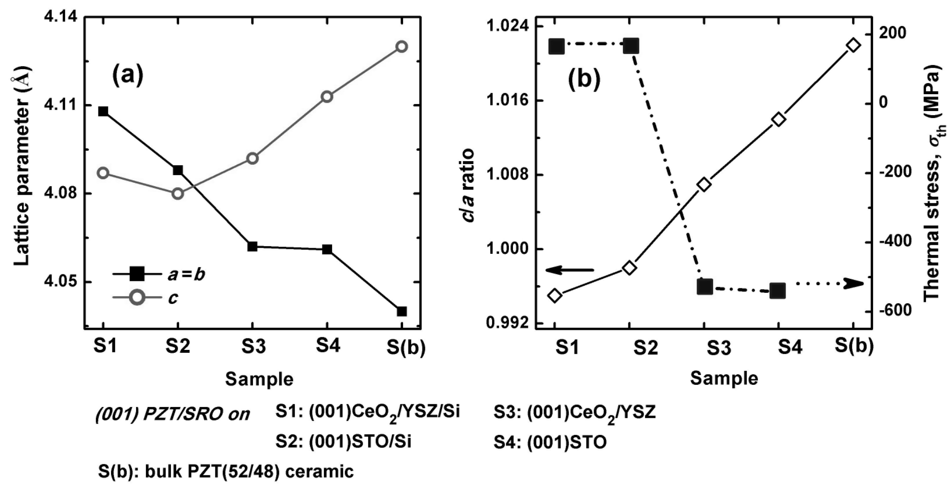

Figure 3.15: (a) Lattice parameters and (b) Variation of the *c*/*a* ratio of PZT thin films at room temperature.

Figures 3.15(a) and 3.15(b) show the relationship between the substrate, the lattice parameter, and the *c*/*a* ratio variation of PZT thin films obtained from the x-ray reciprocal space mapping results, including the in-plane *a*-axis ($a_{//}$) and out-of-plane *c*-axis ($c_{\perp}$) of the *c*-domain. These results reveal that the increase of *c*/*a* ratio of PZT thin films, due to the increase of the out-of-plane lattice parameter (*c*-axis), increased with a decrease in the in-plane lattice parameter (*a*-axis) when the substrate was changed from silicon to single-crystal substrates, such as YSZ and STO. Figure 3.15(b) also shows the *c*/*a* ratios of PZT thin films as functional of the thermal expansion coefficient (α) of the substrate. It is noticeable that the *c*/*a* ratio of PZT film increases as the α-value of the substrate increases. The PZT films grown on Si substrates under biaxial tensile stress while cooling through the Curie temperature tend to relieve such stress through the development of the *a*-domain orientation (*c*/*a* < 1), because the coefficient of thermal expansion for the Si (4.4×10^{-6} K^{-1} [39]) substrate is smaller

than that for the PZT film (6.0×10^{-6} K^{-1} [40-42]). The coefficient of the thermal expansion for the single-crystal such as YSZ (10.9×10^{-6} K^{-1} [43]) and STO (11×10^{-6} K^{-1} [44]) are higher than that for the PZT film, thus compressive stress developed in the PZT films on YSZ or STO substrates during the cooling process. This compressive stress forces the PZT crystalline film to adopt a tetragonal structure with the elongated *c*-axis ($c/a > 1$).

Because film stress has been shown to have such a substantial effect on the ferroelectric and piezoelectric properties, it is important to qualify the thermal stress in PZT thin films [45]. Thermal stress in the thin films (σ_{th}) is induced due to the difference in thermal expansion between the film and substrate during cooling from the deposition temperature to room temperature, and can be estimated using Eq. (3.5) [46]:

$$\sigma_{th} = E_f \int_{T_0}^{T_d} (\alpha_f - \alpha_s) dT \qquad (3.5)$$

where, E_f (=200 GPa [47, 48]) represents the Elastic modulus of the PZT film, T_d (=600 °C) and T_0 (=25 °C) are the film deposition temperature and room temperature, and α_f and α_s are, respectively, thermal expansion coefficients of the PZT film and the substrate.

Table 3.3: Thermal expansion coefficients of substrates and PZT film.

Substrates	Si	YSZ	$SrTiO_3$	PZT
Thermal expansion α_s, α_f (/ °K)	4.4×10^{-6} [39]	10.9×10^{-6} [43]	11.0×10^{-6} [44]	6.0×10^{-6} [40-42]

From these thermal expansion coefficients, the thermal stresses of PZT thin films on Si, YSZ, and STO substrates were estimated to be +184.0, –563.5, and –575.0 MPa, respectively. The minus sign means that the stress is of compressive-type. On the other hand, the thermal stresses introduced in the films by YSZ and STO substrates are compressive with $\alpha_{PZT} < \alpha_{YSZ}$ (or α_{STO}), whereas the stress in the film is tensile on Si substrates with $\alpha_{PZT} > \alpha_{Si}$ (Fig. 3.15(b)).

Fig. 3.12(a) displays the thermal expansion behaviors of the lattice parameters of PZT thin films deposited on different substrates: i) silicon, ii) YSZ and iii) STO. The discontinuous behavior of the lattice parameter of films is ascribed to the cubic phase (*paraelectric*) - tetragonal phase (*ferroelectric*) transition with the estimated Curie temperature (T_c) values of about 410-428, 433 and 450 °C for PZT films grown on Si, YSZ and STO substrates, respectively, when the films were cooled from the growth temperature to room temperature. It is found from Fig. 3.16 that the Curie temperature is decreased under a tensile stress and it is increased under a compressive one. This result is in agreement with the Curie temperature of PZT thin films versus thermal stress incorporated by different substrates, reported by Yamamoto *et al*. [49] and Rossetti *et al*. [50].

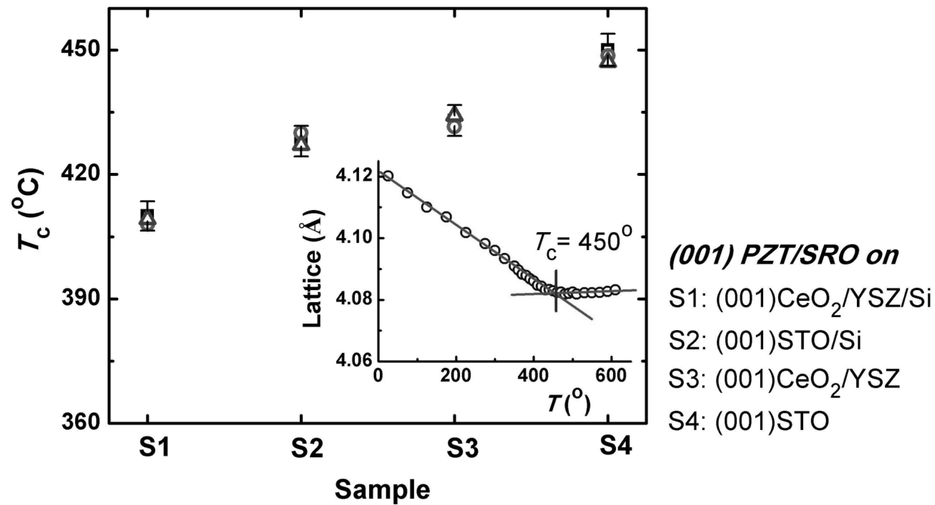

Figure 3.16: Curie temperature (T_c) of PZT thin films grown on different substrates. The inset shows the relationship between temperature and the lattice parameters of STO substrate and *c*-axis of PZT thin film.

3.6 Summary and conclusions

Heteroepitaxial growth of (110)- and (001)-oriented PZT/SRO thin films on the (001)CeO_2/YSZ/Si substrates was succeeded by pulsed laser deposition (PLD). The single YSZ buffer-layer and double CeO_2/YSZ buffer-layers grew epitaxially with a cube-on-cube alignment with the diamond structure of the silicon. By characterizing the crystal structure with HRXRD, we found out that the orientation of PZT thin films can be controlled between (110) and (001), depending on both buffer-layer(s) and with deposition processing of the SRO bottom-electrode, in which:

+ (110)-oriented PZT films were obtained on both (001)YSZ/Si and (001)CeO_2/YSZ/Si substrates and by using SRO bottom-electrodes deposited under normal conditions (600 °C and 0.13 mbar O_2).

+ By introducing of an extra SRO seed-layer (~ 4 Å) deposited at high temperature of 800 °C and reducing O_2 ambient (<10^{-5} mbar), a Sr-rich layer could be obtained on the surface of the (001)CeO_2/YSZ/Si substrate, and then the SRO bottom-electrode was deposited continuously at normal conditions (600 °C and 0.13 mbar O_2). As a result, the PZT/SRO heteroepitaxial structure was oriented toward (001), and the PZT and SRO thin films were rotated 45° in-plane with respect to the structure of the CeO_2, YSZ, and Si.

Reciprocal space mapping technique is used to quantify the in-plane and out-of-plane lattice parameters in epitaxial (001)-oriented PZT thin films and SRO bottom-electrodes grown on various substrates, including silicon substrates such as CeO_2/YSZ/Si and STO/Si, and single crystal substrates as CeO_2/YSZ and STO. It is noticeable that the c/a ratio between out-of-plane (c-axis) and in-plane (a-axis) lattice parameters of PZT thin film increases as the thermal expansion coefficient (α) of the substrate increases. The PZT films grown on Si substrates under tensile stress while cooling through the Curie temperature tend to relieve such stress, because the coefficient of thermal expansion for the Si substrate is smaller than that for the PZT film. Conversely, compressive stress developed in the PZT films on YSZ or STO substrates, due to the higher thermal expansion coefficient of these substrates. This compressive stress forces the PZT crystalline film to adopt a tetragonal structure with an elongated c-axis ($c/a > 1$).

Domain structures of epitaxial PZT thin films were also found to be strongly dependent on the selection of substrate such as Si, YSZ, and STO. Perfectly c-axis oriented films (c-domain oriented) were obtained on (001) YSZ and (001) STO substrates with $c/a > 1$; whereas, the films grown on silicon showed an a-domain oriented with $c/a < 1$. The results clearly demonstrate that the misfit thermal expansion coefficient and its relaxation play a critical role on the domain structure. Effects of thermal residual stress on both ferroelectric and piezoelectric properties of PZT thin films will be discussed in the next chapter.

3.7 References

1. I. Kanno, H. Kotera, K. Wasa, T. Matsunaga, T. Kamada, and R. Takayama, *Crystallographic characterization of epitaxial Pb(Zr,Ti)O_3 films with different Zr/Ti ratio grown by radio-frequency-magnetron sputtering*, J. Appl. Phys. **93** (2003) p. 4091-4096.
2. T. Oikawa, M. Aratani, H. Funakubo, K. Saito, and M. Mizuhira, *Composition and orientation dependence of electrical properties of epitaxial $Pb(Zr_xTi_{1-x})O_3$ thin films grown using metalorganic chemical vapor deposition*, J. Appl. Phys. **95** (2004) p. 3111-3115.
3. R. Herdier, M. Détalle, D. Jenkins, D. Remiens, D. Grébille, and R. Bouregba, *The properties of epitaxial PMNT thin films grown on $SrTiO_3$ substrates*, J. Cryst. Growth **311** (2008) p. 123-127.
4. N. Setter, *Electroceramics: looking ahead*, J. Eur. Ceram. Soc. **21** (2001) p. 1279-1293.
5. S. Trolier-McKinstry and P. Muralt, *Thin films piezoelectrics for MEMS*, J. Electroceram. **12** (2004) p. 7-17.
6. D. J. Laser and J. G. Santiago, *A review of micropumps*, J. Micromech. Microeng. **14** (2004) p. R35-R64.
7. I. -H. Hwang and J. -H. Lee, *Self-actuating biosensor using a piezoelectric cantilever and its optimization*, J. Phys.: Conf. Ser. **34** (2006) p. 362-367.
8. S. -Y. Chen and I. -W. Chen, *Texture development, microstructure evolution, and crystallization of chemically derived PZT thin films*, J. Am. Ceram. Soc. **81** (1998) p. 97-105.
9. S. -Y. Chen and C. -L. Sun, *Ferroelectric characteristics of oriented $Pb(Zr_{1-x}Ti_x)O_3$ films*, J. Appl. Phys. **90** (2001) p. 2970-2974.
10. M. Kondo, K. Maruyama, and K. Kurihara, *Epitaxial ferroelectric thin films on silicon substrates for future electronic devices*, FUJITSU Sci. Tech. J. **38** (2002) p. 46-53.
11. S. Yamauchi and M. Yoshimaru, *Growth of [111]-oriented lead zirconate titanate thin film with smooth surface to improve electrical properties*, Jpn. J. Appl. Phys. **35** (1996) p. 1553-1556.
12. C. J. Kim, D. S. Yoon, J. S. Lee, C. G. Choi, W. J. Lee, and K. No, *Electrical characteristics of (100), (111), and randomly aligned lead zirconate titanate thin films*, J. Appl. Phys. **76** (1994) p. 7478-7482.
13. D. Akai, M. Yokawa, K. Hirabayashi, K. Matsushita, K. Sawada, and M. Ishida, *Ferroelectric properties of sol-gel delivered epitaxial $Pb(Zr_x,Ti_{1-x})O_3$ thin films on Si using epitaxial γ-Al_2O_3 Layers*, Appl. Phys. Lett. **86** (2005) p. 202906(1-3).
14. S. Y. Hou, J. Kwo, R. K. Watts, J. -Y. Cheng, and D. K. Fork, *Structure and properties of epitaxial $Ba_{0.5}Sr_{0.5}TiO_3$/$SrRuO_3$/ZrO_2 heterostructure on Si grown by off-axis sputtering*, Appl. Phys. Lett. **67** (1995) p. 1387-1389.
15. Ø. Nordseth, T. Tybell, and J.K. Grepstad, *Epitaxial (Pb,La)(Zr,Ti)O_3 thin films on buffered Si(100) by on-axis radio frequency magnetron sputtering*, Thin Solid Films **517** (2009) p. 2623-2626.
16. J. S. Speck and W. Pompe, *Domain configurations due to multiple misfit relaxation mechanisms in epitaxial ferroelectric thin films. I. Theory*, J. Appl. Phys. **76** (1994) p. 466-476.
17. G. A. C. M. Spierings, G. J. M. Dormans, W. G. J. Moors, M. J. E. Ulenaers, and P. K. Larsen, *Stresses in Pt/Pb(Zr,Ti)O_3/Pt thin-film stacks for integrated ferroelectric capacitors*, J. Appl. Phys. **78** (1995) p. 1926-1933.

18. S. S. Sengupta, S. M. Park, D. A. Payne, and L. H. Allen, *Origins and evolution of stress development in sol-gel derived thin layers and multideposited coatings of lead titanate*, J. Appl. Phys. **83** (1998) p. 2291-2296.
19. J. -W. Lee, C. -S. Park, M. Kim, and H. -E. Kim, *Effects of Residual Stress on the Electrical Properties of PZT Films*, J. Am. Ceram. Soc. **90** (2007) p. 1077-1080.
20. H. Morioka, K. Saito, S. Yokoyama, T. Oikawa, T. Kurosawa, and H. Funakubo, *Effect of film thickness on ferroelectric domain structure and properties of* $Pb(Zr_{0.35}Ti_{0.65})O_3/SrRuO_3/SrTiO_3$ *heterostructures*, J. Mater. Soc. **44** (2009) p. 5318-5324.
21. T. Kumazawa, Y. Kumagai, H. Miura, M. Kitano, and K. Kushida, *Effect of external stress on polarization in ferroelectric thin films*, Appl. Phys. Lett. **72** (1998) p. 608-610.
22. B. A. Tuttle, J. A. Voigt, T. J. Garino, D. C. Goodnow, R. W. Schwartz, D. L. Lamppa, T. J. Headley, and M. O. Eatough, *Chemically prepared Pb(Zr,Ti)O_3 thin films: The effects of orientation and stress*, in *Proceedings of the Eighth IEEE International Symposium on Applications of Ferroelectrics (ISAF'92)*, Greenville-USA (1992) p. 344-348.
23. C. B. Eom, R. J. Cava, R. M. Fleming, J. M. Phillips, R. B. vanDover, J. H. Marshall, J. W. P. Hsu, J. J. Krajewski, and W. F. Peck, Jr., *Single-Crystal Epitaxial Thin Films of the Isotropic Metallic Oxides* $Sr_{1-x}Ca_xRuO_3$ $(0 \le x \le 1)$, Science **258** (1992) p. 1766-1769.
24. C. B. Eom, R. B. van Dover, J. M. Phillips, D. J. Werder, J. H. Marshall, C. H. Chen, R. J. Cava, R. M. Fleming, and D. K. Fork, *Fabrication and properties of epitaxial ferroelectric heterostructures with ($SrRuO_3$) isotropic metallic oxide electrodes*, Appl. Phys. Lett. **63** (1993) p. 2570-2572.
25. C. L. Chen, Y. Cao, Z. J. Huang, Q. D. Jiang, Z. Zhang, Y. Y. Sun, W. N. Kang, L. M. Dezaneti, W. K. Chu, and C. W. Chu, *Epitaxial* $SrRuO_3$ *thin films on (001)* $SrTiO_3$, Appl. Phys. Lett. **71** (1997) p. 1047-1049.
26. D. C. Worledge and T. H. Geballe, *Negative Spin-Polarization of* $SrRuO_3$, Phys. Rev. Lett. **85** (2000) p. 5182-5185.
27. J. Shin, S. V. Kalinin, H. N. Lee, H. M. Christen, R. G. Moore, E. W. Plummer, and A. P. Baddorf, *Surface stability of epitaxial* $SrRuO_3$ *films*, Surf. Sci. **581** (2005) p. 118-132.
28. C. Mallika and O.M. Sreedharan, *Potentiometric determination of the thermodynamic stability of SrO-RuO_2 system*, J. Alloys and Compounds **191** (1993) p. 219-222.
29. G. Rijnders, D. H. A. Blank, J. Choi, and C. -B. Eom, *Enhanced surface diffusion through termination conversion during epitaxial* $SrRuO_3$ *growth*, Appl. Phys. Lett. **84** (2004) p. 505-507.
30. N. A. Surplice, *The electrical conductivity of calcium and strontium oxides.* Brit. J. Appl. Phys. **17** (1966) p. 175-180.
31. B. Dabrowski, O. Chmaissem, P. W. Klamut, S. Kolesnik, M. Maxwell, J. Mais, Y. Ito, B. D. Armstrong, J. D. Jorgensen, and S. Short, *Reduced ferromagnetic transition temperatures in* $Sr\,Ru_{1-v}O_3$ *perovskites from Ru-site vacancies*, Phys. Rev. B **70** (2004) p. 014423(1-7).
32. W. Siemons, *Nanoscale of properties of complex oxide films*, PhD Thesis, University of Twente, The Netherlands (2008).
33. S. J. Wang, C. K. Ong, L. P. You, and S. Y. Xu, *Epitaxial growth of yttria-stabilized zirconia oxide thin film on natively oxidized silicon wafer without an amorphous layer*, Semicond. Sci. Technol. **15** (2000) p. 836-839.

34. R. Haakenaasen, D.K. Fork, and J.A. Golovchenko, *High quality crystalline $YBa_2Cu_3O_{7-\delta}$ films on thin silicon substrates*, Appl. Phys. Lett. **64** (1994) p. 1573-1575.
35. F. Sánchez, R. Aguiar, V. Trtik, C. Guerrero, C. Ferrater, and M. Varela, *Epitaxial growth of $SrTiO_3$ (00h), (0hh) and (hhh) thin films on buffered Si(001)*, J. Mater. Res. **13** (1998) p. 1422-1425.
36. M. Dekkers, M. D. Nguyen, R. Steenwelle, P. M. te Riele, D. H. A. Blank, and G. Rijnders, *Ferroelectric properties of epitaxial $Pb(Zr,Ti)O_3$ thin films on silicon by control of crystal orientation*, Appl. Phys. Lett. **95** (2009) p. 012902 (1-3).
37. V. Bornand, S. Trolier-McKinstry, K. Takemura, and C. A. Randall, *Orientation dependence of fatigue behavior in relaxor ferroelectric-$PbTiO_3$ thin films*, J. Appl. Phys. **87** (2000) p. 3965-3972.
38. M. Tsukada, H. Yamawaki, and M. Kondo, *Crystal structure and polarization phenomena of epitaxially grown $Pb(Zr,Ti)O_3$ thin-film capacitors*, Appl. Phys. Lett. **83** (2003) p. 4393-4395.
39. G. S. Wang, D. Remiens, E. Dogheche, X. L. Dong, *Effect of thermal strain on structure and polarization fatigue of CSD-derived $PbZr_{0.53}Ti_{0.47}O_3/LaNiO_3$ hetero-structures*, Appl. Phys. A: Mater. Sci. Process. **88** (2007) p. 657-660.
40. J. Wang, H. Zheng, Z. Ma, S. Prasertchoung, M. Wuttig, R. Droopad, J. Yu, K. Eisenbeiser, and R. Ramesh, *Epitaxial $BiFeO_3$ thin films on Si*, Appl. Phys. Lett. **85** (2004) p. 2574-2576.
41. S. Y. Yang, F. Zavaliche, L. Mohaddes-Ardabili, V. Vaithyanathan, D. G. Schlom, Y. J. Lee, Y. H. Chu, M. P. Cruz, Q. Zhan, T. Zhao, and R. Ramesh, *Metalorganic chemical vapor deposition of lead-free ferroelectric $BiFeO_3$ films for memory applications*, Appl. Phys. Lett. **87** (2005) p. 102903(1-3).
42. K. Kurihara, M. Kondo, K. Sato, M. Ishii, N. Wakiya, and K. Shinozaki, *Electrooptic properties of epitaxial lead zirconate titanate films on silicon substrates*, Jpn. J. Appl. Phys. **46** (2007) p. 6929-6932.
43. C. -H. Chen, N. Wakiya, A. Saiki, T. Kiguchi, K. Shinozaki, and N. Mizutani, *Defects in heteroepitaxial CeO_2/YSZ/Si(001) films by precise X-ray rocking curve distribution fitness*, Physica B: Condensed Matter **308-310** (2001) p. 1050-1053.
44. J. Kawashima, Y. Yamada, and I. Hirabayashi, *Critical thickness and effective thermal expansion coefficient of YBCO crystalline film*, Physica C **306** (1998) p. 114-118.
45. V. G. Koukhar, N. A. Pertsev, and R. Waser, *Thermodynamic theory of epitaxial ferroelectric thin films with dense domain structures*, Phys. Rev. B **64** (2001) p. 214103(1-15).
46. M. Ohring, *The Materials Science of Thin Films*, Academic, New York (1991).
47. M. Palacio and B. Bhushan, *Nanotribological and nanomechanical properties of lubricated PZT thin films for ferroelectric data storage applications*, J. Vac. Sci. Technol. A **26** (2008) p. 768-776.
48. K. J. Kwak and B. Bhushan, *Platinum-coated probes sliding at up to 100 mm/s against lead zirconate titanate films for atomic force microscopy probe-based ferroelectric recording technology*, J. Vac. Sci. Technol. A **26** (2008) p. 783-793.
49. T. Yamamoto and H. Matsuoka, *Crystallographic and ferroelectric properties subjected to two-dimensional stress in c-sxis-oriented $PbTiO_3$ thin films*, Jpn. J. Appl. Phys. **33** (1994) p. 5317-5322.
50. G. A. Rossetti, Jr, L. E. Cross, and K. Kushida, *Stress induced shift of the Curie point in epitaxial $PbTiO_3$ thin films*, Appl. Phys. Lett. **59** (1991) p. 2524-2526.

4.
Polarization switching and Role of conductive-oxide electrodes

Abstract. The reduction in switchable polarization of ferroelectric thin films due to electrical stress (polarization fatigue) is a major problem in ferroelectric non-volatile memories. The migration of oxygen vacancies and their entrapment near film-electrode interfaces has been proposed as a cause of fatigue phenomenon. The effect of oxygen vacancies can be explained by the inhibition of the domain switching by pinning of the domain walls, as well as the formation of layers at interfaces (dead-layers) that effectively reduce the total applied electric field across the ferroelectric capacitor. By using conductive-oxide electrodes like $SrRuO_3$ (SRO), the accumulation of oxygen vacancies and the formation of a dead-layer can be prevented; hence, no-reduction in the switchable polarization of ferroelectric thin films is observed.
The ferroelectric characteristics of PZT/SRO capacitors grown on silicon substrates are found to be strongly dependent on their crystalline orientation: (001)-oriented PZT thin films showed a robust high ferroelectric response, while the remnant polarization of (110)-oriented PZT thin films was lower and increased with increasing switching cycles and only showed high response after multiple switching cycles.
Furthermore, the effect of residual stress (either tensile or compressive) on the ferroelectric properties of PZT films was also investigated. Tensile stress tends to cause the domains to align parallel to the film surface, which results in a reduction in polarization. In contrary, compressive stress causes the domains to orient along the longitudinal direction, which in turn caused the increase in polarization.

4.1 Introduction

As mention in chapter 1, ferroelectric oxide films such as $Pb(Zr,Ti)O_3$ (PZT), are useful for electronic and photonic devices because of their ability to retain two stable polarization states, which can form the basis for memory and logic circuitry. Requirements for long-term operation of practical devices such as non-volatile RAM (random access memory) include consistent polarization switching over many (more than 10^{12}) cycles of the applied electric field, and this represents a major challenge [1-3]. The fatigue characteristic is the tendency for the remnant polarization of the ferroelectric capacitors to decrease after repeated polarization switching cycles. Therefore, fatigue is one of the most important factors affecting the quality, as well as the working time of the devices.

In this chapter, we attempt to investigate the fatigue characteristic in PZT thin films grown on Si substrates with conventional metal (Pt) or conductive oxide ($SrRuO_3$, SRO) electrodes. The model to investigate the fatigue mechanism in ferroelectric capacitors based on the accumulation of oxygen vacancies at the film-electrode interfaces is also discussed. The effect of oxygen vacancies accumulation at the interfaces can be quantified by estimation of the interface layer thickness as a function of switching cycles (section 4.4). Therefore, the prevention of oxygen vacancy formation at the interface, using conductive oxide electrodes, leads to a significant reduction of fatigue in PZT/SRO capacitors.

Ferroelectric responses have been recognized to be dependent on the both crystalline orientation and residual stress in ferroelectric films. The orientation dependence of the ferroelectric properties has been investigated through the study of the polarization loops, showing that the (111)-oriented PZT films exhibit higher remnant polarization (P_r) than that of the (001)-oriented film, and the (110)-oriented film has the lowest P_r [4, 5]. In section 4.5, we report dependence of crystalline orientation on the polarization hysteresis loop and polarization switching (fatigue) of epitaxial PZT thin films grown on $SrRuO_3$ coated CeO_2/YSZ/Si substrates.

$Pb(Zr,Ti)O_3$ material which has a perovskite-type structure (ABO_3), is commonly used as a typical ferroelectric material. An electric polarization of PZT (shift up/down of Zr/Ti atom) remains after applying and removing an external electric field, from which a nonvolatile property results. As a result of this behavior, the power consumption required for data storage is very low. It is observed that activation field and coercive field strongly affected by the change in tetragonality. Moreover, it is well-known that the polarization loops of ferroelectric films are not only dependent on the orientation but also on the film quality. For instance, Bornand *et al.* [6] and Tsukada *et al.* [7] have reported the dependence of hysteresis loops as a function of volume fraction of (001)-orientation in the (001)/(100) (denoted as {001})-oriented films, in which higher volume fraction of (001)-orientation, results in a higher P_r value. The ferroelectric properties of the PZT films were also strongly influenced by the residual stress with P_r found to have a higher value with compressive

stress [8]. Tuttle *et al*. [9] observed that compressive stresses on cooling from growth temperature, through the Curie point to room temperature result in domains with their *c*-direction normal to the film surface, while tensile stresses result in domains with their *a*-direction normal to the film surface. However, it is still difficult to distinguish the contribution between orientation and residual stress on ferroelectric as on the piezoelectric properties. One may expect to obtain higher piezoelectric responses for the films with better ferroelectric properties. In section 4.6, we investigate an experimental investigation of the dependence of thin film quality and residual stress on ferroelectric properties of PZT thin films.

Lead zirconate titanate PZT thin films for nonvolatile memory applications have attracted great attention in view of their potential application in memory and micromechanical devices [10, 11]. Polarization and polarization switching characteristics of PZT films are not only strongly dependent on the electrode-types but also on the measurement conditions. While the electrodes affect the fatigue characteristic of PZT films due to the accumulation of oxygen vacancies and the formation of a dead-layer near the interface, the measurement conditions effect fatigue due to the number of ferroelectric domain can be switched in a cycle as a function of applied voltage [12], the speed at which domain can switch with different frequencies [12, 13], as well as the thermal activation process [14] in the ferroelectric capacitors. In section 4.7, the effect of measuring factors, like the ambient temperature, working frequency and applied electric field, on polarization properties of PZT/SRO capacitors was investigated.

4.2 Experimental procedure

A 250-nm-thick epitaxial PZT (Zr/Ti=52/48) thin film was sandwiched between the 100-nm-thick SRO electrodes. This stack was deposited on different buffer-layer(s)/substrate types which have been described in chapter 3. All layers were subsequently grown without breaking the vacuum by PLD using a KrF excimer laser (λ= 248 nm). For electrical characterization, the 200×200 μm^2 capacitors were patterned by a lithography process, and structured by argon etching of the top electrode and wet etching (HF-HCl solution) of the PZT film. The polarization switching and polarization hysteresis loop (*P*-*E*) measurements were performed using the ferroelectric mode of the aixACCT Analyzer TF2000. A Süss MicroTech PM300 manual probe station, equipped with Keithley 4200 Semiconductor characterization system, is used for the capacitance-electric field (*C*-*E*), dielectric constant-electric field (ε-*E*) and leakage current density-electric field (*J*-*E*) measurements. The schematics of PZT thin film capacitors before and after the etching processes are shown in Fig. 4.1. Details of the fabrication process and characterization techniques have also been described in chapter 2.

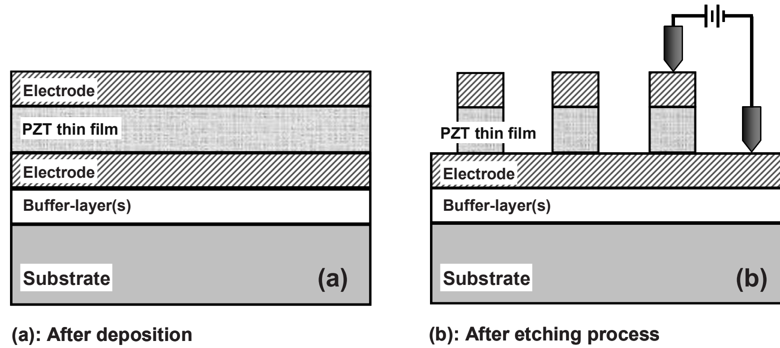

Figure 4.1: Schematic of PZT thin film capacitors (a) after deposition and (b) after etching process.

4.3 Switching process of the polarization hysteresis loop

Ferroelectric materials form domains where the polarization is aligned in various directions in order to minimize energy. When a field is applied, the ferroelectric switches by the nucleation of domains and by the movement of domain walls; and, however, not by the spontaneous reorientation of all of the polarization in a domain at once. The initial stage is nucleation of the opposite domains at the electrode, followed by fast forward propagation of domains across the film (stage-II), and then slower widening of the domains (stage-III), as illustrated in Fig. 4.2(a) [15]. This process is defined as the polarization hysteresis loop.

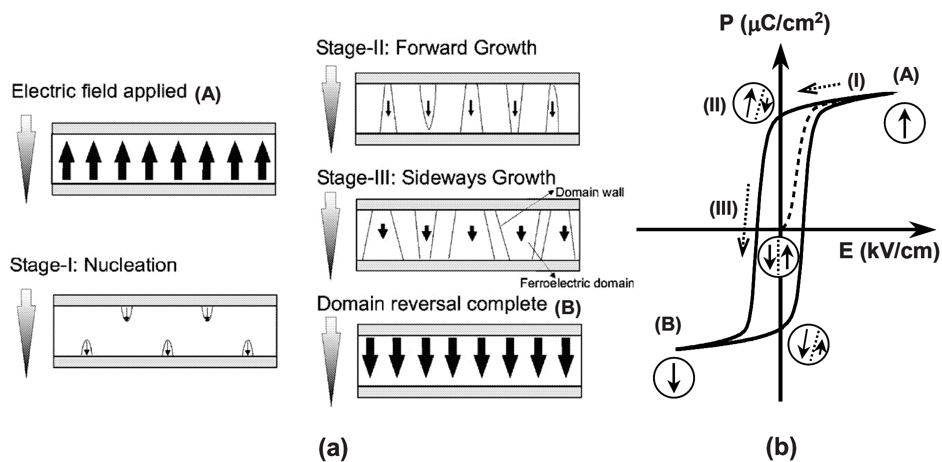

Figure 4.2: (a) Schematic illustration of the three phases of domain switching: stage-I, nucleation (fast); stage-II, forward growth (fast); and stage-III, sideway growth (slow); (b) Polarization hysteresis loop-electric field of a ferroelectric crystal.

The process of a polarization loop (Fig. 4.2(b)) can be divided into 4 steps, as described in Fig. 4.3 [16]. At the first step, the charge injection is illustrated by the presence of the electron (*e*-), which may occur during high-applied field such as saturation polarization (P_s), entering the domain. Next, the injected charge (*e*-) ionizes one of the *B*-site cation, in this case, the Ti^{4+} is converted to Ti^{3+} resulting in what is referred to as defect ionization (Ti^{4+} + $e^- \rightarrow Ti^{3+}$). This might occur quite quickly, perhaps during the removal of the applied field as shown in the hysteresis for the defect ionization (step 2).

The third step in the switching process illustrates the role of the oxygen vacancy. This step, called vacancy migration, suggests that the vacancy migrates toward the defect site. The migration of oxygen vacancies is most likely to occur around the value of field needed to switch the domain (coercive of voltage-field), because this would be when the vacancies are most mobile. It is thought that the presence of oxygen vacancies plays a critical role in stabilizing the defects to become pinning sites. Finally, when the oxygen vacancies become associated with the defect Ti^{3+}, there is a resulting distortion of the oxygen octahedron around the cation that is thought to stabilize the defect and make it an effective domain-wall pinning site. The domain at this point has been rendered unswitchable, and the overall switchable polarization decreases. This process is known as fatigue characteristics.

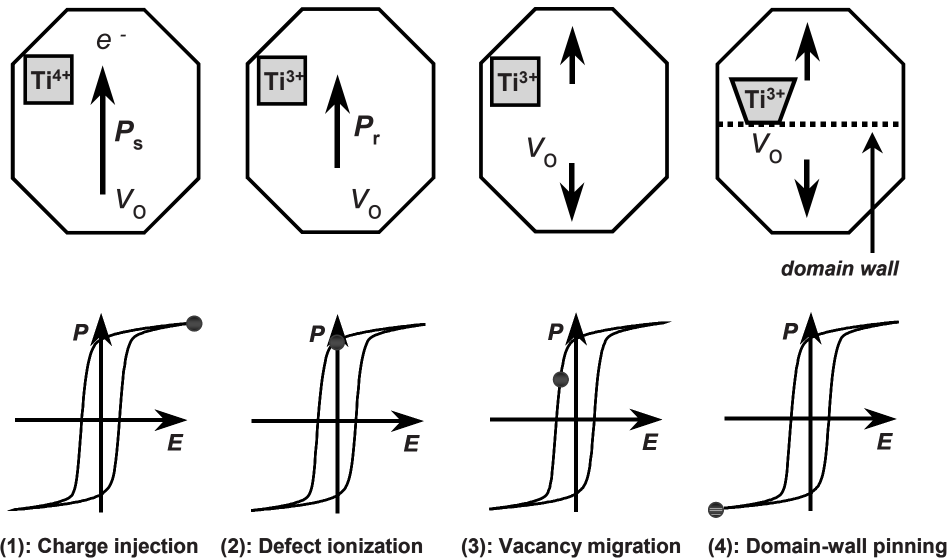

Figure 4.3: Schematic of a single-domain undergoes the polarization hysteresis loop. Within the domain, there are vectors representing the polarization present in the domain and the oxygen vacancy is indicated by the symbol V_O.

4.4 Polarization fatigue in ferroelectric thin films

In order to investigate the polarization fatigue in ferroelectric thin films, 250-nm-thick PZT thin films were grown by PLD on platinized silicon ($Pt/Ti/SiO_2/Si$) substrates. In Fig. 4.4(a), the XRD pattern shows the existence of a (100)-preferred PZT orientation together with a minor (110) peak. For the electrical measurements, Pt top-electrodes with an area of 100×100 μm^2 were made by the stencil patterning technique in combination with PLD [17, 18]. As shown in Fig. 4.4(b), when the polarization switching is continually repeated, the remnant polarization (P_r) decreases slowly and then decreases significantly at 10^5 cycles. After 10^8 cycles, the remnant polarization remains within 40% of the initial value.

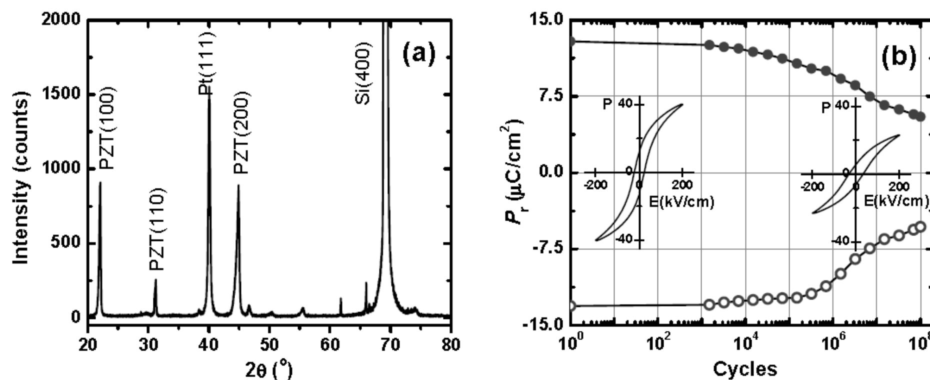

Figure 4.4: (a) XRD pattern of PZT thin films grown on $Pt/Ti/SiO_2/Si$ substrates. (b) Fatigue experiment on $Pt/PZT/Pt/Ti/SiO_2/Si$ capacitors, performed with bipolar switching pulse of 200 kV/cm pulse height and 0.33 ms (1.5 kHz) pulse width, and measured at ±200 kV/cm amplitude and 1 kHz frequency. The insets show the *P-E* loops at initial stage and after 10^8 switching cycles, respectively.

The decrease of polarization (or fatigue characteristics) in ferroelectric capacitors with an increase in the number of switching cycles has been studied. Most of the studies in fatigue characteristics indicate two mechanisms for the decrease of polarization: (i) suppression of the domain switching, and (ii) accumulation of oxygen vacancies after fatigue cycling. Both mechanisms occur near the ferroelectric film-electrode interfaces. The suppression of domain switching is related to the pinning of the domain wall in the ferroelectric films [19, 20] or the inhibition of the near-interfacial nucleation of the opposite domain switching by the entrapped charge [21-24]. Meanwhile, another mechanism involves the formation of interfacial layers[i] near the film-electrode interfaces due to the effect of the accumulation of oxygen vacancies after fatigue cycling, that reduces the total applied electric field across the ferroelectric capacitors and hence

---

[i] The layer with low dielectric constant. Moreover, this is the layer where polarization almost vanishes.

decreases the polarization [3, 25, 26]. Moreover, accumulation of oxygen vacancies would tend to stabilize the trapped charge near the interfaces, which could reduce the local detrapping rate, and then potentially promoting fatigue.

In the fatigued state, the density of oxygen vacancies (V_O) at the interface is possibly much higher than that in the ferroelectric film ("bulk" region), due to the migration and accumulation of oxygen vacancies, which is experimentally confirmed by the Auger electron spectroscopy (AES) [27], and the electron paramagnetic resonance (EPR) [28, 29]. These indicate that the accumulation of oxygen vacancies increased with the switching cycles increasing, and thereby resulting in a decrease in the polarization.

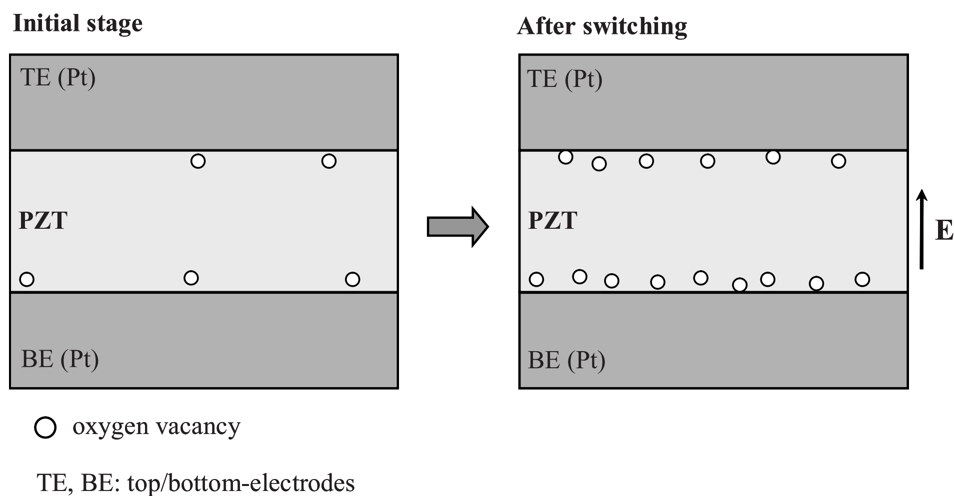

Figure 4.5: Modeling of the accumulation of oxygen vacancies at the film-electrode interfaces in Pt/PZT/Pt/Ti/SiO_2/Si capacitors after fatigue cycling.

Figure 4.5 shows a space-charge model for the behavior of oxygen vacancies after the switching process for PZT/Pt capacitors. According to the Dawber-Scott study [23], mobile charged defects such as oxygen vacancies are easily accumulated near the film-electrode interfaces, because the mobility of the oxygen vacancies is larger than that of lead [30] and form interfacial layers under an external field [31]. When positive or negative electric fields are applied to the top electrodes, oxygen vacancies flow toward the bottom or top electrodes, respectively.

Figure 4.6 illustrates the change in the capacitance of interfacial layer (C_i) in PZT/Pt capacitors as a function of fatigue cycles [32]. Assuming the dielectric constant of interface layer (ε_i, $\varepsilon_i = C_i \times d_i / \varepsilon_0 A$) is a constant, a decrease in C_i would lead to an increase in interfacial layer thickness (d_i) with the switching cycles increasing and resulting in a decrease in the

measured capacitance (C_m). This phenomenon is attributed to the decrease in the remnant polarization of the PZT devices with Pt as the electrodes (Fig. 4.4(b)). Since the electrode has an effect on the fatigue of the PZT capacitors, the adoption of the conducting oxide electrode instead of the metal electrode would further improve the fatigue resistance of the capacitor, because the oxide electrode can act as sinks for oxygen vacancies, thereby preventing their accumulation at the film/electrode interface. This effect will be discussed below.

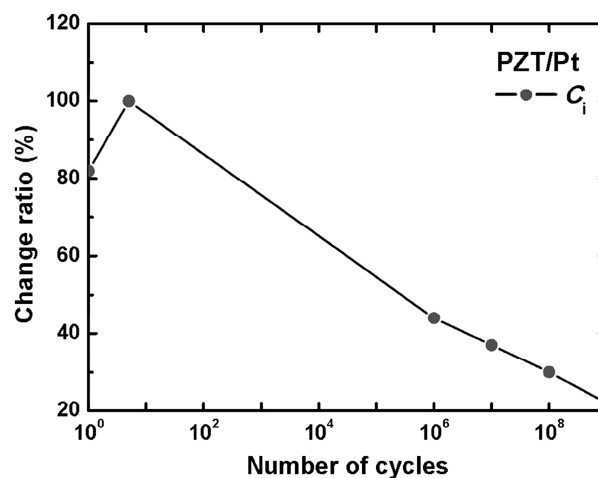

Figure 4.6: The change ratio of the capacitance of interfacial layer (C_i) in PZT/Pt capacitors after various fatigue switching cycles.

In general, a reduced accumulation of oxygen vacancies near the film-electrode interfaces might reduce the suppression of domain switching and interface layer formation, and consequently lead to improvement in the fatigue resistance of the ferroelectric capacitors. It is indicated that the interface between ferroelectric film and the electrode plays an important role in the switching process. In the PZT capacitors using the conductive-oxide layers as the electrodes (e.g., SRO), oxygen vacancy accumulation and interfacial layer formation can be reduced due to the oxide-electrodes act as a sink for oxygen vacancies or by reducing the vacancy concentration through donor doping [21, 22], because the conductive-oxide SRO electrodes can consume the oxygen vacancies by changing their oxygen nonstoichiometry. This model, described in Fig. 4.7, would explain why the conductive-oxide electrodes that have a large tolerance for oxygen deficiency (e.g., SRO) are better than metals such as platinum (Pt) which are ineffective sinks for oxygen vacancies.

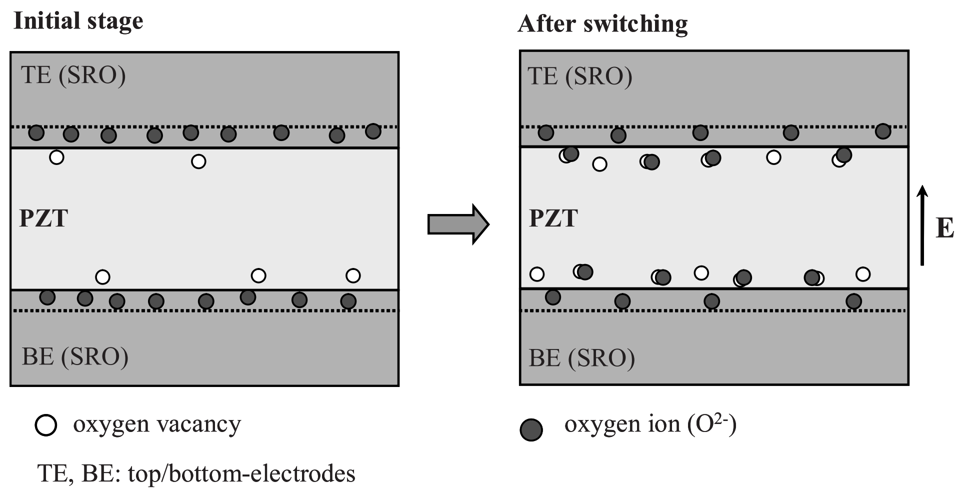

Figure 4.7: Effect of oxide electrodes on the accumulation of oxygen vacancies at the film-electrode interfaces in PZT/SRO capacitors after polarization switching.

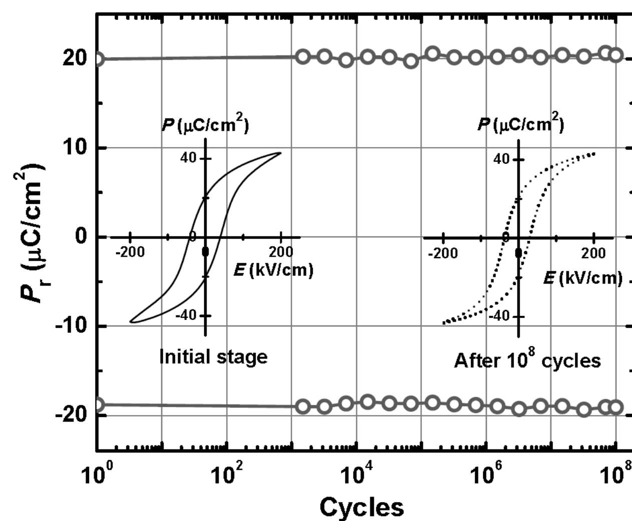

Figure 4.8: Remnant polarization P_r of SRO/PZT/SRO/YSZ/Si capacitors as a function of cumulative switching cycles, performed with bipolar switching pulse of 200 kV/cm pulse height and 0.33 ms (1.5 kHz) pulse width, and measured at ±200 kV/cm amplitude and 1 kHz frequency. The insets show the *P-E* loops at initial stage and after 10^8 switching cycles, respectively.

Figure 4.8 reveals the phenomenon of polarization switching of the SRO/PZT/SRO/CeO_2/YSZ/Si capacitors. In this study, the 250-nm-thick (001)-oriented PZT thin films were used. The measurement was performed using bipolar pulses of 200 kV/cm (pulse height) in combination with the pulse width corresponding to the 1.5 kHz signal (pulse width ~ 0.33 milliseconds), and the polarization hysteresis (*P-E*) loops were measured at $\pm$200 kV/cm amplitude and 1 kHz frequency after certain switching cycles. No degradation of the remnant polarization after 10^8 switching cycles was observed. This indicates that the ferroelectric capacitors using conductive-oxide SRO as the electrodes significant improves polarization switching as compared with the metal electrodes such as platinum (Pt). To confirm the fatigue resistance of PZT/SRO, the *P-E* loops at initial stage and after 10^8 switching cycles were tested at $\pm$200 kV/cm amplitude and 1 kHz frequency. As shown in Fig. 4.8 *insets*, a similar *P-E* loop was observed in both cases.

To examine the role of conductive-oxide electrodes on the reduction of oxygen vacancies after polarization switching, the C_i value was evaluated as a function of switching cycles. The relative independence of C_i value confirms that the accumulation of oxygen vacancies at the PZT/SRO interfaces is prevented after polarization switching.

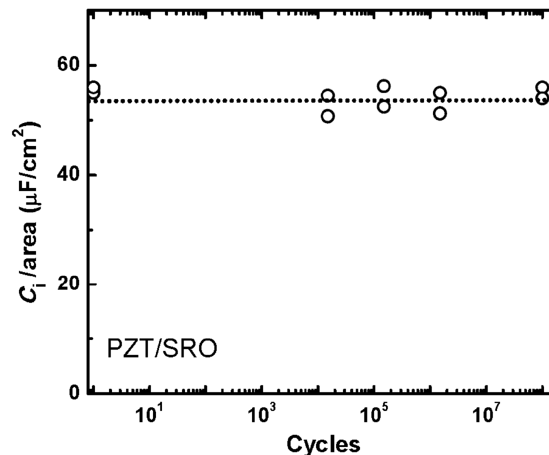

Figure 4.9: Capacitance/area of interfacial layer (C_i /area) in PZT/SRO capacitors as a function of switching cycles.

4.5 Orientation effects on ferroelectric properties

The electrical properties of PZT thin films are known to depend on their crystallographic orientation, microstructure as well as film thickness. In this experiment, we compare the polarization properties of the (110)- and (001)-oriented PZT thin films, which were deposited on SRO buffered CeO_2/YSZ/Si substrates, as shown in chapter 3 section 3.4.

The polarization switching and polarization hysteresis (*P-E*) loops of the (110)- and (001)-oriented PZT thin films are shown in Fig. 4.10. The (001)-oriented PZT film shows a classical ferroelectric polarization loop; whereas the polarization loop of the (110)-oriented PZT film is noticeably degraded. The remnant polarization (P_r) in the (110)-oriented film is considerably lower compared to the (001)-oriented film (13.5 $\mu C/cm^2$ compared to 20.1 $\mu C/cm^2$, respectively). Subsequently, both films are subjected to a high number of switching cycles in order to monitor the ferroelectric response stability. As illustrated in Fig. 4.10(a), the PZT thin film using SRO electrodes in this study show essentially no fatigue; i.e., P_r does not decrease as the number of switching cycles increase. For the (001)-oriented film, P_r remains constant up to 10^8 cycles. Meanwhile, the (110)-oriented film shows an improvement of P_r from 13.5 to 18 $\mu C/cm^2$. P_r now almost equals that of the (001)-oriented film. Furthermore, the polarization loop and switching current after 10^8 cycles, as shown in Figs. 4.10(c) and 4.12(b), look similar for both samples [5].

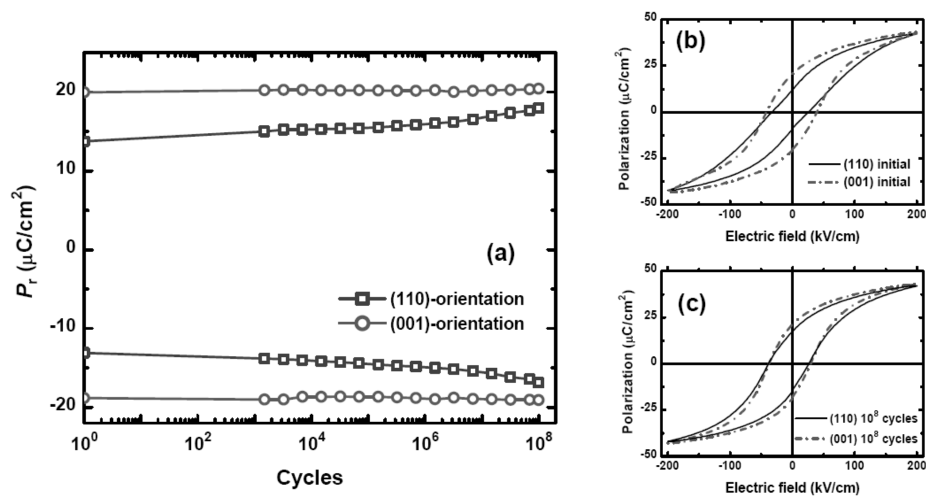

Figure 4.10: (a) Remnant polarization of the (110)- and (001)-oriented PZT thin films versus the number of switching cycles. The measurement was performed with bipolar switching pulse of 200 kV/cm pulse height and 0.33 ms (1.5 kHz) pulse width. *P-E* hysteresis loops were measured with an amplitude of ±5 V (±200 kV/cm) and 1 kHz frequency for the (110)- and (001)-oriented PZT thin films on CeO_2/YSZ/Si substrates at initial stage (b) and after 10^8 switching cycles (c).

As described above, the (001)-oriented PZT/SRO capacitor shows a classical polarization switching behavior in which P_r almost keeps constant with an increase in switching cycles. However, the strange behavior of P_r in the (110)-oriented PZT/SRO capacitor is observed, in which P_r increases with increasing switching cycles up to 10^9 cycles (Fig. 4.11).

To understand the dependence of polarization switching in the (110)-oriented film, the switched polarization (P*) between two opposite polarity pulses and non-switched polarization (P^) between two identical polarization pulses as a function of switching cycles are also presented in Fig. 4.11. The resulting increases of P* value and decreases of P^ value show that the volume-fraction of ferroelectric phase was increased while the volume-fraction of non-ferroelectric phase was decreased with increasing number of switching cycles. We have proposed two models to explain the improvement of remnant polarization in the (110)-oriented PZT films grown on SRO buffered CeO_2/YSZ/Si substrates.

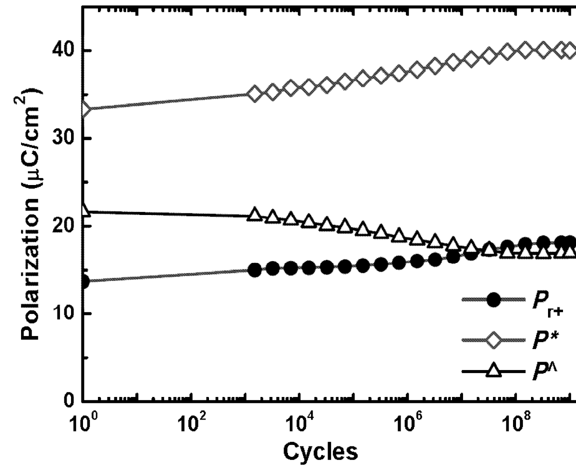

Figure 4.11: Remnant polarization P_{r+}, switched polarization P* and non-switched polarization P^ of the (110)-oriented film as a function of cumulative polarization switching cycles using bipolar switching pulse of 200 kV/cm pulse height and 0.33 ms (1.5 kHz) pulse width, and measured at ±200 kV/cm and 1 kHz.

According to the first model, similar to the case of (001)-oriented PZT thin films, the SRO oxide-electrodes acts as a source of oxygen to compensate for oxygen vacancies at the interfaces, thereby the reduction of P_r after repeated switching cycles is prevented. On the other hand, P_r keeps constant with an increase in switching cycles. However, as can be seen in Fig. 4.11, P_r of the (110)-oriented PZT thin films is monotonically increased up to the switching of 10^9 cycles. This improvement of P_r might be explained by the second model. According to the second model, some spontaneous polarizations were locked by defects at the interfaces between twin-related crystal domains in the (110)-oriented films. These defects were gradually removed to the film/electrode interfaces after repeated

switching cycles and the locked spontaneous polarization were freed. Therefore, the remnant polarization of the (110)-oriented films increases with increasing switching cycles.

As shown in Figs. 4.12(b) and 4.12(d), the switching current of the (001)-oriented film shows only one peak when the ferroelectric domains are switched and it almost keeps constant with increasing switching cycles. Whereas, two peaks appear in the switching current of the (110)-oriented film (Fig. 4.12(a)). In Figs. 4.12(a), the first peak value associated with switching of the ferroelectric domains, which appears at higher electric fields, is found to increase with increasing switching cycles (Fig. 4.12(c)); while the second peak of non-ferroelectric phase at zero electric field decreases and then disappears after 10^5 switching cycles [5], indicating the purely ferroelectric behavior. Thus, the (110)-oriented film undergoes a phase transition from a mixed ferroelectric - antiferroelectric behavior to a ferroelectric behavior after polarization switching.

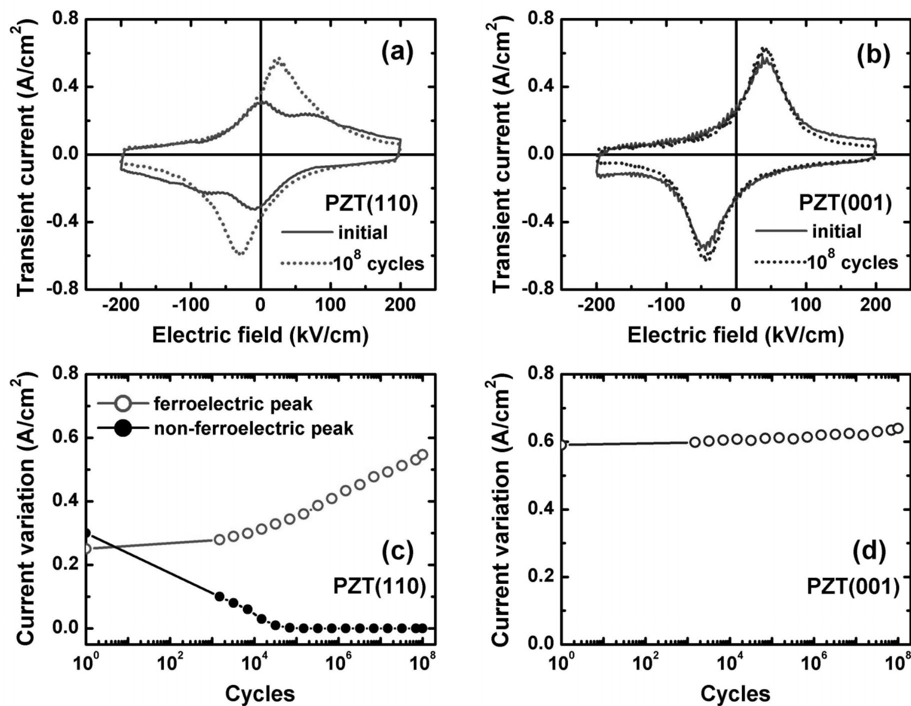

Figure 4.12: Switching current after cyclic switching after various number of switching cycles: 1 cycle (initial stage) and 10^8 cycles for the (a) (110)- and (b) (001)-oriented PZT thin films. (c) and (d) show the variations in the maximum value of the switching current as a function of the number of switching cycles for the (110)- and (001)-oriented PZT thin films, respectively.

The different dynamic ferroelectric behavior of both films most likely originates from the difference in structural properties. Although grain boundaries do exist in the (001)-oriented PZT film, the separated grains are oriented coherently in-plane. This is in contrast with the (110)-oriented PZT film, where the in-plane coherence is poor (chapter 3 section 3.4). In this case, the structural domains, which are not aligned with respect to each other, exist in the SRO film, and hence in the PZT. This also affects the out-of-plane coherence, as can be seen from the differences between the rocking curves.

The grain boundaries between the twin-related crystal domains are formed by defective crystal faces. These disturbed in-plane structural defects form pinning centers for charges and ferroelectric domain walls at the grain boundaries, which significantly increase the leakage current. Figure 4.13(a) shows the leakage current versus electric field for the (110)- and (001)-oriented films at the initial stage and after multiple cycling. It is seen that the leakage current of the (001)-oriented film is smaller than that of the (110)-oriented film at the initial stage. After 10^8 cycles, however, the leakage current is similar for both films. Upon switching, the leakage along grain boundaries and/or domain walls is reduced by removal of pinning centers for the charges [5]. This diminishes the number of shorted polar domains, resulting in a larger total ferroelectric contribution.

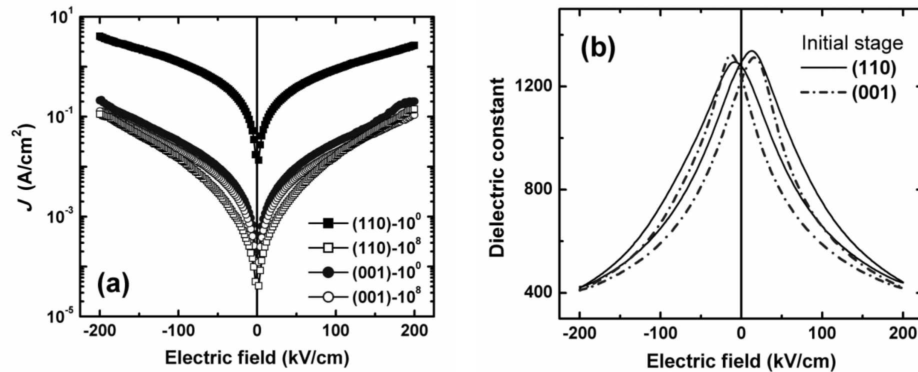

Figure 4.13: (a) Leakage current density (*J*) vs. electric field characteristics of the (110)- and (001)-oriented PZT thin films at initial stage and after 10^8 switching cycles. (b) Dielectric constant of the (110)- and (001)-oriented PZT thin films at 10 kHz frequency.

The dielectric constant (ε) varies with the electric field resulting from the capacitance measurements, as shown in Fig. 4.13(b). As expected for ferroelectric property, the butterfly-shape hysteresis appears in both capacitors. The variation of the dielectric response with the electric field is associated with the domain reorientation process: domain switching from one poling state to the other when the dc field is swept from negative-bias to positive bias and back [33]. The ε-E curve in (110)-oriented PZT capacitor indicates the asymmetry in the maximum dielectric constant values that can be observed in the vicinity of the spontaneous polarization. This confirms that this capacitor contains the space-charge accumulation at the

interface. The (001)-oriented capacitor, however, exhibits a sharper humped ε-*E* loop, and more symmetry in comparison with the (110)-oriented one.

At low field, the main contribution to the high dielectric constant values is due to domain wall vibrations. The peaks in the ε-*E* curves at the coercive field are due to a high domain-wall density and motion. These will be hereafter known as the extrinsic properties of the capacitor. For high field, as the electric fields are beyond the coercive field, most switchable domain have already been aligned along the direction of the electric field, the dielectric constant is small since it is determined mainly by variation of the dipoles [33]. In fact, the complicated domain structure tends to coalesce to a metastable, involving not only the alignment of spontaneous polarization orientation, but also the vanishment of domain-walls. Therefore, it is reasonable to expect that the decreased dielectric constant is attributed to the decrease of the domain-wall density. These will be hereafter known as the intrinsic properties of the capacitor. It can also be seen from Fig. 4.13(b) that the (001)-oriented film capacitor exhibits a sharper humped ε-*E* curve in comparison with the (110)-oriented film, indicating that the (001)-oriented film capacitor has a greater distribution of domains. Moreover, the ε-*E* curve of (001)-oriented film is broader than the (110)-oriented film capacitor at low electric field and similar at high electric field. These imply that the extrinsic properties of the capacitors were much more affected by film orientation than the intrinsic properties.

4.6 Effects of film quality and residual stress on the electrical properties of PZT thin films

Figure 4.14 displays the polarization hysteresis (*P*-*E*) loops of (001)-oriented PZT film capacitors measured with ±200 kV/cm amplitude and at a frequency of 1 kHz. As shown in Fig. 4.14(a), PZT film on STO/Si exhibits larger P_r as compared to PZT film on CeO_2/YSZ/Si. This difference is ascribed to the different peak intensities achieved on both kinds of substrates. From the Fig. 3.9 in chapter 3 section 3.5, as can be seen, the peak intensity and the full-width at half maximum (FWHM) are increased and decreases, respectively, with the STO buffer-layer, compared with the CeO_2/YSZ double buffer-layers (see more in Tab. 4.2). This means that the crystalline quality of PZT film on ($SrTiO_3$) STO/Si is better than that on CeO_2/YSZ/Si substrates.

Although the PZT thin films grown on Si and STO substrates have similar orientation, their *P*-*E* characteristics are substantially different. While a larger P_r value of 46 µC/cm^2 is measured for the films deposited on STO, the P_r value of 20-26 µC/cm^2 is measured for the films deposited on silicon (Fig. 4.14(b)). These results also shown that the films deposited on STO have a very sharp, square and well-saturated hysteresis loop, while the films on silicon have a slanted hysteresis characteristic. The high P_r and well-saturated *P*-*E* loop of PZT films on STO results from the elongated *c*-axis parallel to the film normal (*c*-plane). Conversely, the lower P_r and slanted hysteresis loop shape of PZT films on Si are due to

relaxation in *a-b* plane which comes from the twinning effect between thin film and silicon substrate [5].

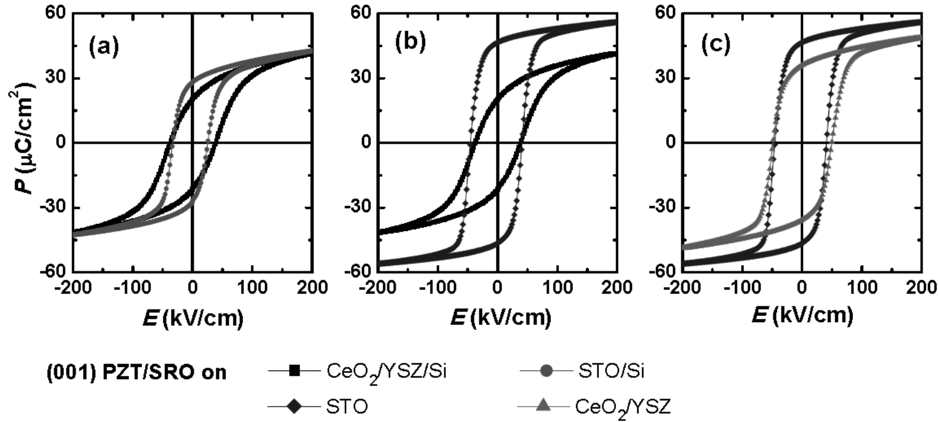

Figure 4.14: Polarization hysteresis (*P-E*) loops of the 250-nm-thick (001)-oriented PZT thin films deposited on different buffer-layers and substrates such as CeO_2/YSZ/Si, STO/Si, CeO_2/YSZ, and STO. All measurements were done at ±200 kV/cm amplitude and 1 kHz frequency.

In PZT thin films, the spontaneous polarization lies along the (001) direction or in an equivalent direction [34]. An increase in the *c*-lattice constant (or *c/a* ratio) implies a larger displacement of the central Ti^{4+} ion, and hence, there is a larger switching polarization [35]. The higher P_r value of the film on STO, in this study, also suggests that the value of P_r increased with increasing c/a ratio. The increase in c/a ratio can be ascribed to the change of the thermal residual stress behavior of thin films from tensile- to compressive-stress. This result has been discussed in chapter 3 section 3.5.

Figure 4.15 presents the crystal structure of PZT as the function of temperature. At high temperature ($T > T_c$, T_c is Curie temperature), PZT is cubic (*a*=*b*=*c*) (Fig. 4.15(a)). The transition from paraelectric phase (at $T > T_c$) to ferroelectric phase (at $T < T_c$) is observed during cooling from the deposition temperature to room temperature. Depend on the compressive or tensile stress generated in the PZT thin films, Figs. 4.15(b) and 4.15(c), the *c*-lattice parameter is increased or decreased, respectively.

As mentioned previously, studies have shown that the residual stress induced in the PZT thin film is known to affect the orientation of the ferroelectric domains [8, 9, 36]. Tensile stress tends to cause the domains originally parallel to the film surface, which results in a reduction in polarization. In contrary, compressive stress causes the domains to orient along the longitudinal direction, which in turn will cause the increase of polarization. These behaviors are observed in Fig. 4.16(a). Furthermore, it can be seen that the remnant polarization increases markedly with increase of the lattice parameter *c/a* ratio (Fig. 4.16(b)).

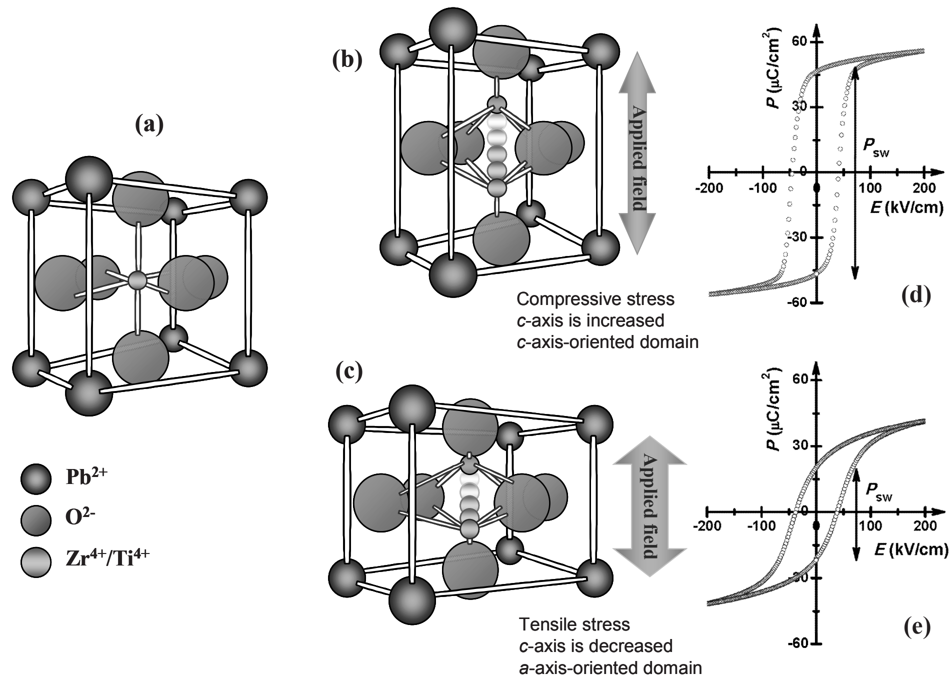

Figure 4.15: (a) Cubic crystal structure of PZT films at $T > T_c$; Structure of PZT films at $T < T_c$ under (b) a compressive stress and (c) a tensile stress. *P-E* hysteresis loops of PZT thin films under (d) compressive and (e) tensile stress, respectively.

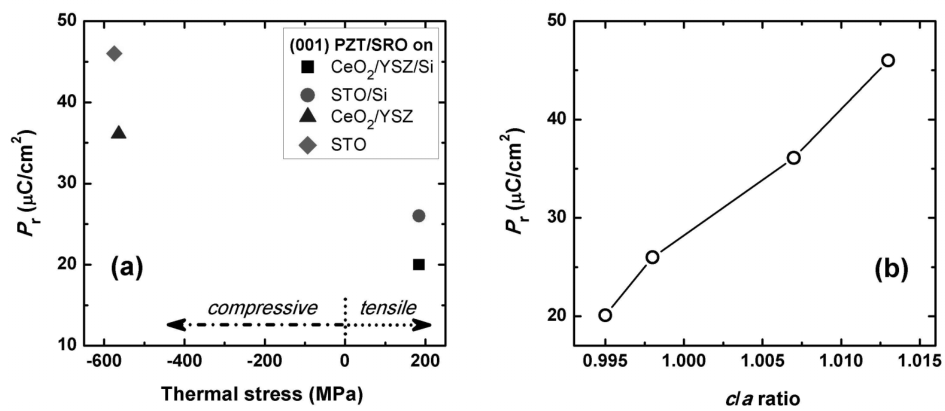

Figure 4.16: Remnant polarization (P_r) of PZT thin films as a function of (a) thermal stress and (b) *c*/*a* ratio.

All (001)-oriented PZT thin film capacitors on different substrates exhibit good ferroelectric switching. To investigate the substrate effect on the polarization switching (or polarization fatigue), the polarization switching measurements were measured using bipolar switching pulse of 200 kV/cm pulse height and 0.33 ms pulse width. Figure 4.17 shows remnant polarization (P_r) and coercive field (E_c) as a function of switching cycles for PZT/SRO capacitors coated CeO_2/YSZ/Si, STO/Si, CeO_2/YSZ, and STO substrates, respectively. It can be seen that all PZT capacitors using conductive-oxide SRO electrodes have fatigue-free characteristics up to 10^8 switching cycles.

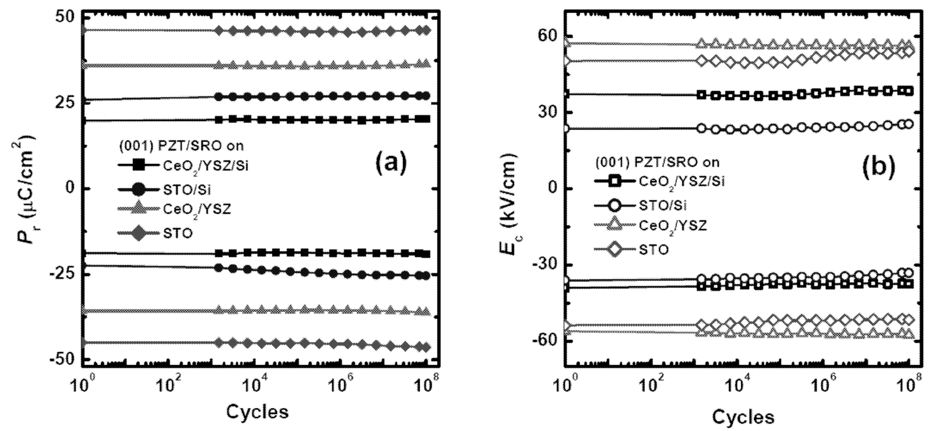

Figure 4.17: (a) Remnant polarization P_r and (b) coercive field E_c of the (001)-oriented PZT thin films grown on different substrates as a function of the switching cycles. The measurement was performed with bipolar switching pulse of 200 kV/cm pulse height and 0.33 ms (1.5 kHz) pulse width. *P-E* hysteresis loops were measured with an amplitude of ±200 kV/cm and 1 kHz frequency.

Table 4.1: Parameters of the 250-nm-thick PZT thin films grown on different substrates.

	Sample			
	PZT (1)	PZT (2)	PZT (3)	PZT (4)
Substrate	Si(001)	Si(001)	YSZ(001)	STO(001)
Buffer-layer(s)	CeO_2/YSZ	STO	CeO_2	none
Top/bottom electrodes	SRO	SRO	SRO	SRO
Film orientation	(001)	(001)	(001)	(001)
FWHM of PZT(002) peak	1.41°	0.51°	0.56°	0.18°
P_r (μC/cm^2)	20.1	26.0	36.1	46.0
P_r / P_s	48.2 %	60.9 %	74.3 %	81.8 %
E_c (kV/cm) from *P-E*	38.2	29.3	49.3	43.7
ε	1220	1100	750	570
E_c (kV/cm) from ε-*E*	16.8	14.5	36.2	32.0

* P_s: the saturation (maximum) polarization.

4.7 Effect of measuring factors on ferroelectric properties of PZT thin films

In order to investigate the effect of measuring factors on the properties of PZT thin films, the 250-nm-thick (001)-oriented epitaxial PZT thin films grown on SRO/STO substrates were used.

4.7.1 Polarization hysteresis loop

Electric-field dependence

Figure 4.18 illustrates how the *P-E* loops evolve as a function of the applied electric-field strength. At low applied electric-field (below E_c), the capacitor does not exhibit ferroelectric hysteresis. The smallest loop in Fig. 4.18(a) shows what one would expect to see for a linear, lossy capacitor with little evidence of ferroelectric switching. As the applied electric-field increases, the *P-E* loop begins to form a square hysteresis loop and indicating ferroelectric switching. Well-saturated hysteresis loops were obtained when the maximum applied electric field exceeds 200 kV/cm.

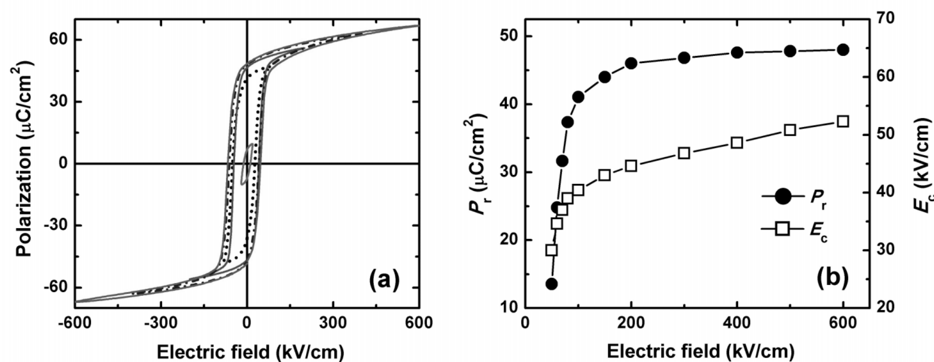

Figure 4.18: (a) Polarization hysteresis loops of PZT/SRO/STO capacitors under 50-400 kV/cm maximum applied electric field and 1 kHz frequency, and (b) remnant polarization P_r and coercive field E_c as a function of maximum applied electric field.

Fig. 4.18(b) shows the dependence of remnant polarization (P_r) and coercive field (E_c) on the applied electric field. Both P_r and E_c values were found to increase with an increase in the amplitude of the electric field. At low electric fields, P_r and E_c initially increased rapidly and with an applied electric field over 200 kV/cm, the P_r is almost saturated while V_c is increased slightly with increasing electric field. Sharper saturation implied that better microscopic homogeneity and a narrower distribution of local coercive field of ferroelectric domains are obtained. It is advantageous for high density applications since bit-to-bit variation will be reduced [37].

At high applied electric fields, where the switching polarization tends to saturate, the leakage current continues to rise (see more in Fig. 4.13(a)), increasing the space-charge at the ferroelectric film-electrode interface and hence the total polarization (or maximum polarization, Fig. 4.18(a)). The increase in the coercive field E_c is accompanied by an increase in the field-induced polarization. The increase in both P_r and E_c values with the increase of applied electric field can be seen in all PZT film structures [38-40].

Frequency dependence

Switching behavior of ferroelectric materials is a process of domain nucleation, domain growth and domain wall motion [41]. The switching time for domains in PZT film is usually in the range of a few hundred nano-seconds, which means that a frequency below 1 MHz provides enough time for full switching of the polarization. In order to investigate how the polarization properties depend on frequency, *P-E* hysteresis loops were measured in the range of 5 Hz – 2 kHz frequency.

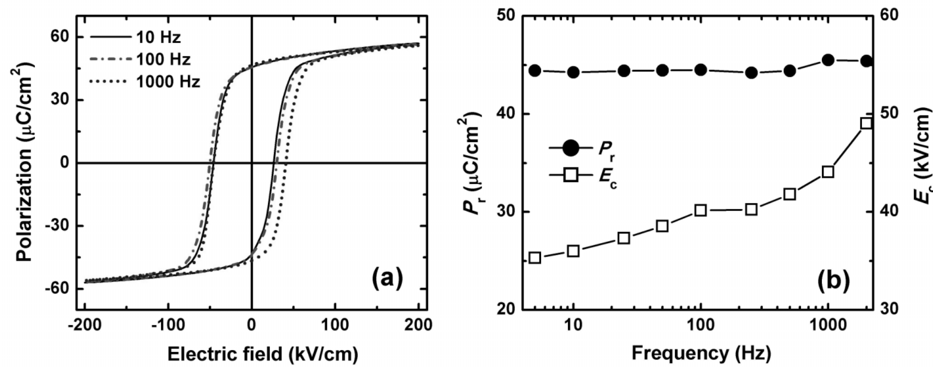

Figure 4.19: (a) Polarization hysteresis loops of PZT/SRO/STO capacitors under ±200 kV/cm applied electric field and different frequencies; (b) Remnant polarization P_r and coercive field E_c as a function of applied frequency.

Figure 4.19 shows the frequency dependence of the *P-E* loop, the remnant polarization (P_r) and the coercive field (E_c). It is shown that while the P_r value is independent of frequency, the E_c value is found to increase with increasing frequency, as shown in Fig. 4.19(b). The reason why the coercive field increases with increasing frequency is that domain switching in ferroelectric materials involves domain-wall motion, which has an increasing resistance and/or viscosity with increasing frequency [2].

Temperature dependence

The decrease of polarization with increasing temperature can be described by the limitation and freeze of domain movement and nucleation [42]. At low temperature, the domain-wall pinning becomes hard because of lower ionic mobility [43]. As the temperature increases, the value of the leakage current density increases due to an increase of the carrier injection and the formation of space-charge (dead-layer) at the ferroelectric film-electrode interface [44]. The formation of a dead-layer would lead to a decrease of the volume fraction: $V_f/[V_f+V_i]$, where V_f and V_i are denoted for volume faction of ferroelectric layer and dead layer, respectively) of 'bulk' ferroelectric layer in the capacitor and then decrease the remnant polarization at high temperature. On the other hand, the decrease of the remnant polarization with increasing temperature may also be due to the improved domain wall mobility.

Furthermore, with increasing temperature, the domain wall motion becomes easier, and thus a smaller electric field is needed to accomplish it. On the other hand, the coercive field was decreased with increasing temperature.

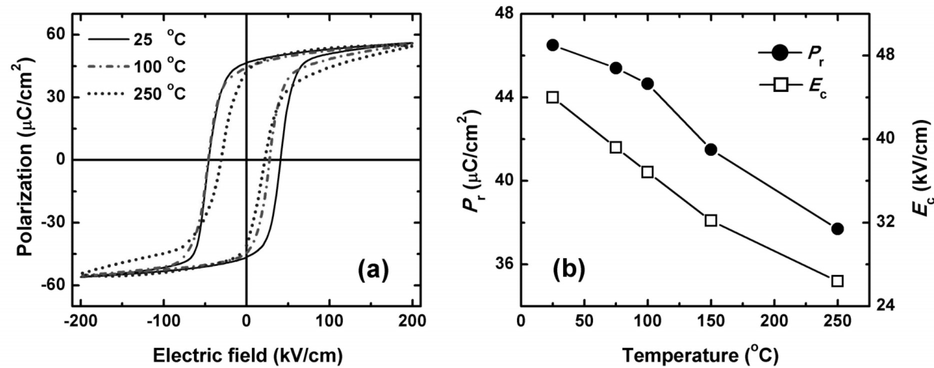

Figure 4.20: (a) Polarization hysteresis loops of PZT/SRO/STO capacitors measured at different temperatures. The *P-E* loops were performed with an amplitude of ±200 kV/cm and 1 kHz frequency; (b) Measured temperature dependence on remnant polarization P_r and coercive field E_c.

As shown in Fig. 4.20, with increasing temperature in the range of 25-250 °C, both P_r and E_c of PZT film capacitors were found to decrease and the *P-E* hysteresis loop was expanded due to the increase of leakage current with increasing temperature. If temperature increases continuously, the *P-E* loop will be increasingly expanded and the ferroelectric behavior of capacitors gradually disappears. The temperature dependence of the ferroelectric properties can be described by the existence of both ferroelectric and anti-ferroelectric (paraelectric) phases in the capacitors. In which, the P_r value decreases with increasing measured temperature due to the decrease in the volume fraction of ferroelectric phase. With increasing temperature, the thermal motion of the atoms will

increase, an eventually they can overcome the energy barrier separating the various orientation. Thus at high temperatures, the distribution of atoms becomes statistical and the crystal behaves as a normal dielectric material (paraelectric phase) and no longer as a polar material. The temperature at which ferroelectric-paraelectric transition occurs is known as the Curie temperature (T_c). The Curie temperature of $PbZr_{0.52}Ti_{0.48}O_3$ films ranges from 350 to 450 ^oC depending on the film thickness, orientation, and so on [45, 46]. This data is also in agreement with the results of Meng *et al*. [47] and Xu *et al*. [48] for PZT/LNO/STO and PZT/Pt/Ti/SiO_2/Si capacitors, respectively.

4.7.2 Polarization switching

Electric-field dependence

The effect of the applied electric field on the polarization switching (fatigue) phenomenon has been widely studied, particularly for the conventional Pt/PZT/Pt structure [14]. In this structure, the polarization (P_{r+}-P_{r-}) decreases clearly when increasing the applied pulse height of bipolar switching. Similar results on PZT/Pt films were reported in the literatures [49-51]. However, applying higher voltages during cycling does not lead to a faster degradation of the polarization but rather to a decrease of the total polarization of these samples.

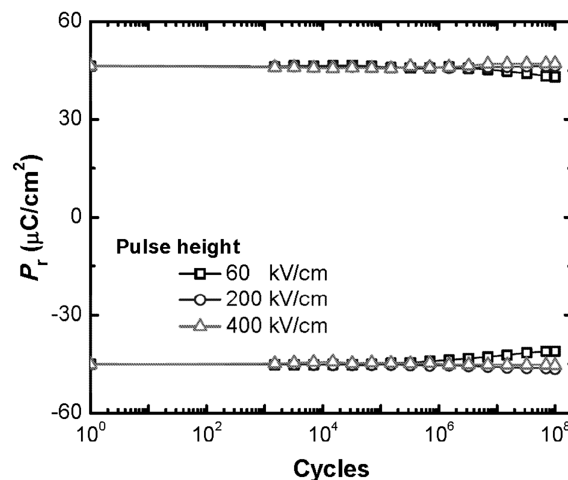

Figure 4.21: Pulse height dependence of polarization switching characteristics in PZT/SRO/STO capacitors.

In order to investigate the effect of pulse height on the polarization switching of PZT/SRO/STO structure, a series of polarization switching measurements were performed where the pulse height was increased from 50 to 400 kV/cm at a cycling frequency of 1 kHz. The polarization hysteresis loops were measured with an amplitude of ±200 kV/cm at a frequency of 1 kHz. The corresponding polarization switching curves are shown in Fig.

4.21. It was demonstrated that the remnant polarization is almost constant and decreases slowly after 10^6 switching cycles in the case of smaller pulse height (e.g., 60 kV/cm) due to the incomplete switching of the ferroelectric phase for these small amplitudes.

Moreover, the study of the polarization switching at different pulse height signals also indicated that the rate of switching was almost independent of the pulse height, indicating the complete switching of all ferroelectric domains when the pulse height is larger than 200 kV/cm.

Frequency dependence

The dependence of remnant polarization (P_r) of Pt/PZT/Pt capacitors on the number switching cycles has been studied by applying a bipolar pulse of varying pulse width (or frequency). However, this characteristic, to date, is still not well-understood. Some researchers have shown that the higher pulse width, the lower the fatigue rate [52-54]. It is also shown that the remnant polarization loss due to fatigue is proportional to N/f^2 [52], with N and f are the number switching cycles and bipolar frequency, respectively. However, results from other studies showed different behaviors. The work by Chae *et al*. [50] and Grossmann *et al*. [55], show a decrease of the polarization is independent of the frequency, and it is only depended on the number switching cycles.

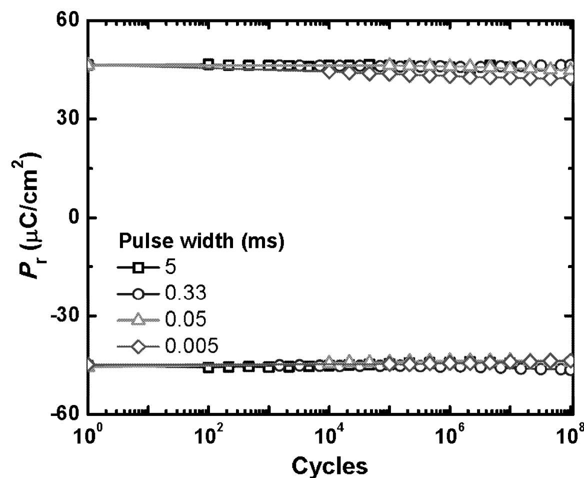

Figure 4.22: Pulse width dependence of polarization switching characteristics in PZT/SRO/STO capacitors.

In order to investigate the bipolar frequency dependence of the PZT/SRO/STO capacitors, in our study, the polarization switching was carried out by applied a bipolar rectangular pulse train of varying pulse width from 0.005 ms (100 kHz) to 5 ms (100 Hz) and at pulse height of 200 kV/cm. After a certain number switching cycles, the remnant polarizations were evaluated from the polarization loops which were measured with an

amplitude of ±200 kV/cm at a frequency of 1 kHz, as shown in Fig. 4.22. It is shown that the pulse width had no effect on the remnant polarization with the number of switching cycles.

Temperature dependence

The temperature dependence of fatigue characteristics must be one of the most important characteristics in view of application requirement and physical properties. In the Pt/PZT/Pt capacitors, fatigue resistance characteristics were reduced and fatigue rate increased with increasing temperature [14, 56]. It can also be seen in the PZT/SRO/STO capacitors where the polarization switching process is decreased with increasing temperature, see Fig. 4.23.

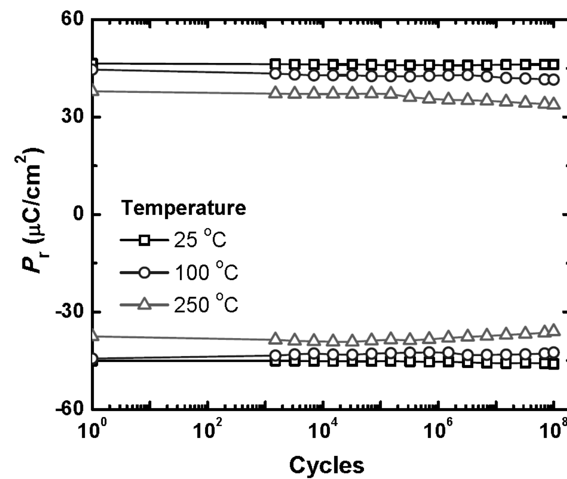

Figure 4.23: Measured temperature dependence of polarization switching characteristics in PZT/SRO/STO capacitors.

The temperature dependence of polarization switching in PZT capacitors is well-known in relation with the domain switching and nucleation behaviors with temperature [42, 47]. Because domain wall motion is a thermally activated process, the domain wall pinning becomes easier because ionic mobility, diffusion, and leakage current were exponentially increased with increasing temperature. It is therefore reasonable to attribute the decrease in remnant polarization to the increase in the domain wall mobility. Furthermore, the temperature dependence in PZT capacitors can be also described by a change in the volume fraction of the ferroelectric phase, in which the volume fraction of the ferroelectric phase is decreased with increasing temperature. At low temperatures, the capacitors are fatigue-free. As the temperature continued to increase over 250 °C, a fatigue signal would be seen in PZT/SRO/STO capacitors after 10^5 cycles. It can be explained by the reduction of effective sinks (conductive oxygen) for oxygen vacancies from SRO electrodes with increasing temperature.

4.8 Summary and conclusions

We have analyzed the effect of the electrode on the fatigue (or polarization switching) characteristics in PZT thin films. PZT thin films on metal electrodes (e.g., Pt) reveal significant fatigue degradation in the polarization with increasing switching cycles. On the contrary, PZT thin films on conductive-oxide electrodes (e.g., $SrRuO_3$) exhibit fatigue-free behavior. In this study, the dependence of fatigue behavior on the electrode materials for PZT thin films may be result of the effect of the film/electrode interface on the domain switching or formation of dead-layers. In this way, the fatigue behavior is observed in PZT/Pt capacitors due to the accumulation of oxygen vacancies near the interface after fatigue switching. A reduced accumulation of oxygen vacancies near the film/oxide-electrode can lead to a fatigue-free response in PZT/oxide-electrode capacitors.

With different crystalline orientations of PZT/SRO layers grown on CeO_2/YSZ buffered (001)Si substrates, we found that the polarization behavior of the (110)- and (001)-oriented PZT thin film as a function of switching cycles is different. The difference between the films most likely originates from the difference in structural properties. The poor in-plane structural coherence of (110)-oriented film is responsible for a significant leakage current reducing the polarization in comparison with the good in-plane coherency in the (001)-oriented film. This is the reason for unstable polarization behavior of the (110)-oriented film, as compared to the extremely constant response of the (001)-oriented one, showing very low leakage current from the beginning. However, after prolonged switching of the (110)-oriented film, the remnant polarization gradually improves because the continued switching slowly removes the leakage paths. Finally, approximately the same values as for the (001)-oriented film are obtained.

Next, we studied the effect of residual stress on the ferroelectric properties of PZT thin films. Here, (001)-oriented PZT/SRO thin films were grown on different substrates, such as CeO_2/YSZ/Si, STO/Si, CeO_2/YSZ, and STO. Due to different thermal expansion coefficients between the PZT film and substrate, thermal tensile stress was induced in the PZT films grown on silicon substrates, while the thermal compressive stress was induced in the PZT films grown on YSZ and STO substrates. Tensile stress tends to cause domains originally parallel to the film surface, which results in a reduction in polarization. In contrary, compressive stress causes the domains to orient along the longitudinal direction, which in turn will cause an increase of the polarization. On the other hand, the enhancement of their polarization might be explained by the increase of the lattice parameter c/a ratio due to the lattice distortion and thermal stress developed in the films.

By controlling the measuring factors such as temperature-frequency-electric field, we can observe the change in polarization switching of PZT thin films. The polarization switching is nearly independent of the fatigue excitation signal (pulse width or pulse height). Experiment data also showed a non-monotonic change of polarization switching

with increasing temperature. At low temperatures, the PZT thin film capacitors are fatigue-free; while, at measured temperature above 250 ^oC, a fatigue behavior is observed.

4.9 References

1. D. -H. Do, P. G. Evans, E. D. Isaacs, D. M. Kim, C. B. Eom, and E. M. Dufresne, *Structural visualization of polarization fatigue in epitaxial ferroelectric oxide devices*, Nature Materials **3** (2004) p. 365-369.
2. J. F. Scott, *Ferroelectric Memories*, Springer-Verlag, Berlin (2000).
3. A. K. Tagantsev, I. Stolichnov, E. L. Colla, and N. Setter, *Polarization fatigue in ferroelectric films: Basic experimental findings, phenomenological scenarios, and microscopic features*, J. Appl. Phys. **90** (2001) p. 1387-1402.
4. S. -Y. Chen and C. -L. Sun, *Ferroelectric characteristics of oriented $Pb(Zr_{1-x}Ti_x)O_3$ films*, J. Appl. Phys. **90** (2001) p. 2970-2974.
5. M. Dekkers, M. D. Nguyen, R. Steenwelle, P. M. te Riele, D. H. A. Blank, and G. Rijnders, *Ferroelectric properties of epitaxial $Pb(Zr,Ti)O_3$ thin films on silicon by control of crystal orientation*, Appl. Phys. Lett. **95** (2009) p. 012902(1-3).
6. V. Bornand, S. Trolier-McKinstry, K. Takemura, and C. A. Randall, *Orientation dependence of fatigue behavior in relaxor ferroelectric-$PbTiO_3$ thin films*, J. Appl. Phys. **87** (2000) p. 3965-3972.
7. M. Tsukada, H. Yamawaki, and M. Kondo, *Crystal structure and polarization phenomena of epitaxially grown $Pb(Zr,Ti)O_3$ thin-film capacitors*, Appl. Phys. Lett. **83** (2003) p. 4393-4395.
8. T. Kumazawa, Y. Kumagai, H. Miura, M. Kitano, and K. Kushida, *Effect of external stress on polarization in ferroelectric thin films*, Appl. Phys. Lett. **72** (19980 p. 608-610.
9. B. A. Tuttle, J. A. Voigt, T. J. Garino, D. C. Goodnow, R. W. Schwartz, D. L. Lamppa, T. J. Headley, and M. O. Eatough. *Chemically prepared $Pb(Zr,Ti)O_3$ thin films: The effects of orientation and stress*, in *Proceedings of the Eighth IEEE International Symposium on Applications of Ferroelectrics (ISAF'92)*, Greenville-USA (1992) p. 344-348.
10. J. F. Scott and C. A. Paz de Araujo, *Ferroelectric Memories*, Science **246** (1989) p. 1400-1405.
11. C. A. Paz de Araujo, J. D. Cuchiaro, L. D. McMillan, M. C. Scott, and J. F. Scott, *Fatigue-free ferroelectric capacitors with platinum electrodes*, Nature **374** (1995) p. 627-629.
12. P. C. Joshi and S. B. Desu, *Structural and electrical characteristics of rapid thermally processed ferroelectric $Bi_4Ti_3O_{12}$ thin films prepared by metalorganic solution deposition technique*, J. Appl. Phys. **80** (1996) p. 2349-2357.
13. L. M. Eng, *Nanoscale domain engineering and characterization of ferroelectric domains*, Nanotechnology **10** (1999) p. 405–411.
14. T. Mihara, H. Watanabe, and C. A. Paz de Araujo, *Polarization fatigue characteristics of sol-gel ferroelectric $Pb(Zr_{0.4}Ti_{0.6})O_3$ thin-film capacitors*, Jpn. J. Appl. Phys. **33** (1994) p. 3996-4002.

15. M. Dawber, K. M. Rabe, and J. F. Scott, *Physics of thin-film ferroelectric oxides*, Rev. Mod. Phys. **77** (2005) p. 1083-1130.
16. M. A. Rodriguez, G. Brennecka, B. Tuttle, and T. Tissot, *Diagnosis of Ln-doped PZT films via microdiffraction: correlation of properties to observed FWHM*, in *International Centre for Diffraction Data*, Newtown Square, Pennsylvania, USA (2003).
17. P. M. te Riele, *Direct patterning of oxides by pulsed laser stencil deposition*, PhD Thesis, University of Twente, The Netherlands (2008).
18. P. M. te Riele, G. Rijnders, and D. H. A. Blank, *Ferroelectric devices created by pressure modulated stencil deposition*, Appl. Phys. Lett. **93** (2008) p. 233109 (1-3).
19. W. L. Warren, D. Dimos, B. A. Tuttle, R. D. Nasby, and G. E. Pike, *Electronic domain pinning in* $Pb(Zr,Ti)O_3$ *thin films and its role in fatigue*, Appl. Phys. Lett. **65** (1994) p. 1018-1020.
20. A. Gruverman, B. J. Rodriguez, R. J. Nemanich, and A. I. Kingon, *Nanoscale observation of photoinduced domain pinning and investigation of imprint behavior in ferroelectric thin films*, J. Appl. Phys. **92** (2002) p. 2734-2739.
21. A. K. Tagantsev, Cz. Pawlaczyk, K. Brooks, and N. Setter, *Built-in electric field assisted nucleation and coercive fields in ferroelectric thin films*, Integr. Ferroelectr. **4** (1994) p. 1-12.
22. A. K. Tagantsev, I. Stolichnov, N. Setter, J. S. Cross, and M. Tsukada, *Non-Kolmogorov-Avrami switching kinetics in ferroelectric thin films*, Phys. Rev. B **66** (2002) p. 214109 (1-6).
23. D. Matthew and J. F. Scott, *A model for fatigue in ferroelectric perovskite thin films*, Appl. Phys. Lett. **76** (2000) p. 1060-1062.
24. J. F. Scott and D. Matthew, *Oxygen-vacancy ordering as a fatigue mechanism in perovskite ferroelectrics*, Appl. Phys. Lett. **76** (2000) p. 3801-3803.
25. P. K. Larsen, G. J. M. Dormans, D. J. Taylor, and P. J. van Veldhoven, *Ferroelectric properties and fatigue of* $PbZr_{0.51}Ti_{0.49}O_3$ *thin films of varying thickness: Blocking layer model*, J. Appl. Phys. **76** (1994) p. 2405-2413.
26. A. M. Bratkovsky and A. P. Levanyuk, *Abrupt Appearance of the Domain Pattern and Fatigue of Thin Ferroelectric Films*, Phys. Rev. Lett. **84** (2000) p. 3177-3180.
27. J. F. Scott, C. A. Araujo, B. M. Melnick, L. D. McMillan, and R. Zuleeg, *Quantitative measurement of space-charge effects in lead zirconate-titanate memories*, J. Appl. Phys. **70** (1991) p. 382-388.
28. W. L. Warren, B. A. Tuttle, and D. Dimos, *Ferroelectric fatigue in perovskite oxides*, Appl. Phys. Lett. **67** (1995) p. 1426-1428.
29. W. L. Warren, K. Vanheusden, D. Dimos, G. E. Pike, and B. A. Tuttle, *Oxygen Vacancy Motion in Perovskite Oxides*, J. Am. Ceram. Soc. **79** (1996) p. 536-538.
30. J. Chen, M. P. Harmer, and D. M. Smyth, *Compositional control of ferroelectric fatigue in perovskite ferroelectric ceramics and thin films,* J. Appl. Phys. **76** (1994) p. 5394-5398.
31. A. Q. Jiang, J. F. Scott, M. Dawber, and C. Wang, *Fatigue in artificially layered* $Pb(Zr,Ti)O_3$ *ferroelectric films*, J. Appl. Phys. **92** (2002) p. 6756-6761.

32. J. J. Lee, C. L. Thio, and S. B. Desu, *Electrode contacts on ferroelectric $Pb(Zr_xTi_{1-x})O_3$ and $SrBi_2Ta_2O_9$ thin films and their influence on fatigue properties*, J. Appl. Phys. **78** (1995) p. 5073-5078.
33. H. B. Sharma, H. N. K. Sarma, and A. Mansingh, *Fatigue in sol-gel derived barium titanate films*, J. Appl. Phys. **85** (1999) p. 341-346.
34. J. Ishida, T. Yamada, A. Sawabe, K. Okuwada, and Keisuke Saito, *Large remanent polarization and coercive force by 100% 180° domain switching in epitaxial $Pb(Zr_{0.5}Ti_{0.5})O_3$ capacitor*, Appl. Phys. Lett. **80** (2002) p. 467 - 469.
35. V. Nagarajan, I. G. Jenkins, S. P. Alpay, H. Li, S. Aggarwal, L. Salamanca-Riba, A. L. Roytburd, and R. Ramesh, *Thickness dependence of structural and electrical properties in epitaxial lead zirconate titanate films*, J. Appl. Phys. **86** (1999) p. 595-602.
36. G. S. Wang, D. Remiens, E. Dogheche, and X. L. Dong, *Effect of thermal strain on structure and polarization fatigue of CSD-derived $PbZr_{0.53}Ti_{0.47}O_3/LaNiO_3$ hetero-structures*, Appl. Phys. A: Mater. Sci. & Process. **88** (2007) p. 657-660.
37. D. Wu, A. Li, and N. Ming, *Structure and electrical properties of $Bi_{3.15}Nd_{0.85}Ti_3O_{12}$ ferroelectric thin films*, J. Appl. Phys. **95** (2004) p. 4275-4281.
38. J. -E. Lim, D. -Y. Park, J. K. Jeong, G. Darlinski, H. J. Kim, C. S. Hwang, S. -H. Kim, C. -Y. Koo, H. -J. Woo, D. -S Lee, and J. Ha, *Dependence of ferroelectric performance of sol-gel-derived $Pb(Zr,Ti)O_3$ thin films on bottom-Pt-electrode thickness*, Appl. Phys. Lett. **81** (2002) p. 3224-3226.
39. K. -W. Lee and W. -J. Lee, *Relaxation of remanent polarization in $Pb(Zr,Ti)O_3$ thin film capacitors*, Jpn. J. Appl. Phys. **41** (2002) p. 6718-6723.
40. S. -H. Kim, J. G. Hong, S. K. Streiffer, and A. I. Kingon *The effect of RuO_2/Pt hybrid bottom electrode structure on the leakage and fatigue properties of chemical solution derived $Pb(Zr_xTi_{1-x})O_3$ thin films*, J. Mater. Res. **14** (1999) p. 1018-1025.
41. Ch. Bahr, C. J. Booth, D. Fliegner, and J. W. Goodby, *Critical adsorption at the free surface of a smectic liquid crystal possessing a second-order phase transition*, Phys. Rev. Lett. **77** (1996) p. 1083-1086.
42. Q. M. Zhang, H. Wang, N. Kim, and L. E. Cross, *Direct evaluation of domain-wall and intrinsic contributions to the dielectric and piezoelectric response and their temperature dependence on lead zirconate-titanate ceramic*, J. Appl. Phys. **75** (1994) p. 454-459.
43. C. J. Brennan, R. D. Parrella, and D. E. Larsen, *Temperature dependent fatigue rates in thin-film ferroelectric capacitors*, Ferroelectrics **151** (1994) p. 33-38.
44. J. C. Shin, C. S. Hwang, H. J. Kim, and S. O. Park, *Leakage current of sol-gel derived $Pb(Zr, Ti)O_3$ thin films having Pt electrodes*, Appl. Phys. Lett. **75** (1999) p. 3411-3413.
45. B. Jaffe, W. R. Cook, and H. Jaffe, *Piezoelectric Ceramics*, Academic Press London, London (1971).

46. S. -H. Bae, K. -B. Jeon, and B. -M. Jin, *Dielectric properties of $PbZr_xTi_{1-x}O_3/PbZrO_3$ multilayer thin films*, Mater. Res. Bull. **36** (2001) p. 1931-1937
47. X. J. Meng, J. L. Sun, X. G. Wang, T. Lin, J. H. Ma, S. L. Guo, and J. H. Chu, *Temperature dependence of ferroelectric and dielectric properties of $PbZr_{0.5}Ti_{0.5}O_3$ thin film based capacitors*, Appl. Phys. Lett. **81** (2002) p. 4035-4037.
48. F. Xu, S. Trolier-McKinstry, W. Ren, B. Xu, Z. -L. Xie, and K. J. Hemker, *Domain wall motion and its contribution to the dielectric and piezoelectric properties of lead zirconate titanate films*, J. Appl. Phys. **89** (2001) p. 1336-1348.
49. F. Yang, M. H. Tang, Y. C. Zhou, F. Liu, Y. Ma, X. J. Zheng, J. X. Tang, H. Y. Xu, W. F. Zhao, Z. H. Sun, and J. He, *Fatigue mechanism of the ferroelectric perovskite thin films*, Appl. Phys. Lett. **92**, (2008) p. 022908 (1-3).
50. B. G. Chae, C. H. Park, Y. S. Yang, and M. S. Jang, *Asymmetry in fatigue and recovery in ferroelectric $Pb(Zr,Ti)O_3$ thin-film capacitors*, Appl. Phys. Lett. **75** (1999) p. 2135-2137.
51. P. J. Schorn, D. Brauhaus, U. Bottger, R. Waser, G. Beitel, N. Nagel, and R. Bruchhaus, *Fatigue effect in ferroelectric $PbZr_{1-x}Ti_xO_3$ thin films*, J. Appl. Phys. **99** (2006) p. 114104(1-5).
52. S. B. Majumder, Y.N. Mohapatra, and D.C. Agrawal, *Fatigue resistance in lead zirconate titanate thin ferroelectric films: Effect of cerium doping and frequency dependence*, Appl. Phys. Lett. **70** (1997) p. 138-140.
53. A. Jiang, M. Dawber, J. F. Scott, C. Wang, P. Migliorato, and M. Gregg, *Studies of switching kinetics in ferroelectric thin films*, Jpn. J. Appl. Phys. **42** (2003) p. 6973-6982.
54. J. -Y. Hwang, S. -A. Lee, S. -Y. Jeong, and C. -R. Cho, *Temperature-dependent fatigue rate in ferroelectric $Bi_{3.25}La_{0.75}Ti_3O_{12}$ thin films*, Europhys. Lett. **76** (2006) p. 88-94.
55. M. Grossmann, D. Bolten, O. Lohse, U. Boettger, R. Waser, and S. Tiedke, *Correlation between switching and fatigue in $PbZr_{0.3}Ti_{0.7}O_3$ thin films*, Appl. Phys. Lett. **77** (2000) p. 1894-1896.
56. H. M. Duiker, P. D. Beale, J. F. Scott, C. A. Paz de Araujo, B. M. Melnick, J. D. Cuchiaro, and L. D. McMillan, *Fatigue and switching in ferroelectric memories: Theory and experiment*, J. Appl. Phys. **68** (1990) p. 5783-5791.

5.

Dependence of film thickness and composition on ferroelectric properties

Abstract. Highly (110)-oriented epitaxial PZT(52/48) film with SRO electrodes have been fabricated on (001) YSZ/Si and (110) $SrTiO_3$ (STO) substrates by pulsed laser deposition (PLD). The film thickness effect on the structure and electrical properties of PZT films were investigated. An increase in remnant polarization and dielectric constant values were observed with increasing film thickness. It is believed that the interfacial layers and residual stress between PZT films and substrates play the most important factors in the change of electrical properties with film thickness.

Furthermore, the ferroelectric and dielectric properties of epitaxial PZT thin films as a function of the Zr/Ti ratio have also been investigated. It was found that the maximum dielectric constant is achieved from the film near the morphotropic phase boundary (MPB) composition (Zr/Ti=52/48) and showed the same trend as PZT bulk ceramics. Moreover, the ferroelectric phase is transferred from rhombohedral- to tetragonal-phase when the Zr/Ti ratio is varied ranging from 60/40 to 20/80, which results in an increase in remnant polarization and squareness of *P-E* hysteresis loop.

5.1 Introduction

The interfaces between the ferroelectric film and electrode in the ferroelectric capacitors are of crucial importance. The influence of interfaces has been found to be essential to the fatigue endurance of ferroelectric thin film capacitors as a function of switching cycles. As mentioned previously, the polarization fatigue characteristics are observed in the PZT film deposited on metal-electrode (like Pt) [1, 2]. Whereas, a PZT film grown on an oxide-electrode (such as $SrRuO_3$) results in fatigue-free performance [3]. More discussions on the fatigue characteristics in the PZT thin film capacitors have been presented in chapter 4.

On the other hand, the influence of an interfacial layer has been proposed as the explanation for the change in polarization with film thickness. It is speculated that this polarization behavior is from reduced interfacial effect with increasing film thickness. The existing interfacial layer is responsible for a shearing the polarization hysteresis loop [4]. It is proposed to explain the increase of remnant polarization as well as the decrease of coercive field with an increase in film thickness [5]. A better understanding of the PZT film properties evolution with the film thickness necessitates studying the dynamic behavior of the domains. In section 5.4, we report the fabrication of (110)-oriented epitaxial PZT films up to 2000 nm on both Si(001) and STO(110) substrates. The dependence of ferroelectric and dielectric properties on the film thickness has also been investigated.

In the ferroelectric PZT system, the phase diagram consists mainly of two different regions: The Ti-rich tetragonal region with a space group of *P*4*mm*, and the Zr-rich rhombohedral region with a space group of *R*3*m* [6]. In the case of PZT bulk materials, maximum values of polarization, dielectric constant and piezoelectric coefficient have been observed at the morphotropic phase boundary (MPB) composition [7]. The MPB of PZT is located at a PZO:PTO of 52:48 and separates the Ti-rich tetragonal phase from the Zr-rich rhombohedral phase [6]. The large number of possible polarization directions and the consequent extrinsic contribution at this boundary are thought to give rise to their superior properties [6, 8]. However, due to the influence of substrate clamping, the polarization showed a different trend than bulk PZT ceramics [9].

To investigate the evidence for composition-dependent ferroelectric properties, we have performed a study based on the experimental results of the ferroelectric and dielectric properties of PZT thin films with various Zr/Ti molar ratios (60/40, 52/48, 40/60 and 20/80), as presented in section 5.5.

5.2 Experimental procedure

In the present study, to investigate the effect of film thickness on the ferroelectric properties, the (110)-oriented PZT (Zr/Ti : 52/48) films ranging from thickness of 75 to 2000 nm were growth on SRO buffered YSZ/Si(001) and STO(110) substrates using pulsed laser deposition (PLD). Moreover, in order to investigate the effect of Zr/Ti molar ratios on the

properties of PZT films, 250-nm-thick PZT thin films with Zr/Ti ratios of 60/40, 52/48,40/60 and 20/80 were used.

The surface morphology and film thickness of the PZT films were observed using an atomic force microscopy (AFM) and determined by scanning electron microscopy (SEM) on cross-section specimens, respectively. The crystal structure was examined by high-resolution x-ray diffraction (XRD, Bruker D8 Discover).

The polarization hysteresis (*P-E*) loop and the polarization switching (fatigue) characteristics were done using a ferroelectric film test system (TF 2000 Analyzer). *P-E* hysteresis loops were measured at ±200 kV/cm amplitude and 1 kHz frequency. Polarization switching tests were performed using bipolar electric-field pulses with amplitude of 200 kV/cm (pulse height) at a frequency of 1.5 kHz (pulse width: 0.33 milliseconds). The capacitance (*C-E*, *C-f*) and the leakage current density-electric field (*J-E*) were measured a Süss MicroTech PM300 manual probe-station equipped with Keithley 4200 Semiconductor characterization system. The capacitance-electric field (*C-E*) curves were recorded using an *ac* signal at 10 kHz frequency and 100 mV amplitude with the *dc* bias sweeping from -200 to +200 kV/cm and then back to -200 kV/cm while the capacitance-frequency (*C-f*) measurements were swept in the range of 10kHz - 1MHz. The corresponding dielectric responses were calculated from these *C-E* and *C-f* measurements.

5.3 Interfaces between ferroelectric films and electrodes

5.3.1 Principle of the electrical contact at the interface

In the ferroelectric samples, the PZT layers are usually slightly *p*-type doped (or *p*-type semiconductor) due to the lead (Pb) vacancies, although the bulk PZT ceramics are *n*-type semiconductors. The reported value for the PZT electron affinity (χ) is 3.5 eV [10]. The accumulation of oxygen vacancies near the electrodes can result in the formation of a very thin *n*-type oxygen deficient region, which are created during fatigue cycles.

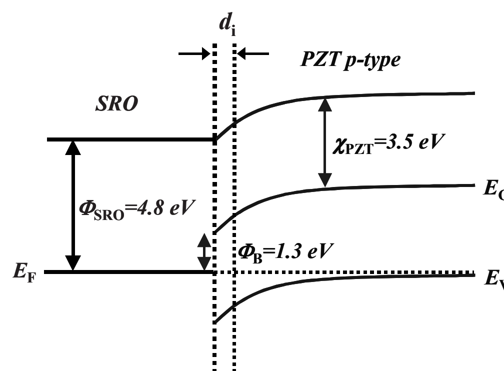

Figure 5.1: Schottky contact of conductive-oxide SRO electrode and *p*-type PZT film.

In Fig. 5.1 the energy band structure of an electrode/film interface in contact is sketched. E_F, E_C and E_V denote the Fermi level, valence band and conduction band, respectively. Because of the different Fermi level in the semiconductor, the band bending is also different. The Schottky barrier height (Φ_B) is redefined as the difference between the electron affinity (χ) of the semiconductor and the work function of the electrode (Φ_E) and is given by [11-13]:

$$\Phi_B = \Phi_E - \chi \tag{5.1}$$

Moreover, another important factor of Schottky contact is the interfacial layer (or depletion layer). The width of interfacial layer (d_i) at the interface supports a potential drop (called as the built-in voltage, V_{bi}):

$$V_{bi} = \Phi_E - \Phi_S \tag{5.2}$$

where, Φ_S is the work function of the semiconductor (or ferroelectrics) . The interfacial layer in the ferroelectric film is discussed in detail below.

5.3.2 "Intrinsic" interfacial layer fabrication

The formation of an intrinsic interfacial layer (or dead-layer) occurs most commonly in the fabrication of multilayers or ferroelectric film capacitors in particularly. It is natural to assume that this dead layer occurs because of defects and/or reaction between ferroelectric film and electrode in fabricating thin-film capacitors [14, 15] or the formation of Pb-deficient layer on the Pt/Ti/SiO_2/Si substrate [16, 17] as well as the film/electrode interface roughness.

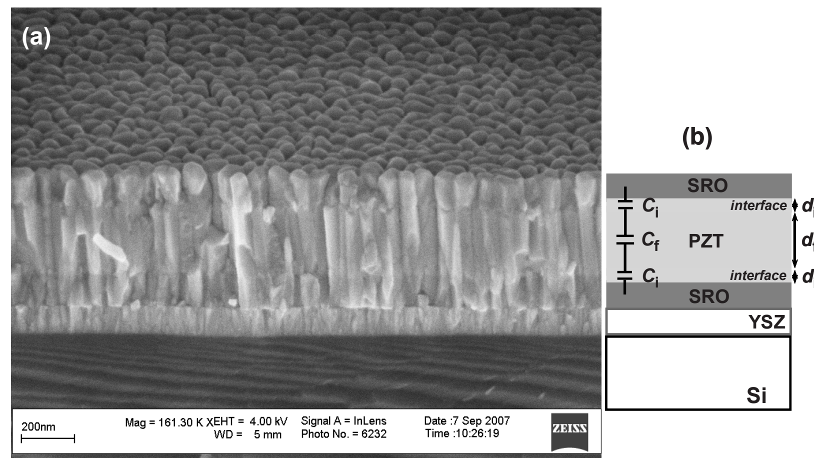

Figure 5.2: (a) The cross-sectional SEM of homogeneous structure of PZT thin film capacitors, and (b) Schematic of series capacitor structure formed from bulk ferroelectric layer and two interfacial-layers.

It can be seen that densely columnar-like structures grew in the region of the bottom electrode and penetrated through the PZT film, as shown in Fig. 5.2(a). On the other aspect, growth of columnar structure causes larger interface roughness between the PZT film and electrodes.

In Fig. 5.3, the composition variation through the depth profile of the SRO/PZT/SRO structure was characterized using x-ray photoelectron spectroscopy (XPS). The horizontal axis is the depth into the sample down to the PZT/SRO interface. Each layer can be clearly distinguished and there is no interfacial reaction between the SRO and the PZT film. The overall composition of the film is uniform along with depth. Chemical composition of the film (atomic concentration Pb:Zr:Ti = 48:28:24 or molar ratio Pb:Zr:Ti = 0.96:0.54:0.48 ≈1:0.52:0.48) was determined by Electron spectroscopy for chemical analysis (ESCA).

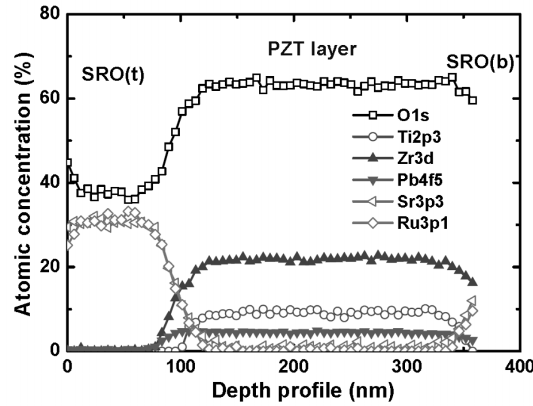

Figure 5.3: XPS depth profile of the SRO/PZT/SRO films deposited on YSZ/Si substrate.

According to the widely accepted model for metal-ferroelectric-metal (MFM) structure as shown in Fig. 5.1(b), where whole structure is treated as a ferroelectric bulk capacitor with the capacitance C_f in series with the interfacial capacitance C_i (between the electrode and ferroelectric bulk), the measured capacitance C_m of the MFM structure can be expressed as follows [18-20]:

$$\frac{1}{C_m} = \frac{1}{C_i} + \frac{1}{C_f} + \frac{1}{C_i} = \frac{1}{\varepsilon_0 \varepsilon_f A} d_f + \frac{2}{C_i} \tag{5.1}$$

where ε_0 and ε_f are the vacuum permittivity (ε_0=8.854×10^{-12} F/m) and dielectric constant of the ferroelectric bulk, while d_f and A are the thickness of the ferroelectric bulk and the area of the capacitor, respectively.

Assuming that the thickness of the interfacial layer (d_i) is very thin with regard to the whole thickness of the ferroelectric film (d), so that:

$$(5.1) \Leftrightarrow \frac{1}{C_m} = \frac{2}{C_i} + \frac{1}{\varepsilon_0 \varepsilon_f A}(d - d_i) \approx \frac{2}{C_i} + \frac{1}{\varepsilon_0 \varepsilon_f A} d \tag{5.2}$$

According to the Eq. (5.2), the plot of $1/C_m$ as a function of film thickness should be a straight line. The intercept will give the C_i value. The calculation of C_i value is described in section 5.4.

5.3.3 "Extrinsic" interfacial layer formation

According to the discussion in chapter 4, the electric fatigue behavior in $PZT/Pt/Ti/SiO_2/Si$ capacitors is a result of the electromigration of oxygen vacancies after repeated switching cycles to form extended defects capable of pinning domains which would lead to the formation of interfacial layers between the metal electrode and the ferroelectric film. The higher concentration of oxygen vacancy in the fatigue PZT/Pt capacitor tends to increase the thickness of interfacial layer [18, 21].

Figure 5.4 illustrates the change in the ratio of C_i and C_m of PZT/Pt capacitors with the number of switching cycles. Assuming the dielectric constant of interfacial layer is constant, therefore, a decrease in C_i value leads to an increase in the thickness of the interfacial layer (d_i) and also results in a decrease of the measured (effective) capacitance C_m.

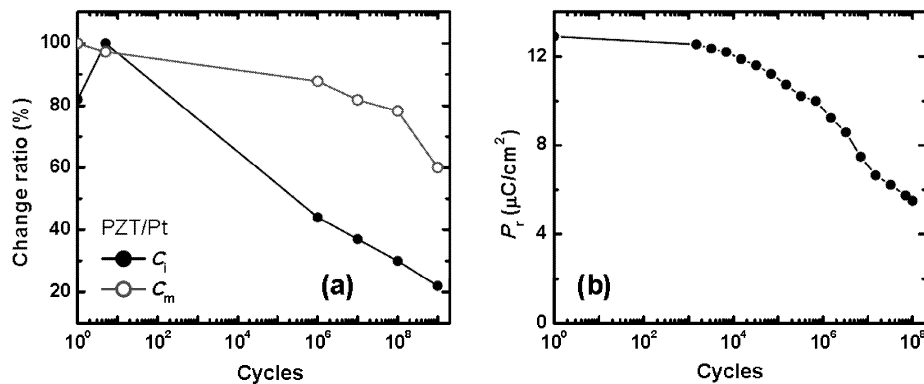

Figure 5.4: (a) The change ratio of the capacitance of interfacial layer (C_i) and of the measured capacitance (C_m) after various fatigue switching cycles, and (b) Remnant polarization vs. switching cycles for PZT/Pt capacitors.

As discussed in section 4.4, the C_i value was almost independence of the switching cycles. It confirms that the accumulation of oxygen vacancies at the PZT/SRO interfaces is prevented during polarization switching. As a result, the fatigue-free behavior is also observed in the PZT/SRO thin films (Fig. 5.5).

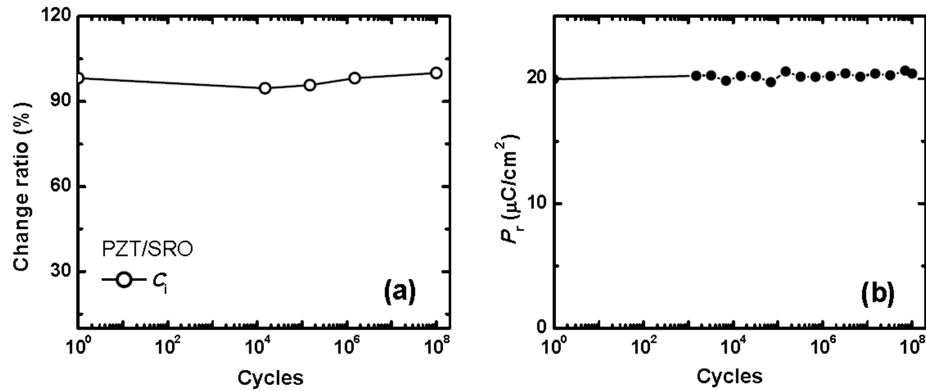

Figure 5.5: (a) The change ratio of the interfacial capacitance (C_i) after various switching cycles, and (b) Remnant polarization vs. switching cycles for the (001)-oriented PZT/SRO/CeO_2/YSZ/Si capacitors.

5.3.4 Leakage current mechanisms in ferroelectric film capacitors

The leakage current is an important characteristic of ferroelectric film capacitors. The leakage current is a sensitive electrical probe of the electrode materials of the electrode-ferroelectric film-electrode structure [22, 23]. It can be attributed to the differences in the work functions of the electrode materials, which in turn result in differences in the ferroelectric film/electrode contacts, including either the holes (carrier mobility and/or carrier concentration) distribution in the case of Ohmic contact or the barrier height in the case of the Schottky emission [22, 24, 25]. On the other hand, the leakage current density (*J*) is also affected by the ferroelectric film thickness, in which the *J* value decreases with increasing film thickness [26]. The leakage current density in the ferroelectric capacitors can be divided into two regions: the linear *J-E* curve in the low electric-field region and non-linear *J-E* curve in the high electric-field region, respectively.

- ***Low applied electric-field region***

The structure of PZT films can be considered as a series array of grains, grain boundaries, and film-electrode interfaces. The field dependence of the *J-E* characteristics of the films is a combined response of these three parts. Variations in the influence of each part would give rise to variations in *J-E* characteristics.

At low electric field, the current is determined by the contact properties at the film-electrode interface. Previous studies assume that an Ohmic contact exists between the electrode and the PZT film [24, 27, 28]. Since the work function of PZT (about 3.5 eV) [29] is much smaller than that of either electrode material such as 5.3 eV for Pt or 4.8 eV for

$SrRuO_3$ [10], the contact must be hole-injecting to the film in nature, i.e., Ohmic contact with respect to holes [24, 30]. Its current dominated by Ohmic current (J_{Oh}) is express as:

$$J_{Oh} = E \exp\left(-\Delta E_{ac} / k_B T\right) \quad (5.3)$$

where E is the external electric field, ΔE_{ac} is the activation energy of electron, k_B is the Boltzmann's constant and T is the measuring temperature.

Figure 5.6(a) shows the leakage current density as a function of the electric field for the 250-nm-thick (110)-oriented PZT films grown on SRO buffered YSZ/Si substrates with a *dc*-bias field ranging from 0 to -200 kV/cm and from 0 to +200 kV/cm, respectively. The leakage current density with the top SRO electrode under a negative bias field was slightly higher than that under a positive bias field. In fact, the leakage current density in the two opposite directions was limited by the two interfaces between the SRO-electrodes and PZT film. The positive leakage current density was limited by the interface between the bottom electrode and the film (bottom-interface), while the negative leakage current density was limited by the interface between the top electrode and the film (top-interface). Therefore, the electrical quality is slightly better at the bottom-interface than that at the top-interface. The asymmetric *J-E* curves may be associated with the different interfacial roughness between bottom electrode-film (roughness: 1.2 nm for SRO/YSZ/Si) and film-top electrode interfaces (roughness: 2.4 nm for PZT/SRO/YSZ/Si).

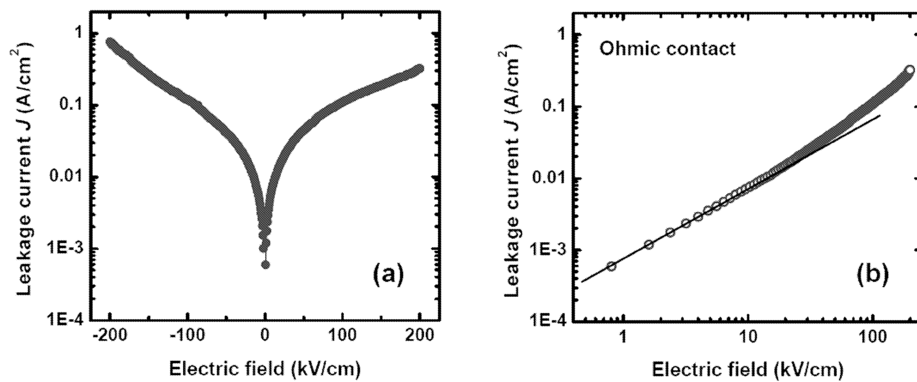

Figure 5.6: (a) Leakage current density (J) versus electric field (E) characteristics for the SRO/PZT/SRO/YSZ/Si capacitor; (b) The *J-E* characteristics in terms of log(J) vs log(E) (Ohmic contact). The (110)-oriented PZT thin films with a thickness of 250 nm were used.

In the log(J) versus log(E) plot (Fig. 5.6(b)), the current increases linearly with external electric field in the low electric field (<30 kV/cm) region, indicating that Ohm's law dominates conduction in the low field because the density of thermally generated carriers in films is predominant over the injected charge carriers.

- ***High applied electric-field region***

With increasing the external electric field above 30 kV/cm, the current increases non-linearly which implies that current conduction is governed by other mechanisms, such as Schottky emission, Poole-Frenkel (PF) emission, Fowler-Nordheim (FN) current as well as space-charge-limited current (SCLC). It is generally accepted that leakage current of ferroelectric films can be controlled by various mechanisms, as shown in Tab. 5.1.

Table 5.1: Basic conduction processes in insulators [31].

Process	Expression	Voltage and temperature dependence
Schottky emission	$J_{Sch} = A^*T^2 \exp\left(-\frac{q\phi_B}{k_BT}\right)\exp\left[\left(\frac{q^3}{4\pi\varepsilon_0\varepsilon_r}\right)^{1/2}\frac{\sqrt{E}}{k_BT}\right]$	$\ln J \sim \sqrt{E}$ $\ln J/T^2 \sim 1/T$
Poole-Frenkel (PE) emission	$J_{PE} = BE\exp\left(-\frac{q\phi_t}{k_BT}\right)\exp\left[\left(\frac{q^3}{4\pi\varepsilon_0\varepsilon_r}\right)^{1/2}\frac{\sqrt{E}}{k_BT}\right]$	$\ln J/E \sim \sqrt{E}$ $\ln J \sim 1/T$
SCLC	$J_{SCLC} = \frac{9}{8}\mu\varepsilon_0\varepsilon_r\frac{E^2}{d^3}$	$J \sim E^2$
Fowler-Nordheim (FN)	$J_{FN} = AE^2\exp\left(-\frac{B}{E}\right)$	$\ln J/E^2 \sim 1/E$

The Schottky emission generated by the thermionic effect is caused by the electron transport across the potential energy barrier given by the band arrangement at the electrode-ferroelectric interface. The leakage current density in the Schottky emission is quantified by the following equation [24, 31]:

$$J_{Sch} = A^*T^2 \exp\left(-\frac{q\phi_B}{k_BT}\right)\exp\left[\left(\frac{q^3}{4\pi\varepsilon_0\varepsilon_r}\right)^{1/2}\frac{\sqrt{E}}{k_BT}\right] \tag{5.4}$$

where A^* is the effective Richardson constant, T is the measuring temperature, k_B is the Boltzmann's constant, q and ϕ_B are the electronic charge and the Schottky barrier height, E is the external electric field, ε_0 and ε_r are the vacuum permittivity and the dielectric constant of the ferroelectric layer, respectively.

In the case of the Poole-Frenkel (PE) emission, the electronic conduction as a bulk-controlled conduction mechanism through an insulator can occur due to the hopping of the charge carriers from one trap to another under a bias field. The PE current is given by the equation [31]:

$$J_{PE} = BE\exp\left(-\frac{q\phi_t}{k_BT}\right)\exp\left[\left(\frac{q^3}{4\pi\varepsilon_0\varepsilon_r}\right)^{1/2}\frac{\sqrt{E}}{k_BT}\right] \tag{5.5}$$

where B is a constant and ϕ_t is the trap level.

Under space-charge-limited current (SCLC), the carriers form a freely moving space charge due to the reduced conductivity of the insulator, and the number density of the free carriers causes an electric field gradient, which limits the current density. The SCLC current is related to *E* by the following relation [32]:

$$J_{SCLC} = \frac{9}{8}\mu\varepsilon_0\varepsilon_r\frac{E^2}{d^3} \tag{5.6}$$

where μ is the mobility of the charge carriers and *d* is the film thickness.

Another mechanism of conduction in ferroelectric capacitor can be considered as a tunneling current from the electrode adjacent to the ferroelectric layer follows the Fowler-Nordheim (FN) relation [33, 34]:

$$J_{FN} = AE^2\exp\left(-\frac{B}{E}\right) \tag{5.7}$$

where both *A* and *B* are constants that depend on the work function of the electrodes.

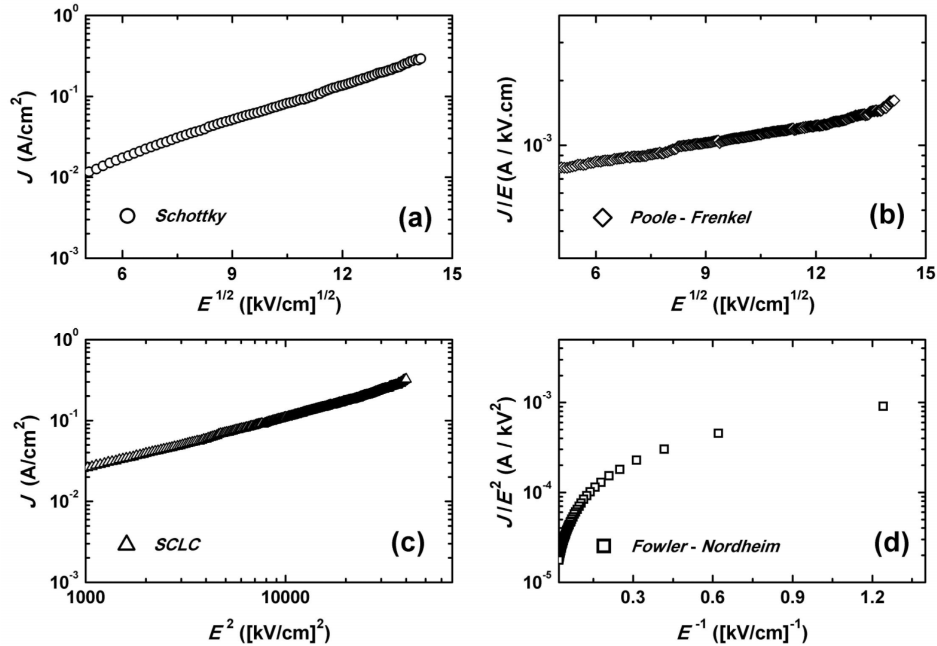

Figure 5.7: *J-E* characteristics in the form of the (a) Schottky emission, (b) Poole-Frenkel (PF) emission, (c) space-charge-limited current (SCLC), and (d) Fowler-Nordheim (FN) plots for SRO/PZT/SRO/YSZ/Si capacitors.

Figure 5.7 shows the leakage current density of the PZT film capacitors in the high field region (of more than 30 kV/cm), where the *J-E* curves are plotted with the relationship

between log(J) vs. $E^{1/2}$ (a), log(J/E) vs. $E^{1/2}$ (b), log(J) vs. log(E^2) and log(J/E^2) vs. E^{-1}, respectively. It is indicated that a linear relationship between log(J) and $E^{1/2}$, log(J) and log(E^2), implying the Schottky emission and/or SCLC are the dominant conduction mechanism of these capacitors in a high electric field region. On the other hand, the bulk-controlled (SCLC) and interface-controlled (Schottky) can be used to demonstrate the current in these films.

Because the function of SCLC conduction does not show a dependence of the leakage current on with temperature; therefore, the Schottky thermionic emission is used to investigate the effect of temperature on the leakage current mechanism of PZT thin films. Figure 5.8 shows a linear dependence of leakage current on the square root of electric field, and the J value increases with increasing measured temperature.

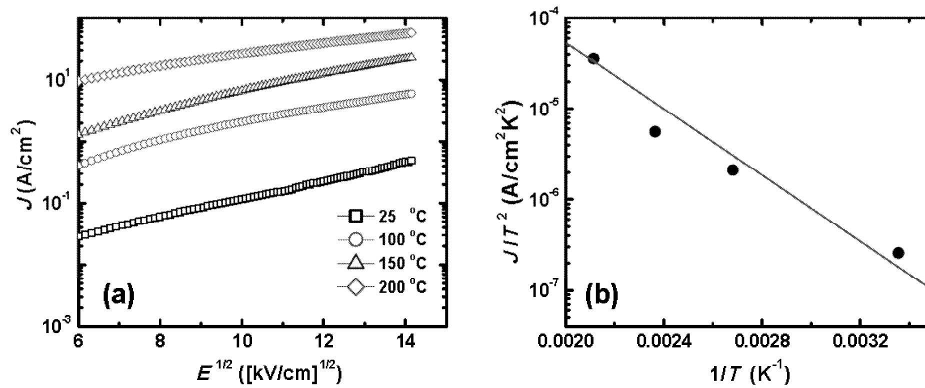

Figure 5.8: Leakage current density of PZT thin film as a function of measured temperature: (a) J vs. $E^{1/2}$, and (b) J/T^2 vs $1/T$, generated by the following Schottky emission.

5.4 Effect of film thickness on the properties of PZT film capacitors

In this study, the ferroelectric and dielectric properties of PZT films with thickness ranging from 75 nm to 2000 nm are investigated along with the effect of the electrode/film interfaces on the thickness dependence of these properties.

5.4.1 PZT films on silicon substrates

A. Film structure and Morphology

Figure 5.9 shows the XRD spectra of the PZT films with SRO buffered YSZ/Si substrates. The corresponding thicknesses of these PZT films are 250, 500 and 1000 nm, respectively. It is evident that the PZT and SRO films are highly (110)-oriented, indicating that SRO films are suitable electrodes for the oriented and/or epitaxial growth of PZT films, because of structural and chemical similarity between them. A detailed discussion on the growth mechanism of PZT films was presented in chapter 3.

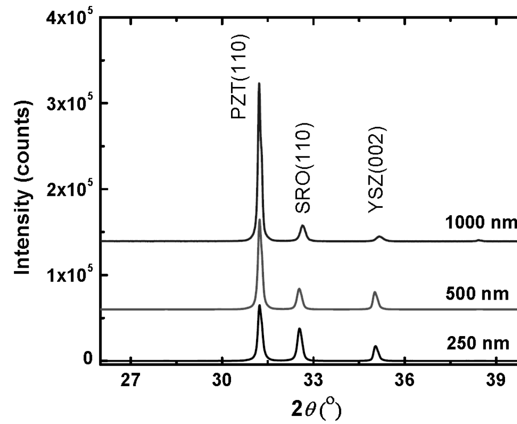

Figure 5.9: XRD spectra of PZT films grown on SRO buffered YSZ/Si substrates with different thicknesses: 250, 500 and 1000 nm.

Figures 5.10(a)-5.10(b) show the SEM cross sectional images of the PZT films deposited on SRO buffered YSZ/Si substrates. It can be seen that densely packed columnar structures grew in the region of the bottom electrode and penetrated through the film. The widths of the columnar structures are about 55-65 nm and they are almost independent of the film thickness. The film surface microstructure was investigated using AFM images as shown in Figs. 5.10(c)-5.10(d). The images reveal that the surfaces appear to be dense, smooth and crack-free. The rms surface roughness tended to increase with film thickness; for instance, the rms value increases from 6.1 to 7.2 nm when the film thickness increases from 250 to 500 nm.

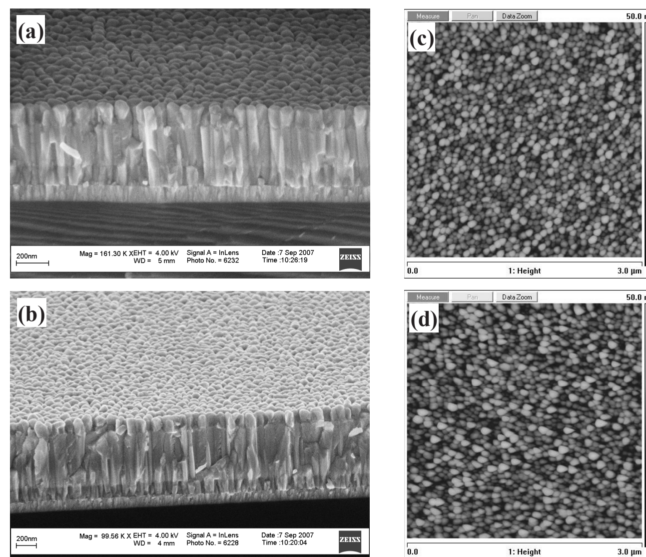

Figure 5.10: (a,b) SEM images of cross-sectional morphology, and (c,d) AFM images of PZT films with film thickness of 250 and 500 nm, respectively.

B. Polarization properties

Show in Figs. 5.11(a)-5.11(b) are a series polarization hysteresis (*P*-*E*) loops for PZT films between 75 and 1000 nm in thickness, measured at a frequency of 1 kHz and a maximum electric field of ±200 kV/cm. When the thickness reaches 500-1000 nm, the *P*-*E* loops became squarer. Above thickness of 1000 nm, there was little further change in switching behavior and polarization hysteresis loop lied down. Values of the remnant polarization (P_r) and coercive field (E_c) were plotted against film thickness in Figs. 5.11(c)-5.11(d). With increasing the film thickness, both P_r and E_c were considerably changed. Until 750 nm-thick, the values of P_r increased and E_c decreased sharply. The values of P_r and E_c at initial stage were 8.4 μC/cm^2 and 29.4 kV/cm at 75 nm-thick, and they were reasonably saturated to 20.4 μC/cm^2 and 25.7 kV/cm at 750 nm-thick, respectively.

It is speculated that this polarization behavior is from reduced interfacial effect with increasing film thickness. It has been suggested that the effect of dielectric dead-layer which is an insulating and non-ferroelectric layer formed at the ferroelectric/electrode interface has an effect on the polarization behavior. Tagantsev *et al.* [35] suggested that the dielectric dead-layer is responsible for a shearing of the hysteresis loop. The existing interfacial layer (dead-layer) is proposed to explain the increase of E_c with decreasing film thickness [4].

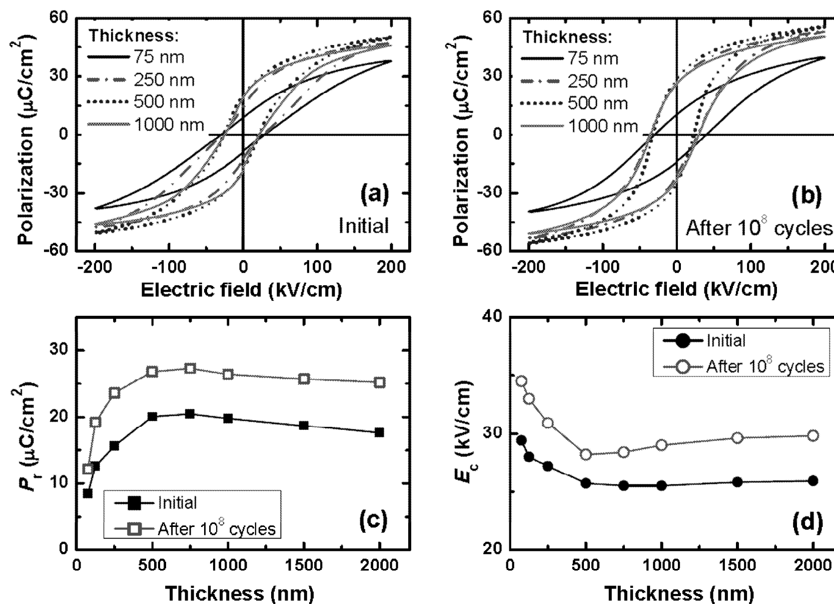

Figure 5.11: Polarization hysteresis loops, of the (110)-oriented PZT films grown on SRO buffered YSZ/Si, measured at maximum driving field of ±200 kV/cm and frequency of 1 kHz for each thickness at (a) initial stage and (b) after 10^8 cycles; (c) Remnant polarization (P_r) and (d) coercive field (E_c) as a function of film thickness.

The effect of interfacial layer on the polarization properties of PZT films can be described by the formation of the depolarizing field (E_i) which is given as [35]:

$$E_i = -\frac{Pd_i}{\varepsilon_i t_f} \tag{5.8}$$

where P and t_f are the polarization and thickness of the PZT film, d_i and ε_i are the thickness and dielectric constant of the interfacial layer, respectively.

Because the thickness of the interfacial layer is an order-of-magnitude thinner than that of the PZT films, the "effective" electric field (E_f) across the PZT film is given by Eq. (5.9):

$$E_f = E - \frac{Pd_i}{\varepsilon_i t_f} \tag{5.9}$$

where E is the "external" applied electric field. As seen in Tab. 5.2, the E_f value increases with an increase of film thickness and leads to the increase in the remnant polarization.

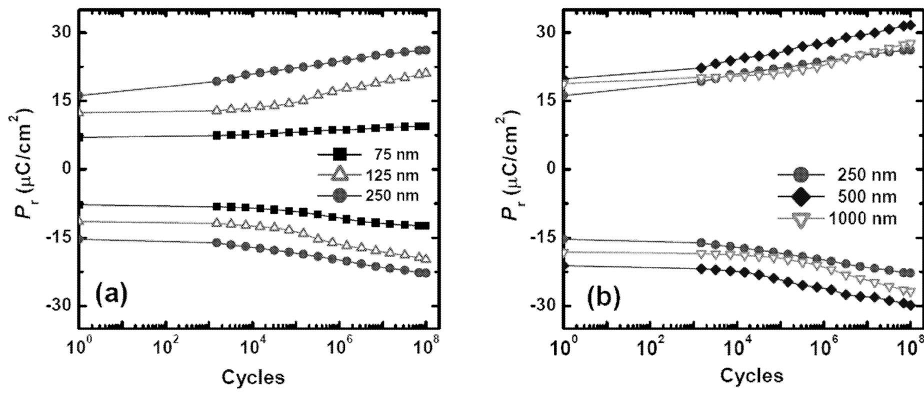

Figure 5.12: Polarization switching of the (110)-oriented PZT films grown on SRO buffered YSZ/Si as a function of film thickness from 75 to 1000 nm. The measurements were carried out by applied a bipolar rectangular pulse with pulse width of 0.5 ms (1 kHz) and at pulse height of 200 kV/cm. The remnant polarizations were evaluated from the polarization loops which measured with an amplitude of ±200 kV/cm at a frequency of 1 kHz.

On the other hand, as the film thickness increases, the switching of domains (both 180° and non-180°) might be increased with the reduction of substrate constraints, which leads to increase P_r. At higher thicknesses (e.g., 1000 nm-thick), the PZT films get softened, which reduces the P_r value irrespective of the substrate [5]. The decrease of E_c values with increasing film thickness is attributed to the constant thickness of the surface and dielectric dead-layer while the ferroelectric 'bulk' layer region increases with increasing film thickness.

Figure 5.12 shows the polarization of a series of PZT films with different film thickness as a function of polarization switching cycles. All of the samples exhibited fatigue-free behavior up to 10^8 switching cycles. The fatigue-free behavior in the PZT/SRO capacitors was discussed in chapter 4.

C. Capacitance and dielectric responses

The capacitance-electric field (*C-E*) characteristics of PZT thin films have been studied by Chai *et al*. [36] and Lin *et al*. [37], in which they showed that two factors control the *C-E* characteristics: (i) domain switching, and (ii) distribution of space-charge in the film. The research shows that the capacitance varies non-linearly with the applied voltage (or electric field), due to the domains switching from one orientation to another when the *dc* voltage is swept from negative-bias to positive-bias, for instance.

The voltage dependence of capacitance of PZT film capacitors is shown in Fig. 5.13(a). These capacitance-electric field (*C-E*) curves of 250-1000 nm-thick PZT films were recorded using an *ac* signal at 10 kHz frequency and 100 mV amplitude with the *dc* bias sweeping from -200 to +200 kV/cm and then back to -200 kV/cm. The dielectric constant-electric field (ε-*E*) curves were estimated from capacitance measurements, as shown in Fig. 5.13(b). As expected for ferroelectric behavior, the butterfly-shaped peaks behavior appear. The variation of the dielectric response with the *dc*-bias is associated with the domain reorientation process. At low fields, the main contribution to the dielectric constant is the increase in the polarization due to 180°-domain reversal (hereafter known as the extrinsic property) [38]. For high fields, most switchable domains have already been aligned along the direction of the *dc*-field; the dielectric constant is small since it is determined mainly by variations of the dipoles (hereafter known as the intrinsic property).

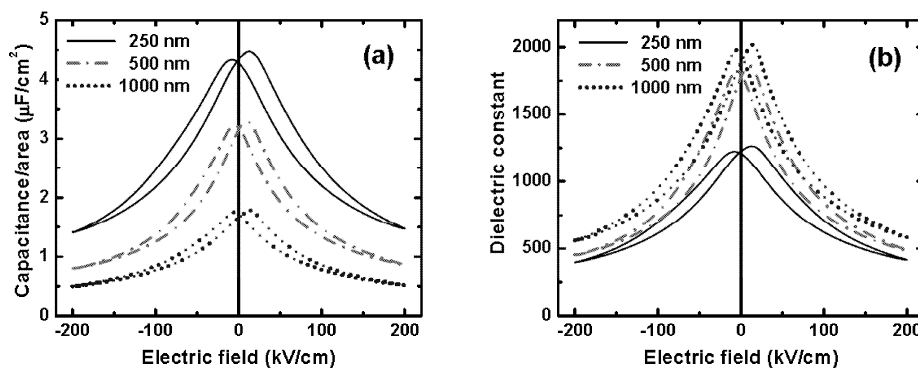

Figure 5.13: Thickness dependence of (a) capacitance-electric field (*C-E*) and (b) Dielectric constant-electric field (ε-*E*) curves. In this study, the (110)-oriented PZT films with different thickness were used.

The position-shift of the peaks in the ε-E curves representing the coercive field is distinctly asymmetric during the sweep-up and sweep-down of the applied electric field, which means that an internal-bias field has built up in the PZT capacitors due to the asymmetric space-charge distribution between top and bottom interfaces.

Figure 5.14(a) shows a frequency sweep from 10 kHz to 1 MHz of the dielectric constant (ε) and dielectric loss ($\tan\delta$) of the PZT film capacitors with different thickness. The dielectric constant is higher at lower frequency due to the contribution from space-charge polarization and reduced slowly with an increase of frequency. In the low frequency range, the dielectric relaxation can be due to the ionic space charges, such as the oxygen vacancies, defects, and interfacial polarization. Waser *et al.* [39] suggested that the oxygen vacancy plays an important role in the resistance degradation and the dielectric degradation in PZT films. A sharp increase in $\tan\delta$ values was observed in a high frequency region (above 100 kHz), due to the finite resistance of the film-electrode interface and the coupling of the capacitive element of grain boundaries with the dipoles [40, 41].

The dielectric constant of PZT films at an *ac* amplitude of 4 kV/cm and 10 kHz frequency is shown in Fig. 5.14(b). It is shown that the dielectric constant is increased drastically in the range of 75 and 1000 nm film thicknesses and increased gradually in thicker films up to 2000 nm. At 2000 nm-thick, it saturated at 2010. The improvement of the dielectric constant with increasing PZT film thickness may be explained by the contribution of the interfacial layer being more and more attenuated with increasing thickness. On the contrary, dielectric loss decreases slightly as the PZT thickness increases (Tab. 5.2).

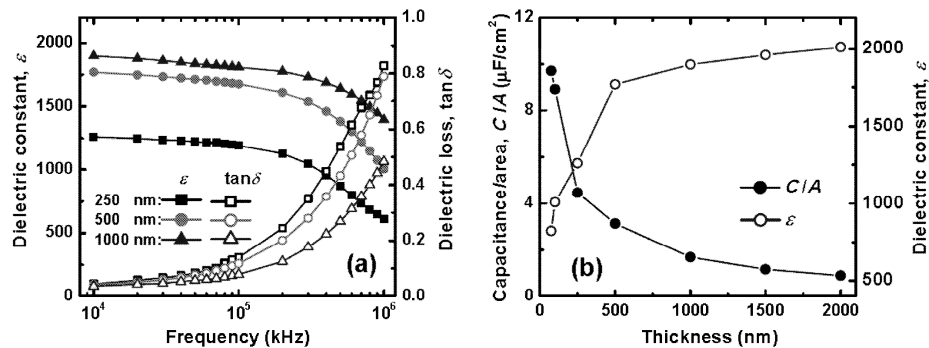

Figure 5.14: (a) Frequency dependence of the dielectric constant (ε) and dielectric loss ($\tan\delta$) for different thickness, and (b) Thickness dependence of the capacitance and dielectric constant of PZT film capacitors.

In order to rule out the applicability of the interfacial layer in PZT capacitors, we performed C-E measurements on films with different thicknesses. The plot of the reciprocal

of measured capacitance (C_m) versus film thickness (d), Fig. 5.15(a), can be well fitted to a straight line in agreement with Eq. (5.2). The intercept with the ordinate axis-yields an interfacial capacitance (C_i), which is induced by electric field penetration into the electrode, of 16.5 nF. The relationship between interfacial permittivity (ε_i) and interfacial layer thickness (d_i) can be expressed by:

$$\frac{d_i}{\varepsilon_i} = \frac{\varepsilon_0 A}{C_i} \tag{5.10}$$

where ε_0 (= 8.854×10^{-12} F/m) is the vacuum permittivity and A is the plate area of the capacitor.

From Eq. (5.10) and C_i=16.5 nF, we obtained:

$$\frac{d_i}{\varepsilon_i} = 0.215[nm] \tag{5.11}$$

On the other hand, the presence of the interfacial layer in PZT film capacitors can be investigated by the voltage drop due to the interfacial layer. It is believed that there exists a coercive field, which is thickness independent in MFM structures, and can be express by [42]:

$$V_c = V_i + E_c d \tag{5.12}$$

where V_c and E_c are coercive voltage and coercive field, d is the film thickness, and V_i is the voltage drop due to the interfacial layer.

The measured data can be described by a linear relation between V_c and d. The intercept with the ordinate axis yields a voltage drop V_i of 0.06 [V].

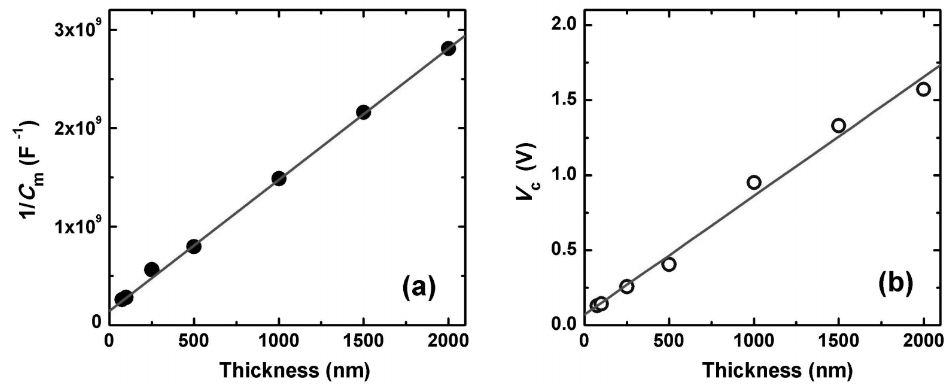

Figure 5.15: Linearly of the (a) reciprocal measured capacitance and (b) coercive voltage (V_c), based on the results from Fig. 5.13(a), as a function of film thickness.

D. Leakage current density

The leakage current density-electric field (*J-E*) curves of the PZT film capacitors with different thicknesses are shown in Fig. 5.16. By applying positive-bias electric fields, the results of *J-E* measurements exhibit a tendency of the leakage current density to decrease with increasing film thickness, for instance, the 1000 nm-thick PZT film has a leakage current density of approximately 10^{-5} A/cm^2 at 10 kV/cm, three orders of magnitude lower than that of the 250 nm-thick film. The values of *J* at 10 kV/cm (Ohmic region) and 200 kV/cm (Schottky region) were plotted as a function of film thickness in Fig. 5.17.

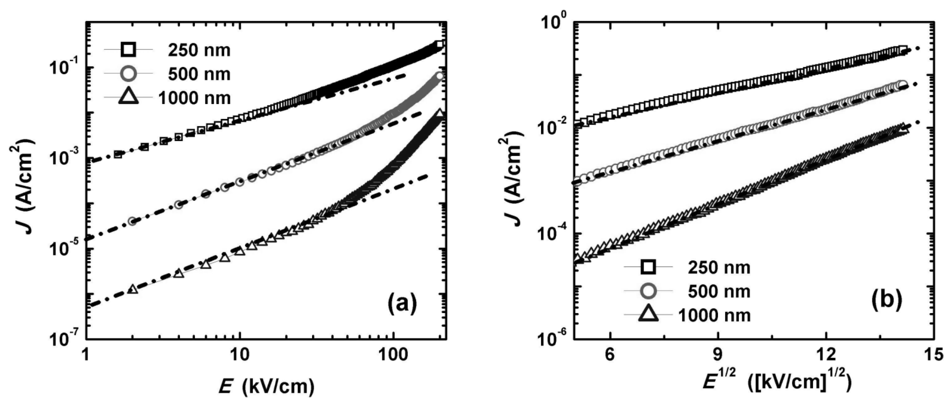

Figure 5.16: Positive leakage current density versus electric field (*J-E*) characteristics for PZT films of different thicknesses: (a) Ohmic contact and (b) Schottky emission model.

As also shown in this Fig. 5.16, the leakage current densities seem to have the Ohmic property ($J \propto E$) in the low applied electric field region (E < 30 kV/cm) and at higher field, the currents increase as a function of $E^{1/2}$ ($J \propto E^{1/2}$) following the Schottky emission model.

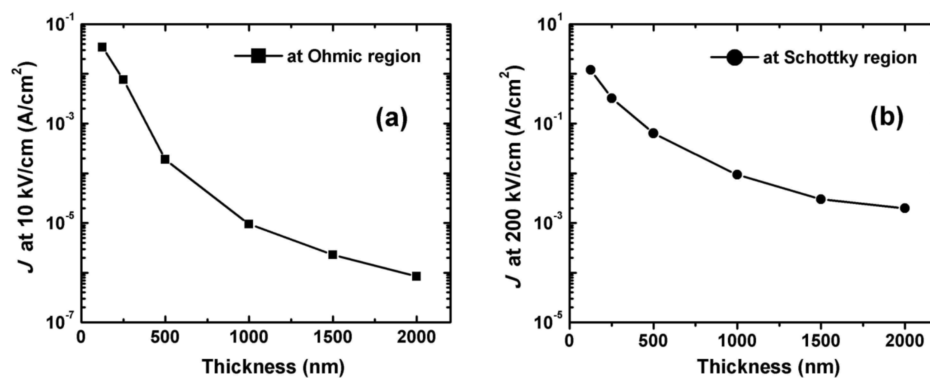

Figure 5.17: Current evolution versus film thickness (a) at 10 kV/cm (Ohmic contact region) and (b) at 200 kV/cm (Schottky emission region).

According to Eq. (5.4), the Schottky emission model can be rewritten as:

$$J_{Sch} = A^* T^2 \exp\left(-\frac{q\phi_B}{k_B T}\right)\exp\left[\left(\frac{q^3}{4\pi\varepsilon_0 \varepsilon d}\right)^{1/2}\frac{\sqrt{V}}{k_B T}\right] \tag{5.13}$$

$$\Leftrightarrow \ln J_{Sch} = \ln\left(A^* T^2\right) - \frac{q\phi_B}{k_B T} + \frac{1}{k_B T}\left(\frac{q^3}{4\pi\varepsilon_0 \varepsilon d}\right)^{1/2}\sqrt{V} \tag{5.14}$$

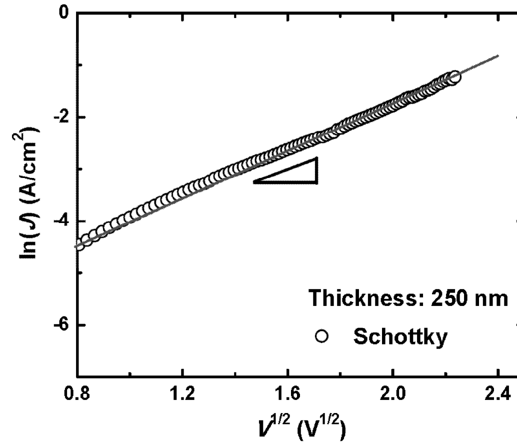

Figure 5.18: Variations of ln(*J*) as a function of applied voltage $V^{1/2}$ at room temperature for the 250-nm-thick (110)-oriented PZT film capacitor.

The $\varepsilon \times d$ value in Eq. (5.14) can be calculated from the slope of the linear fitting in the Schottky conduction region of Fig. 5.18, and a value of 180 [nm] is obtained. Assuming most of the applied voltage drop occurs across the interfacial layer, the *d* and ε here should be the interfacial layer d_i and the interfacial-layer dielectric constant ε_i, so that:

$$\varepsilon_i \times d_i = 180[nm] \tag{5.15}$$

From Eqs. (5.11) and (5.15), a system of equations is established as:

$$\begin{cases} \varepsilon_i \times d_i = 180 \\ \dfrac{d_i}{\varepsilon_i} = 0.215 \end{cases} \tag{5.16}$$

From Eq. (5.16), we calculated ε_i = 29 and d_i = 6.2 nm for the 250 nm-thick PZT film.

Table 5.2: Parameters for the (110)-oriented PZT films with various film thicknesses.

Film thickness d [nm]	P_r [μC/cm^2]	E_c [kV/cm]	J at 200 kV/cm [A/cm^2]	ε	tanδ	ε_i	d_i [nm]
75	8.4	30.4	3.2	822	0.082	26.8	6.1
125	12.6	28.0	1.2	1007	0.056	28.4	6.0
250	15.6	27.2	0.32	1218	0.044	29.0	6.2
500	20.4	25.7	0.064	1770	0.041	34.9	6.6
1000	19.8	25.5	0.009	1900	0.036	36.8	7.1
1500	18.8	25.8	0.003	1960	0.035	38.9	7.4
2000	18.2	25.9	0.001	2010	0.034	40.1	7.7

5.4.2 PZT films on $SrTiO_3$ substrates

In this study, the effect of film thickness on the properties of the PZT films grown on SRO coated (110) $SrTiO_3$ (STO) substrates was investigated. Figure 5.19(a) shows the results of the XRD scans measured around PZT(110) peak for 100, 250, and 500 nm-thick PZT films. Figure 5.19(b) indicates the variation of the a-lattice parameters of PZT films on Si and STO substrates as a function of film thickness. It was found that the a-parameters increased with film thicknesses irrespective of the substrate. For thinner PZT films (< 500 nm), the a-parameters exhibited a rapid increase and then a gradual increase at thicker films. The almost saturated lattice parameter obtained at high thickness (> 1000 nm) is due to the decrease of the influence of epitaxial mismatch between the PZT films and the substrates.

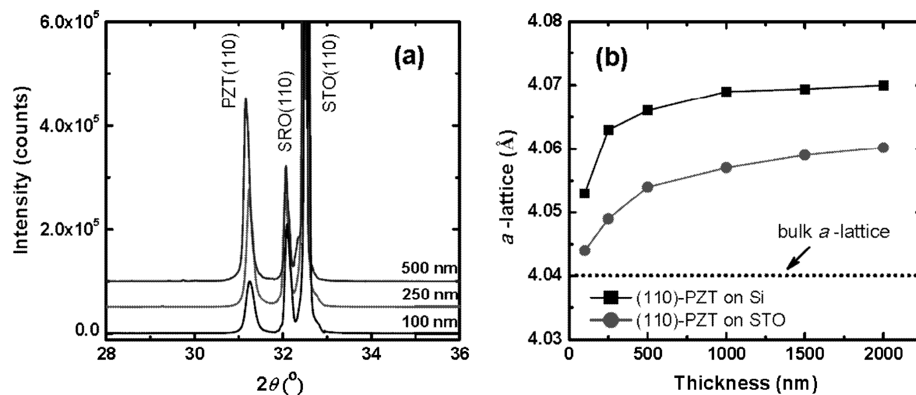

Figure 5.19: (a) XRD spectra of PZT films grown on SRO buffered STO substrates with different thicknesses: 100, 250 and 500 nm, and (b) a-lattice parameter plotted as a function of film thickness of the (110)-oriented PZT films grown on SRO buffered YSZ/Si and SRO buffered STO substrates.

Furthermore, the variation of the *a*-parameters of PZT films on Si was similar to that of films on STO, however the effect was more pronounced. These results shown that the PZT films deposited on STO substrates under compressive stress which have the *a*-lattice parameters smaller than those on Si substrates under tensile stress (Fig. 5.20). As discussed in chapter 4, the PZT film under compressive stress results in *c*-domain orientation, whereas, *a*-domain orientation is generated in the PZT film under tensile stress. The result is a large P_r value of 45 μC/cm^2 for the 500 nm-thick PZT film grown on STO, while a small P_r value of 20.4 μC/cm^2 for the film on Si (see Figs. 5.11 and 5.21). This relationship is also investigated by Tuttle *et al.* for PZT film deposited on sapphire (under compressive stress) which exhibits superior ferroelectric properties as compared to film deposited on silicon substrate (under tensile stress) [43].

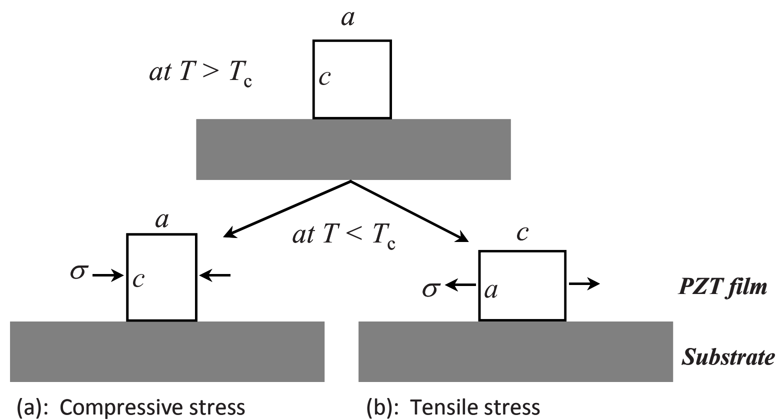

Figure 5.20: Effect of the residual stress, during cooling from deposition temperature to room temperature, on the domain orientation in ferroelectric films under: (a) compressive stress and (b) tensile stress.

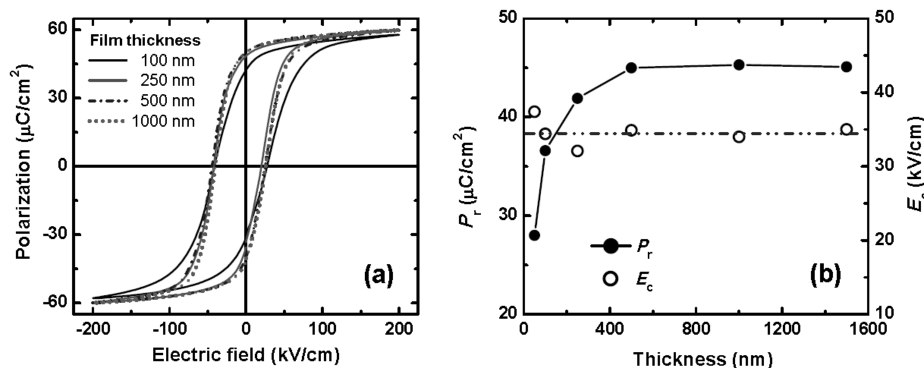

Figure 5.21: (a) Polarization hysteresis loops measured at maximum driving field of ±200 kV/cm and frequency of 1 kHz for each film thickness and (b) Remnant polarization (P_r) and coercive field (E_c) as a function of film thickness.

Figure 5.22 shows the fatigue characteristics of (110)-oriented PZT films on SRO buffered STO substrates as a function of film thickness. These results indicate that the remnant polarization (P_r) values keep almost constant with increasing the repeated switching cycles.

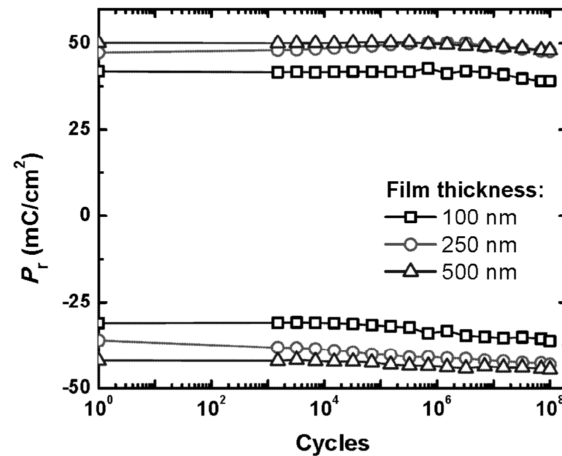

Figure 5.22: Polarization switching of the PZT/SRO/STO capacitors as a function of film thickness from 100 to 500 nm. The measurements were carried out by applied a bipolar rectangular pulse with pulse width of 0.5 ms (1 kHz) and at pulse height of 200 kV/cm. The remnant polarizations were evaluated from the polarization loops which measured with an amplitude of ±200 kV/cm and a frequency of 1 kHz.

5.5 Effect of Zr/Ti ratio on the properties of PZT thin film capacitors

Since PZT material has a polar axis, this material shows different electric properties depending on orientations, residual stress, film thickness and composition [3, 9, 44]. To investigate the relationships between the effects of film composition on the polarization and dielectric properties, in this study, we have performed an extensive study based on the experimental results of the polarization and dielectric properties of 250-nm-thick PZT films with four different compositions (Zr/Ti = 60/40, 52/48, 40/60 and 20/80).

5.5.1 PZT thin films on silicon substrates

A. Film structure

In order to investigate the crystalline structure of the PZT thin films with different Zr/Ti ratios, x-ray diffraction (XRD) was used. In this study, whatever the Zr/Ti ratio, we have maintained the same deposition conditions. Figure 5.23(a) shows the XRD patterns of PZT thin films grown on SRO buffered YSZ/Si with Zr/Ti ratios of 60/40, 52/48, 40/60 and 20/80.

The patterns show that all the films consist of mainly the (110)-oriented perovskite phase and without the pyrochlore phase. Due to the various Zr/Ti ratios, change in position of PZT(110) peak of diffraction is observed. The PZT(110) peak position shifts toward a higher angle when the Zr/Ti ratio is varied ranging from 60/40 to 20/80. Furthermore, the intensity of (110)-oriented peak decreases slightly in the Zr/Ti range of 60/40 and 20/80, and moreover, it is significantly broadened with a ratio of 20/80.

Figure 5.23(b) shows the composition variation of PZT thin films when the Zr/Ti ratios are 60/40, 52/48, 40/60 and 20/80. With a decrease of Zr/Ti ratio, the *a*-lattice parameter decreases.

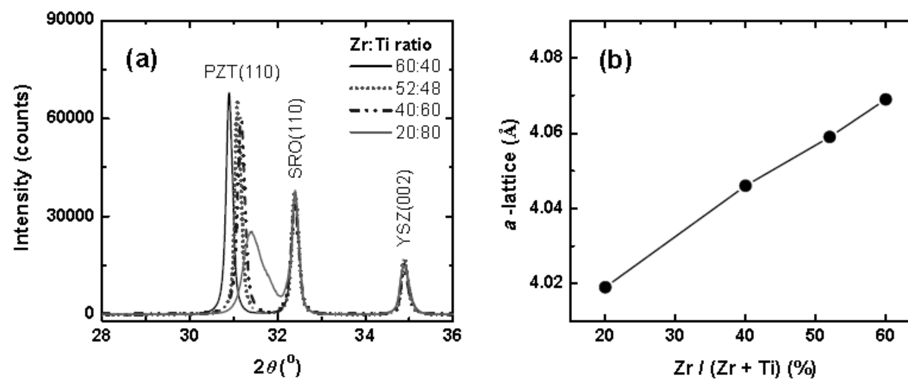

Figure 5.23: (a) Evolution of (110) orientation with Zr/Ti ratio as evidenced by XRD patterns, and (b) *a*-lattice parameter plotted as a function of Zr/Ti ratio of PZT films grown on SRO buffered YSZ/Si.

B. Polarization properties

Studies on the deformation in the polarization hysteresis loop of PZT films with different Zr/Ti ratios are important for the understanding of ferroelectric properties as well as the application of ferroelectric films. Figure 5.24 indicates the differences in ferroelectric properties among the PZT thin films fabricated from the targets with Zr/Ti ratios of 60/40, 52/48, 40/60 and 20/80. The tetragonal film fabricated from the target with a Zr/Ti ratio of 20/80 exhibits a well saturated rectangular loop with a large remnant polarization (P_r) and a large coercive field (E_c) of 38 $\mu C/cm^2$ and 56.6 kV/cm. Slim ferroelectric *P–E* hysteresis loop was observed in the rhombohedral film fabricated from the target with Zr/Ti molar ratio of 60/40 (Fig. 5.24(b)).

The plots of the average values of the P_r and E_c are shown as a function of Zr/Ti ratio of PZT thin films in Fig. 5.25. With increasing Ti-rich composition, larger P_r and high E_c values are observed. A similar trend was also reported for PZT films with varying Zr/Ti ratios fabricated by the sol-gel process [9].

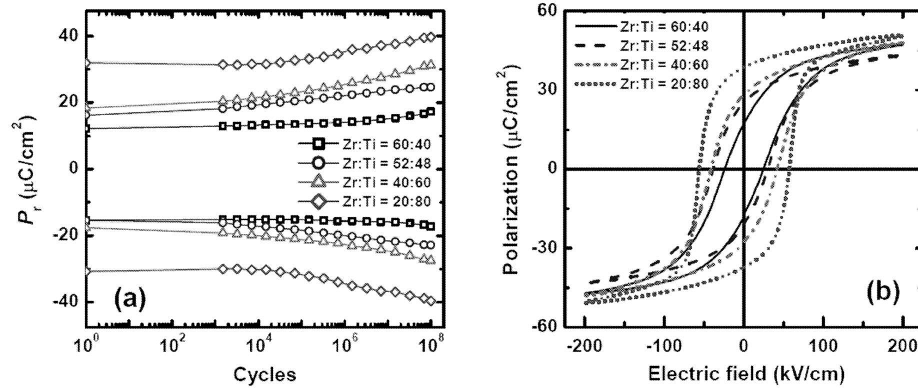

Figure 5.24: Zr:Ti ratio dependence of (a) polarization switching, $\pm P_r$ and (b) polarization hysteresis (*P-E*) loops for the (110)-oriented PZT thin film capacitors.

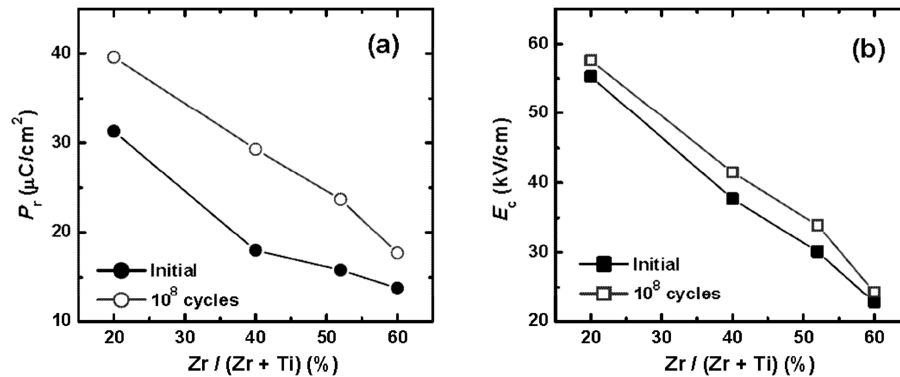

Figure 5.25: (a) Remnant polarization P_r and (b) coercive field E_c of the (110)-oriented PZT thin film capacitors as a function of Zr/Ti ratio.

It is more reasonable to explain the hysteresis loop shape in terms of the activity of domain walls. The large difference between saturation and remnant polarization in PZT films is most likely a result of the hysteresis loop shape explained in terms of the activity of domain walls. In other words, the large difference between saturation and remnant polarization in PZT films is most likely a result of significant domain reversal after the removal of the electric field. The main difference in *P-E* hysteresis loops between Zr/Ti ratios was in the squareness of the hysteresis. This squareness is given by the ratio P_r/P_s, where P_s is the saturation polarization plotted against the Zr/Ti ratio in Fig. 5.26(a). It is clear that the P_r/P_s values are enhanced with decreasing Zr content. On the other hand, the squareness of *P-E* loops is increased with decreasing Zr/Ti ratio.

Figure 5.26(b) shows the Q_{sw}/Q_{nsw} ratio as a function of Zr/Ti ratio. The PZT(60/40) film (rhombohedral phase) shows a small remnant polarization (P_r) compared to the saturated polarization (P_s), indicating large non-switching charges ($Q_{nsw} = P_s - P_r$). On the other hand, PZT(20/80) film (tetragonal phase) exhibit a well saturated rectangular loop with large remnant polarization. The non-switching charge is known to be related to the capacitance of the ferroelectric film. The films near the morphotropic phase boundary (MPB) that have large dielectric constant exhibit a large non-switching charge. For actual memory device application, the signal to noise ($Q_{sw}/Q_{nsw} \sim S/N$) ratio is a very important parameter and is related to the ratio of switching ($Q_s = P_r + (-P_r)$) to non-switching charges [45]. It can be said that the S/N ratio tends to increase with Ti content.

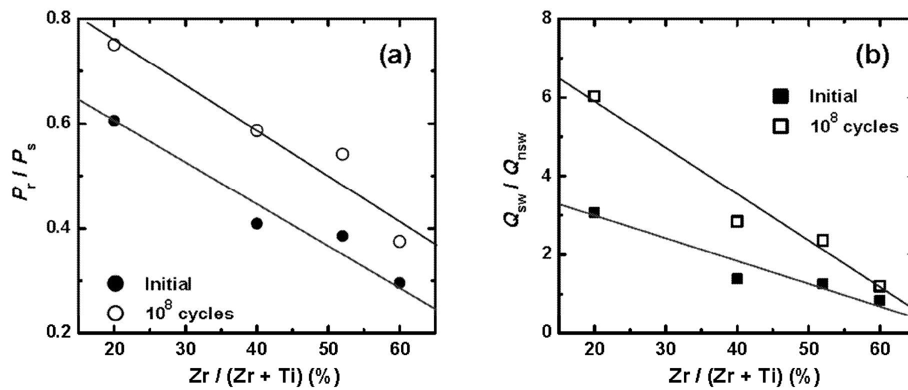

Figure 5.26: Zr/Ti ratio dependence of (a) P_r/P_s and (b) Q_{sw}/Q_{nsw} values for the (110)-oriented PZT thin film capacitors.

C. Dielectric responses

The dielectric constant-electric field (ε-E) curves for various Zr/Ti ratios in PZT thin film capacitors, which reveal the nonlinearity of ferroelectric film capacitors, are shown in Fig. 5.27. The measurements were carried out at a frequency of 10 kHz and *ac* signal of 4 kV/cm by sweeping from –200 to +200 kV/cm and back again. The rhombohedral films exhibit a sharp humped ε-E curver, and its behavior is kept until a Zr/Ti ratio of 40/60, indicating that a large fraction of domain switching is due to non-180° domain wall switching. It can be seen that even though there is the same (110)-oriented film, however, the switching process of the tetragonal phase with the Zr/Ti ratio of 20/80, which is governed by 180° domain wall motion, is different from that of the rhombohedral phase [46].

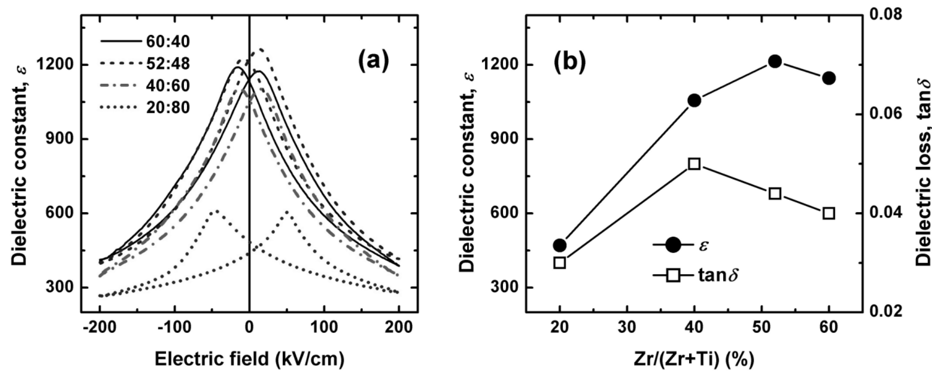

Figure 5.27: (a) Dielectric constant-electric field (ε-E) curves and (b) dielectric constant and dielectric loss for the (110)-oriented PZT thin film capacitors as a function of Zr/Ti ratio.

The dielectric constant (ε) and dielectric loss (tanδ) are shown as a function of Zr/Ti ratio of PZT thin film capacitors in Fig. 5.27(b). The ε and tanδ became larger as the titanium content increased in the rhombohedral films, and the PZT films with a Zr/Ti ratio of 52/48 had the best dielectric constant. It is shown that this is the same trend as bulk PZT ceramics [6, 47]. The tetragonal film shows a smaller value of dielectric constant.

5.5.2 PZT thin films on $SrTiO_3$ substrates

In this study, the effect of Zr/Ti ratio on the properties of the PZT thin films grown on SRO coated (001) STO substrates was also investigated. The XRD patterns, in Fig. 5.28(a), of the PZT thin films with Zr/Ti ratios of 60/40, 52/48, 40/60 and 20/80 show only peaks of the (001)-orientation. As the Zr/Ti ratio decreases, the peak position shifts towards a smaller angle, and leads to an increase in the *c*-lattice parameter (Fig. 5.28(b)). The films with Zr/Ti ratios of 60/40, 52/48 and 40/60 have unsplit peaks and mainly crystallize in the rhombohedral phase. The PZT(20/80) film, with a broad peak, crystallizes in the tetragonal phase. The lattice parameters of the epitaxial PZT thin films are presented in Fig. 5.28(b) as a function of Zr/Ti ratio. This result demonstrated that the phase diagram of the epitaxial PZT thin films is essentially distorted from that of bulk PZT ceramics [48].

Similar to those of the (110)-oriented PZT thin films grown on silicon substrates, the squareness hysteresis loop (high P_r/P_s and Q_{sw}/Q_{nsw}), larger P_r and high E_c values with increasing Ti-rich composition are observed in the (001)-oriented PZT thin films grown on STO substrates, as illustrated in Figs. 5.29 and 5.30. From the above observation, it is apparent that tetragonal PZT thin films display switching characteristics most similar to those of ideal single crystals.

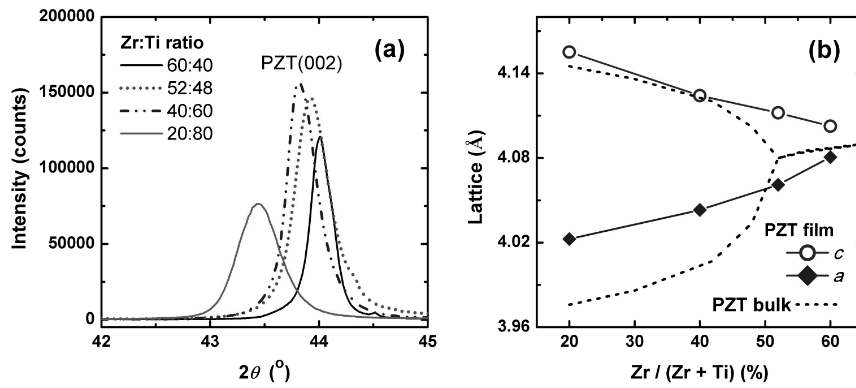

Figure 5.28: (a) Evolution of (001) orientation with Zr/Ti ratio as evidenced by XRD patterns, and (b) Lattice parameters (*a* and *c*) as a function of Zr/Ti ratio of PZT films grown on SRO buffered STO substrates. The dotted line indicate the PZT bulk data (Ref. [48]).

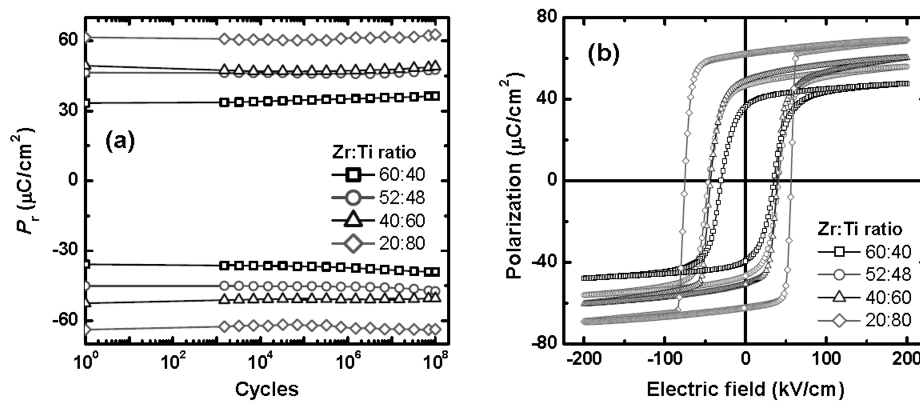

Figure 5.29: Zr/Ti ratio dependence of (a) polarization switching $\pm P_r$ and (b) polarization hysteresis (*P*-*E*) loops for the (001)-oriented PZT thin film capacitors.

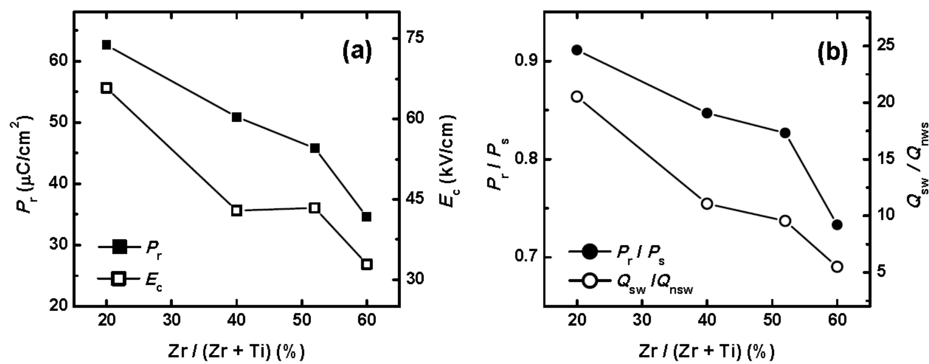

Figure 5.30: Zr/Ti ratio dependence of (a) P_r/P_s and (b) Q_{sw}/Q_{nsw} values for the (001)-oriented PZT thin film capacitors.

In comparison to the PZT thin films on Si, however, the broad peaks of capacitance of (001)-oriented PZT thin films on STO is observed for Zr/Ti ratios of 60/40, 52/48 and 40/60, indicating the contribution of non-180° domain wall switching (Fig. 5.31(a)). Whereas, the switching process of the tetragonal phase in PZT(20/80) film is governed by 180° domain wall motion, due to the sharp peak of *C-E* curve. Furthermore, the film near the MPB (Zr/Ti=52/48) exhibits large dielectric constant and it is similar to the films on silicon substrates. The tendency for a maximum dielectric constant around MPB composition, as shown in Figs. 5.27(b) and 5.31(b) for (110)- and (001)-oriented films, respectively, is almost the same as that reported for bulk PZT ceramics [6, 47, 49] and thin films [50]. This suggests that the change in dielectric constant with Zr/Ti ratio did not depend on the film orientation and film stress.

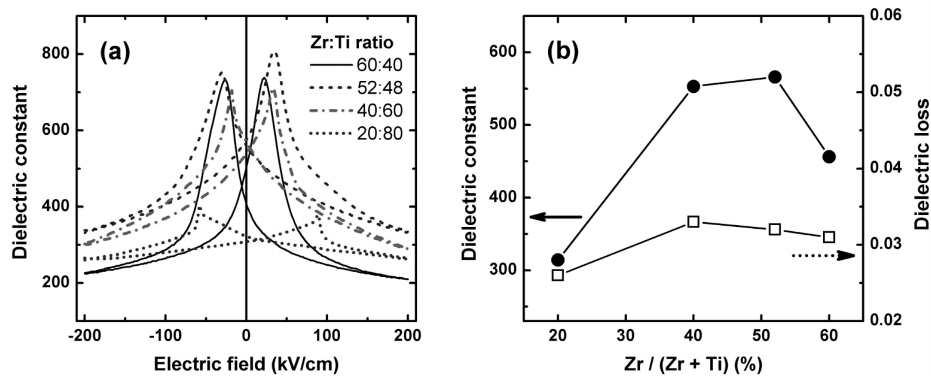

Figure 5.31: (a) Dielectric constant-electric field (ε-*E*) curves and (b) dielectric constant and dielectric loss for the (001)-oriented PZT thin film capacitors as a function of Zr/Ti ratio.

5.6 Summary and conclusions

In this chapter, the variations of the polarization and dielectric properties of PZT films as a function of film thickness were investigated. As the PZT film thickness increased, the remnant polarization and dielectric constant increased and saturated at 500-1000 nm with these values of 20.4 $\mu C/cm^2$ and 2010 for the (110)-oriented PZT films grown on SRO coated YSZ/Si, respectively, whereas, the coercive field decreased with increasing film thickness.

The suggested explanations for such thickness dependence include residual stress in the thin films and the existence of interfacial layer at the electrode/film interface. As the film thickness increases, the tensile stress in PZT film on Si is decreased and leads to an increase of the remnant polarization. Moreover, with increasing film thickness, the

switching of domains might be increased with the reduction of interfacial layer effect, which also leads to an improved remnant polarization.

In the PZT films on STO with compressive stress, the polarization is still increased although the compressive stress decreased with increasing film thickness (in fact, at the same film thickness, the remnant polarization increases with an increase in compressive stress). In other words, we believed that the existence of interfacial layer had a larger effect on the properties of PZT films with film thickness than that of the residual stress.

The effects that the Zr/Ti ratio had on crystal structure and electrical properties were systematically investigated. The thin films with a high Ti-content exhibit more abrupt domain switching and a larger signal to noise (Q_{sw}/Q_{nsw}) ratio of the polarization hysteresis loop. On the other hand, the squareness of *P-E* loops significantly improved with decreasing Zr/Ti ratio, corresponding to the increase of the *c*/*a* ratio of the PZT unit cell. It was observed that an observable peak in dielectric constant exists for the PZT thin films with a composition near the MPB (Zr/Ti = 52/48) composition, showing the same trend as bulk PZT ceramics.

5.7 References

1. M. Dawber and J. F. Scott, *A model for fatigue in ferroelectric perovskite thin films*, Appl. Phys. Lett. **76** (2000) p. 1060-1062.
2. P. Gerber, C. Kügeler, U. Ellerkmann, P. Schorn, U. Böttger, and R. Waser, *Effects of ferroelectric fatigue on the piezoelectric properties (d_{33}) of tetragonal lead zirconate titanate thin films.* Appl. Phys. Lett. **86** (2005) p. 112908(1-2).
3. M. Dekkers, M. D. Nguyen, R. Steenwelle, P. M. te Riele, D. H. A. Blank, and G. Rijnders, *Ferroelectric properties of epitaxial $Pb(Zr,Ti)O_3$ thin films on silicon by control of crystal orientation*, Appl. Phys. Lett. **95** (2009) p. 012902(1-3).
4. A. K. Tagantsev and I.A. Stolichnov, *Injection-controlled size effect on switching of ferroelectric thin films*, Appl. Phys. Lett. **74** (1999) p. 1326-1328.
5. D. M. Kim, C. B. Eom, V. Nagarajan, J. Ouyang, R. Ramesh, V. Vaithyanathan, and D. G. Schlom, *Thickness dependence of structural and piezoelectric properties of epitaxial $Pb(Zr_{0.52}Ti_{0.48})O_3$ films on Si and $SrTiO_3$ substrates*, Appl. Phys. Lett. **88** (2006) p. 142904(1-3).
6. B. Noheda, D. E. Cox, G. Shirane, J. A. Gonzalo, L. E. Cross, and S. E. Park, *A monoclinic ferroelectric phase in the $Pb(Zr_{1-x}Ti_x)O_3$ solid solution*, Appl. Phys. Lett. **74** (1999) p. 2059-2061.
7. B. Jaffe, J. William, R. Cook, and H. Jaffe, *Piezoelectric Ceramics*, Academic Press, New York (1971).

8. B. Noheda, D. E. Cox, G. Shirane, S. E. Park, L. E. Cross, and Z. Zhong, *Polarization Rotation via a Monoclinic Phase in the Piezoelectric 92% $PbZn_{1/3}Nb_{2/3}O_3$-8% $PbTiO_3$*. Phys. Rev. Lett. **86**, (2001) p. 3891-3894.
9. S. -H. Kim, J. -S. Yang, C. Y. Koo, J. -H. Yeom, E. Yoon, C. S. Hwang, J. -S. Park, S. -G. Kang, D. -J. Kim, and J. Ha *Dielectric and electromechanical properties of $Pb(Zr,Ti)O_3$ thin films for piezo-microelectromechanical system devices*, Jpn. J. Appl. Phys. **42** (2003) p. 5952-5955.
10. J. F. Scott, *Device Physics of Ferroelectric Thin-Film Memories*, Jpn. J. Appl. Phys. **38** (1999) p. 2272-2274.
11. B. Nagaraj, S. Aggarwal, and R. Ramesh, *Influence of contact electrodes on leakage characteristics in ferroelectric thin films*, J. Appl. Phys. **90** (2001) p. 375-382.
12. L. Pintilie and M. Alexe, *Metal-ferroelectric-metal heterostructures with Schottky contacts. I. Influence of the ferroelectric properties*, J. Appl. Phys. **98** (2005) p. 124103(1-8).
13. L. Pintilie, I. Boerasu, M. J. M. Gomes, T. Zhao, R. Ramesh, and M. Alexe, *Metal-ferroelectric-metal structures with Schottky contacts. II. Analysis of the experimental current-voltage and capacitance-voltage characteristics of $Pb(Zr,Ti)O_3$ thin films*, J. Appl. Phys. **98** (2005) p. 124104(1-9).
14. M. Shimizu, H. Fujisawa, S. Hyodo, S. Nakashima, H. Niu, H. Okino, and T. Shiosaki, *Effects of sputtered Ir and IrO_2 electrodes on the properties of PZT thin films deposited by MOCVD*, in *Mater. Res. Soc. Symp. Proc.*, Boston-USA (1997) p. 159-164.
15. S. -T. Kim, H. -H. Kim, M. -Y. Lee, and W. -J. Lee *Investigation of Pt/Ti Bottom Electrodes for $Pb(Zr,Ti)O_3$ Films*, Jpn. J. Appl. Phys. **36** (1997) p. 294-300.
16. S. -O. Chung, J. W. Kim, G. H. Kim, C. O. Park, and W. J. Lee *Formation of a lead zirconate titanate (PZT)/Pt interfacial layer and structural changes in the Pt/Ti/SiO_2/Si substrate during the deposition of PZT thin film by electron cyclotron resonance plasma-enhanced chemical vapor deposition,* Jpn. J. Appl. Phys. **36** (1997) p. 4386-4391.
17. W. Wu, K. H. Wong, C. L. Choy, and Y. H. Zhang, *Top-interface-controlled fatigue of epitaxial $Pb(Zr_{0.52}Ti_{0.48})O_3$ ferroelectric thin films on $La_{0.7}Sr_{0.3}MnO_3$ electrodes*, Appl. Phys. Lett. **77** (2000) p. 3441-3443.
18. X. J. Meng, J. L. Sun, J. Yu, L. X. Bo, C. P. Jiang, Q. Sun, S. L. Guo, and J. H. Chu, *Changes in the interface capacitance for fatigued lead-zirconate-titanate capacitors*, Appl. Phys. Lett. **78** (2001) p. 2548-2550.
19. B. Chen, H. Yang, L. Zhao, J. Miao, B. Xu, X. G. Qiu, B. R. Zhao, X. Y. Qi, and X. F. Duan, *Thickness and dielectric constant of dead layer in Pt/$(Ba_{0.7}Sr_{0.3})TiO_3$/$YBa_2Cu_3O_{7-x}$ capacitor*, Appl. Phys. Lett. **84** (2004) p. 583-585.
20. M. Stengel and N. A. Spaldin, *Origin of the dielectric dead layer in nanoscale capacitors*, Nature **443** (2006) p. 679-682.

21. J. J. Lee, C. L. Thio, and S. B. Desu, *Electrode contacts on ferroelectric* $Pb(Zr_xTi_{1-x})O_3$ *and* $SrBi_2Ta_2O_9$ *thin films and their influence on fatigue properties*, J. Appl. Phys. **78** (1995) p. 5073-5078.
22. I. Stolichnov, A. Tagantsev, N. Setter, J. S. Cross, and M. Tsukada, *Control of leakage conduction of high-fatigue-endurance* $(Pb,La)(Zr,Ti)O_3$ *film ferroelectric capacitors with* $Pt/SrRuO_3$ *electrodes* Applied Physics Letters, 1999. **75**(12): p. 1790-1792.
23. Y. Masuda and T. Nozaka, *The influence of various upper electrodes on fatigue properties of perovskite* $Pb(Zr,Ti)O_3$ *thin films*, Jpn. J. Appl. Phys. **42** (2003) p. 5941-5946.
24. T. Mihara and H. Watanabe, *Electronic conduction characteristics of sol-gel ferroelectric* $Pb(Zr_{0.4}Ti_{0.6})O_3$ *thin-film capacitors: Part I*, Jpn. J. Appl. Phys. **34** (1995) p. 5664-5673.
25. A. J. Hartmann, M. Neilson, R. N. Lamb, K. Watanabe, and J. F. Scott, *Ruthenium oxide and strontium ruthenate electrodes for ferroelectric thin-films capacitors*, Appl. Phys. A: Mater. Sci. & Process. **70** (2000) p. 239-242.
26. M. -T. Chentir, E. Bouyssou, L. Ventura, and C. Anceau, *Leakage current evolution versus dielectric thickness in lead zirconate titanate thin film capacitors*, J. Appl. Phys. **105** (2009) p. 061605(1-7).
27. T. Mihara and H. Watanabe, *Electronic conduction characteristics of sel-gel ferroelectric* $Pb(Zr_{0.4}Ti_{0.6})O_3$ *thin-film capacitors: Part II*, Jpn. J. Appl. Phys. **34** (1995) p. 5674-5682.
28. C. Sudhama, A. C. Campbell, P. D. Maniar, R. E. Jones, R. Moazzami, C. J. Mogab, and J. C. Lee, *A model for electrical conduction in metal-ferroelectric-metal thin-film capacitors*, J. Appl. Phys. **75** (1994) p. 1014-1022.
29. B. Nagaraj, S. Aggarwal, T. K. Song, T. Sawhney, and R. Ramesh, *Leakage current mechanisms in lead-based thin-film ferroelectric capacitors*, Phys. Rev. B **59** (1999) p. 16022(1-6).
30. J. Lappalainen and V. Lantto, *Extrinsic conductivity in ferroelectric PZT film capacitors made by laser ablation deposition*, Physica Scripta. **T79** (1999) p. 220-224.
31. S. M. Sze, *Physics of semiconductor devices*, John Wiley & Sons, New York (1981).
32. J. F. Scott, *Ferroelectric memories*, Springer, Berlin (2000).
33. J. -L. Chen, H. -M. Chen, and J. Y. -M. Lee, *An investigation on the leakage current and time dependent dielectric breakdown of ferroelectric lead-zirconate-titanate thin film capacitors for memory device applications*, Appl. Phys. Lett. **69** (1996) p. 4011-4013.
34. A. -Q. Jiang, H. J. Lee, C. S. Hwang, and T. -A. Tang, *Resolving the Landauer paradox in ferroelectric switching by high-field charge injection*, Phys. Rev. B **80** (2009) p. 024119(1-7).
35. A. K. Tagantsev, M. Landivar, E. Colla, and N. Setter, *Identification of passive layer in ferroelectric thin films from their switching parameters*, J. Appl. Phys. **78** (1995) p. 2623-2630.
36. F. K. Chai, J. R. Brews, and R. D. Schrimpf, *Profiling of electrical doping concentration in ferroelectrics*, J. Appl. Phys. **82** (1997) p. 2517-2527.

37. C. H. Lin, P. A. Friddle, C. H. Ma, A. Daga, and H. Chen, *Effects of thickness on the electrical properties of metalorganic chemical vapor deposited $Pb(Zr,Ti)O_3$ (25--100 nm) thin films on $LaNiO_3$ buffered Si*, J. Appl. Phys. **90** (2001) p. 1509-1515.

38. Y. Masuda, *Variation of dielectric constant affected by domain structure and electric-field-induced strain in ferroelectric ceramics*, Jpn. J. Appl. Phys. **33** (1994) p. 5549-5554.

39. R. Waser, T. Baiatu, and K.-H. Härdtl, *dc Electrical Degradation of Perovskite-Type Titanates: I, Ceramics*, J. Am. Ceram. Soc. **73** (1990) p. 1645-1653.

40. P. C. Joshi and S.B. Krupanidhi, *Structural and electrical characteristics of $SrTiO_3$ thin films for dynamic random access memory applications*, J. Appl. Phys. **73** (1993) p. 7627-7634.

41. M. D. Nguyen, R.J.A. Steenwelle, P. M. te Riele, J. M. Dekkers, D. H. A. Blank, and G. Rijnders. *Growth and properties of functional oxide thin film for PiezoMEMS*, in *EUROSENSORS XXI*, Dresden-Germany (2008).

42. P. K. Larsen, G. J. M. Dormans, D. J. Taylor, and P. J. van Veldhoven, *Ferroelectric properties and fatigue of $PbZr_{0.51}Ti_{0.49}O_3$ thin films of varying thickness: Blocking layer model*, J. Appl. Phys. **76** (1994) p. 2405-2413.

43. B. A. Tuttle, J. A. Voigt, T. J. Graino, D. C. Goodnow, R. W. Schwartz, D. L. Lamppa, T. J. Headley, and M. O. Entongh. *Chemically prepared Pb(Zr,Ti)O3 thin films: the effects of orientation and stress*, in *Proceedings of the Eighth IEEE International Symposium on Applications of Ferroelectrics*, New York (1992) p. 344-348.

44. S. Y. Yang, F. Zavaliche, L. Mohaddes-Ardabili, V. Vaithyanathan, D. G. Schlom, Y. J. Lee, Y. H. Chu, M. P. Cruz, Q. Zhan, T. Zhao, and R. Ramesh, *Metalorganic chemical vapor deposition of lead-free ferroelectric $BiFeO_3$ films for memory applications,* Appl. Phys. Lett. **87** (2005) p. 102903(1-3).

45. T. Mihara, H. Yoshimori, H. Watanabe, and C. A. Paz de Araujo, *Characteristics of Bismuth layered $SrBi_2Ta_2O_9$ thin-film capacitors and comparison with $Pb(Zr,Ti)O_3$*, Jpn. J. Appl. Phys. **34** (1995) p. 5233-5239.

46. N. Bar-Chaim, M. Brunstein, J. Grunberg, and A. Seidman, *Electric field dependence of the dielectric constant of PZT ferroelectric ceramics*, J. Appl. Phys. **45** (1974) p. 2398-2405.

47. X. -H. Du, J. Zheng, U. Belegundu, and K. Uchino, *Crystal orientation dependence of piezoelectric properties of lead zirconate titanate near the morphotropic phase boundary*, Appl. Phys. Lett. **72** (1998) p. 2421-2423.

48. G. Shirane and K. Suzuki, *Crystal structure of $Pb(Zr-Ti)O_3$*, J. Phys. Soc. Japan **7** (1952) p. 333.

49. T. Yamamoto, *Ferroelectric properties of the $PbZrO_3$-$PbTiO_3$ system,* Jpn. J. Appl. Phys. **35** (1996) p. 5104-5108.

50. C. M. Foster G.-R. Bai, R. Csencsits, J. Vetrone, R. Jammy, L. A. Wills, E. Carr, and J. Amano, *Single-crystal $Pb(Zr_xTi_{1-x})O_3$ thin films prepared by metal-organic chemical vapor deposition: Systematic compositional variation of electronic and optical properties*, J. Appl. Phys. **81** (1997) p. 2349-2357.

6.
Relationships between ferroelectric and piezoelectric properties in PZT films

Abstract. The following chapter investigates the relationship between electrical and mechanical properties in PZT films.

The effects of the fabricated characteristics of PZT films, such as film thickness, Zr/Ti composition and thermal residual stress, on the piezoelectric coefficient (d_{33}) are discussed. The contributions of domain-wall displacement (extrinsic contribution) and lattice variation (intrinsic contribution) on the d_{33} coefficient are also investigated. In the PZT films with different thicknesses, the increase in d_{33} coefficient with increasing film thickness is mainly caused by the intrinsic contribution. Whereas, the maximum d_{33} value is achieved near the morphotropic phase boundary (MPB) composition due to the coexistence of ferroelectric tetragonal and ferroelectric rhombohedral phases, which indicates that the d_{33} coefficient in PZT films with various Zr/Ti ratio is mainly governed by extrinsic contribution. Furthermore, elemental factors that affect the d_{33} coefficient, like polarization and dielectric constant, were analyzed based on the semi-empirical equation.

6.1 Introduction

Ferroelectric thin films have become an object of intensive research for memory-related and microelectromechanical system (MEMS) applications such as sensors, actuators, and energy harvesters [1-5]. Among ferroelectric materials, $Pb(Zr,Ti)O_3$ (PZT) films are considered the most promising for these applications since they can induce high mechanical properties under applied voltage [6, 7]. To develop PZT films for MEMS device applications, it is necessary to understand the effects contributing to the observed piezoelectric and the related ferroelectric properties. The high values in the polarization and piezoelectric coefficient are essential for these applications.

In chapter 4 and chapter 5, we reported the influence of film thickness, Zr/Ti composition and film orientation on the electrical (polarization and dielectric constant) properties of PZT films. In these chapters, the effects of the residual stress, interfacial layer as well as intrinsic and/or extrinsic contributions were discussed. These effects on the piezoelectric coefficient are presented in this chapter.

In PZT bulk ceramics and thin films, the piezoelectric properties are mainly dominated by the contributions from the domain-wall motion (extrinsic contribution) and atomic lattice variation (intrinsic contribution) [8]. In this chapter, understanding of whether the extrinsic or intrinsic contribution, which dominates the piezoelectric properties in PZT thin films, is presented. This is very important for controlling or improving the piezoelectric coefficient (d_{33}) of PZT thin films.

Furthermore, effective electrostriction coefficients (Q_{eff}) of the PZT films, determined using a linearized electrostriction equation that relates piezoelectric coefficient with the polarization and dielectric constant, are calculated and compared with other proposed ones.

6.2 Experimental procedure

In the present study, the $Pb(Zr,Ti)O_3$ films were deposited using the PLD technique. In order to investigate the effect of film thickness on the properties of (110)-oriented PZT films grown on SRO/YSZ/Si, the film thickness was varied from 75 to 2000 nm substrates by controlling the deposition time. Furthermore, the 250-nm-thick (110)-oriented PZT thin films with Zr/Ti ratios of 60/40, 52/48, 40/60 and 20/80 were used to verify the effect of composition on the piezoelectric properties of the films. To estimate the effect of residual stress, the 250-nm-thick (001)-oriented PZT thin films grown on SRO-buffered CeO_2/YSZ/Si, STO/Si, CeO_2/YSZ, and STO substrates were used. Details on the fabrication and structure of these films were presented in chapter 2, chapter 3 and chapter 5.

The polarization hysteresis (*P-E*) loops were measured using a ferroelectric film test system (TF 2000 Analyzer). *P-E* hysteresis loops were performed at $\pm$200 kV/cm amplitude and 1 kHz frequency. The capacitance-electric field (*C-E*) was measured using a Süss MicroTech PM300 manual probe-station equipped with Keithley 4200 Semiconductor

characterization system. The capacitance-electric field (*C-E*) curves were recorded using an *ac* signal at 4 kV/cm amplitude and 10 kHz frequency with the *dc* bias sweeping from -200 to +200 kV/cm and then back to -200 kV/cm. The corresponding dielectric responses were calculated from these *C-E* measurements.

In this study, the out-of-plane displacement in the thickness direction of the film was measured using the double-beam laser Doppler interferometer (LDV, Polytec MSA-400) [9]. The longitudinal piezoelectric coefficient (d_{33}) is derived under small *ac* field (8 kV/cm) and 8 kHz frequency, superimposed on a *dc* bias (up to 200 kV/cm). Details on this measurement can be seen in chapter 2. Experimental setup for measuring the piezoelectric coefficient of piezoelectric films is shown in Fig. 6.1.

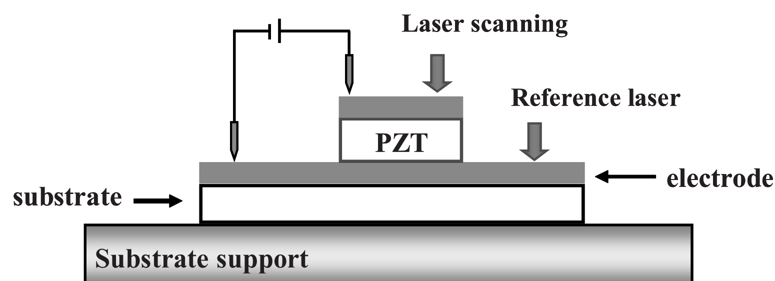

Figure 6.1: Schematic view of the measurement set-up for the d_{33} coefficient.

6.3 Piezoelectric responses in PZT films

6.3.1 Piezoelectric hysteresis loop

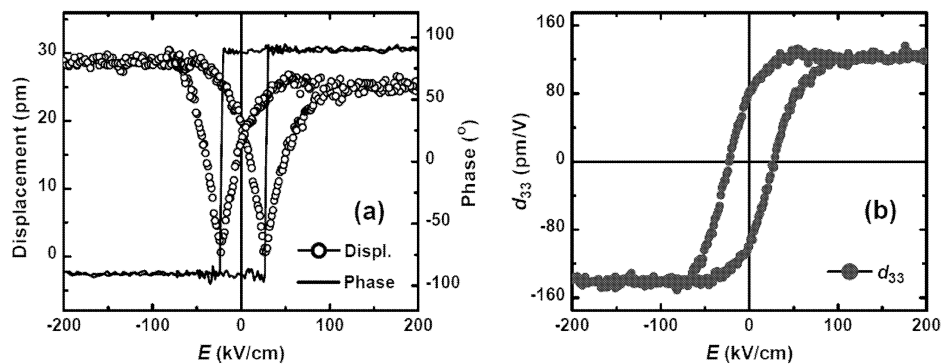

Figure 6.2: (a) Piezoelectric displacement curve and piezoelectric phase, and (b) Piezoelectric hysteresis loop, of the 250-nm-thick (110)-oriented PZT thin film.

Figure 6.2(a) shows the piezoelectric displacement and phase of the 250-nm-thick (110)-oriented PZT thin film deposited on SRO/YSZ/Si substrate. As expected, the piezoelectric signal changes sign (a 180° phase shift) at the coercive field ($\pm E_c$) due to polarization switching. The corresponding d_{33}-E loop is shown in Fig. 6.2(b). The remnant d_{33} coefficient of 92 pm/V at zero *dc* bias field and the maximum d_{33} coefficient of 124 pm/V at high *dc* bias field are obtained.

Shown in Fig. 6.3(a) is the strain (*S-E*) and dielectric-constant (ε-*E*) curves in PZT thin films under a maximum field of 200 kV/cm. A similar butterfly-shape is observed in both cases. In addition, it is known that the ε-*E* and *S-E* curves, which are performed in a nearly quasi-static way, can deliver more information on the ferroelectric domain reversal under applied electric field than normal (dynamic) polarization hysteresis (*P-E*) loops. In this film, the average coercive fields obtained from ε-*E* and *S-E* curves are about 10.6 and 15.4 kV/cm, respectively. These values are much less than the coercive field obtained from *P-E* loop (E_c = 27.2 kV/cm), as shown in Fig. 6.3(b). This difference may be due to the fact that the *dc* bias-voltage ramp rate was much slower than that of the stimulus-voltage in the *P-E* measurement [10].

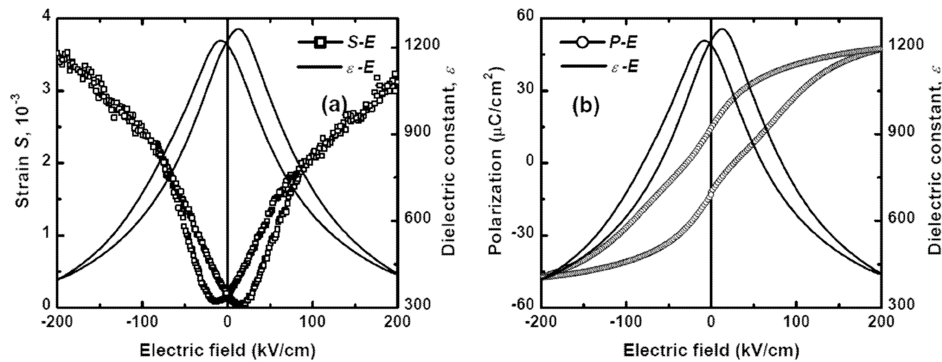

Figure 6.3: (a) Strain and dielectric constant curves, and (b) Polarization loop and dielectric constant curve, of the 250-nm-thick (110)-oriented PZT thin film.

As discussed above, the piezoelectric and dielectric properties in PZT films contain both intrinsic and extrinsic contributions. The extrinsic contribution refers to the domain-walls motion while the intrinsic contribution refers to the atomic lattice variation. Under an external electric field, domain-walls (180° and non-180°) motion increases the volume fraction of domain variants most closely aligned to the applied field at the expense of other variants. However, while non-180° domain-walls are both ferroelastically (piezoelectric) and ferroelectrically (dielectric) response, 180° domain-walls are only ferroelectrically response, as shown in Fig. 6.4. Therefore, while both types of domain-walls contribute to the dielectric properties, only non-180° domain-wall motion contributes to the piezoelectric properties [11].

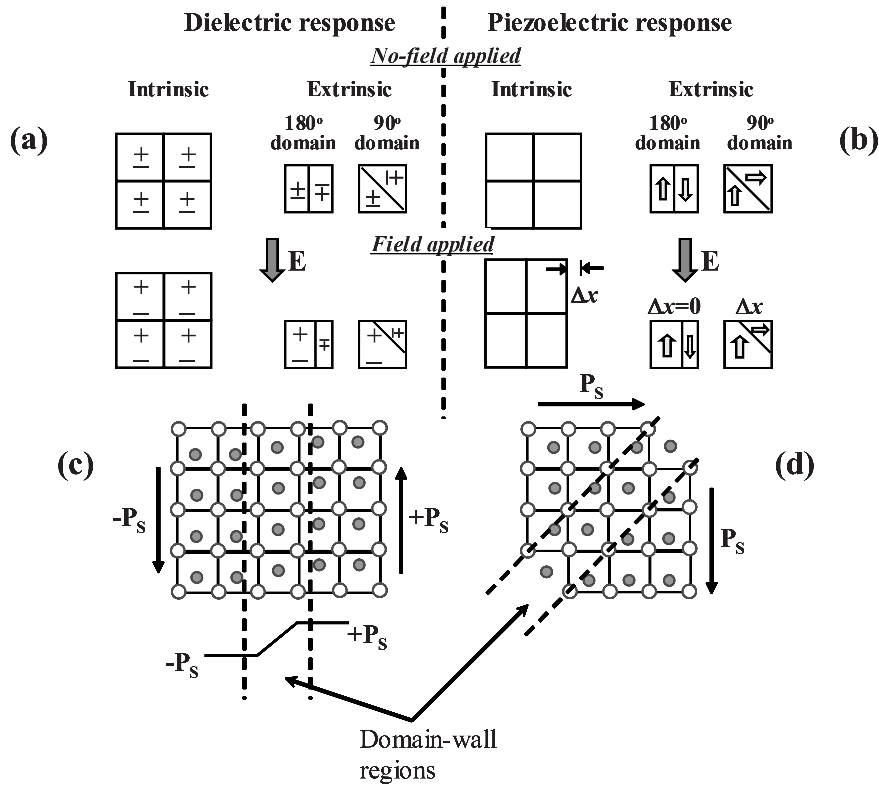

Figure 6.4: The effects of intrinsic and extrinsic (180° and 90° domain-walls) contributions on (a) Dielectric response and (b) Piezoelectric response; (c) and (d) show the schematic view of 180° and 90° domain-wall regions, respectively.

To investigate the effect of domain-wall contribution to the dielectric and piezoelectric responses of PZT films, the Rayleigh law has been utilized. For ferroelectric films, the Rayleigh law can be described in terms of the weak *ac* field and given by Eqs. (6.1) and (6.2):

$$\varepsilon(E_{ac}) = \varepsilon_{initial} + \alpha_{\varepsilon}E_{ac} \quad (6.1)$$

$$d_{33}(E_{ac}) = d_{33,\text{initial}} + \alpha_{d}E_{ac} \quad (6.2)$$

where E_{ac} is the *ac* field, $\varepsilon_{\text{initial}}$ is the initial dielectric constant, α_{ε} and α_{d} are the Rayleigh coefficients.

Figure 6.5 depicts the variations of the dielectric constant and d_{33} coefficient as a function of *ac* field. As the *ac* field increased, the dielectric constant of PZT thin films steadily increased (Fig. 6.5(a)). This indicates that both intrinsic and extrinsic (domain-walls) contributions had significant effects on the dielectric constant. From a linear fit, the initial dielectric constant and the Rayleigh constant can be defined from the intercept and slope, as 1060 and 50 [cm/kV], respectively.

To investigate the effect of non-180° domain-walls contribution, piezoelectric displacement (δ) of the PZT films are measured as a function of *ac* field, as shown in Fig. 6.5(b). Results show that the d_{33} (d_{33} = δ/V_{ac}) coefficients remain constant with *ac* fields, indicating that the non-180° domain-wall does not contribute to the piezoelectric properties. In this case, only intrinsic effects contribute to the piezoelectric properties of PZT thin films.

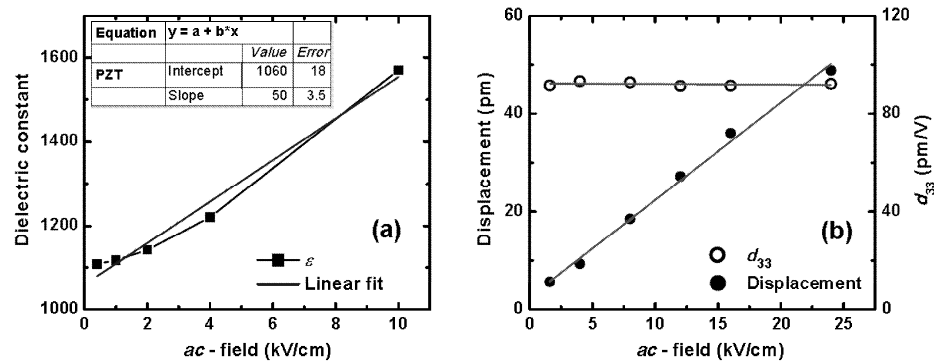

Figure 6.5: *ac* field dependence of (a) dielectric constant and (b) d_{33} coefficient, of the 250-nm-thick (110)-oriented PZT thin film.

The dielectric constant of the films as a function of the amplitude of small *ac* signals is also investigated at a 10 kHz frequency and zero *dc* bias fields (Fig. 6.5(a)) that defined from ε-E curves in Fig. 6.6. Unlike the d_{33}, which showed small nonlinearlity with *ac* field, the dielectric constant of PZT thin films showed very large amplitude dependence. With increasing *ac* field, giving rise to the increase of domain oscillations, and therefore, the dielectric constant is increased.

The dielectric constant of the PZT thin film as a function of the amplitude of *ac* field was investigated at a 10 kHz frequency, as shown in Fig. 6.6, with the *dc* bias field sweeping from -200 to +200 kV/cm and then back. At low *dc*-fields, the main contribution to the dielectric constant is the increase in the polarization due to domain reversal (extrinsic contribution). Whereas, at high *dc*-fields, most switchable domains have already been aligned along the direction of the *dc*-field; the dielectric constant is small since it is determined mainly by variations of the dipoles (intrinsic contribution) [12, 13]. Therefore, the dielectric constant measured at large applied *dc*-fields will approach the intrinsic dielectric constant because the film is approaching a single-domain state.

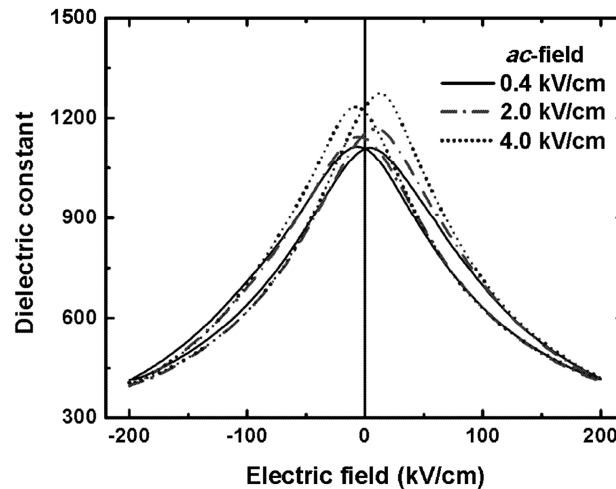

Figure 6.6: Dielectric constant-electric field (ε-*E*) curves as a function of *ac* field amplitude of the 250-nm-thick (110)-oriented PZT thin film.

It can be seen from Fig. 6.6 that the ε-*E* curve of higher applied *ac*-field is broad and higher than that of lower applied *ac*-field at low *dc*-fields region and similar at high *dc*-fields. These imply that the extrinsic contribution of the film was much more affected by *ac*-field amplitude than the intrinsic contribution. The large difference between the nonlinearity in piezoelectric coefficients and dielectric constants, as shown in Fig. 6.5, suggests that 180° domain-wall motion is much more significant than non-180° domain-wall motion. As a result, a majority of the extrinsic contribution to the dielectric constant in PZT thin films is mostly from the 180° domain-wall motion.

6.3.2 Piezoelectric displacement response

The piezoelectric displacement of PZT film capacitors can be observed by LDV. The scanning area covered on the top-electrode (2D scan). The size of PZT capacitors is actually equal to that of the PZT layers and top-electrodes. The clear edge between the displacement of the top-electrode and the surroundings indicates a sharp deformation of the voltage-excited area under the top-electrode. Moreover, the active part of the capacitor is always observed to vibrate anti-phase with respect to the passive surroundings. Figures 6.7(a)-6.7(b) shows the rectangle-shape of the three-dimensional (3D) piezoelectric displacement of the scanning area in which the relative movement between the substrate and voltage-excited part is clearly seen.

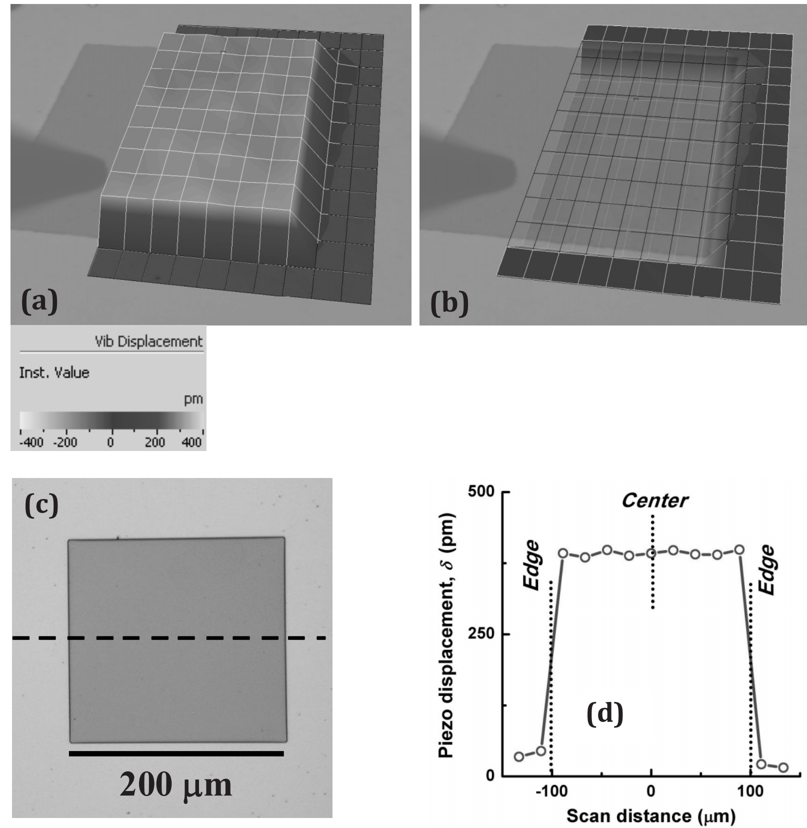

Figure 6.7: Two-dimension scanning result of the piezoelectric displacement response of the 250-nm-thick (110)-oriented PZT film. An 8 kHz and 4 V *ac*-voltage (or 160 kV/cm *ac*-field) was applied on the film via a probe: (a) 3D-upward response and (b) 3D-downward response; (c) Schematic of a PZT capacitor, and (d) A line scan profile of piezoelectric displacement response across the top-electrode of measured capacitor (200μm × 200μm).

To define the piezoelectric displacement of PZT capacitors, a line scan across the top-electrodes is also measured, as shown in Fig. 6.7(d). The line scan can be finished in a very short time in comparison with the 2D scan and the result provides enough information of the piezoelectric displacement. In this case, the piezoelectric displacement of the top electrode (δ_{top}) can be measured at the highest point of the top-electrode regardless of the bending of the substrate. The apparent piezoelectric coefficient (d_{33}) is calculated according to:

$$d_{33} = \frac{\delta_{top}}{V} \tag{6.3}$$

where *V* is the *ac* driving voltage. The apparent d_{33} coefficient is calculated as 98 pm/V by dividing the step height as 392 pm with an amplitude of 4 V. Results showed that the d_{33} coefficients, which are defined from both measurements such as piezoelectric hysteresis loop and piezoelectric displacement, are almost similar.

6.4 Ferroelectric-piezoelectric relationship in PZT films

In this study, we have systematically investigated the effects of film thickness, Zr/Ti ratio, and thermal residual stress on the longitudinal piezoelectric coefficients of PZT films. Moreover, the relations between electrical and mechanical nonlinear behaviors in PZT films are also discussed.

6.4.1 Film thickness effects

Figure 6.8(a) shows the piezoelectric hysteresis (d_{33}-*E*) loops of the (110)-oriented PZT films grown on SRO coated YSZ/Si with different thicknesses. All piezoelectric hysteresis loops showed that better squareness was achieved with increasing film thickness consistent with *P-E* hysteresis loops.

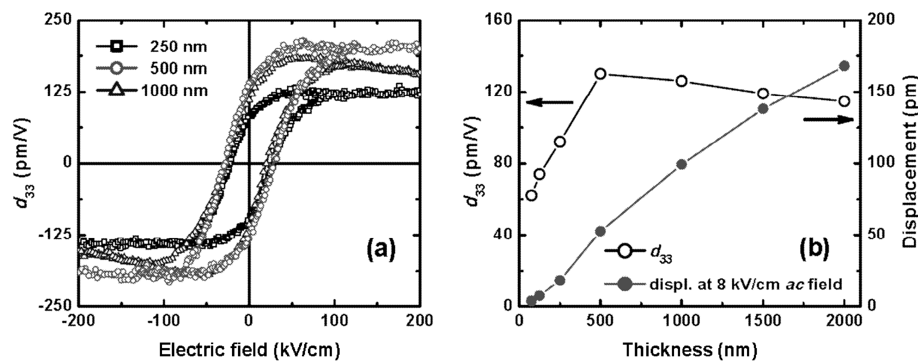

Figure 6.8: (a) Piezoelectric hysteresis loops and (b) d_{33} coefficient and piezoelectric displacement, of the (110)-oriented PZT films as a function of film thickness. The piezoelectric measurements were done at an *ac* field of 8 kV/cm and 8 kHz frequency with the *dc* bias sweeping from -200 to +200 kV/cm.

The thickness dependence of the d_{33} coefficient is plotted in Fig. 6.8(b). It is illustrated that the d_{33} coefficient increased from 64 to 132 pm/V with film thickness in the range of 75 - 500 nm and slightly decreased for the thicker films (1000 - 2000 nm). Like the polarization property, in the range of 75 - 500 nm film thickness, this variation in the piezoelectric property was attributed to the interfacial layer at the film/electrode interface. With increasing film thickness, the effect of interfacial layer is decreased, thus leading to a large d_{33} coefficient of PZT thin films. A slight decrease in the d_{33} coefficient with the thicker films (1000 - 2000 nm) is observed, because the PZT films get softened at these films.

As the discussion in section 6.3, the effect of non-180° domain-wall motion in response to the d_{33} coefficients is negligible. This means that the increase in the d_{33} coefficient with increasing film thickness is mainly caused by the intrinsic contribution.

In general, the piezoelectric coefficient d_{33} of a monodomain single-crystal ferroelectric can be expressed as a function of its relative dielectric constant (ε_r) and spontaneous polarization (P_s):

$$d_{33} = 2Q_{33}\varepsilon_0\varepsilon_r P_s \tag{6.4}$$

where Q_{33} is the electrostriction coefficient which only weakly depends on the external parameters and ε_0 vacuum permittivity. This equation can also be applicable to multidomain polycrystalline ferroelectrics. In this case, the Q_{33} coefficient is replaced with the effective electrostriction coefficient (Q_{eff}).

For this calculation, the "intrinsic" dielectric constant (ε_r) was estimated by constructing a linear fit to the highest field dielectric constant (from the 120 to 200 kV/cm range) and extrapolating back to zero field, as shown in Fig. 6.9(b). This is required to remove the contribution to the dielectric constant of 180° domain-wall, because such domain-wall does not contribute to the piezoelectric response.

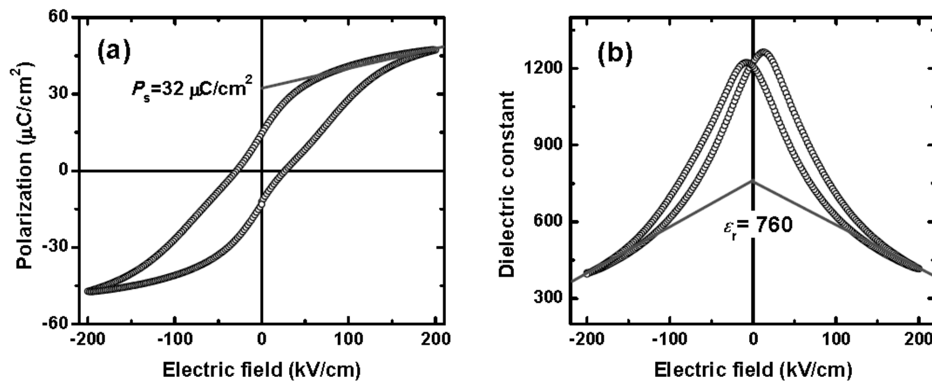

Figure 6.9: (a) Measured *P-E* loop and estimated spontaneous polarization (P_s) and (b) Measured ε-*E* curve and estimated relative dielectric constant (ε_r), of the 250-nm-thick (110)-oriented PZT thin film.

Using Eq. (6.4), the Q_{eff} coefficient of the PZT dilms as a function of film thickness is shown Fig. 6.10(b). The reduction of Q_{eff} with increasing film thickness might occur due to the substrate clamping, as discussed in detail in Ref. [14].

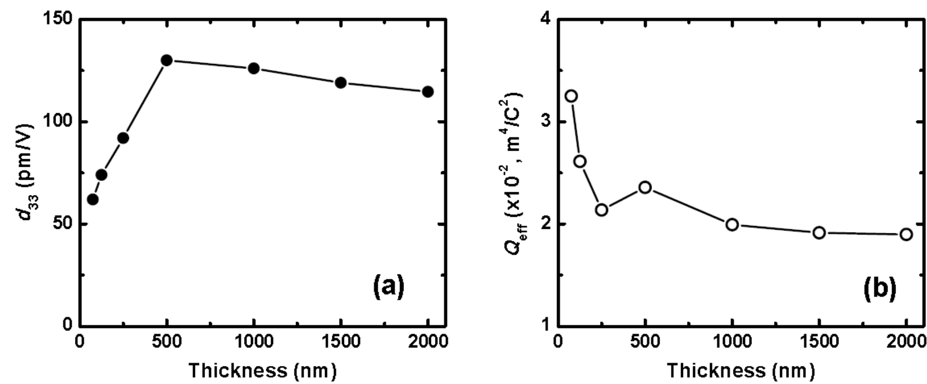

Figure 6.10: (a) d_{33} coefficients and (b) Q_{eff} coefficients, of the 250-nm-thick (110)-oriented PZT films as a function of film thickness.

6.4.2 Zr/Ti composition effects

In order to investigate the effect of composition on the piezoelectric responses, 250-nm-thick (110)-oriented PZT thin films with Zr/Ti of 60:40, 52:48, 40:60 and 20:80 were grown on SRO/YSZ/Si substrates. Figure 6.11(a) shows the piezoelectric hysteresis (d_{33}-E) loops for different compositions.

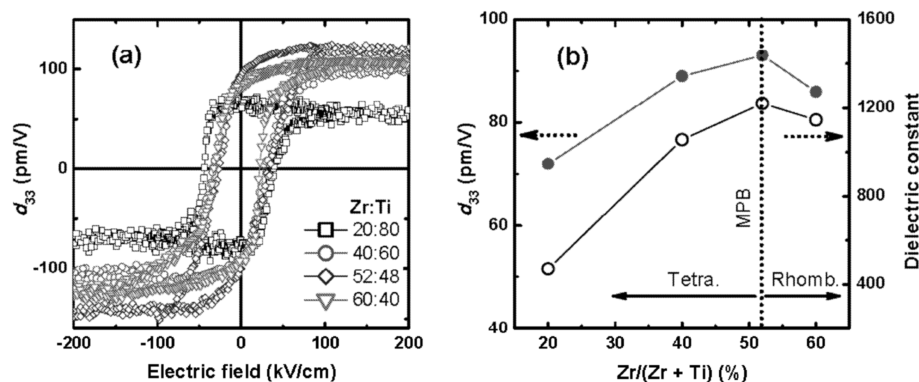

Figure 6.11: (a) Piezoelectric hysteresis loops and (b) d_{33} coefficients, of the (110)-oriented PZT thin films plotted as a function of Zr/Ti ratio.

It should be noted that measured d_{33} values are effective d_{33}, which is the d_{33} coupled to the substrate. Better squareness in d_{33}-E loops is achieved in tetragonal symmetry consistent with the P-E loops. Compositional distribution of effective piezoelectric coefficient (d_{33}) and dielectric constant (ε), extracted from Figs. 5.27(a) and 6.11(a) is plotted in Fig. 6.11(b). The composition of maximum d_{33} coefficient (= 92 pm/V) perhaps

referred to as the morphotropic phase boundary (MPB) composition, and consequently the composition of highest electromechanical activity, identical to the reported ceramic composition. The same behavior is also reported in other studies [15-17]. It is speculated that the trend in d_{33} coefficient and dielectric constant is well matched with composition (Zr/Ti ratio) and is governed by extrinsic contribution.

In Fig. 6.12(b), the Q_{eff} coefficient of PZT thin films is plotted as a function of Zr content. It is shown that, similar to bulk PZT ceramics [18], tetragonal films show consistently larger Q_{eff} than rhombohedral films.

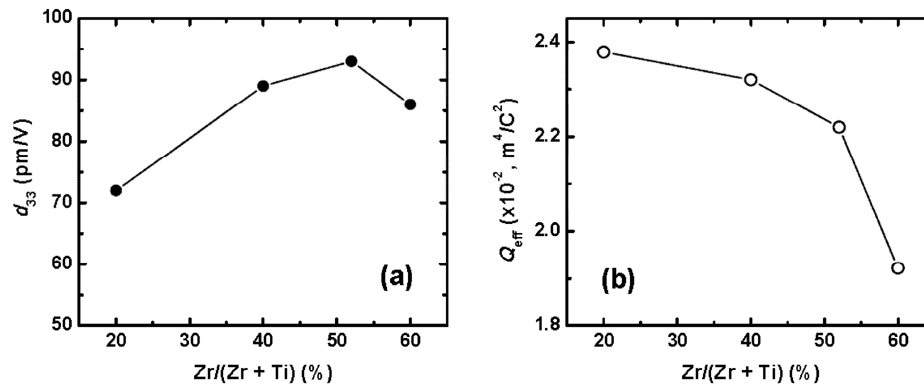

Figure 6.12: (a) d_{33} coefficients and (b) Q_{eff} coefficients, of the (110)-oriented PZT thin films plotted as a function of Zr/Ti ratio.

6.4.3 Thermal residual stress effects

As discussed in chapter 4 section 4.6, we studied the effect of residual stress on the ferroelectric properties of PZT thin films. There, the 250-nm-thick (001)-oriented PZT(52/48) thin films and SRO electrodes deposited on different substrates, such as CeO_2/YSZ/Si, STO/Si, CeO_2/YSZ, and STO. Due to different thermal expansion coefficients between the PZT film and substrate, a thermal tensile stress is induced in the PZT films grown on silicon substrates, while a thermal compressive stress is induced in the PZT films grown on YSZ and STO substrates. Tensile stress tends to cause domains originally parallel to the film surface, which results in a reduction in the polarization. In contrary, compressive stress causes the domains to orient along the longitudinal direction, which causes in an increase of the polarization.

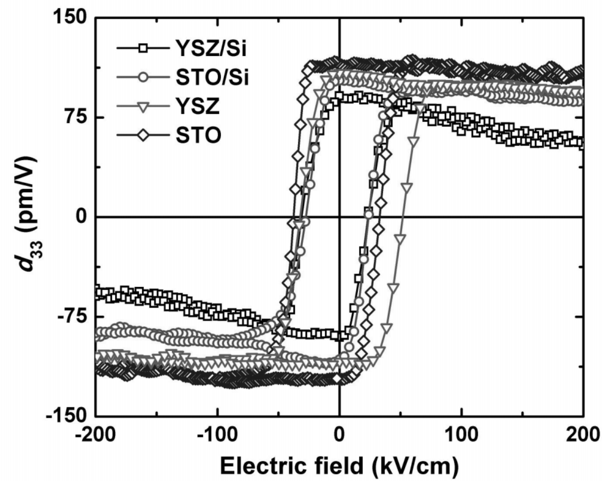

Figure 6.13: (a) Piezoelectric hysteresis loops of the 250-nm-thick (001)-oriented PZT thin films grown on SRO buffered CeO_2/YSZ/Si, STO/Si, CeO_2/YSZ and STO substrates.

In Fig. 6.13 the d_{33} hysteresis loops of PZT thin films grown on different substrates are plotted. It was confirmed that at the coercive field, the phase signal from the lock-in amplifier is reversed by 180°. The best squareness of the piezoelectric loops is obtained for the PZT film on the STO substrate, consistent with its *P-E* loop. The remnant piezoelectric coefficients (d_{33}) are obtained as 86, 98, 106, and 114 pm/V for films on SRO buffered CeO_2/YSZ/Si, STO/Si, YSZ and STO substrates, respectively. These values were close to that of other PZT thin films using LNO electrodes [9]. Results in Tab. 6.1 show that both P_r and d_{33} values of PZT thin films are improved under compressive stress; however, the change in d_{33} values is not proportional to that of the P_r values.

Table 6.1: Effect of substrate characteristics on polarization, dielectric constant, piezoelectric coefficient and electrostriction coefficient of PZT thin films.

Substrate	P_s (μC/cm^2)	ε_r	d_{33} (pm/V)	Q_{eff} ($\times 10^{-2}$) (m^4/C^2)
CeO_2/YSZ/Si	25.3	780	86	2.46
STO/Si	30.6	660	98	2.74
CeO_2/YSZ	39.5	511	106	2.96
STO	49.7	440	114	2.94
Bulk PZT ceramics			233 [19]	3.40 [20]

The Q_{eff} coefficients are given in Tab. 6.1 for PZT thin films grown on different substrates. The data indicates that the Q_{eff} coefficients of PZT thin films on YSZ and STO substrates are systematically larger than that of films on silicon substrates. This difference may be related to grain boundaries and defects in the films, in which the leakage current of films grown on silicon substrates is much larger than that of films on YSZ and STO substrates. The reduction in d_{33} and Q_{eff} coefficients of PZT thin films in comparison with bulk ceramics might be attributable to clamping from the stiff substrate.

6.5 Summary and conclusions

The dielectric and piezoelectric coefficients of PZT thin films having tetragonal, near-morphotropic phase boundary (MPB), and rhombohedral symmetries were measured. Better squareness in d_{33}-E loops was achieved in tetragonal symmetry consistent with P-E loops. The remnant d_{33} coefficients were maximized near the MPB composition, and the trend of d_{33} values strongly depends on the dielectric constant. These results indicated that the piezoelectric coefficient in the PZT thin films with composition (Zr/Ti ratio) is governed by the extrinsic (domain-walls) contribution such as that found in bulk PZT ceramics rather than the intrinsic (lattice variation) contribution. Moreover, the effective electrostriction coefficients (Q_{eff}), evaluated from the relationship between the ferroelectric properties (polarization, dielectric constant) and the piezoelectric coefficients, show consistently larger Q_{eff} values in the tetragonal films.

The piezoelectric coefficient (d_{33}) is shown to increase with increasing film thickness in the thickness range of 75 to 500 nm. This effect is attributed to the decrease in the effect of the interfacial layer between the film and the electrode with increasing film thickness. Moreover, the results also suggested that non-180° domain wall motion (extrinsic contribution) in response to the d_{33} coefficient is negligible. Therefore, the increase in d_{33} coefficient with increasing film thickness is mainly caused by the intrinsic contribution.

Lastly, we have investigated the effect of thermal residual stress on the piezoelectric properties of PZT thin films. In this study, the thermal stress in PZT thin films can be controlled by changing the substrate. Due to different thermal expansion coefficients between PZT films and substrates, thermal tensile stress induced in the PZT films grown on silicon substrates, while thermal compressive stress induced in the PZT films grown on YSZ and STO substrates. The results show that the d_{33} coefficients are improved under compressive stress.

6.6 References

1. J. Baborowski, S. Hediger, P. Muralt, and Ch. Wuetrich, *Fabrication and characterization of micromachined accelerometers based on PZT thin films*, Ferroelectrics **224** (1999) p. 283-290.
2. D. J. Laser and J. G. Santiago, *A review of micropumps*, J. Micromech. Microeng. **14** (2004) p. R35-R64.
3. K. S. Yun and E. Yoon, *Micropumps for MEMS/NEMS and Microfluidic Systems,* MEMS/NEMS Handbook Techniques and Applications, vol. 4, T. L. Cornelius (Editor), Springer-Verlag (2006) p. 121-153.
4. Y. -C. Hsu, C. -C. Wu, C. -C. Lee, G. Z. Cao, and I. Y. Shen, *Demonstration and characterization of PZT thin-film sensors and actuators for meso- and micro-structures*, Sensors and Actuators A **116** (2004) p. 369-377.
5. W. J. Choi, Y. Jeon, J. -H. Jeong, R. Sood, and S. G. Kim, *Energy harvesting MEMS device based on thin film piezoelectric cantilevers*, J. Electroceram. **17** (2006) p. 543-548.
6. Y. B. Jeon, R. Sood, J. -H. Jeong, and S. G. Kim, *MEMS power generator with transverse mode thin film PZT*, Sensors and Actuators A **122** (2005) p. 16-22.
7. K. Kanda, I. Kanno, H, Kotera and K. Wasa, *Simple Fabrication of Metal-Based Piezoelectric MEMS by Direct Deposition of $Pb(Zr, Ti)O_3$ Thin Films on Titanium Substrates*, J. Microelectromech. Syst. **18** (2009) p. 610-615.
8. L. E. Cross, *Ferroelectric ceramics: tailoring properties for specific applications*, Ferroelectric Ceramics, N. Setter and E.L. Colla (Editor), Birkhäuser, Basel, Switzerland (1993) p. 1-85.
9. R. Herdier, D. Jenkins, E. Dogheche, D. Remiens, and M. Sulc, *Laser Doppler vibrometry for evaluating the piezoelectric coefficient d_{33} on thin film*, Rev. Sci. Instrum. **77** (2006) p. 093905(1-5).
10. D. Wu, Y. Xia, A. Li, Z. Liu, and N. Ming, *Electrical properties of chemical-solution-derived $Bi_{3.54}Nd_{0.46}Ti_3O_{12}$ ferroelectric thin films*, J. Appl. Phys. **94** (2003) p. 7376-7378.
11. S. Trolier-McKinstry, N. B. Gharb, and D. Damjanovic, *Piezoelectric nonlinearity due to motion of 180° domain walls in ferroelectric materials at subcoercive fields: A dynamic poling model*, Appl. Phys. Lett. **88** (2006) p. 202901(1-3).
12. P. Yang, G. R. Burns, and M. A. Rodriguez, *Field-induced strain associated with polarization reversal in a rhombohedral ferroelectric ceramic*, J. Mater. Res. **18** (2003) p. 2869-2873.

13. H. B. Sharma, H. N. K. Sarma, and A. Mansingh, *Fatigue in sol-gel derived barium titanate films*, J. Appl. Phys. **85** (1999) p. 341-346.

14. A. L. Kholkin, Ch. Wutchrich, D. V. Taylor, and N. Setter, *Interferometric measurements of electric field-induced displacements in piezoelectric thin films*, Rev. Sci. Instrum. **67** (1996) p. 1935-1941.

15. H. D. Chen, K. R. Udayakumar, C. J. Gaskey, and L. E. Cross, *Electrical properties' maxima in thin films of the lead zirconate-lead titanate solid solution system*, Appl. Phys. Lett. **67** (1995) p. 3411-3413.

16. S. -H. Kim, J. -S. Yang, C. Y. Koo, J. -H. Yeom, E. Yoon, C. S. Hwang, J. -S. Park, S. -G. Kang, D. -J. Kim, and J. Ha, *Dielectric and electromechanical properties of $Pb(Zr,Ti)O_3$ thin films for piezo-microelectromechanical system devices*, Jpn. J. Appl. Phys. **42** (2003) p. 5952-5955.

17. R. A. Wolf and S. Trolier-McKinstry, *Temperature dependence of the piezoelectric response in lead zirconate titanate films*, J. Appl. Phys. **95** (2004) p. 1397-1406.

18. M. J. Haun, Z. Q. Zhuang, E. Furman, S. -J. Jang, and L. E. Cross, *Electrostrictive Properties of the lead Zirconate Titanate Solid-Solution System*, J. Am. Ceram. Soc. **72** (1989) p. 1140-1144.

19. D. A. Berhncourt, C. Cmolik, and H. Jaffe, *Piezoelectric properties of polycrystalline lead titanate zirconate compositions*, PROC. IRE, vol. 48 (1960) p. 220-229.

20. Q. M. Zhang, W. Y. Pan, S. J. Jang, and L E. Cross, *Domain wall excitations and their contributions to the weak-signal response of doped lead zirconate titanate ceramics*, J. Appl. Phys. **64** (1988) p. 6445-6451.

7.
Integration of epitaxial PZT films onto silicon cantilever beams

Abstract. This chapter reports on the piezoelectric-MEMS micro-fabrication process and the behavior of piezoelectric stacks actuated silicon cantilevers. All oxide layers in the piezoelectric stacks, such as buffer-layer/bottom-electrode/film/top-electrode: YSZ/$SrRuO_3$/Pb(Zr,Ti)O_3/$SrRuO_3$, were grown epitaxially on the Si template of the SOI substrates by pulsed laser deposition (PLD). By using an analytical model and finite element simulation, the initial bending of the cantilevers was calculated. These theoretical analyses are in good agreement with the experiment results which were determined using white light interferometry. The dependences of the cantilever displacement, resonance frequency and quality factor on the cantilever geometry have been investigated using laser-Doppler vibrometry. The cantilever displacement ranged from 0.03 to 0.42 μm/V, whereas the resonance frequency and quality factors values changed from 1010 to 18.6 kHz and 614 to 174, respectively, as the cantilever length increased from 100 to 800 μm. Furthermore, the effect of the conductive-oxide electrodes on the stability of the piezoelectric displacement of the cantilevers has also been studied.

7.1 Introduction

Devices utilizing piezoelectric microelectromechanical systems (pMEMS) have many current applications such as AFM cantilevers [1], accelerometers [2], micropumps [3, 4], and biosensors [5]. To improve the actuation or sensing characteristics of such devices, piezoelectric thin films can be used. The high ferroelectric and piezoelectric properties of lead zirconate titanate (PZT) make it the most used piezoelectric material over other piezoelectric materials such as aluminum nitride (AlN) and zinc oxide (ZnO) [6, 7]. In this chapter, we present the integration of piezoelectric PZT thin films deposited by pulsed laser deposition (PLD) onto silicon-based cantilevers.

Next to piezo-mechanical properties, the stability of the polarization of piezoelectric devices is a major problem which limits the devices lifetime. Platinum (Pt) is the commonly used electrode material for PZT based piezoelectric transducers. However, it has been shown in literature that using a Pt electrode with PZT film causes a decrease in the saturation and remnant polarization values with increasing switching cycles. This decrease is known as fatigue [8-10]. Fatigue characteristics in the PZT films can be explained by the accumulation of oxygen vacancies at the electrode/film interface which inhibits the domain switching [11], and the formation of an interface layer that can reduce the effective electric field applied across the capacitor [12]. Metallic-oxide electrodes, such as $SrRuO_3$ [13, 14] and $LaNiO_3$ [15, 16], are known to reduce the polarization fatigue, through compensation of the oxygen vacancies at the electrode-PZT interface by changing their oxygen nonstoichiometry.

Cantilever beams are the most ubiquitous structures in the field of MEMS. MEMS cantilevers are commonly fabricated from silicon (Si), or silicon nitride (Si_3N_4). The fabrication process typically involves undercutting the cantilever structure to release it, often with an anisotropic wet or reactive ion etching (RIE) technique. A large number of research groups are attempting to develop cantilever arrays as biosensors for medical diagnostic applications [5].

In this work, the properties of microcantilevers fabricated on SOI wafer with PZT thin film transducers are presented. Thin film piezoelectric transducers were fabricated by pulsed laser deposition (PLD) of yttria-stabilized zirconia (8YSZ) buffer layer, strontium ruthenate (SRO: $SrRuO_3$) bottom electrode, $Pb(Zr_{0.52}Ti_{0.48})O_3$ (PZT) piezoelectric layer and SRO top electrode. The YSZ buffer-layer provides good electrical insulation between the Si substrate and the bottom electrode with a relative dielectric constant of ~30. Because of the high chemical stability, this buffer-layer is employed to prevent the diffusion of lead into silicon substrate. Furthermore, it also acts as a crystallization template for the piezoelectric stack allowing epitaxial layer growth.

In section 7.2 the deposition of the piezoelectric stack, cantilever fabrication and measurement techniques are described. In section 7.4 the effect of thermal residual stress,

induced by the thermal expansion coefficient mismatch between film and substrate, on the cantilever initial bending was obtained from experiment and theoretical analyses (simulation and calculation). Furthermore, the dependence of the electromechanical and mechanical resonance properties on the cantilever geometry was also discussed in section 7.5. The effects of film thickness and conductive-oxide electrode on the displacement of the cantilevers were investigated in section 7.6 and 7.7, respectively.

7.2. Cantilever fabrication and experimental methods

7.2.1 Deposition of multilayer piezoelectric stack

Figure 7.1 shows flowchart of the piezoelectric PZT cantilever fabrication process. Devices were fabricated on a (100) SOI wafer with a 5 μm-thick silicon layer and a 2 μm-thick SiO_2 buried oxide (BOX) layer, as shown in Fig. 7.1(F1). The silicon-membrane was fabricated using deep reactive-ion etching (DRIE) from the backside of the wafer. The BOX layer that acts as an etch stop in DRIE process is then removed by buffered-hydrofluoric acid (BHF) (Fig. 7.1(F2)). The resulting thickness of the Si-membrane is 5 μm. Then, the pre-patterned SOI wafer was cut into substrates with dimensions of 20×20 mm^2. It is known as the pre-patterned SOI substrate.

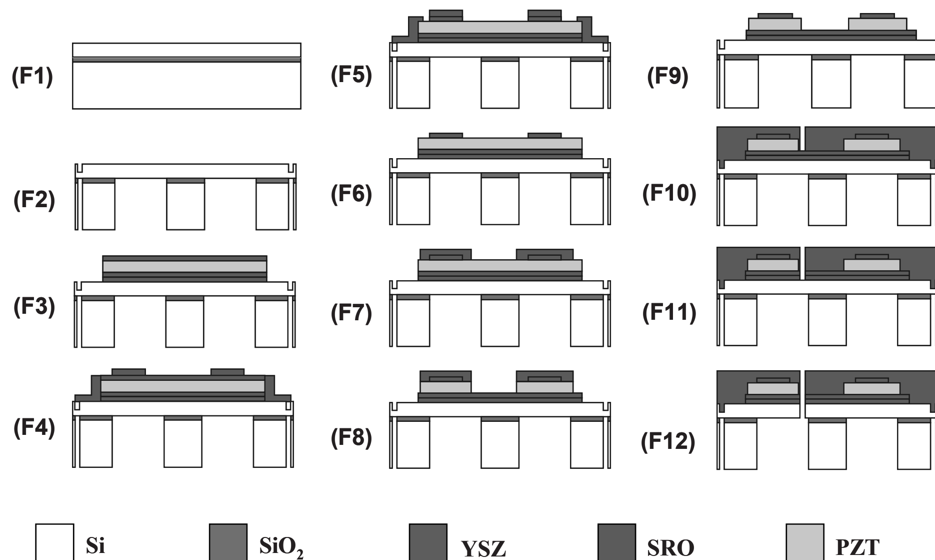

Figure 7.1: Fabrication process of the piezoelectric PZT films on pre-patterned SOI substrates.

The deposition of a multilayer SRO/PZT/SRO/YSZ began with the deposition of a 100 nm-thick YSZ buffer-layer on top of the SOI to act as a barrier layer against lead diffusion during PZT deposition. Next, a 100 nm-thick SRO electrode and a 1 μm-thick PZT layer were deposited. Deposition of the piezoelectric stack is completed with a 100 nm-thick SRO top electrode layer deposition (Fig. 7.1(F3)). All layers in the piezoelectric stack were deposited by pulsed laser deposition. Details of the deposition conditions of the multilayer stack are published previously [17] and can be seen in Tab. 7.1.

Table 7.1: Deposition conditions of piezoelectric stack in the cantilevers.

Parameter(s)	YSZ buffer layer	SRO bottom electrode	PZT layer	SRO top electrode
Temperature (^oC)	800	600	600	600
Pressure (mbar/gas)	0.020 Ar/0.021 O_2	0.13 O_2	0.1 O_2	0.13 O_2
Fluence (J/cm^2)	2.1	2.5	3.5	2.5
Spot-size (mm^2)	3.35	1.9	3	1.9
Thickness (μm)	0.1	0.1	1	0.1

7.2.2 Cantilever fabrication

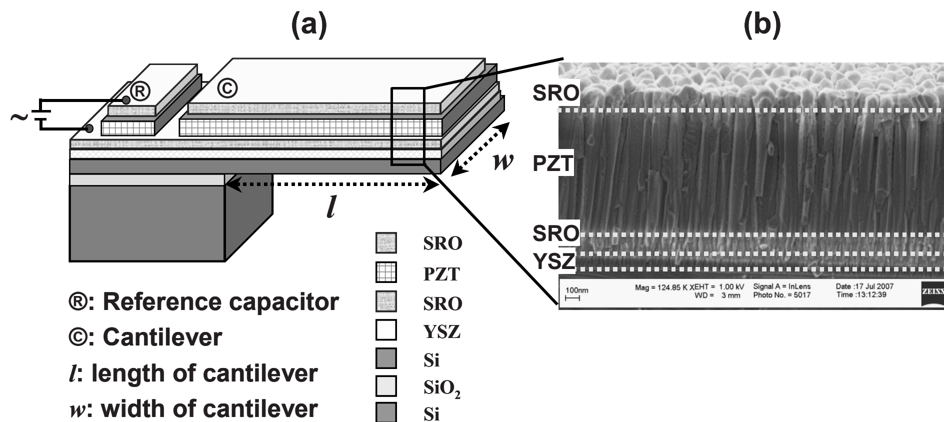

Figure 7.2: (a) Three-dimensional schematic concept, and (b) Cross-sectional scanning electron microscopy (SEM) of a PZT cantilever.

Figures 7.1(F4) - 7.1(F12) show the fabrication of piezoelectric cantilevers by the MEMS microfabrication process, including photolithography and etching. First, the top SRO layer was etched by Ar-ion beam-etching (steps F4-F5). Next, the PZT film was removed by sequential wet-etching with *HF* and *HCl* solutions (steps F7-F8). Then, the bottom SRO

electrode and YSZ buffer-layer were also Ar-ion beam etched (steps F10-F11). Finally, the release etch for forming the cantilever (step F12) was performed by a deep reactive-ion etching (DRIE) using a mixture of SF_6, O_2 and C_4F_8 gases. The final structure of the cantilevers is depicted in Fig. 7.2.

7.2.3 Characterization methods

The polarization hysteresis (*P-E*) loop was measured at ±200 kV/cm amplitude and 1 kHz frequency, using a ferroelectric film test system (TF 2000 Analyzer). A Süss MicroTech PM300 manual probe-station equipped with Keithley 4200 Semiconductor characterization system is used for the capacitance measurement. The capacitance-electric field (*C-E*) curve was performed using an *ac* signal of 1 kV/cm and 10 kHz frequency with the *dc* bias sweeping from -200 to +200 kV/cm and then back to -200 kV/cm. The corresponding dielectric constant was calculated from this *C-E* curve.

The cross-section of the film was observed by a high-resolution scanning electron microscopy (HRSEM, Zeiss LEO 1550) and used to define the film thickness, as well as the microstructural properties of PZT films.

The Polytech MSA-400 Micro System Analyzer is used for the analysis and visualization of structural vibration and surface topography in microstructures such as cantilevers and MEMS devices in general. Fully integrating a microscope with a scanning laser Doppler vibrometry (LDV) and a white-light interferometer allows for the measurements of the actuation and initial bending of the cantilevers, respectively. A schematic diagram of the measurement system using a LDV is shown in ref. [18].

7.3 Structure and ferroelectric properties of cantilevers

Figure 7.2(b) shows a cross-sectional view of a cantilever structure. A 1 μm-thick PZT layer was deposited between two conductive-oxide electrodes on a silicon cantilever as the active material. The columnar-structure with a uniform thickness and an average columnar-width of 60-70 nm was observed by cross-sectional scanning electron microscopy (SEM). The x-ray diffraction (XRD) scan showed that piezoelectric stack on the cantilevers have (110)-preferential orientation. The epitaxial growth of PZT films on silicon has been investigated in section 3.4, chapter 3. The ferroelectric properties for the PZT film cantilevers were characterized using polarization and dielectric constant measurements, as shown in Fig. 7.3. The remnant polarization P_r was measured to be 20.4 μC/cm^2 and the coercive field E_c was 36 kV/cm. The dielectric constant calculated from the capacitance measurement is 1360 (at $E_{applied}$ = 0 kV/cm).

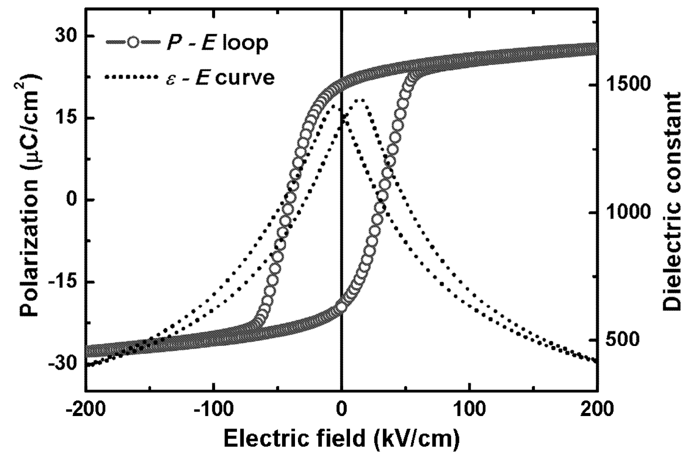

Figure 7.3: Polarization hysteresis (*P-E*) loop and dielectric constant (*ε-E*) curve for the PZT film cantilever after device fabrication. The *P-E* loop was done at ±200 kV/cm amplitude and 1 kHz frequency while the dielectric constant curve was measured at 1 kV/cm and 10 kHz frequency.

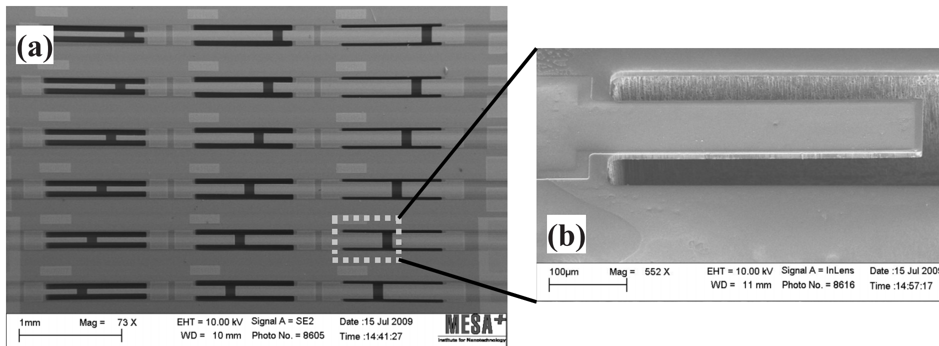

Figure 7.4: (a) SEM images of the fabricated microcantilever arrays with dimensions of 100-800 μm in length and 50-150 μm in width, and (b) Image of a fabricated cantilever beam consisting of PZT layer on SOI substrates. Both bottom-electrode and a PZT layer have the exact dimensions as the supporting Si beam, while the top-electrode has a 10 μm overlay offset.

The scanning electron microscopy (SEM) image of piezoelectric PZT film cantilever arrays is given in Fig. 7.4. The measured dimensions of the device are listed in Tab. 7.2. Both the width and the length of the cantilevers were uniform and consistent with the designed patterns. Figure 7.4(b) provides the detail top-view of the cantilever with 400 μm in length and 100 μm in width.

Table 7.2: Cantilevers dimensions.

Thickness, *t*:	μm
Si anchor	500 ± 25
SiO_2 (anchor)	2 ± 0.1
Si beam	5 ± 0.5
YSZ buffer-layer	0.1
$SrRuO_3$ bottom-electrode	0.1
$PbZr_{0.52}Ti_{0.48}O_3$ layer	1
$SrRuO_3$ top-electrode	0.1
Length, *L* (μm):	100-800
Width, *w* (μm):	50-150

7.4 Initial bending of cantilevers

In general, ferroelectric cantilevers consist of various layers with a certain amount of a residual stress that may cause initial bending. Residual stress originates from the mismatch in the thermal expansion coefficients of the materials, lattice mismatch in epitaxial relation, orientation change and phase transition during thin film growth. The residual stress within the individual layers causes a stress gradient in the cantilever, the whole structure will bend upwards or downwards depending on the sign of the stress gradient. Because the coefficient of thermal expansion for the Si (4.4×10^{-6} K^{-1} [19]) substrate is smaller than the PZT film (6.0×10^{-6} K^{-1} [20, 21]), the thermal tensile stress is developed in the PZT film during the cooling process from the deposition temperature to room temperature. Figure 7.5 shows the schematic of the bending of the wafer and cantilever for a PZT thin film under the tensile stress.

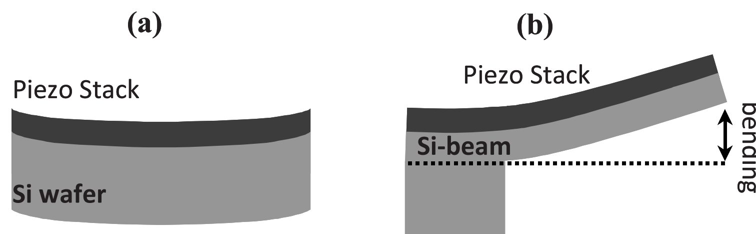

Figure 7.5. Schematic of the bending of the wafer (a) and cantilever (b).

The residual stress-induced initial bending (b_0) of the fabricated cantilevers was calculated from the analytical solution using Eq. (7.1) [22]:

$$b_0 = r[1-\cos(\frac{L}{r})] \approx \frac{L^2}{2r} \quad (7.1)$$

where L is the length of cantilever and r is radius of the curvature, 1-cos(L/r) ≈ $L^2/2r^2$ due to $L << r$. r is calculated using Eq. (7.2) [23]. In our case the width of the Si cantilever beam and the PZT film is identical. The difference in thermal expansion coefficients of silicon and PZT causes strain in the materials during cooling from the deposition temperature to the room temperature.

$$\frac{1}{r}=\frac{6t_S t_P(t_S+t_P)[\sigma_P E_S-\sigma_S E_P]}{(E_S t_S^2)^2+(E_P t_P^2)^2+2E_S E_P t_S t_P(2t_S^2+3t_S t_P+2t_P^2)} \quad (7.2)$$

where E, σ and t are the elastic modulus, residual stress and thickness, respectively. The subscripts S and P represent silicon cantilever and PZT film, respectively.

Table 7.3: Material properties and geometrical dimensions used in the numerical simulation and calculation of PZT cantilevers.

	Silicon	PZT
Elastic modulus, E (GPa)	169.8 [24]	200 [25, 26]
Residual stress, σ (MPa)	30 [27]	113 [28]
Density, ρ (kg/m^3)	2330 [29]	7700 [30]
Thickness, t (μm)	5	1
Thermal expansion (10^{-6} K^{-1})	4.4	6.0
Length, L (μm)	100-800	
Width, w (μm)	50-150	

Experimentally, an initial bending of the cantilever which represents a deflection of about 4.0 μm for a 400 μm-long cantilever was observed as shown in Fig. 7.6(a). This initial bending is due to the stress induced during the fabrication process. For comparison, a finite element simulation of the piezoelectric cantilever was carried out using the INTELLISUITE software package as shown in Fig. 7.6(b). The measured and simulated initial-bending as a function of position along length are plotted in Fig. 7.6(c). It is shown that the experimental results closely correspond with the simulated values. The values of elastic modulus, residual stress and density of silicon and PZT used in the simulations and calculations were taken from the published literature and are listed in Tab. 7.3. The elastic modulus of PZT varies from 25 to 260 GPa as quoted in literature [31, 32] and it seems that a higher value of the elastic modulus of PZT is more appropriate for the designed values of the cantilever as observed from Figs. 7.6(c) and 7.7. In the PZT cantilevers, the thickness of the buffer-layer and electrodes is an order-of-magnitude thinner than that of the PZT film and the Si beam. Consequently, the effect of the buffer-layer and electrode can be ignored in the simulation and calculation.

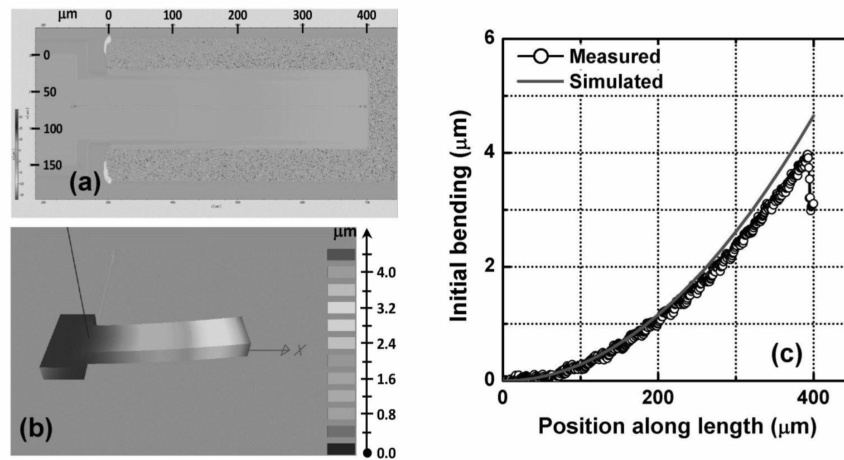

Figure 7.6: Experimental initial bending determined by the laser white-light interferometer, and FEA simulation of the cantilever: (a) Experiment and (b) Simulation of initial bending for 400 µm-long cantilever; (c) The cantilever initial bending as a function of position along the length of cantilever.

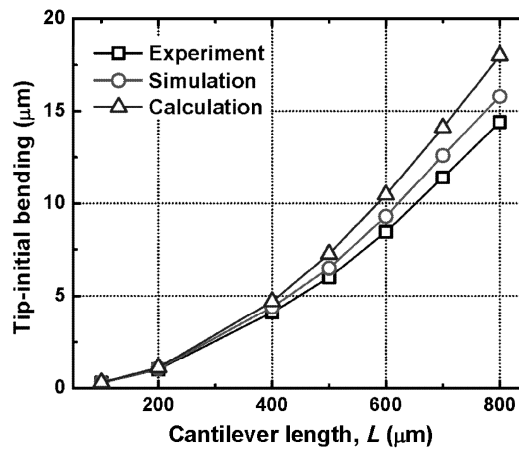

Figure 7.7: Relationship between cantilever length and tip-initial bending (experiment, simulation and calculation).

The tip-initial bending values of the cantilevers with lengths ranging from 100 to 800 µm are plotted in Fig. 7.7. The initial-bending/cantilever-length ratio increased from 0.003 to 0.018 with the cantilever length in the range of 100-800 µm. It is indicated that, moreover, the experiment results are in good agreement with the results obtained from the simulation and the calculation. However, the difference between the simulated and

calculated values of the initial bending is about 10%. The reason for the deviation is that the analytical model of Eq. (7.2) assumes infinite cantilever width, whereas the simulation is fully three-dimensional. Therefore, these simulations and calculations can be used to optimize the geometric design and to predict the cantilever performance.

7.5 Dynamic behavior of cantilevers

Electromechanical behavior

The LDV technique was used to measure the electromechanical behavior (displacement) of a cantilever actuated with a sinusoidal voltage. Cantilever displacement was measured at 6 $V_{p\text{-}p}$ amplitude and 8 kHz frequency (well below resonance frequency). Figures 7.8(a)-7.8(b) show a typical piezoelectric vibration response of a cantilever with 400 μm in length and 100 μm in width. The laser scanning area covered both the top electrode and the surrounding PZT film. The effect of the actuation amplitude on the 400 μm-long cantilever was evaluated by applying a sine wave signal of an *ac*-voltage between 2 and 12 $V_{p\text{-}p}$ (peak-to-peak) at a frequency of 8 kHz. Results shown in Fig. 7.8(c) indicate that the tip-displacement was proportional to the applied voltage for both upward and downward bending.

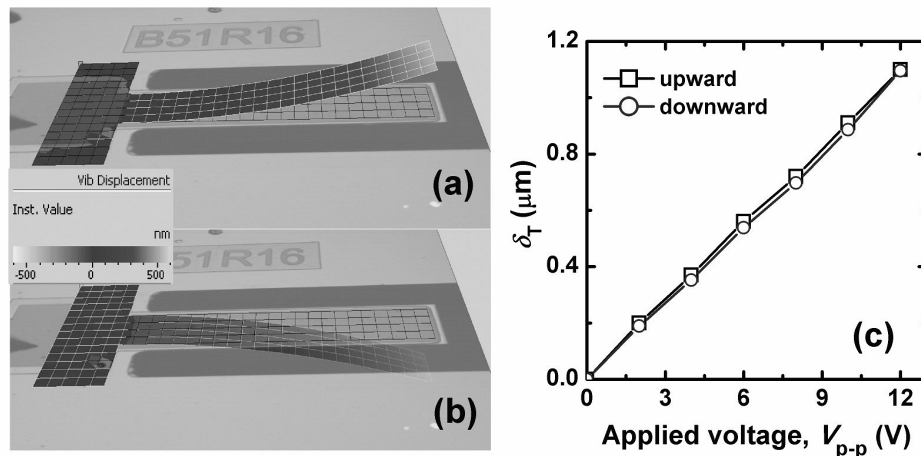

Figure 7.8: Displacement of the 400 μm-long and 100 μm-width cantilever at 6 $V_{p\text{-}p}$ amplitude and 8 kHz frequency: (a) upward and (b) downward responses of the cantilevers; (c) Tip-displacement as a function of applied voltage at 8 kHz.

The cantilever bending displacement as a function of position along the length of the cantilever is shown in Fig. 7.9(a), the fixed end of the cantilever is at position 0 in the figure. The upward tip-displacement is found to be 0.54 μm. The relationship between

displacement (δ) and position along length (x) of this cantilever was found to follow the theoretical quadratic equation: $\delta = c.x^2$ precisely, with $c=3.3\times10^{-6}$ μm^{-1} as shown in the inset of Fig. 7.9(a). The displacement profile along the width of the cantilever, as shown in Fig. 7.9(b), is almost a straight line. The results of the displacement profile show that the bending shape of cantilever is nearly cylindrical, and only the bending along the length is significant.

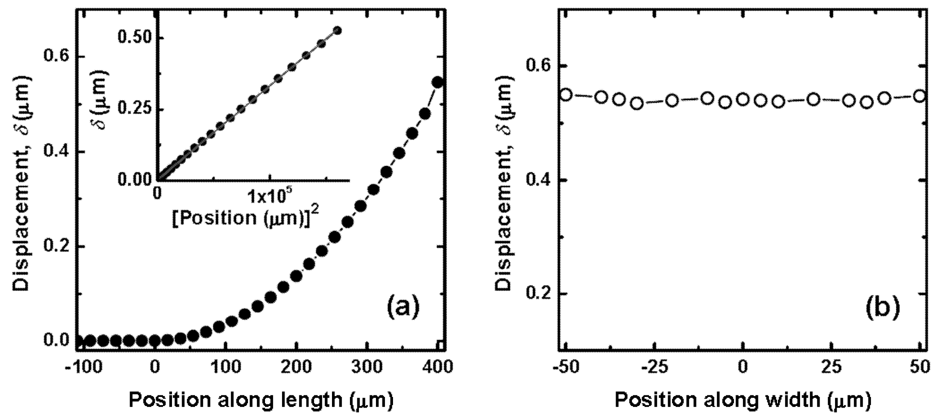

Figure 7.9: The measured displacement configurations of the surface cantilever with length L = 400 μm and width w = 100 μm: (a) upward displacement along beam length at the middle of the beam and (b) upward displacement along beam width at the free end (tip) of the cantilever.

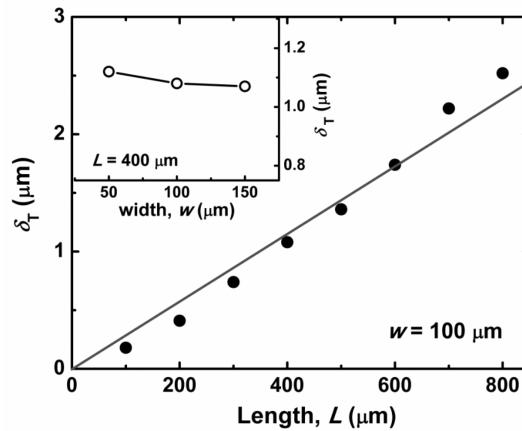

Figure 7.10: Plot of the tip-displacement (δ_T) versus length for the 100 μm-wide cantilevers. Inset figure shows the tip displacement for varying widths of the 400 μm-long cantilevers. The measurement was done at 6 V_{p-p} amplitude and 8 kHz frequency.

To investigate the effect of cantilever geometry on the cantilever displacement, the measured tip-displacements for PZT cantilevers with various lengths and widths are illustrated in Fig. 7.10. Tip-displacement (δ_T) increases from 0.2 to 2.56 μm when the length in the range of 100 to 800 μm for the 100 μm-width cantilevers, while δ_T changes slightly from 1.12 to 1.05 μm when the width increases from 50 to 150 μm for the 400 μm-long cantilevers. The measured results indicate that the length is the critical factor in determining the displacement of the cantilever since it has the largest effect on the displacement.

In contrast to the observations of Figs. 7.7 and 7.9, the relation between tip displacement and length, as shown in Fig. 7.10, is almost linear. This is in disagreement with the simple theory of Eqs. (7.1) and (7.2), which predicts a constant radius of curvature, so for small L/r a quadratic dependence on length. We should take into account that the measurements were taken at 8 kHz. If this value is getting close to resonance, some amplification of vibration is to be expected. The effect will however be most prominent for the longer cantilevers, with the lowest resonance frequency. This will cause an increase of tip displacement with length, which is contrary to what we observe. On basis of Eq. (7.1) we can only conclude that strain induced by the piezoelectric layer decreases with cantilever length. The origin could be electronic, since the leakage current of the PZT stack increases with increasing cantilever length. Or the reason could lie in a deterioration of piezoelectric properties as cantilever length increases.

Mechanical resonance behavior

To evaluate the performance of cantilever beams as sensors and actuators, oscillation characteristics were measured as a function of frequency. LDV was used for the measurement of resonance frequency. In this measurement, the *ac* sine-wave of 0.1 $V_{p\text{-}p}$ superimposed with a *dc* voltage of 0.2 V was applied to the actuation top-electrode while the bottom-electrode was grounded. Figure 7.11 shows the resonance peaks obtained on the experimental cantilever array in a frequency range of 10 kHz to 2 MHz. The resonance frequency decreases with an increase in the cantilever length, as shown in Fig. 12(a). For a piezoelectric cantilever of length L, the first resonance frequency (f_r) is written as [33, 34]:

$$f_r = 0.161 \frac{t_{cant}}{L^2} \sqrt{\frac{E_{cant}}{\rho_{cant}}} \tag{7.3}$$

The thickness of cantilever is represented by t_{cant} (= t_S + t_P). E_{cant} (= $(E_S t_S + E_P t_P)/t_{cant}$) and ρ_{cant} (= $(\rho_S t_S + \rho_P t_P)/t_{cant}$) indicate the elastic modulus and density of the cantilever, respectively. In these equations, the elastic modulus (E) and density (ρ) of the cantilever are calculated using the mixing rule [35].

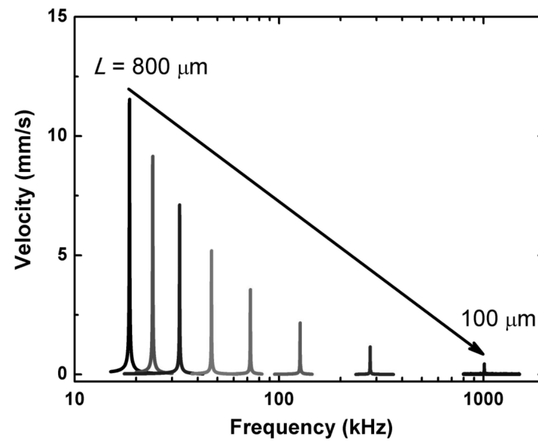

Figure 7.11: First-mode resonance frequency peaks for varying lengths (100-800 μm) of the 100 μm-wide cantilevers.

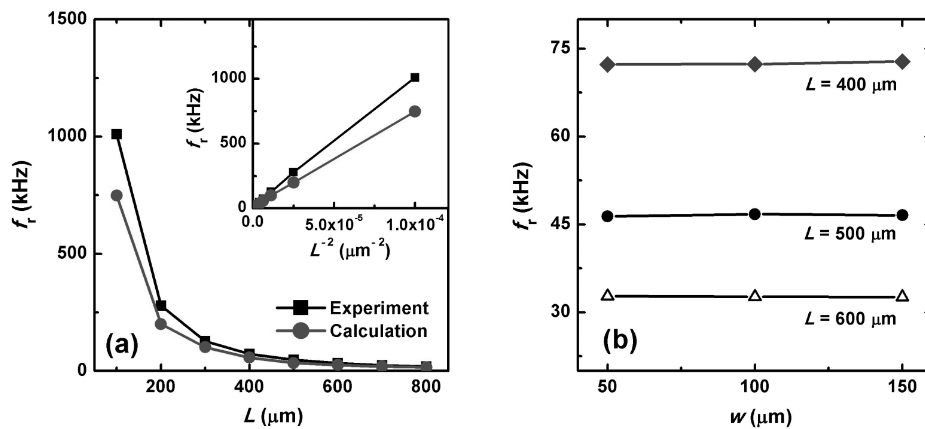

Figure 7.12: First-mode resonance frequency as a function of (a) the cantilever length (*L*) and (b) the cantilever width (*w*). The resonance frequency for each cantilever obeys the theoretical equation. The inset shows the first mode resonance frequencies are inversely proportional to the square of the length of the cantilevers.

Giving the cantilever thickness, the elastic modulus and density profile in the thickness direction and according to Eq. (7.3), the resonance frequency is expected to increase with a decreasing cantilever length as L^{-2}. In Fig. 7.12(a), we plot the first-mode resonance frequency as a function of the cantilever length. The squares represent the measured resonance frequencies, whereas the circles represent the calculated frequecies obtained

using Eq. (7.3). As expected, the resonance frequency of the cantilever is inversely proportional to L^2, as shown in the inset of Fig. 7.12(a). It was observed that, when the cantilever length is longer than 400 μm, the measured resonance frequencies are closed to the theoretical values; while for the shorter cantilevers, a deviation was observed. Furthermore, according to the Eq. (7.3), the resonance frequency of the cantilever does not depend on the cantilever width. The data presented in Fig. 7.12(b) shows that the relation between the measured resonance frequencies and the width of the cantilever beam is almost independent.

As discussed above, the static and dynamic behaviors of the cantilevers have been described via the deflection and vibration characteristics. Static behavior is used for determining the surface stress in the piezoelectric stack or the performance of the cantilever sensors, whereas the dynamic behavior is used as microbalance or determining the additional mass adsorbed onto the functionalized surface of the cantilever. Using dynamic behavior, mass changes in the picogram range can be observed [36, 37]. In dynamic behavior, the cantilevers are excited to its fundamental resonance frequency. The adsorbed molecules increase the mass of the cantilever and cause a corresponding decrease in resonance frequency. Changes in cantilever resonance frequency provide a direct measure of the adsorbed molecules mass if the spring constant (k) remains fixed. The change in mass in relation to the change in resonance frequency is given as [37]:

$$\Delta m = \frac{k}{4\pi^2}\left(\frac{f_0^{\,2} - f_m^{\,2}}{f_0^{\,2} f_m^{\,2}}\right) \tag{7.4}$$

where Δm is the mass added to the cantilever, and f_0 and f_m are the fundamental resonant frequencies before and after the mass addition. It is readily observed from equation (7.4) that the higher fundamental resonance frequency will lead to higher cantilever sensitivity in measuring the mass change. Therefore, for improving the cantilever sensitivity, a high resonance frequency is required.

A parameter, which is used extensively in characterizing the mechanical response of the microcantilevers, is the quality factor (Q-factor)). The resolving quality of the resonance curve can be expressed as a Q-factor [38, 39]:

$$Q = 2\pi \frac{E_{\max}}{E_{lost}} = \frac{f_r}{\Delta f} \tag{7.5}$$

where E_{max} is the maximum energy stored, E_{lost} is the total energy lost in a period, f_r is the resonance frequency and Δf is the full-width-at-half-maximum (FWHM) of the resonance curve. A higher Q-factor cantilever generally has a higher displacement at the resonance frequency and improves sensor performance.

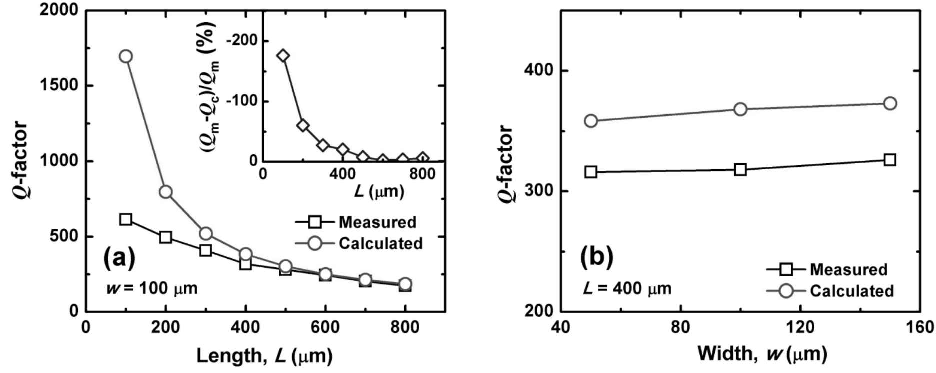

Figure 7.13: *Q*-factor (mode 1) of the cantilevers (a) with width of 100 μm and as a function of the cantilever length, and (b) with length of 400 μm and as a function of the cantilever width. The inset shows the different values, $(Q_m\text{-}Q_c)/Q_m$, between the measured (Q_m) and the calculated (Q_c) *Q*-factors as the function of the cantilever length.

The relationship between the *Q*-factor at first vibration mode and the cantilever length is illustrated in Fig. 7.13. Clearly, shorter cantilever length will contribute to larger cantilever *Q*-factor. As was mentioned above, a large *Q*-factor is an important consideration when optimizing the system level response of a resonance frequency device. An excellent *Q*-factor as high as 614 was obtained for the cantilever when *L* was 100 μm. The *Q*-factor, however, is almost independent of the cantilever width, as shown in Fig. 13(b).

Under atmospheric pressure conditions, air damping is believed to be the most important energy dissipation mechanism in the cantilever. Accurate models and approaches for the prediction of air damping are therefore very important to the design of high-performance resonating cantilevers. According to the oscillating sphere model in viscous fluid, the influence of air damping on the *Q*-factor of a cantilever at the first resonance frequency is estimated as [34]:

$$Q = 0.161 \frac{wt_{cant}^2}{3L} \frac{1}{R(1+R/t_b)\mu} \sqrt{\rho_{cant} E_{cant}} \tag{7.6}$$

where *R* ($\cong \sqrt{wL/\pi}$) is the radius of the oscillating sphere, μ is the viscosity of surrounding air, and t_b is the thickness of the boundary layer which vibrates perpendicular to the direction of the motion with frequency f_r. t_b is calculated as follows:

$$t_b = \sqrt{\frac{\mu}{\pi \rho_a f_r}} \tag{7.7}$$

with ρ_a is the density of surrounding air. Under atmospheric pressure conditions, μ = 1.82×10^{-5} Pa.s and ρ_a = 1.205 kg/m^3 [40].

Figure 13 also shows the calculated *Q*-factors from Eq. (7.6), compared to the measured values. As shown in Fig. 7.13(a), for cantilevers with L > 500 μm, the calculated and measured *Q*-factor values are almost similar. However, deviations from this relationship were found when L < 500 μm, in which the different ratios between the measured and calculated *Q*-factor values increased with decreasing cantilever length (Fig 7.13(a) *inset*). The change in the different ratio, in this study, may be related to the PZT film cantilever itself. A possible reason of the low measured *Q*-factors for the shorter cantilevers, as compared to the calculated values, may be by the surface loss mechanism [41].

By using the above technique, the resonance frequency of a 800 μm-long cantilever is also investigated. Figure 14 shows the frequency spectrum of the cantilever excited by a signal of 0.1 V_{p-p} with frequencies between 10 kHz and 2 MHz. The first four modes are found to be are 18.7, 115.8, 323.5 and 632.6 kHz. The insets of Fig. 14 illustrate the corresponding modal shapes obtained using the laser scanning.

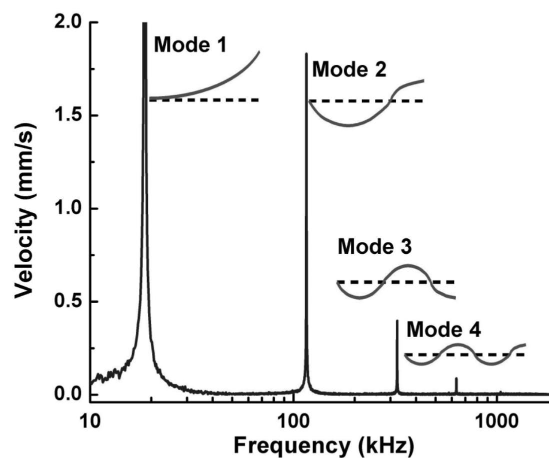

Figure 14: Typical frequency response of a cantilever with 800 μm in length and 100 μm in width. The corresponding modal shapes are shown in the insets.

Figure 7.15(a) shows the *Q*-factor dependence on cantilever length at different resonance modes. Clearly, the *Q*-factors of the cantilevers increased at the second, third, and fourth for 400 μm, 600 μm, and 800 μm-long cantilevers, respectively, and then decreased at higher resonance modes. The decrease of *Q*-factors at their resonance modes can be explained by the energy dissipation from support loss. The support loss *Q* factor Q_{sup} of the cantilever can be calculated as [42]:

$$Q_{\text{sup}} = \beta \left(\frac{L}{t} \right)^3 \tag{7.8}$$

In which the coefficient β decreases with the increase of resonance mode due to the larger vibration amplitude near the substrate. Furthermore, the *Q*-factors of the shorter cantilevers, at the first and second modes, are also higher than those of the longer ones.

The observed *Q*-factor variation can be described by frequency dependence, where higher resonance frequency of a mode implies a higher *Q*-factor of that mode (Fig. 7.15(b)). The *Q*-factors for resonance frequencies below 500 kHz appear to be linearly dependent on resonance frequency (dotted line). For frequencies above 500 kHz, however, the apparent *Q*-factor of 520 is assumed to be the maximum quality factor.

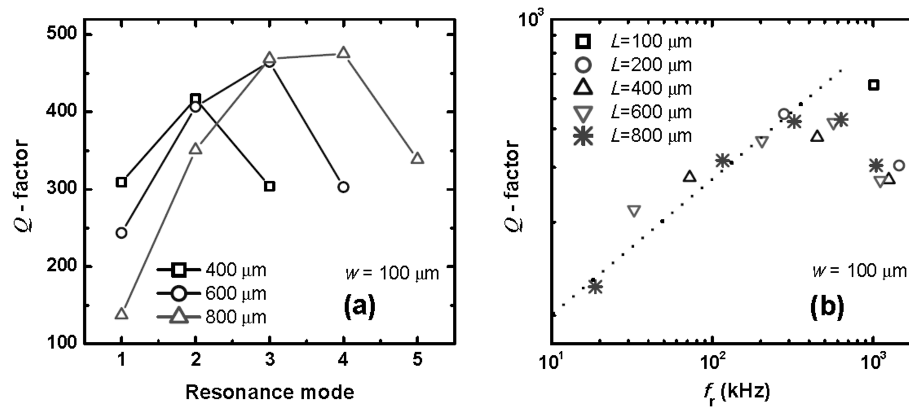

Figure 7.15: (a) *Q*-factor dependence on resonance mode and cantilever length, and (b) *Q*-factors of all measured flexural modes for each of the length of the cantilevers, graphed as a function of the resonance frequency, of the modes for a width of 100 μm.

The almost linear dependence between the *Q*-factors and the resonance frequencies is also studied by Blom *et al*. [34] and Lévêque *et al*. [43]. In their studies, they derived an expression for the *Q*-factor caused by air damping, which is applicable for the cantilevers at pressures of approximately 25 Pa and/or below.

7.6 Effect of film thickness and gold-layer coating

In the development of biosensors based on piezoelectric cantilever for application in biology, healthcare, and food technology, the cantilever surface must be coated with a functionalized layer for adsorption of specific chemical compounds. Adsorbed molecules will add to the mass of the cantilever and thereby cause a change in the resonance frequency which can be detected. For mass-detection applications, a gold-layer coating on

the cantilever is frequently utilized. The use of gold is due to the large selection materials that can be adsorbed by means of thiol chemistry as described in recent studies by Ziegler [44] and Ramos *et al*. [45]. The structure of the cantilever is depicted in Fig. 7.16 with a gold-layer coating on top of the cantilever.

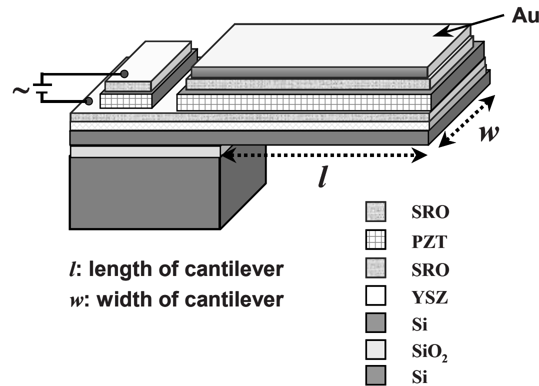

Figure 7.16: Three-dimensional schematic concept with a gold-layer coating of the cantilever.

As the discussed in chapter 6, we have presented the effect of film thickness on the piezoelectric coefficient (d_{33}) of PZT film capacitors, in which the d_{33} coefficients increase with increasing film thickness in thickness range of 75 to 500 nm. And the d_{33} coefficients decrease with the thicker films. In this part, the changes in the tip-displacement of PZT film cantilevers with different film thickness are shown in Fig. 7.17.

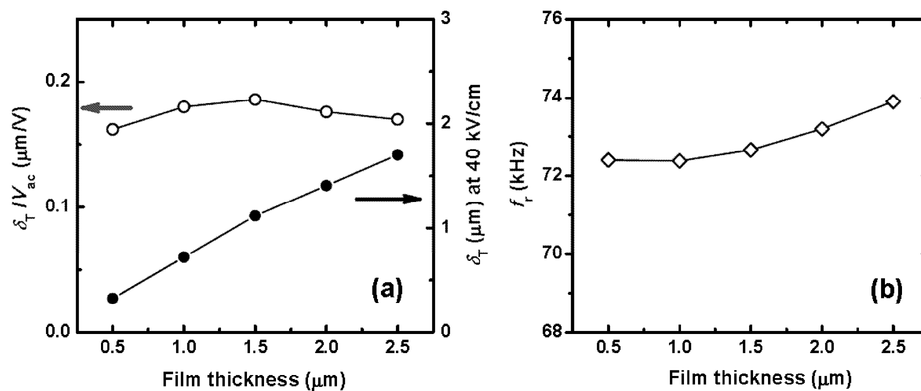

Figure 7.17: (a) Tip-displacement (δ_T) at an *ac* signal of 40 kV/cm and 8 kHz frequency and δ_T/V_{ac}, and (b) resonance frequency (f_r) of PZT film cantilevers as a function of film thickness.

Figure 7.17(a) shows that the tip-displacement (δ_T) increases near linearly with increasing film thickness, measured at an *ac* signal of 40 kV/cm and 8 kHz. This is due to the increase of applied *ac* voltage ($V_{ac}= E_{ac} \times d$, where *d* is film thickness) with increasing film thickness. The δ_T/V_{ac} values increase with film thickness in range of 0.5 to 1.5 μm and slightly reduce with increasing film thickness continuously. The film thickness dependence on resonance frequency is made evident by the first mode from Fig. 7.17(b). It is seen that increasing thickness results in higher resonance frequencies, in a manner similar to that calculated values from Eq. (7.3).

In order to investigate the effect of gold (Au) coating layer on top of PZT film cantilevers, the displacement and resonance frequency of these cantilevers were evaluated. As shown in Fig. 7.18, the resonance frequencies of PZT film cantilevers are decreased with an Au-coating layer. Assuming that Au-layer coating does not affect the spring constant of the cantilever, the mass of the Au-layer coating can be calculated as [46]:

$$f_r = \frac{1}{2\pi}\sqrt{\frac{k}{m^*}} \tag{7.9}$$

$$f_r' = \frac{1}{2\pi}\sqrt{\frac{k}{m^* + \Delta m}} \tag{7.10}$$

$$\frac{\Delta m}{m^*} = 1 - \frac{f_r'^2}{f_r^2} \tag{7.11}$$

where f_r and f_r' are the resonance frequencies of the cantilevers without and with an Au-coating layer, *k* is the spring constant, m^* and Δm are the effective mass of the cantilever and the loading mass (mass of Au-coating layer), respectively.

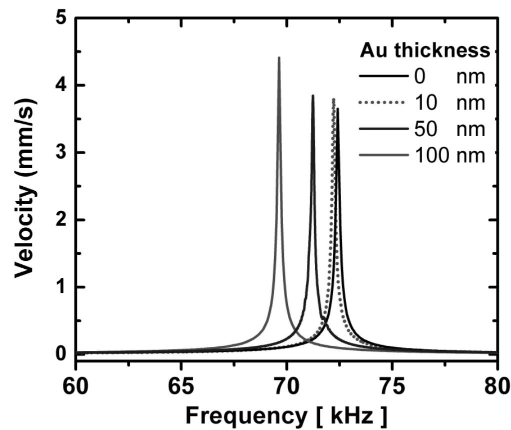

Figure 7.18: Resonance frequency spectra of the cantilevers with the Au-coating layers.

Table 7.4 shows the measured Au-coating layers on top of the cantilevers. It shows that the measured values are closed to the estimated ones, which defined from the Au layer thickness fabrication.

Table 7.4: Effect of Au-layer coating on the cantilever resonance frequency.

Au thickness (nm)	0	10	50	100
Estimated Au-mass (μg)	0	0.0077	0.0386	0.0772
Resonance frequency (kHz)	72.38	72.28	70.75	68.20
Measured Au-mass (μg)	0	0.0110	0.0352	0.0644

7.7 Effect of conductive-oxide electrodes

As mentioned previously, studies have shown that the piezoelectric properties of PZT films decrease with repeated working cycles and the effect is more pronounced for the films with platinum electrodes [47]. This behavior is generally attributed to the migration of oxygen vacancies from PZT film to the film-electrode interface that inhibits the polarization switching by pinning domain walls [11]. Moreover, due to the formation of the interfacial layers at film-electrode interfaces, the effective electric field applied to the capacitor is reduced, and hence the decrease in the polarization [10].

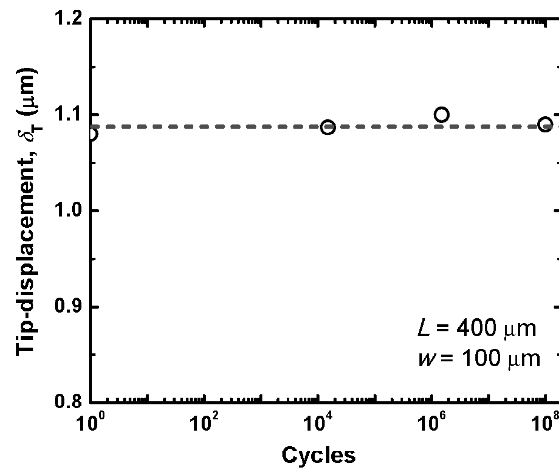

Figure 7.19: Tip-displacement as a function of the number of working cycles of the 400 μm-long cantilever.

The polarization fatigue is also responsible for the decrease the displacement of the PZT/Pt piezoelectric stacks with increasing switching cycles. This problem can be solved by using conductive oxide electrodes in the piezoelectric stack, which prevents the accumulation of oxygen vacancies at the interface and the formation of an interfacial layer. Therefore, no decrease of the ferroelectric (*remnant polarization*) properties of PZT/SRO capacitors are observed until 10^8 switching cycles, as shown in our previous study [14]. Figure 7.19 reveals the phenomenon of tip-displacement of the 400 μm-long cantilever as a function of the number of working cycles. It is noted that the displacement fatigue did not occur up to 10^8 cycles.

7.8 Summary and conclusions

Piezoelectric epitaxial PZT thin films grown on silicon cantilevers were designed, analysed and simulated successfully. Using SRO as the top- and bottom-electrodes allowed the use of typical wet and dry etching processes, thus permitting a design based completely on standard microfabrication processes. In this study, the piezoelectric cantilever arrays with beam lengths ranging from 100 to 800 μm with widths ranging from 50 to 150 μm were obtained. The main focus is on the development of piezo-cantilevers for optimization of the fabrication process.

Tensile residual stress was generated in the PZT thin films and that causes an upward deflection of the cantilever. The error between experiment and simulation is in the range of 7-10% depending on the cantilever length. The difference between the simulated and calculated values of the initial bending is about 10%. Therefore, the simulations and calculations can be used to optimize the geometric design and to predict the cantilever initial bending for further studied. This is an important step for testing facilities.

Next, the effects of cantilever geometry on the displacement and *Q*-factor were investigated. Increasing the cantilever length results in an increase of the tip-displacement and a decrease of the *Q*-factor. The cantilever width, however, did not greatly affect the mechanical properties of the cantilever. Therefore, the cantilever width can be reduced without sacrificing their properties.

Furthermore, the piezoelectric cantilevers with conductive-oxide SRO electrodes showed neither polarization nor actuation fatigue up to 10^8 cycles, which clearly indicates that the piezoelectric PZT film cantilevers can work stable for a long period of time. As a result, the SRO/PZT/SRO thin-film stacks have great potential to serve as sensors and actuators for many MEMS applications.

7.9 References

1. N. Satoh, K. Kobayashi, S. Watanabe, T. Fujii, T. Horiuchi, H. Yamada H, and K. Matsushige, *Dynamic-mode AFM using the piezoelectric cantilever: investigations of local optical and electrical properties*, Appl. Surf. Sci. **188** (1992) p. 425-429.
2. J. Baborowski, S. Hediger, P. Muralt, and Ch. Wuetrich, *Fabrication and characterization of micromachined accelerometers based on PZT thin films*, Ferroelectrics **224** (1999) p. 283-290.
3. D. J. Laser and J. G. Santiago, *A review of micropumps*, J. Micromech. Microeng. **14** (2004) p. R35-R64.
4. K. S. Yun and E. Yoon, *Micropumps for MEMS/NEMS and Microfluidic systems,* in *MEMS/NEMS Handbook Techniques and Applications*, T. L. Cornelius (Editor), Springer-Verlag (2006) p. 121-153.
5. J. H. Lee, K. H. Yoon, K. S. Hwang, J. Park, S. Ahn, and T. S. Kim, *Label free novel electrical detection using micromachined PZT monolithic thin film cantilever for the detection of C-reactive protein*, Biosens. Bioelectron. **20** (2004) p. 269-275.
6. B. P. Zhu, D. W. Wu, Q. F. Zhou, J. Shi, and K. K. Shung, *Lead zirconate titanate thick film with enhanced electrical properties for high frequency transducer applications*, Appl. Phys. Lett. **93** (2008) p. 012905(1-3).
7. J. C. Doll, B. C. Petzold, B. Ninan, R. Mullapudi, and B. L. Pruitt, *Aluminum nitride on titanium for CMOS compatible piezoelectric transducers*, J. Micromech. Microeng. **20** (2010) p. 025008(1-8).
8. J. F. Scott, *Ferroelectric Memories*, Springer-Berlin (2000).
9. P. Gerber, C. Kügeler, U. Ellerkmann, P. Schorn, U. Böttger, and R. Waser, *Effects of ferroelectric fatigue on the piezoelectric properties (d_{33}) of tetragonal lead zirconate titanate thin films*, Appl. Phys. Lett. **86** (2005) p. 112908(1-2).
10. A. K. Tagantsev, I. Stolichnov, E. L. Colla, and N. Setter, *Polarization fatigue in ferroelectric films: Basic experimental findings, phenomenological scenarios, and microscopic features*, J. Appl. Phys. **90** (2001) p. 1387-1402.
11. M. Dawber and J. F. Scott, *A model for fatigue in ferroelectric perovskite thin film*, Appl. Phys. Lett. **76** (2000) p. 1060-1062.
12. P. K. Larsen, G. J. M. Dormans, D. J. Taylor, and P. J. van Veldhoven, *Ferroelectric properties and fatigue of $PbZr_{0.51}Ti_{0.49}O_3$ thin films of varying thickness: Blocking layer model*, J. Appl. Phys. **76** (1994) p. 2405-2413.
13. V. Bornand, S. Trolier-McKinstry, K. Takemura, and C. A. Randall, *Orientation dependence of fatigue behavior in relaxor ferroelectric-$PbTiO_3$ thin films*, J. Appl. Phys. **87** (2000) p. 3965-3972.
14. M. Dekkers, M. D. Nguyen, R. Steenwelle, P. M. te Riele, D. H. A. Blank, and G. Rijnders, *Ferroelectric properties of epitaxial $Pb(Zr,Ti)O_3$ thin films on silicon by control of crystal orientation*, Appl. Phys. Lett. **95** (2009) p. 012902(1-3).
15. M. -S. Chen, T. -B. Wu, and J. -M. Wu, *Effect of textured $LaNiO_3$ electrode on the fatigue improvement of $Pb(Zr_{0.53}Ti_{0.47})O_3$ thin films*, Appl. Phys. Lett. **68** (1996) p. 1430-1432.

16. B. G. Chae, Y. S. Yang, S. H. Lee, M. S. Jang, S. J. Lee, S. H. Kim, W. S. Baek, and S. C. Kwon, *Comparative analysis for the crystalline and ferroelectric properties of Pb(Zr,Ti)O_3 thin films deposited on metallic $LaNiO_3$ and Pt electrodes*, Thin Solid Films **410** (2002) p. 107-113.
17. M. D. Nguyen, R. J. A. Steenwelle, P. M. te Riele, J. M. Dekkers, D. H. A. Blank, and G. Rijnders, *Growth and properties of functional oxide thin films for PiezoMEMS*, in *EUROSENSORS XXII*, Dresden-Germany (2008) p. 810-813.
18. H. Maiwa, J. A. Christman, S. H. Kim, D. J. Kim, J. P. Maria, B. Chen, S. K. Streiffer, and A. I. Kingon, *Measurement of piezoelectric displacements of Pb(Zr, Ti)O_3 thin films using a double-beam interferometer*, Jpn. J. Appl. Phys. **38** (1999) p. 5402-5405.
19. G. S. Wang, D. Rémiens, E. Dogheche, and X. L. Dong, *Effect of thermal strain on structure and polarization fatigue of CSD-derived $PbZr_{0.53}Ti_{0.47}O_3/LaNiO_3$ hetero-structures*, Appl. Phys. A: Mater. Sci. Process. **88** (2007) p. 657-660.
20. J. Wang, H. Zheng, Z. Ma, S. Prasertchoung, M. Wuttig, R. Droopad, J. Yu, K. Eisenbeiser, and Ramesh R, *Epitaxial $BiFeO_3$ thin films on Si*, Appl. Phys. Lett. **85** (2004) p. 2574-2576.
21. K. Kurihara, M. Kondo, K. Sato, M. Ishii, N. Wakiya, and K. Shinozaki, *Electrooptic properties of epitaxial lead zirconate titanate films on silicon substrates*, Jpn. J. Appl. Phys. **46** (2007) p. 6929-6932.
22. M. Y. Al Aioubi, V. Djakov, S. E. Huq, and P. D. Prewett, *Deflection and load characterisation of bimorph actuators for bioMEMS and other applications*, Microelectron. Eng. **73-74** (2004) p. 898-903.
23. W. H. Chu, M. Mehregany, and R. L. Mullen, *Analysis of tip deflection and force of a bimetallic cantilever microactuator*, J. Micromech. Microeng. **3** (1993) p. 4-7.
24. R. S. Gates and J. R. Pratt, *Prototype cantilevers for SI-traceable nanonewton force calibration* Meas. Sci. Technol. **17** (2006) p. 2852-2860
25. M. Palacio and B. Bhushan, *Nanotribological and nanomechanical properties of lubricated PZT thin films for ferroelectric data storage applications*, J. Vac. Sci. Technol. A **26** (2008) p. 768-776.
26. K. J. Kwak and B. Bhushan, *Platinum-coated probes sliding at up to 100 mm/s against lead zirconate titanate films for atomic force microscopy probe-based ferroelectric recording technology*, J. Vac. Sci. Technol. A **26** (2008) p. 783-793.
27. S. Park, D. Kwak, H. Ko, T. Song, and D. Cho, *Selective silicon-on-insulator (SOI) implant: a new micromachining method without footing and residual stress*, J. Micromech. Microeng. **15** (2005) p. 1607-13.
28. T. Kobayashi, M. Ichiki, T. Noguchi, and R. Maeda, *Deflection of wafers and cantilevers with Pt/LNO/PZT/LNO/Pt/Ti/SiO_2 multilayered structure*, Thin Solid Films **516** (2008) p. 5272-5276.
29. M. J. Madou, *Fundamentals of Microfabrication: The Science of Miniaturization*, Second Edition, CRC Press (2002).
30. S. Sherrit, H. D. Wiederick, B. K. Mukherjee, and M. Sayer, *An accurate equivalent circuit for the unloaded piezoelectric vibrator in the thickness mode*, J. Phys. D: Appl. Phys. **30** (1997) p. 2354-2363.
31. B. Piekarski, D. DeVoe, M. Dubey, R. Kaul, and J. Conrad, *Surface micromachined piezoelectric resonant beam filters*, Sensors and Actuators A **91** (2001) p. 313-320.

32. T. H. Fang, S. R. Jian, and D. S. Chuu, *Nanomechanical properties of lead zirconate titanate thin films by nanoindentation*, J. Phys.: Condens. Matter **15** (2003) p. 5253-5259.

33. M. Alvarez, J. Tamayo, J. A. Plaza, K. Zinoviev, C. Dominguez, and L. M. Lechuga, *Dimension dependence of the thermomechanical noise of microcantilevers*, J. Appl. Phys. **99** (2006) p. 024910(1-7).

34. F. R. Blom, S. Bouwstra, M. Elwenspoek, and J. H. J. Fluitman, *Dependence of the quality factor of micromachined silicon beam resonators on pressure and geometry*, J. Vac. Sci. & Technol. B **10** (1992) p. 19-26.

35. Q. M. Wang and L. E. Cross, *Determination of Young's modulus of the reduced layer of a piezoelectric RAINBOW actuator*, J. Appl. Phys. **83** (1998) p. 5358-5363.

36. Y. Lee, G. Lim, and W. Moon, *A piezoelectric micro-cantilever bio-sensor using the mass-micro-balancing technique with self-excitation*, Microsyst. Technol. **13** (2006) p. 563-567.

37. L. Johnson, A. K. Gupta, A. Ghafoor, D. Akin, and R. Bashir, *Characterization of vaccinia virus particles using microscale silicon cantilever resonators and atomic force microscopy*, Sensors and Actuators B **115** (2006) p. 189–197.

38. K. Y. Yasumura, T. D. Stowe, E. M. Chow, T. Pfafman, T. W. Kenny, B. C. Stipe, and D. Rugar *Quality factors in micron- and submicron-thick cantilevers*, J. Microelectromech. Syst. **9** (2000) p. 117-125.

39. J. H. Park, T. Y. Kwon, D. S. Yoon, H. Kim, and T. S. Kim, *Fabrication of microcantilever sensors actuated by piezoelectric $Pb(Zr_{0.52}Ti_{0.48})O_3$ thick films and determination of their electromechanical characteristics*, Adv. Funct. Mater. **15** (2005) p. 2021-2028.

40. J. Lu, T. Ikehara, Y. Zhang, R. Maeda, and T. Mihara, *Energy Dissipation Mechanisms in Lead Zirconate Titanate Thin Film Transduced Micro Cantilevers*, Jpn. J. Appl. Phys. **45** (2006) p. 8795-800.

41. Y. Jinling, T. Ono, and M. Esashi, *Energy dissipation in submicrometer thick single-crystal silicon cantilevers*, J. Microelectromech. Syst. **11** (2002) p. 775-783.

42. Z. Hao, A. Erbil, and F. Ayazi, *An analytical model for support loss in micromachined beam resonators with in-plane flexural vibrations*, Sensors and Actuators A **109** (2003) p. 156-164.

43. G. Lévêque, P. Girard, S. Belaidi, G. C. Solal, *Effects of air damping in noncontact resonant force microscopy*, Rev. Sci. Instrum. **68** (1997) p. 4137-4144.

44. C. Ziegler, *Cantilever-based biosensors*, Anal. Bioanal. Chem. **379** (2004) p. 946-959.

45. D. Ramos, M. Arroyo-Hernandez, E. Gil-Santos, H. D. Tong, C. Van Rijn, M. Calleja, and J. Tamayo, *Arrays of Dual Nanomechanical Resonators for Selective Biological Detection*, Anal. Chem. **81** (2009) p. 2274-2279.

46. J. H. Lee, K. H. Yoon, K. S. Hwang, J. Park, S. Ahn, T. S. Kim, *Label free novel electrical detection using micromachined PZT monolithic thin film cantilever for the detection of C-reactive protein*, Biosen. Bioelectron. **20** (2004) p. 269-275.

47. A. L. Kholkin, E. L. Colla, A. K. Tagantsev, D. V. Taylor, and N. Setter, *Fatigue of piezoelectric properties in $Pb(Zr,Ti)O_3$ films*, Appl. Phys. Lett. **68** (1996) p. 2577-2579.

Summary

In this thesis, the integration of lead zirconate titanate $Pb(Zr,Ti)O_3$ (PZT) thin films into piezoelectric microelectromechanical systems (MEMS) based on silicon is studied. In these structures, all epitaxial oxide layers (thin film/electrode/buffer-layer(s)) were deposited by pulsed laser deposition (PLD).

Initial work was on the PLD technique of epitaxial PZT thin films on $SrRuO_3$ (SRO) bottom-electrodes buffered different substrates like silicon and single-crystal oxide substrates including $SrTiO_3$ (STO) and YSZ (chapter 3). First, orientation control of PZT thin films on silicon has been studied. We found that by using a seed-layer (~4 Å) of Ru-deficient $Sr_nRu_{n-1}O_{3n-2}$ between SRO bottom-electrode and CeO_2/YSZ buffered (001)Si substrates, the orientation of PZT thin films can be switched from (110) to (001). In order to investigate ferroelectric domain formation in PZT thin films from the point of view of the thermal residual stress (tensile and compressive stress), epitaxial PZT thin films were deposited on different substrates. PZT thin films grown on low thermal expansion substrates, such as silicon, were preferentially *a*-domain oriented (the film stress is tensile). Whereas, PZT thin films grown on high thermal expansion substrates, as in the case of (001)STO or (001)YSZ substrate, were preferentially *c*-domain oriented (the film stress is compressive).

Next, in chapter 4, the effects of the electrodes (metal and metallic oxide) on the polarization switching characteristics in PZT films are investigated. Thin films of PZT(52/48) deposited on platinized silicon substrates exhibit significant degradation (fatigue) in polarization by the repetition of switching cycles. The fatigue behavior observed in PZT/Pt capacitors relates to pinning of domain walls and inhibiting switching of the domains, due to the accumulation of oxygen vacancies near the interface after switching. When the conductive-oxide SRO electrodes were substituted for Pt, the accumulation of oxygen vacancies near the interface was prevented, and therefore the fatigue-free behavior was observed in the PZT/SRO capacitors up to 10^8 switching cycles. Furthermore, we have also determined the relationships between ferroelectric properties and domain orientations of epitaxial PZT(52/48) thin films. PZT thin films that were *c*-domain oriented had higher remnant polarizations and lower dielectric constants than thin films that were *a*-domain oriented.

In chapter 5, the polarization and dielectric constant responses in the epitaxial (110)-oriented PZT thin films are studied with changing film thickness (75 – 2000 nm) and for a wide range of Zr/Ti compositions (60/40, 52/48, 40/60 and 20/80). It is observed that a maximum dielectric constant is achieved near the morphotropic phase boundary (MPB) composition, showing the same trend as bulk PZT ceramics. Better squareness in *P-E* hysteresis loops higher values of remnant polarization are obtained in tetragonal compositions. These values of remnant polarization and the dependence of remnant polarization on composition are quite different from those of the bulk PZT ceramics where remnant polarization exhibits a maximum at the MPB. Moreover, the films with a high Ti-content exhibit more abrupt domain switching and a larger signal to noise (Q_{sw}/Q_{nsw}) ratio of the polarization hysteresis loop.

The effects film thickness on the microstructure and electrical properties of PZT(52/48) films have been also investigated in this chapter. In the film thickness range investigated, the microstructure and crystalline structure almost do not change with thickness. The thickness dependence of the remnant polarization and the dielectric constant is interpreted in terms of the interfacial layer at the film/electrode interface. The increased remnant polarization and dielectric constant is due to the reduction of interfacial effect in PZT films with an increase in film thickness. Moreover, the reduction of interfacial effect also leads to the decrease in coercive field.

In chapter 6, we have reported the relationship between ferroelectric and piezoelectric properties in PZT thin films. The position of the MPB, as determined from significant enhancements in the effective piezoelectric coefficient and dielectric constant, coincides with the bulk PZT ceramics. Values of maximum piezoelectric coefficient (d_{33}) and dielectric constant are 92 pm/V and 1220, respectively, observed for the MPB composition. These results indicated that the piezoelectric coefficient in the PZT thin films with various Zr/Ti composition ratios is governed by the extrinsic (domain-walls) contribution such as that found in bulk PZT ceramics rather than the intrinsic (lattice variation) contribution. Moreover, the effective electrostriction coefficients (Q_{eff}), evaluated from the relationship between the ferroelectric properties (spontaneous polarization, relative dielectric constant) and the piezoelectric coefficients, show consistently larger values in the tetragonal films.

The effect of the interfacial layer on the piezoelectric properties was studied by changing the film thickness. The increased d_{33} coefficient (64-132 pm/V) with the film thickness (75-500 nm) was due to the decrease in the effect of interfacial layer. In addition, the increase in the d_{33} coefficient with increasing film thickness is mainly caused by the intrinsic contribution. Moreover, in chapter 6, we have also investigated the effect of thermal residual stress on the piezoelectric properties of PZT thin films. Due to different thermal expansion coefficients between the PZT films and the substrates, thermal tensile stress is induced in the PZT films grown on silicon substrates, while thermal compressive

stress is induced in the PZT films grown on YSZ and STO substrates. The results show that the d_{33} and Q_{eff} coefficients increased in the films with compressive stress. However, we found that the d_{33} and Q_{eff} values are significantly smaller than those in bulk PZT ceramics, most probably due to substrate clamping.

In chapter 7, the integration of ferroelectric PZT thin films onto Si cantilever beams was investigated. The main focus of this chapter is on the development of piezo-cantilevers for optimization of the fabrication process as well as for understanding of the potential applications. As the results, using the PLD technique and MEMS micro-fabrication processes, piezoelectric PZT cantilever arrays with beam lengths ranging from 100 to 800 μm with widths ranging from 50 to 150 μm were designed and fabricated.

The investigation of initial bending on the cantilever geometry (length, width, and thickness), due to the residual stress originating from the mismatch in the thermal expansion between the silicon beam and the piezoelectric film, is an important parameter for sensing applications. The advantage of using finite-element analysis (FEA) software IntelliSuite™ is that we can define the initial bending of the cantilever. The ratio of the tip-initial bending to the cantilever length is found to be 0.5-1.8%. The error between experiment and simulation is in the range of 7-10% depending on the cantilever length. The difference between the simulated and calculated values of the initial bending is about 10%. Therefore, the simulations and calculations can be used to optimize the geometric design and to predict the cantilever initial bending for further studied. This is an important step for testing facilities.

Increasing the cantilever length results in an increase of the tip-displacement and a decrease of the resonance frequency. The cantilever width, however, did not greatly affect the sensitivity of the cantilever. Short cantilever length improves the *Q*-factor and it is predicted to improve the sensor sensitivity for a small mass detection device. Since measured results suggested that the sensor sensitivity was insensitive to the cantilever width, therefore, the cantilever width can be reduced without sacrificing sensor performance. Furthermore, the piezoelectric cantilevers with conductive-oxide SRO electrodes showed neither polarization nor actuation fatigue up to 10^8 cycles, which clearly indicates that the piezoelectric PZT film cantilevers can work stable for a long period of time. As a result, the SRO/PZT/SRO thin-film stacks have great potential to serve as sensors and actuators for many MEMS applications.

Samenvatting

Dit proefschrift beschrijft het onderzoek naar de integratie van lood zirconium titanaat (PZT) dunne lagen, piezoelektrische micro-elektromechanische systemen in silicium (Si) technologie. Opeenvolgende epitaxiale lagen (dunne film/elektroden/buffer-lagen) zijn allen gedeponeerd met behulp van gepulste laser depositie (PLD).

Eerst is onderzoek gedaan naar de epitaxiale groei van PZT dunne lagen met PLD op strontium ruthanaat (SRO) gebufferde substraten zoals silicium en één-kristal oxiden, waaronder strontium titanaat (STO) en yttrium gestabiliseerd zirkonium oxide (YSZ) (hoofdstuk 3). Hierin is de controle van de kristalorientatie van dunne lagen PZT op silicium bestudeerd. Door een kiemlaag (4 Å) van Ru-arm $Sr_nRu_{n-1}O_{3n-2}$ tussen de SRO onder elektrode en het CeO_2/YSZ gebufferde Si te gebruiken kan de oriëntatie van PZT lagen van (110) naar (001) gedraaid worden. Om de invloed van ferroelektrische domeinformatie in PZT films in relatie tot de thermische restspanning (comprimerend en rek) te kunnen onderzoeken zijn epitaxiale PZT dunne lagen gegroeid op verschillende substraten. PZT lagen die gegroeid zijn op substraten met een lage thermische expansie, zoals silicium, vertonen bij voorkeur een *a*-domein oriëntatie (er is een rekspanning in de laag). Anderzijds, PZT dunne lagen gegroeid op substraten met hoge thermische expansie, zoals in het geval van (001)STO en (001)YSZ substraten, vertonen bij voorkeur een *c*-domein oriëntatie (er is een compressieve spanning in de laag).

Vervolgens is in hoofdstuk 4 het effect van de electrodes (metaal en metaal-oxide) op de polariseerbaarheid van PZT lagen onderzocht. Dunne lagen PZT (52/48) gedeponeerd op Si substraten met platina elektroden vertonen een significante degradatie (fatigue) in polarisatie na veelvuldig schakelen. Het fatigue gedrag waargenomen in de PZT/Pt capaciteiten is gerelateerd aan het dynamische gedrag van domein grenzen en verhindering van schakelen van de domeinen door accumulatie van zuurstof vacatures aan het grensvlak tussen laag en elektrode. Deze accumulatie kan worden tegengegaan wanneer de Pt elektrodes worden vervangen door oxidisch-geleidende SRO elektrodes, waardoor fatigue-vrij gedrag in de PZT/SRO capaciteiten tot 10^8 schakelmomenten kan worden waargenomen. Bovendien is het verband tussen het schakelgedrag en de domein oriëntatie van epitaxiale PZT(52/48) lagen bepaald. PZT lagen die *c*-domein zijn geöriënteerd vertonen een hogere remanente polarisatie en een lagere diëlektrische constante dan lagen die *a*-domein zijn geöriënteerd.

In hoofdstuk 5 zijn het polarisatie gedrag en de diëlektrische constante van (100) georiënteerde dunne lagen bestudeerd met verschillende laagdiktes (75 – 2000 nm) en een grote variatie in Zr/Ti verhouding (60/40, 52/48, 40/60 en 20/80). De maximale diëlektrische constante werd gevonden in de compositie bij de morfotropische fase grens (MPB), net zoals in bulk PZT keramiek. *P-E* hysterese loops met eenduidig schakelgedrag en hogere remanente polarisaties worden behaald in tetragonale composities. De waarde en afhankelijkheid van deze remanente polarisatie met betrekking tot de compositie zijn daarentegen in ruime mate verschillend van die in bulk PZT keramiek, waar de remanente polarisatie een maximum bij de MPB vertoont. Bovendien laten de dunne lagen met een hoog Ti-gehalte een abrupter domein schakel gedrag en een groter signaal ruisverhouding (Q_{sw}/Q_{nsw}) van de hysterese polarisatie loop zien.

De effecten van de laagdikte op de microstructuur en elektrische eigenschappen van PZT(52/48) dunne lagen zijn ook in dit hoofdstuk behandeld. In het onderzochte laagdikte bereik is er nagenoeg geen dikteafhankelijkheid van de microstructuur en elektrische eigenschappen. De dikteafhankelijkheid van de remanente polarisatie en diëlektrische constante kan worden uitgelegd aan de hand van de invloed van de grenslaag tussen elektrode en dunne laag. De verhoogde remanente polarisatie en diëlektrische constante wordt veroorzaakt door een kleinere invloed van het effect van de tussenlaag wanneer de laagdikte toeneemt. Dit leidt bovendien tot een lager coërcief veld.

In hoofdstuk 6 is het verband tussen de ferro- en piezo-elektrische eigenschappen in PZT dunne lagen gerapporteerd. De compositieafhankelijkheid van de MPB, zoals vastgesteld door observatie van significant hogere waardes van de effectieve piezoelektrische coëfficiënt en diëlektrische constante, komt overeen met die voor bulk PZT keramiek. De maximale waardes voor de piezoelektrische coëfficiënt (d_{33}) en diëlektrische constante zijn respectievelijk 92 pm/V and 1220 voor de MPB compositie. De piezoelektrische coëfficiënt in PZT dunne lagen met verschillende Zr/Ti composities wordt gedomineerd door excentrieke (domein-grens) bijdragen zoals in bulk PZT, in plaats van intrinsieke (rooster variatie) bijdragen. Bovendien vertoont de effectieve elektrostrictie coëfficiënt (Q_{eff}), berekend uit de verhouding tussen de ferro elektrische eigenschappen (spontane polarisatie, relatieve diëlektrische constante) en de piezoelektrische coëfficiënten, consequent hogere waardes in tetragonale lagen.

Het effect van de tussenlaag op de piezo elektrische eigenschappen is bestudeerd door de laagdikte te veranderen. De toename van de d_{33} coëfficiënt (64-132 pm/V) met de laagdikte (75-500 nm) wordt veroorzaakt door de afname van het effect van de tussenlaag. De toename van de d_{33} coëfficiënt is verder voornamelijk aan de intrinsieke bijdragen worden toegeschreven.

Bovendien is in hoofdstuk 6 ook het effect van de thermische restspanning op de piezo elektrische eigenschappen van de PZT lagen onderzocht. Door het verschil in thermische uitzettings coëfficiënt tussen laag en substraat wordt een thermische rekspanning

geïnduceerd in PZT gegroeid op silicium, terwijl er een thermische compressieve spanning wordt geïnduceerd in PZT gegroeid op YSZ en STO. De resultaten laten zien dat de d_{33} en Q_{eff} coëfficiënten toenemen in dunne lagen onder compressieve spanning. Deze waarden zijn echter significant lager dan die in bulk PZT keramiek, hoogstwaarschijnlijk doordat de laag vastgeklemd zit op het substraat.

In hoofdstuk 7 is de integratie van PZT lagen in Si cantilever beams (MEMS) onderzocht. Bij de ontwikkeling van piezo-cantilevers zoals beschreven in dit hoofdstuk is voornamelijk op de optimalisatie van het fabricage proces gericht, maar ook het begrip van de potentiële applicaties. Uiteindelijk zijn met behulp van PLD en het MEMS fabricage proces piezoelektrische cantilever arrays ontworpen en gerealiseerd. De lengte van de cantilever beams variëerde van 100 tot 800 μm, en de breedte van 50 tot 150 μm.

De bijdrage van de initiële buiging van de cantilever (lengte, breedte en dikte), veroorzaakt door de rest spanning door het verschil in thermische uitzetting coëfficiënt tussen de silicium beam en de piezo elektrische laag, is een belangrijke parameter voor sensor toepassingen. Het voordeel van het gebruik van eindig-element analyse (FEA) software IntelliSuite™ is dat de initiële buiging van de cantilever gedefiniëerd kan worden. De verhouding tussen de initiële tip buiging en de cantilever lengte bleek 0.5-1.8%. De foutmarge tussen experiment en simulatie bleek in de order van 7-10%, afhankelijk van de cantilever lengte. Het verschil tussen de gesimuleerde en berekende waardes van de initiële buiging bleek 10%. Hieruit blijkt dat de simulaties en berekeningen gebruikt kunnen worden voor het geometrische design en de initiële buiging van de cantilever kunnen voorspellen. Dit is van groot belang voor test faciliteiten.

Een toenemende cantilever lengte resulteert in toenemende tip uitwijkingen en een afname van de resonantie frequentie. Echter, variatie in de breedte van de cantilever veranderde de gevoeligheid nagenoeg niet. Korte cantilevers verhogen de Q-factor, waardoor dit de gevoeligheid voor kleine massadetectiesystemen significant kan verbeteren. Doordat metingen uitwijzen dat de sensor gevoeligheid niet afhankelijk is van de breedte van de cantilever, kan deze breedte vermindert worden zonder dat dit ten koste gaat van de prestaties van de sensor. Bovendien is in piezoelektrische cantilevers met oxidisch geleidende SRO elektrodes geen polarisatie of actuatie fatigue waargenomen tot 10^8 schakelingen, waaruit blijkt dat de PZT dunne film cantilevers lang en stabiel kunnen funtioneren. Hierdoor heeft de SRO/PZT/SRO dunne film configuratie een grote potentie voor toepassingen als sensor en actuator in meerdere MEMS systemen.

List of publications

1. Matthijn Dekkers*, Minh D. Nguyen*, Ruud Steenwelle, Paul M. te Riele, Dave H. A. Blank, and Guus Rijnders, *Ferroelectric properties of epitaxial $Pb(Zr,Ti)O_3$ thin films on silicon by control of crystal orientation*, Appl. Phys. Lett. **95** (2009) p. 012902(1-3) (* *equal contribution*)
   (as a part of chapters 3 & 4)
2. Minh D. Nguyen, Matthijn Dekkers, Ruud Steenwelle, Evert Houwman, Xin Wan, Dave H. A. Blank, and Guus Rijnders, *Residual stress effects on ferroelectric and piezoelectric properties of $Pb(Zr,Ti)O_3$ thin films*, Appl. Phys. Lett. (submitted for publication)
   (as a part of chapters 3 , 4 & 6)
3. M. D. Nguyen, H. Nazeer, K. Karakaya, S. V. Pham, R. Steenwelle, M. Dekkers, L. Abelmann, D. H. A. Blank, and G. Rijnders, *Characterization of epitaxial $Pb(Zr,Ti)O_3$ thin films deposited by pulsed laser deposition on silicon cantilevers*, J. Micromech. Microeng. (submitted for publication)
   (as a part of chapter 7)
4. Minh D. Nguyen, Matthijn Dekkers, Ruud Steenwelle, Dave H. A. Blank, and Guus Rijnders, *Epitaxial growth of PZT thin films and Relationship between the crystal structure and the electrical-mechanical properties*, in preparation.
   (as a part of chapters 3 , 4 & 6)
5. Vu Ngoc Hung, Le Van Minh, Bui Thi Huyen, and Nguyen Duc Minh, *Improvement of electrical property for $Pb(Zr_{0.53}Ti_{0.47})O_3$ ferroelectric thin film deposited by sol-gel method on SRO electrode*, J. Phys.: Conf. Ser. **187** (2009) p. 012063(1-6).

Contribution to scientific meetings

Oral presentations

1. M. D. Nguyen, K. Karakaya, P. M. te Riele, D. H. A. Blank, A. J. H. M. Rijnders, *Piezoelectric materials for MEMS applications*, The 3rd IEEE International Conference on Nano/Micro Engineered and Molecular Systems, Sanya-China (2008) p. 315-318.
2. M. D. Nguyen, R. J. A. Steenwelle, P. M. te Riele, J. M. Dekkers, D. H. A. Blank, and G. Rijnders, *Ferroelectric and dielectric properties of Pb(Zr,Ti)O_3 thin film capacitors*, The 4th Annual IEEE International Conference on Nano/Micro Engineered and Molecular Systems, Shenzhen-China (2009) pp. 644-647.
3. Minh Nguyen, Ruud Steenwelle, Matthijn Dekkers, Dave HA Blank and Guus Rijnders, *Control of the Crystallographic Orientation of PZT Thin Films on Silicon Substrates by a Single Process Step*, MRS Fall Meeting, Boston-USA (2009).
4. R. J. A. Steenwelle, J. M. Dekkers, M. D. Nguyen, D. H. A. Blank, & A. J. H. M. Rijnders, *Control of the crystallographic orientation of PZT thin films on silicon substrates by a single process step in Pulsed Laser Deposition*, E-MRS Spring meeting, Strasbourg-France (2009).
5. R. J. A. Steenwelle, J. M. Dekkers, M. D. Nguyen, D. H. A. Blank, & A. J. H. M. Rijnders, *Thin Film PiezoMEMS by Pulsed Laser Deposition - Anisotropy of piezoelectric properties*, The 12th International Meeting on Ferroelectricity and 18th IEEE International Symposium on Applications of Ferroelectrics (IMF-ISAF), Xian-China (2009).

Poster presentations

1. M. D. Nguyen, R. J. A. Steenwelle, P. M. te Riele, J. M. Dekkers, D. H. A. Blank, and G. Rijnders, *Growth and properties of functional oxide thin films for PiezoMEMS*, EUROSENSORS XXII, Dresden-Germany (2008) p. 810-813.
2. T. M. Stawski, O. F. Göbel, M. D. Nguyen, R. J. A. Steenwelle, S. A. Veldhuis, J. E. ten Elshof, A. J. H. M. Rijnders, and D. H. A. Blank, *Ferroelectric materials and their applications in devices*, MESA+ Annual Meeting, Enschede-The Netherlands (2008).
3. R. Steenwelle, M. D. Nguyen, M. Dekkers, E. Houwman, M. Matthew, G. Rijnders, and D. H. A. Blank, *Oxide electronics on Si: adding new functionalities to Si-technology, MESA+ - University of Münster workshop*, Enschede-The Netherlands (2008).
4. R. J. A. Steenwelle, M. D. Nguyen, J. M. Dekkers, A. C. de Waal, X. Wan, D. H. A. Blank, & A. J. H. M. Rijnders, *Piezo-electric MEMS by Pulsed Laser Deposition*, Annual MESA+ meeting, Enschede (2009).
5. R. J. A. Steenwelle, M. D. Nguyen, J. M. Dekkers, X. Wan, A. J. H. M. Rijnders, & D. H. A. Blank, *Thin film PiezoMEMS by Pulsed Laser Deposition*, Piezo 2009 - Electroceramics for End Users, Zakopane-Poland (2009).

Acknowledgements

To my family, colleagues and friends

This thesis is a result of my research at the Inorganic Materials Science (IMS) group, MESA+ Institute for Nanotechnology, University of Twente, The Netherlands.

I would like to thank all the people who have contributed to this work. First of all I am most grateful to my supervisors, Prof. Dave H. A. Blank and Prof. Guus Rijnders for giving me the opportunity to work on an exciting project and for their encouragement and scientific guidance throughout my PhD program.

Special thanks go to all (present and former) members of the Inorganic Materials Science (IMS) group. Thank you all for your help and an enjoyable working environment. Dear Koray, Paul and Matthijn, thank for your great support in sample preparation and characterization. Dear Ruud, I have thoroughly enjoyed time we spent together in taking the PZT characteristics and your "weekend music-party". Dear Brian, thank you for my thesis correcting. Many thanks are given to Marion for all administration assistance. At the last four months of the research, I have profited enormously from working with my colleagues in SolMateS company, thank you very much for your kindness and your assistance.

There are a number of members in IMS, MESA+ and other groups that made my work easier and pleasant. Dear Gerrit (IMS), thank you very much for your help with the XRD experiments. Frank and Dick (ICE), thanks for your support in sample preparation with the PLD technique. Thanks to Mark, Rico and Gerard (MESA+) for their help with the SEM, TEM and XPS measurements; Remco (TST) and Sander (SC), for the assistance with the laser Doppler vibrometer and capacitance/leakage current measurements. Ellen and Shuo (C2V), for the lithography mask fabrication and for the nice discussions about the etching processes. Hammad (TST), I cannot forget our discussions about the cantilevers and often after 6:00 PM.

I would like to thank the members of my thesis committee for their time, interest and useful comments as regard the dissertation.

Before doing PhD at the University of Twente, I had studied at the International Training Institute for Materials Science (ITIMS), Hanoi University of Technology,

Vietnam. I would like to express my deep gratitude to Prof. Than Duc Hien and Dr. Nguyen Khac Man, who were my former supervisors during my study at ITIMS as an MSc student, for their continuous support encouragements. Thanks also to the other ITIMS members: Prof. Nguyen Phu Thuy, Prof. Nguyen Duc Chien, Assoc. Prof. Vu Ngoc Hung, Assoc. Prof. Nguyen Van Hieu, Assoc. Prof. Nguyen Thanh Huy, Assoc. Prof. Nguyen Anh Tuan, Assoc. Prof. Nguyen Phuc Duong, … for their constant support. Special thanks should also be given to ITIMS'99 and my colleagues there. I cannot forget the memories we had during two years MSc course.

I would also like to acknowledge all Vietnamese friends in The Nertherlands: Hien-Nhu's family, Tu-An's family, Ha-Hanh's family, Trung-Thanh's family, "ITIMSese" Tom Aarnink, anh Cuong, Phong, Hao, Lan Anh, So, Chau, Tuan, Hieu, Tan, Trang, Viet Anh, Duc, Quyen, Nhi, Huong, Son, Tuyen, Tri (UT); Huy, Ha, Thanh, Van Anh, Nga (UvA); Trung-Hong's family, An (TU Delf). Thank you all for the warm friendship and care during the years.

With all my heart, I would like to thank my grandparents, my parents and parents-in-law for their unconditional love and patience. I am especially grateful to my wife, Giang, for her patience, her enthusiastic support, and her continuous understanding, and my sons, Manh-Dung, who are my source of happiness.

This work was funded by the Smart-Mix Program (Smart-Pie) of the Netherlands Ministry of Economic Affairs and the Netherlands Ministry of Education, Culture and Science and by the Vietnamese Overseas Scholarship Program under MOET-VOSP Project 322.

Enschede, May 2010